

Terahertz Waveguides: A Study of Microwires and Porous Fibres

by

Shaghik Atakaramians

Bachelor in Electrical Engineering (Outstanding Graduate),
Iran University of Science and Technology (IUST), Iran, 2000,
Masters in Electrical Engineering (major: Microwave Engineering),
University of Tehran, Iran, 2002.

Thesis submitted for the degree of

Doctor of Philosophy

in

Physics, Faculty of Sciences
and

Electrical and Electronic Engineering
Faculty of Engineering, Computer and Mathematical Sciences
The University of Adelaide, Australia

January, 2011

Supervisors:

Prof Derek Abbott, School of Electrical & Electronic Engineering

Dr Shahraam Afshar V., School of Chemistry & Physics

Dr Bernd M. Fischer, School of Electrical & Electronic Engineering

Prof Tanya M. Monro, School of Chemistry & Physics



© 2011

Shaghik Atakaramians

All Rights Reserved

Contents

Contents	iii
Abstract	vii
Statement of Originality	ix
Acknowledgments	xi
Conventions	xv
Publications	xvii
List of Figures	xxi
List of Tables	xxvii
Chapter 1. Introduction and Motivation	1
1.1 THz waveguides	2
1.2 Thesis overview	6
1.3 Summary of original contribution	8
Chapter 2. Review of THz generation, detection and waveguides	11
2.1 Introduction	12
2.1.1 Objective and framework	15
2.2 Generation and detection of THz pulses	15
2.2.1 Terahertz sources	16
2.2.2 Terahertz detectors	17
2.2.3 THz radiation generation and detection based on photoconductive antennas	20
2.3 Terahertz waveguides	23
2.3.1 Metallic waveguides	25
2.3.2 Dielectric Waveguides	35
2.4 Chapter Summary	55

Chapter 3. THz microwires	61
3.1 Introduction	62
3.1.1 Objective and framework	62
3.2 Optical Nanowires	62
3.3 Dielectric properties of the bulk materials in THz	64
3.4 Microwires	72
3.4.1 Electric and magnetic field distributions	74
3.4.2 Power fraction and effective area	79
3.5 Signal degradation in THz microwire	83
3.5.1 Loss mechanisms	84
3.5.2 Dispersion mechanisms	95
3.6 Chapter Summary	102
Chapter 4. THz porous fibres: concept and modelling	105
4.1 Introduction	106
4.1.1 Objective and framework	106
4.2 Sub-wavelength air-hole in a dielectric waveguide	107
4.3 Concept of THz porous fibre	109
4.4 THz characteristics of porous fibre	121
4.4.1 Power fraction and effective area	121
4.4.2 Loss and confinement	124
4.4.3 Dispersion	130
4.5 Chapter Summary	135
Chapter 5. Porous fibres: design, fabrication and cleaving	139
5.1 Introduction	140
5.1.1 Objective and framework	143
5.2 Porous fibre fabrication based on extrusion	144
5.3 Cleaving of extremely porous polymer fibres	150
5.3.1 Semiconductor dicing (SD) saw	151
5.3.2 Focused ion beam (FIB) milling	155
5.3.3 UV 193 nm laser	156
5.4 Modelling of fabricated porous fibres	160
5.5 Chapter Summary	164

Chapter 6. THz characterization of porous fibres	167
6.1 Introduction	168
6.1.1 Objective and framework	171
6.2 Characterization of waveguides	171
6.3 Porous fibre characterisation	172
6.3.1 First characterisation technique	173
6.3.2 Second characterisation technique: probing the evanescent field . .	181
6.4 Chapter Summary	197
Chapter 7. Conclusion and future work	203
7.1 Introduction	204
7.2 Thesis summary and author's contribution	204
7.3 Potential future directions	207
7.3.1 Mode profile of THz microwire and porous fibre	207
7.3.2 THz beam coupling into THz microwire and porous fibre	207
7.3.3 Bending loss of the THz microwire and porous fibre	208
7.3.4 THz microwire as a biosensor	208
7.3.5 THz porous fibre as a biosensor	209
7.4 Chapter summary	209
Appendix A. Derivation microwire equations	211
Appendix B. Data processing algorithms	217
B.1 Conventional THz-TDS analysis program	218
B.1.1 Main mfile	218
B.1.2 Functions	219
B.2 THz waveguide analysis program	224
B.2.1 Main mfile	224
B.2.2 Functions	227
B.3 Microwire	229
B.3.1 Main mfile	229
B.3.2 Functions	230
B.4 Porous fibre	233
B.4.1 Main mfile	234

Appendix C. Equipment for THz measurements	243
Bibliography	245
Glossary	259
Acronyms	261
Biography	263

Abstract

This Thesis reports the development of fibres to guide terahertz (THz) or T-ray radiation. It demonstrates the theoretical studies of THz microwires (air-clad solid core fibres) and a new form of waveguide: the *porous* fibre. Porous fibre has an arrangement of sub-wavelength featured air-holes in the cross-section, resulting in improved confinement of the propagating mode while retaining the low loss characteristic compared to air-clad sub-wavelength waveguide or microwires. Porous fibres also offer lower frequency dependent loss and dispersion compared to microwires. Furthermore, introducing asymmetrical discontinuity leads to high birefringence, which is comparable to recently achieved high birefringence in photonic crystal fibres.

Furthermore, this thesis involves the first successful fabrication of highly porous polymer fibres, with both symmetrical and asymmetrical discontinuities, via an extrusion process. In order to achieve rapid and reproducible waveguide cross-sections three different cleaving techniques—based on the use of a semiconductor dicing saw, focused ion beam milling, and a 193 nm ultraviolet laser—have been investigated for cleaving of polymer porous fibres.

Finally, two different techniques have been utilised for characterisation of porous fibres. The first approach leads to the first experimental verification of frequency dependence of effective refractive indices of polymer porous fibres and microwires. The second approach exploits a micromachined photoconductive probe-tip for sampling of the THz pulse along the waveguide, from which the frequency dependent absorption coefficient and refractive index are determined. Moreover, the evanescent field distribution of porous fibres as a function of frequency is measured for the first time.

Statement of Originality

This work contains no material that has been accepted for the award of any other degree or diploma in any university or other tertiary institution to Shaghik Atakaramians and, to the best of my knowledge and belief, contains no material previously published or written by another person, except where due reference has been made in the text.

I give consent to this copy of the thesis, when deposited in the University Library, being available for loan, photocopying, and dissemination through the library digital thesis collection, subject to the provisions of the Copyright Act 1968.

I also give permission for the digital version of my thesis to be made available on the web, via the University's digital research repository, the Library catalogue, the Australasian Digital Thesis Program (ADTP) and also through web search engines, unless permission has been granted by the University to restrict access for a period of time.

12 January 2011

Signed

Date

Acknowledgments

I would like to express my deep gratitude to my supervisors, Prof Derek Abbott, Dr Shahraam Afshar V., Dr Bernd M. Fischer, and Prof Tanya M. Monro. Their encouraging attitude has been valuable through out my candidature, and helped me to grow as an engineer and scientist. I have learned many positive and life time skills from my supervisors, which cannot be summarised in a few lines. However, I would like to highlight the ones that have inspired me the most. There is nothing defined as impossible in Derek's world. Any result of the work is treated as a major discovery by Shahraam's enthusiasm and readiness for discussion. Shahraam's passion about research has driven me towards my limits and consequently better outcomes. Bernd's feedback on my research caused me to look at problems differently. Being a young female scientist, Tanya has been my inspiration for what I can also achieve.

My thesis has been an exceptionally rewarding and memorable journey. During this journey I have worked with many Engineers, Scientists, and Technicians, who have broaden my view and approach to tackle problems. Special thanks to Dr Heike Ebendorff-Heidepriem, deputy director of Centre of Expertise in Photonics (CoEP) from School of Chemistry and Physics at University of Adelaide, for her assistance and guidance on fibre fabrication process and proof reading of Chapters 3 and 5, and Dr Michael Nagel from Institute of Semiconductor Electronics (ISE) at RWTH Aachen University for his assistance with analysing and interpreting the waveguide experimental results.

I acknowledge informative discussions with A/Prof Chris Coleman, A/Prof Christophe Fumeaux, and Dr Brian H.-W. Ng from School of Electrical and Electronic Engineering at University of Adelaide, Prof John Canning from Interdisciplinary Photonics Laboratories (iPL) at University of Sydney, and Prof Barry Luther-Davies from the Australian National University (ANU).

I would like to thank Mr Ian R. Linke, Mr Alban P. O'Brien, Mr Brandon F. Pullen, and Mr Pavel Simcik from School of Electrical & Electronic Engineering (EEE), and Mr Herbert Foo, and Mr Kevin Kuan from School of Chemistry and Physics for their continuous technical support and interest in my work. Special thanks to Mr Roger Moore from CoEP for fibre drawing.

I gratefully acknowledge the assistance of Mr Leonard Green for focused ion beam milling from Australian Microscopy and Microanalysis Research Facility (AMMRF), the Micro-Engineering staff in the development of the fibre dicing procedure the Defence Science and Technology Organisation (DSTO) Edinburgh Adelaide, and Dr Kevin Cook for UV laser cleaving from iPL at University of Sydney.

Thanks go to my friends and colleagues from the University of Adelaide; at School of Electrical and Electronic Engineering: Dr Withawat Withayachumnankul, and Dr Gretel Png for their assistance with L^AT_EX and applying for grant applications, Mr Henry Ho for T-ray laboratory hardware and experimental assistance, Dr Jegathisvaran Balakrishnan, Mr Benjamin S. Y. Ung, Mr Hungyen Lin for their company and encouragement in the T-ray laboratory; at School of Chemistry and Physics: Dr Kris Rowland, and Mr Wenqi Zhang for their assistance with FEMLAB codes, and other people in Adelaide T-ray group and CoEP, with whom I have had great moments.

Thanks go to my overseas colleagues from RWTH Aachen University, Germany, Mr Markus Wächter and Mr Mohammad Awad for assistance with THz hardware during my visit.

I am grateful for the discussion with external academics: Prof Daniel Grischkowsky, Prof James Harrington, Prof Daniel Mittleman, Prof Milica Popovic, and Prof Peter Siegel.

I gratefully acknowledge A/Prof Ole Bang from the Department of Photonics Engineering, Technical University of Denmark for supplying the COC billet, Naoki Sugimoto at Asahi Glass Japan for supplying the bismuth glass samples, and Prof David N. Jamieson at The University of Melbourne for supplying the diamond samples.

During my candidature, administrative work has been assisted by Ms Rose-Marie Descalzi, Ms Colleen Greenwood, Ms Philomena Jensen-Schmidt, Ms Ivana Rebellato, Mr Danny Di Giacomo, and Mr Stephen Guest at School of EEE and Ms Sara Boffa, and Ms Olivia Towers from School of Chemistry and Physics. Other supporting people include the IT support officers, David Bowler, and Mark J. Innes from EEE and Ramona Adorjan from School of Chemistry and Physics. People who helped augment my academic writing skills in the early days are Dr Christina Era and Dr Michelle Picard.

Major financial support has been provided by Australian Endeavour International Postgraduate Scholarship (EIPRS) and the University of Adelaide Scholarship for Postgraduate Research. Travel grants were from the School of EEE, and Research Abroad Scholarship at the University of Adelaide, Australian Research Council Nanotechnology Network

(ARCNN) Overseas Travel Fellowship, and IEEE SA Section Travel Scholarship. The Adelaide T-ray program has been supported by the ARC, the Sir Ross and Sir Keith Smith Fund, DSTO, and NHEW P/L.

At last but not the least, I would like to sincerely thank my husband, Gevik, and my parents, Destrik and Soorik, for their endless and tremendous support, encouragement, and generous patience. I would like to welcome the addition of our little princess Biayna to our family.

Conventions

Typesetting This thesis is typeset using the L^AT_EX₂ε software. T_EXnicCenter is used as an effective interface to L^AT_EX.

Referencing The Harvard style is used for referencing and citation in this thesis.

Spelling Australian English spelling is adopted, as defined by the Macquarie English Dictionary (Delbridge 2001).

System of units The units comply with the international system of units recommended in an Australian Standard: AS ISO 1000—1998 (Standards Australia Committee ME/71, Quantities, Units and Conversions 1998).

Physical constants The physical constants comply with a recommendation by the Committee on Data for Science and Technology: CODATA (Mohr and Taylor 2005).

Frequency band definition It is preferable to refer to the spectral band from 0.1 to 10 THz as ‘T-rays’, according to an argument by Abbott and Zhang (2007). T-rays have frequencies that correspond to the so-called ‘Terahertz-gap.’ Thus in the field, when we refer to ‘terahertz radiation’ this is an alternative form for T-rays. In this context, the term ‘terahertz radiation’ is understood as meaning ‘radiation in the terahertz-gap’ or T-rays and the word ‘terahertz’ is not to be confused with the units of terahertz that span three decades from 10¹² Hz.

Publications

Journal Articles

1. **Atakaramians S.**, Afshar V. S., Nagel M., Rasmussen H. K., Bang O., Monro T. M., and Abbott D., “Direct probing of evanescent field for characterization of porous terahertz fibers,” *Appl. Phys. Lett.*, **vol. 98**, 121104, 2011.
2. **Atakaramians S.**, Cook K., Ebendorff-Heidepriem H., Afshar V. S., Canning J., Abbott D., and Monro T. M., “Cleaving of extremely porous polymer fibers,” *IEEE Photonics*, **vol. 1** (6), pp. 286–292, 2009.
3. **Atakaramians S.**, Afshar V. S., Nagel M., Ebendorff-Heidepriem H., Fischer B. M., Abbott D., and Monro T. M., “THz porous fibers: design, fabrication and experimental characterization,” *Optics Express*, **vol. 17** (19), pp. 14053–14062, 2009.
4. **Atakaramians S.**, Afshar V. S., Fischer B. M., Abbott D., and Monro T. M., “Low loss, low dispersion and highly birefringent terahertz porous fibers,” *Optics Communications*, **vol. 282**(1), pp. 36–38, 2009.
5. **Atakaramians S.**, Afshar V. S., Fischer B. M., Abbott D., and Monro T. M., “Porous fibers: a novel approach to low loss THz waveguides,” *Optics Express*, **vol. 16** (12), pp. 8845–8854, 2008.
6. Withayachumnankul W., Png G., Yin X., **Atakaramians S.**, Jones I., Lin H., Ung B. S. Y., Balakrishnan J., Ng B. W.-H., Ferguson B., Mickan S. P., Fischer B. M., and Abbott D., “T-ray sensing and imaging,” *Proceedings of the IEEE, Special Issue on: T-ray Biosensing and Security*, **vol. 95** (8), pp. 1528-1558, 2007.

Conference Articles

1. **Atakaramians S.**, Afshar V. S., Nagel M., Monro T. M., and Abbott D., “A new technique to measure loss, effective refractive index and electric field distribution of THz porous fibers,” *CLEO/QELS*, Baltimore, Maryland, 2011, accepted.

2. **Atakaramians S.**, Franke H., Abbott D., Monro T. M., and Fumeaux C., “Application of full-wave electromagnetic solvers to micro/nano-structured fibres,” *ACOLS/ACOFT*, Adelaide, Australia, pp. 473-474, December 2009.
3. Ebendorff-Heidepriem H., Afshar V. S., Warren-Smith S. C., Zhang W. Q., Ruan Y., **Atakaramians S.**, and Monro T. M., “Fibres with subwavelength features: fabrication and novel guidance properties,” *ACOLS/ACOFT*, Adelaide, Australia, pp. 28-29, December 2009.
4. **Atakaramians S.**, Afshar V. S., Nagel M., Ebendorff-Heidepriem H., Fischer B. M., Abbott D., and Monro T. M., “Experimental investigation of dispersion properties of THz porous fibers,” *The 34th International IEEE Conference on Infrared, Millimeter, and Terahertz Waves*, Busan, Korea, September 2009, D.O.I.: 10.1109/ICIMW.2009.5324967.
5. **Atakaramians S.**, Afshar V. S., Nagel M., Ebendorff-Heidepriem H., Fischer B. M., Abbott D., and Monro T. M., “Experimental validation of low dispersion and high birefringence properties of THz polymer porous fibers,” *The 18th International Conference on Plastic Optical Fibers*, Sydney, Australia, September 2009.
6. Fumeaux C., Baumann D., **Atakaramians S.**, and Li E. P., “Considerations on paraxial Gaussian beam source conditions for time-domain full-wave simulations,” *25th Annual Review of Progress in Applied Computational Electromagnetics*, California, USA, pp. 401-406, March 2009.
7. **Atakaramians S.**, Afshar V. S., Fischer B. M., Abbott D., and Monro T. M., “Highly birefringent, low loss and low dispersion THz waveguides with sub-wavelength porous structure,” *EOS Annual Meeting 2008*, Paris, France, September-October 2008.
8. **Atakaramians S.**, Afshar V. S., Fischer B. M., Abbott D., and Monro T. M., “Porous fibers: Low loss, low dispersion waveguides for terahertz transmission,” *33rd International IEEE Conference on Infrared, Millimeter, and Terahertz Waves*, Pasadena, California, USA, September 2008, D.O.I: 10.1109/ICIMW.2008.4665703.
9. **Atakaramians S.**, Afshar V. S., Fischer B. M., Abbott D., and Monro T. M., “Porous fiber: a novel THz waveguide, *OECC/ACOFT*, Sydney, Australia, art. no. ThE-3, July 2008.

10. **Atakaramians S.**, Afshar V. S., Fischer B. M., Abbott D., and Monro T. M., “Loss mechanisms for T-ray microwires,” *Joint 32nd International IEEE Conference on Infrared Millimeter Waves and 15th International Conference on Terahertz Electronics*, Cardiff, UK, pp. 811–812, September 2007.
11. Afshar Vahid S., **Atakaramians S.**, Fischer B. M., Ebendorff-Heidepriem H., Monro T. M., and Abbott D., “Low loss, low dispersion T-ray transmission in microwires,” *CLEO/QELS*, Baltimore, Maryland, art. no. JWA105, 2007.
12. **Atakaramians S.**, Afshar V. S., Fischer B. M., Ebendorff-Heidepriem H., Monro T. M., and Abbott D., “Low loss terahertz transmission,” *Proceedings SPIE Micro- and Nanotechnology: Smart Materials, Nano- and Micro-Smart Systems*, vol. **6414**, art. no. 64140I, Adelaide, Australia, December 2006.
13. **Atakaramians S.**, Afshar Vahid S., Fischer B. M., Ebendorff-Heidepriem H., Monro T. M., and Abbott D., “Terahertz waveguides and materials,” *Joint 31st International IEEE Conference on Infrared Millimeter Waves and 14th International Conference on Terahertz Electronics*, Shanghai, China, p. 281, September 2006, D.O.I.: 10.1109/ICIMW.2006.368489.

List of Figures

1.1	Terahertz band in the electromagnetic spectrum	3
1.2	Thesis outline and original contribution	7
<hr/>		
2.1	Primary methods of generation, and detection of single-mode THz pulses .	14
2.2	THz generation in non-linear media	17
2.3	THz generation from accelerating electrons	18
2.4	THz generation from lasers	19
2.5	Coherent detection of THz radiation	20
2.6	Generation of THz radiation from a PC antenna	21
2.7	Schematic diagram of a dipole, strip-line and bow-tie PC switches	22
2.8	Detection of THz radiation from a PC antenna	23
2.9	Circular and rectangular cross-section metallic waveguides	27
2.10	Parallel-plate waveguide and interconnect	28
2.11	Bare metal wire experimental setup	31
2.12	Sommerfeld wire experimental set-up I	32
2.13	Sommerfeld wire experimental set-up II	32
2.14	Metallic slit waveguide experimental set-up	34
2.15	Single dielectric ring (pipe) waveguide and the experimental set-up	38
2.16	Hollow-core microstructured band-gap fibre	41
2.17	THz Bragg fibres	44
2.18	Bragg fibre experimental set-up	46
2.19	Hollow-core microstructured Kagomé fibres	47
2.20	Sub-wavelength air-clad dielectric fibre experimental arrangement	51
2.21	Solid-core microstructured fibre and the experimental arrangement I	53
2.22	Solid-core microstructured fibre and experimental arrangement II	54
2.23	Schematic of a dielectric slit rectangular and tube waveguides, and electric field enhancement	54

3.1	Optical nanowires	63
3.2	Glass and polymer samples	65
3.3	T-Ray 2000 TM system	66
3.4	Experimental setup	67
3.5	Determination of the THz dielectric properties from reference and sample pulses	71
3.6	Dielectric properties of the glass and polymer materials	72
3.7	Normalised electric fields of the fundamental mode	75
3.8	Normalised magnetic fields of the fundamental mode	76
3.9	Normalised Poynting vector distribution of the fundamental mode	77
3.10	Normalised Poynting vector distribution of the fundamental mode	78
3.11	Enhancement of the electric field in the lower refractive index medium	80
3.12	Power fraction and effective area of microwires	82
3.13	Scalar and vectorial effective area of a PMMA microwire	83
3.14	Dielectric waveguide	86
3.15	Effective loss of COC, PMMA, F2, SF6, SF57 and bismuth microwires	88
3.16	Contribution of transverse- and z -components of electric field on α_{eff}	89
3.17	Bend loss and critical bend radius of microwires	92
3.18	Correlation of the bend loss and effective area	93
3.19	Total loss: effective material and bend losses	95
3.20	Comparison of our results with Chen <i>et al.</i> (2006)	96
3.21	Material dispersion of the polymer and glass samples	98
3.22	Effective refractive indices, phase velocity and group velocity of PMMA and bismuth microwires	100
3.23	Waveguide dispersion of PMMA and bismuth microwires	101

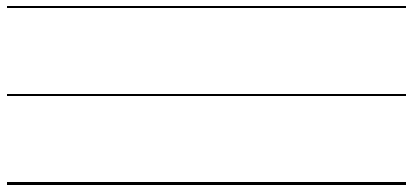
4.1	The electric field enhancement inside the central bore of a hollow core fibre	108
4.2	Power profile distribution of a porous fibre with triangular lattice	112
4.3	Numerical simulation steps of the full geometry of a PMMA porous fibre	114

4.4	Electric and magnetic field distributions of the fundamental mode	116
4.5	Numerical simulation steps of a quarter geometry of a PMMA porous fibre	118
4.6	Impact of the solution region dimension on the porous fibre parameters . .	119
4.7	Impact of the finite-element dimensions on the porous fibre parameters . .	120
4.8	Effective refractive index of three porous fibres and a microwire as a func- tion of core diameter	122
4.9	Power fraction of three porous fibres and a microwire as a function of core diameter	123
4.10	Effective area of three porous fibres and a microwire as a function of core diameter	125
4.11	Effective material loss of three porous fibres and a microwire as a function of core diameter	126
4.12	Normalised effective area versus effective material loss of three porous fibres and a microwire	127
4.13	Sketch of a bent waveguide	128
4.14	Fraction of power radiated for a porous fibre and microwire as a function of effective material loss for two different bend radii	129
4.15	Signal degradation due to the frequency dependence of the host material loss for a porous fibre and microwire	130
4.16	Different shapes of sub-wavelength air-holes in porous fibres and their nor- malised power distribution	131
4.17	Effective material loss of porous fibres with symmetrical and asymmetrical shaped sub-wavelength air-holes	133
4.18	Normalised group velocity of four porous fibres (symmetrical and asym- metrical sub-wavelength air-holes) and a microwire	134
4.19	Modal birefringence of four porous fibres (symmetrical and asymmetrical sub-wavelength air-holes) and a microwire	136
<hr/>		
5.1	Cross-section of porous preforms and fibres fabricated employing stacking and structured molding approach	142
5.2	Preform extrusion process	145
5.3	Designed die exit cross-sections	146

5.4	Photograph of the cross-sections of the extruded polymer porous preforms	148
5.5	Fibre drawing tower and porous fibre cross-sections	149
5.6	SEM images of cleaved end-face of PMMA porous fibres using a conventional blade and heating up the blade before hand	152
5.7	Images of SD saw machine	153
5.8	SEM images of SD saw cleaves	154
5.9	Images of FIB milling machine	155
5.10	SEM images of FIB milling cleaves	156
5.11	Schematic of the UV cleaving setup	157
5.12	SEM images of UV cleaves	158
5.13	Side-view images of UV cleaves	159
5.14	Progression of UV cleave	160
5.15	THz modelling of the <i>ideal</i> and <i>real</i> polymer porous fibres	163

6.1	Standard THz measurement systems employed for characterisation of THz waveguides	170
6.2	Schematic of the THz-TDS setup I for waveguide characterisation	174
6.3	Images of the waveguide holders	175
6.4	Measured THz signals and spectral amplitudes of PMMA porous fibres and a microwire	177
6.5	Effective material loss and effective refractive index of PMMA porous fibres and a microwire	179
6.6	Measured THz signals and spectral amplitudes of PMMA rectangular porous fibres	180
6.7	Absorption coefficients and effective refractive indices of a PMMA rectangular porous fibre	181
6.8	Output coupler for sampling THz pulses	182
6.9	The image of the probe-tip detector	183
6.10	Schematic of the THz-TDS setup for waveguide characterisation	185
6.11	Measured THz signal and spectrum	186
6.12	System parameters variation in time	187

6.13	Spectral amplitude variation in time	188
6.14	Image of a section of the experimental setup	189
6.15	Three methods employed for input coupling into the waveguides	190
6.16	Measured THz signal, spectrum amplitude, and THz properties of a 600 μm COC spider-web porous fibre	193
6.17	Monitoring the alignment of the probe-tip	194
6.18	Measured THz signal, spectrum amplitude, and THz properties of a 540 μm diameter COC spider-web porous fibre	199
6.19	Measured THz signal with and without waveguide in the system	200
6.20	Frequency-dependent radial field distribution of a 600 μm diameter COC spider-web porous fibre	201



List of Tables

2.1	Characteristics of ultrafast photoconductive materials	22
2.2	Summary of key parameters of THz metallic waveguides	57
2.3	Summary of key parameters of THz hollow-core dielectric waveguides	58
2.4	Summary of THz solid-core dielectric waveguides	59
3.1	Composition of heavy metal oxide glasses	65
C.1	List of equipment used at University of Adelaide A	244
C.2	List of equipment used at University of Adelaide B	244

Introduction and Motivation

THIS chapter introduces THz waveguides and outlines the motivation for the work in this Thesis. The structure of the Thesis and the contents of the Chapters are outlined, and the original contributions are summarised.

1.1 THz waveguides

The terahertz (THz) or T-ray part of the electromagnetic spectrum is located between millimetre wave and infrared frequencies. Although there are no clearly defined limits for this region, it is generally defined to be from 0.1 THz to 10 THz in the literature (Sakai 2005, Abbott and Zhang 2007). Different communities use different units to describe the THz spectrum. In this thesis we use THz (10^{12} Hz) as the spectral unit, however other units can also be used. The units and relevant equations are as follows:

- Frequency: $f \Rightarrow 0.1 - 10$ THz
- Angular frequency: $\omega = 2\pi f \Rightarrow 0.628 - 62.8$ rad/s
- Time: $t = 1/f \Rightarrow 0.1 - 10$ ps
- Wavelength: $\lambda = c/f \Rightarrow 30 \mu\text{m} - 3$ mm
- Wavenumber: $\bar{k} = k/2\pi = 1/\lambda \Rightarrow 3.3 - 333$ cm^{-1}
- Photon energy: $hf = \hbar\omega \Rightarrow 410 \mu\text{eV} - 41$ meV

where, c is the speed of light in free space, h is Planck's constant. Figure 1.1 illustrates the terahertz band or T-ray region of electromagnetic spectrum together with the units commonly used to describe the spectrum.

Historically, the principal applications of the THz region have been molecular spectral analysis and astronomical and atmospheric remote sensing used by chemists and astronomers, respectively. This part of the frequency spectrum was little explored because of the difficulty involved in generation of this radiation and a lack of a perceived need. However, during the last three decades the hardware has evolved to some measure and there have been many publications on terahertz spectroscopic applications (Mittleman 2003).

NOTE:
This figure is included on page 3 of the print copy of
the thesis held in the University of Adelaide Library.

Figure 1.1. Terahertz band in the electromagnetic spectrum. (a) Broad view of electromagnetic spectrum, (b) expanded view of the terahertz band or T-ray region of electromagnetic spectrum and its overlap with the neighboring bands, microwave and optics, and (c) other commonly used units, i.e. time, wavenumber, wavelength, and photon energy, to describe the THz spectrum, after Withayachumnankul (2009).

Terahertz spectroscopic techniques have many applications, such as detecting and identifying of weapons and chemical and explosive materials concealed beneath physical layers such as clothing or packing materials (Federici *et al.* 2005, Tonouchi 2007). This is achieved due to penetration of THz radiation through non-polar, dry, and non-metallic materials and the possibility of material characterisation, classification or recognition by means of T-ray spectroscopy (Sakai 2005, Naftaly and Miles 2007, Fischer *et al.* 2007). The classical vibration of polar molecules lies in the THz frequency range, which makes THz pulses suitable for studying molecular dynamics, e.g. rotational and vibrational modes (Png 2010). Moreover, being at sub-millimetre wavelengths, THz radiation is of low energy and non-ionizing (Fitzgerald *et al.* 2002).

The efficient transmission of THz signals using waveguides has been a major challenge since early days of THz science (Auston *et al.* 1980, Smith *et al.* 1981, Ketchen *et al.* 1986). Terahertz pulses, also known as (sub)picosecond pulses, were optically excited and sampled utilizing electrooptic switches embedded into microstrip transmission lines (Smith *et al.* 1981) or radiating antennas (Mourou *et al.* 1981b, Mourou *et al.* 1981a). Therefore, intermediate transmission media, waveguides and antennas, were inevitable in between the excitation and sampling points. Meanwhile, the pulse traveling through these transmission media were distorted due to frequency dependent loss and dispersion (Cooper 1985). This was until Auston *et al.* (1984) proposed photoconductive dipole antennas for transmitting and receiving THz pulses, where no waveguide was required in between. Subsequently, the optical techniques were employed to manipulate and improve the coupling efficiency of the generated and detected pulses (Fattinger and Grischkowsky 1988) and new design of photoconductive antennas were merged to boost the radiation power and bandwidth (van Exter *et al.* 1989a). Eventually in 1989, the first free-space tightly coupled THz spectroscopy system was proposed (van Exter *et al.* 1989a, van Exter *et al.* 1989b). Since then many preliminary proof-of-principle studies have been carried out in spectroscopy systems, where terahertz radiation propagates in free space.

However, for biomedical applications these systems have limitations such as large diffraction limited focal spot size leading to the need for inconveniently large biosamples (Abbott and Zhang 2007), and the resulting systems are quite large thus not easy to integrate with optical and infrared techniques. Terahertz waveguides provide a promising approach for overcoming these hurdles and potentially provide low-cost and robust THz integrated systems. Moreover, waveguides are essential when the application point is inaccessible or far away from the emitter, i.e. medical applications such as endoscopy, toxic gas detection in

a closed environment, and sensing, where a strong interaction of THz pulses with a tiny amount of sample is required. In some of the applications such as sensing, even a short length of low-loss waveguide structure can be beneficial. Furthermore, the THz radiation confinement to the waveguide allows improved interactions between the THz radiation and sample, particularly when the sample is located inside the waveguide, which reduces the complexity of the terahertz optical hardware needed (Nagel *et al.* 2006a, Mendis *et al.* 2009, Chin *et al.* 2009). By contrast, in free space spectroscopy systems, the THz radiation is focused by optical hardware to better interact with sample and the focus is maintained for a short length or Rayleigh range. Terahertz waveguides also are a step towards the possibility of integrating photonics with systems-on-a-chip (SoC) to create future intelligent biosensors (Eshraghian 2006).

During the last two decades, there has been a great challenge to achieve low loss and low dispersion waveguides for undistorted propagation of THz pulses; a more detailed review of waveguides is conducted in Chapter 2. The frequency dependent loss and dispersion distort the shape of THz pulses. Therefore, loss and dispersion are the primary parameters in THz waveguides that one aims to minimize in order to transmit the THz frequencies over a distance without pulse broadening. Developing a guiding structure for such a broad spectrum with minimum signal distortion is intricate. For well developed parts of the frequency spectrum, such as microwave and optics, there are waveguides in which it is possible to tailor the loss and dispersion. For THz pulses propagating in free-space different structures, coming from either microwave or optics, have been proposed in the literature for THz frequencies, each of them addressing either or both primary parameters, such as hollow metallic circular waveguides (McGowan *et al.* 1999, Gallot *et al.* 2000), hollow metallic rectangular waveguides (Gallot *et al.* 2000), sapphire fibres (Jamison *et al.* 2000), plastic ribbon waveguides (Mendis and Grischkowsky 2000), air-filled parallel-plate waveguides (Mendis and Grischkowsky 2001b, Mendis and Grischkowsky 2001a), plastic photonic crystal fibres (Han *et al.* 2002), coaxial waveguides (Jeon and Grischkowsky 2004), metal wire waveguides (Wang and Mittleman 2004, Jeon *et al.* 2005, Wächter *et al.* 2005), parallel-plate photonic waveguides (Bingham and Grischkowsky 2008), metal sheet waveguides (Jeon and Grischkowsky 2006), the dielectric-filled parallel-plate waveguides (Mendis 2006), low-index discontinuity terahertz waveguides (split rectangular and tube waveguides) (Nagel *et al.* 2006b), and metallic slit waveguides (Wächter *et al.* 2007).

Unfortunately for a broad THz spectrum this is still a challenge, i.e. there is a great demand for low-loss and low-dispersion waveguide for undistorted transmission of THz

frequencies, which will open up new opportunities in further development of compact THz systems and consequently lab-on-chip systems. Among different non-planar waveguides proposed for THz guidance, we mainly concentrate on THz dielectric waveguides in this work. At the outset of this work, dielectric sub-wavelength waveguide (Chen *et al.* 2006) was one of the promising state-of-the-art approaches for THz guidance, in terms of low-loss ($\alpha_{\text{eff}} = 0.01 \text{ cm}^{-1}$ at 0.3 THz). A disadvantage of this waveguide is that the propagating mode is only loosely confined to the structure, i.e. any perturbation in the vicinity of the waveguide leads to strong radiation losses. Therefore, improving the mode confinement while maintaining the low-power characteristics of the fibres is the main aim of this thesis. Moreover, having THz and fibre expertise, and facilities of glass and polymer fibre fabrication in The University of Adelaide provided the infrastructure for us to investigate these THz dielectric waveguides further.

In Section 1.2 of this chapter, the structure of this thesis and the content of each chapter are summarised. This is followed by Section 1.3, where the original contribution of this research has been emphasised.

1.2 Thesis overview

As outlined in Fig. 1.2, the thesis encompasses seven chapters. The original contributions of this thesis are provided in Chapters 3 to 6—the parts that lie between the two orange lines shown in Fig.1.2 below. The fundamentals necessary for understanding the main idea of each chapter is provided in the respective chapters. An additional review chapter revolving around THz generation, detection, and guiding devices is given in Chapter 2 to provide context. The detailed description for each chapter of the thesis is as follows:

Chapter 1: Introduction provides an overview of the THz spectrum and guiding devices, and outlines the motivation for the work in this Thesis. The structure of the Thesis and the contents of the Chapters are outlined. A summary of the original contributions are also provided in this chapter.

Chapter 2: Review of THz generation, detection and waveguides contains a brief review of different schemes of generation and detection of broadband and continuous-wave THz radiation with a special focus on generation and detection with photoconductive antennas. This Chapter also includes a literature review of THz waveguides (mostly aimed

	Chapter 1	Introduction
	Chapter 2	Review of THz generation, detection and waveguides
Original contribution	Chapter 3	THz microwires
	Chapter 4	THz porous fibres: concept and modelling
	Chapter 5	Porous fibres: design, fabrication, and cleaving
	Chapter 6	THz characterization of porous fibres
	Chapter 7	Conclusion and future work

Figure 1.2. Thesis outline and original contribution. The thesis is composed of seven chapters in total. The original contribution of this work lies in between the two orange lines.

at dielectric waveguides) in terms of loss and dispersion values, and the experimental set-up employed for characterisation of these waveguides.

Chapter 3: THz microwires includes the investigation of air-clad dielectric THz waveguides with diameters smaller than the operating wavelength. First, the THz dielectric properties of bulk polymer and glass samples are investigated. Then normalised field distribution, power fraction, effective area, and signal degradation (loss and dispersion) of microwires made up of these materials are evaluated and compared. The studies show that effective material losses less than 0.01 cm^{-1} are achievable for microwires operating in a regime where most of the mode power is in the air-clad. This indicates that the mode is weakly confined to the guiding structure and makes them susceptible to any gentle bend and environmental perturbation.

Chapter 4: THz porous fibres: concept and modelling revolves around a novel class of dielectric waveguide with a porous transverse cross-section that is created by arranging sub-wavelength air-holes. The guiding properties such as normalised field distribution, power fraction, effective area, and signal degradation (loss and dispersion) of these porous fibres are evaluated and quantitatively compared to that of a microwire. The effect of asymmetrical sub-wavelength air-holes on the guiding properties of porous fibres especially loss and dispersion are also investigated. The studies illustrate that the insertion of sub-wavelength air-holes improves the confinement of the propagating mode, while retaining the low loss and dispersion properties compared to that of a microwire.

Chapter 5: Porous fibers: design, fabrication and cleaving involves design and fabrication of first THz polymer porous fibres exploiting the extrusion technique. Furthermore, three different cleaving techniques, based on the use of a semiconductor dicing saw, focused ion beam milling, and a 193 nm ultraviolet laser, are investigated for cleaving of highly porous polymer fibres. In order to investigate the variation of designed and fabricated fibre cross-sections, the effective loss and effective refractive index of both cross-sections are numerically modelled and compared.

Chapter 6: THz characterisation of porous fibres includes investigation of loss and refractive index of the propagating mode of fabricated polymer porous fibres. Two different techniques are employed for characterisation of porous fibre. The first technique requires different lengths of waveguide, while the second technique exploits sampling of the THz pulse by utilising a probe-tip. Thus, no cleaving of the waveguide is required. Furthermore, for the first time the evanescent field distribution of porous fibres as a function of frequency is measured.

Chapter 7: Conclusion and future work includes the major outcomes, author's contribution, and conclusions of this work. It also contains recommendation for future work.

Several appendices provide supporting information and technical details. Appendix A provides the derivation of eigenvalue value equation, and electric and magnetic field equations for the hybrid modes of a microwire by solving the vectorial Maxwell's equations in cylindrical coordinates. Appendix B includes data processing algorithms. It contains MATLAB codes to extract the frequency dependent dielectric parameters (refractive index and absorption coefficient) of bulk material and fibre from the THz-TDS measurements. It also includes the analytical MATLAB files employed for analysing microwires, and numerical FEM algorithms implemented in MATLAB for analysing porous fibres. Appendix C describes the equipment used to characterised the THz microwire and porous fibres.

1.3 Summary of original contribution

This thesis involves a number of original contributions in the field of THz waveguides, as declared in this section.

The THz properties of four glasses and two polymers have been investigated. The concept of guiding through air-clad sub-wavelength waveguides, microwires, has been examined

in detail. For this purpose we evaluate propagating mode properties, i.e. effective refractive index, field distribution, power fraction, effective area, effective material, and bend losses, and dispersion for all glass and polymer materials. The vectorial form of Maxwell's equations are employed to evaluate the propagation constants of the modes. Moreover, the Poynting vector is employed for representation of the energy flux of the propagating mode and evaluation of waveguide parameters. We illustrate that regardless of the fibre material employed, an effective material loss less than 0.01 cm^{-1} is achievable for microwires (Withayachumnankul *et al.* 2007). We demonstrate that the diameter at which the low material loss is achieved, the higher limit of the microwire loss when most of the mode is in the core, and the frequency dependence of the loss and dispersion depend on the hosting material properties. We show that the dominant loss mechanism in microwires is the effective material loss provided that the waveguide is kept straight, which allows the bend loss to be neglected.

Low losses are achieved in microwires, because almost all of the modal power propagates in the air medium surrounding the structure. This, however, results in weak confinement of the guided mode within the structure that makes it susceptible to any small perturbation on the surface or vicinity of the structure, since a large portion of the guided power can be readily coupled into radiation modes. Furthermore, the guided modes within these structures suffer strong bend loss. We propose a novel class of dielectric waveguides, THz porous fibres, to improve the confinement of the mode while still maintaining the low loss characteristics (Atakaramians *et al.* 2008e). These waveguides have porous transverse cross-section, i.e. sub-wavelength features in the core, which leads to enhancement and confinement of the field within the holes. For similar loss values, porous fibers enable reduced distortion (frequency dependent loss and dispersion) of a broadband THz pulse compared to microwires. We also demonstrate for the first time that introducing asymmetrical sub-wavelength air-holes in the core of porous fibres leads to a birefringence $|n_x - n_y| \approx 0.026$. This value is comparable to achieved high birefringences of ≈ 0.021 at 0.3 THz (Cho *et al.* 2008) in THz solid-core microstructured fibres, and ≈ 0.025 at 1550 nm (Chen *et al.* 2004) in photonic crystals fibres. It is almost an order of magnitude higher than the birefringence of ≈ 0.001 at 1 THz (Ren *et al.* 2008) in THz air-core microstructured Bragg fibres.

In addition, this thesis demonstrates the first design and fabrication of highly porous polymer THz waveguides. Two different porous fibres, with symmetrical and asymmetrical

sub-wavelength features, with porosities higher than 50% have been fabricated successfully for the first time exploiting the extrusion technique (Atakaramians *et al.* 2008e). The numerical analysis of waveguide cross-sections based on SEM images of fabricated waveguides reveals that the fabricated waveguides are almost similar to the designed cross-sections. Using conventional blades for cleaving of polymer porous fibres compresses and deforms the rather soft polymer fibre structure. In collaboration with researchers at MicroEngineering group at DSTO Edinburgh Adelaide, Australian Microscopy and Microanalysis Research Facility (AMMRF), and Interdisciplinary Photonics Laboratories (iPL) at University of Sydney, several techniques have been investigated for cleaving of THz polymer porous fibres. The investigations reveal that employing the UV laser leads to fast and reproducible cleaves (Atakaramians *et al.* 2009d).

Moreover, in collaboration with researchers at Institut für Halbleitertechnik at RWTH Aachen University, we demonstrate the first experimental characterization of effective refractive indices (n_{eff}) of symmetrical and asymmetrical porous fibres (Atakaramians *et al.* 2008e). Finally, the first THz waveguide experimental setup has been constructed in Adelaide exploiting a sampling probe-tip. The probe-tip allows sampling the propagating mode along the waveguide, eliminating the need for cleaving of porous fibres. Employing the probe-tip permits the measurement of the frequency-dependent radial field distribution of the porous waveguide for the first time in the literature.

These original contributions of this Thesis serve to advance THz radiation transmission through the waveguides and its broad impact may be envisaged in the applications of THz sensing, where a strong interaction of THz radiation and sample under investigation can be achieved utilising waveguides.

Chapter 2

Review of THz generation, detection and waveguides

THIS chapter reviews previous work on THz waveguide development. For a better understanding of characterisation systems, different schemes for the generation and detection of broadband and continuous-wave THz radiation are reviewed briefly.

2.1 Introduction

Terahertz radiation bridges the gap between microwave and optical wavelengths, shown in Fig. 1.1. This region of spectrum has not been explored much until the last two decades, mainly because of technical difficulties involved in making efficient and compact THz sources and detectors. Since this part of the spectrum is located between the technologically well-developed microwave and infrared spectral regions, the THz gap has been benefited from the generation and detection technologies emerging from both regions. Terahertz waveguides are no exception either, i.e. several waveguide solutions based on technologies from both electronics and photonics have been studied to lower the frequency dependent loss and dispersion within the structure and enable undistorted propagation of subpicosecond pulses.

Figure 2.1(a) illustrates a primary method utilised to produce and detect picosecond pulses (Auston *et al.* 1980). The short pulses are generated and sampled by photoconductive switches incorporated into microstrip transmission lines¹. The system consists of an aluminum strips and a ground plane, and a photoconducting amorphous silicon film. The optical pulses are focused onto the photoconductive gap (25 μm) for generating and sampling of picosecond pulses. A mode locked rhodamine 6G dye laser with pulse duration of 3.5 ps and 82 MHz repetition rate at 580 nm wavelength is used for this purpose. The picosecond optical pulses generated and sampled in with this method are employed for time-resolved measurements of the impulse response of a gallium arsenide (GaAs) field-effect transistor (Smith *et al.* 1981). One limitation of the microstrip line configuration is that the system suffers from reflections (ringing) at the generation point. Also the microstrip configuration leads to high dispersion (broadening of the pulse while propagating) because of the dielectric substrate (Cooper 1985).

Figure 2.1(b) shows another primary electrooptic method of generation, guidance, and detection of THz pulses (Ketchen *et al.* 1986, Grischkowsky 2000, Grischkowsky *et al.* 1987), which is still used today. An aluminum coplanar transmission line² fabricated on a silicon-on-sapphire (SOS) substrate is employed for generation and detection of THz radiation. The THz (subpicosecond electrical) pulses are obtained by photoconductive

¹A type of electrical transmission line that consists of a conducting strip separated from a ground plane by a dielectric substrate (Gupta *et al.* 1996).

²A type of electrical transmission line that consists of a conducting strip on a dielectric substrate with two ground electrodes running adjacent and parallel to the strip (Wen 1969, Nguyen 2000).

shortening of the biased coplanar transmission line. The resulting electrical pulse propagates through the line and is measured by a photoconductive switch. A colliding-pulse mode locked dye laser with a 70 fsec laser pulse and 100 MHz repetition rate is used for generation and detection of the pulses. The generated subpicosecond pulse (0.6 ps) is broadened to 2.6 ps after traveling 8 mm in the coplanar transmission configuration (Ketchen *et al.* 1986). Thenceforth, far infrared spectroscopy utilizing coplanar transmission lines was reported (Sprik *et al.* 1987). However, the coplanar transmission line suffers from strong frequency dependent loss due to Cherenkov-like radiation³, which is equivalent to the loss process of leaky waveguides in the frequency domain (Grischkowsky *et al.* 1987, Grischkowsky 2000).

The total observed loss owing to the dielectric and metal materials within microstrip and coplanar transmission lines THz systems is very high. The reported loss for thin-film microstrip and coplanar transmission lines are $\alpha = 18 \text{ cm}^{-1}$ and $\alpha = 14 \text{ cm}^{-1}$ at 1 THz, respectively; the loss increases as frequency increases with f and f^3 dependence, respectively (McGowan *et al.* 1999).

In these primary electrooptic methods used for excitation and sampling of pico/subpicosecond pulses, intermediate dielectric transmission media are inevitably present. However, a pulse traveling through such a transmission medium is distorted due to frequency dependent loss and dispersion (Cooper 1985). In 1989, the first free-space tightly coupled THz spectroscopy system was proposed by van Exter *et al.* (1989a) and the first sample investigated was water vapor (van Exter *et al.* 1989b, Dexheimer 2008). The technique employed for generation and detection of subpicosecond pulses allows a very low loss propagation of THz radiation in free space (almost zero loss and dispersion) and eliminates the lossy planar waveguides. Optical hardware (e.g. mirrors and lenses) are exploited for steering, focusing, and efficient coupling of the pulses between excitation and detection points. Meanwhile, waveguides are required when the application point is inaccessible (where the optical techniques cannot be employed such as endoscopy), a stronger interaction of THz radiation with the sample is required, it is required to confine the pulse in a

³Accelerating electric charges emits electromagnetic radiation, while uniform motion of electrical charges does not. However, when the group velocity of moving charges are faster than the phase velocity of the electromagnetic wave in the material, this results in an electromagnetic radiation (shock wave), which is characterised by a Cherenkov cone and is known as Cherenkov radiation. As an example this happens for picosecond pulses propagating on coplanar transmission lines (Grischkowsky *et al.* 1987, Withayachumnankul 2009)

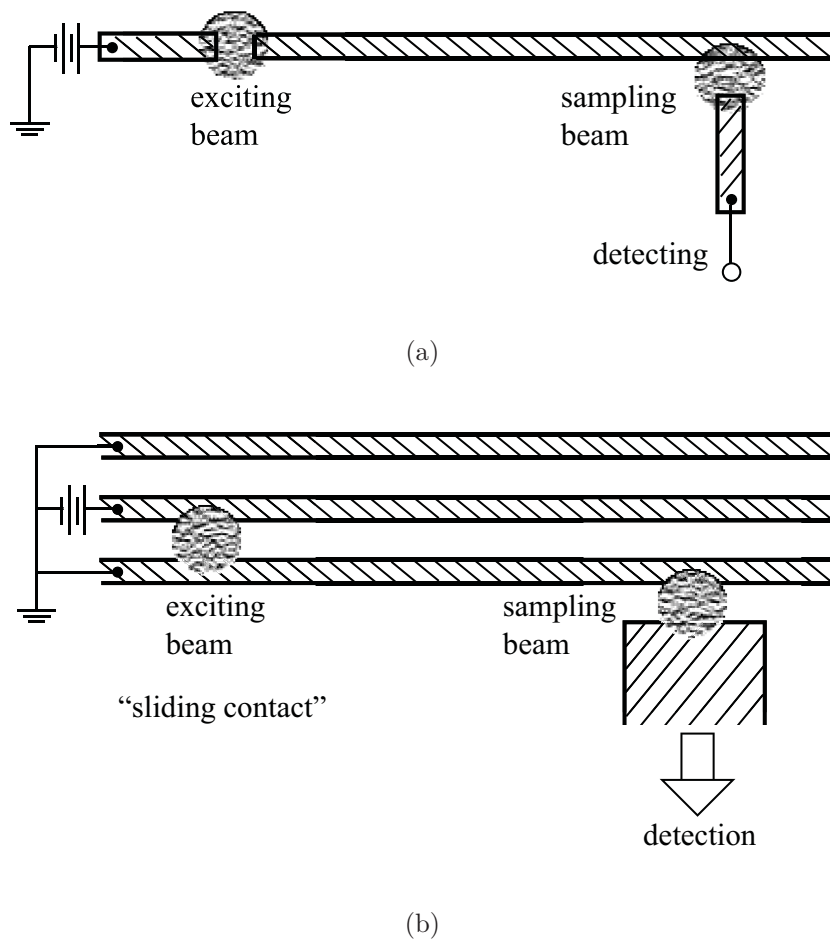


Figure 2.1. Primary methods of generation, and detection of single-mode THz pulses. (a)- A microstrip line composed of an aluminum metal line is evaporated on an amorphous silicon film. The picosecond pulses are obtained and sampled by photoconductive shortening of the $5 \mu\text{m}$ gaps. A mode locked rhodamine 6G dye laser with pulse duration of 3.5 ps and 82 MHz repetition rate at 580 nm wavelength is used for this purpose. After Auston *et al.* (1980). (b)- A coplanar transmission line composed of aluminum metal lines lithographically fabricated on a silicon-on-sapphire substrate. The THz (sub-picosecond electrical) pulses are obtained by photoconductive shortening of the charged coplanar transmission line. The resulting electrical pulse propagates on transmission line and is measured by a photoconductive switch. A colliding-pulse mode locked dye laser with 70 fsec laser pulse is used for generation and detection of the pulses. The excitation point (sliding contact) is moved to measure the propagation effects. After Grischkowsky (2000) and Grischkowsky *et al.* (1987). The excitation and sampling beams are shown with circular patches on the figures.

subwavelength regime and/or focus the beam to a smaller spot size to beat the diffraction limit.

Thus a whole new era has started for THz waveguides, where non-planar guiding techniques arising from the fields of microwave and optics have emerged. Nonetheless, in parallel there has been plenty of research conducted to improve the loss and dispersion mechanisms in coplanar waveguides, resulting in modified planar single wire waveguides also known as Goubau transmission lines (Treizebre *et al.* 2005, Akalin *et al.* 2006, Xu and Bosisio 2007, Dazhang *et al.* 2009). This focus on coplanar waveguides is mainly due to the fact that such waveguides seem straightforward for integrating THz functions inside microfluidic channels or for achieving on-chip THz circuitry.

2.1.1 Objective and framework

Section 2.2 presents a very brief review of different methods available for the generation and detection of THz pulses. This review aims to support our later review (in Section 6) of the different experimental methods used for characterisation of the waveguides in the subsequent sections. Since THz sources and detectors, used later in this thesis, for the characterisation of dielectric waveguides are based on photoconductive antennas, this generation and detection technique is explained more in detail in Subsection 2.2.3. Then in Section 2.3, we review non-planar waveguide structures proposed in the literature for guidance of THz radiation that is coupled into free space after generation. The experimental methods proposed to characterise each waveguide are also included in this review. Due to the diversity of waveguides we have divided the THz waveguides into two main categories: metallic waveguides and dielectric waveguides explained respectively in Subsections 2.3.1 and 2.3.2. The key features of waveguides discussed in Section 2.3 are summarised in Figs. 2.2, 2.3 and 2.4 at the end of the chapter.

2.2 Generation and detection of THz pulses

Technological advances in optics and electronics have resulted in many different types of THz emitters and detectors. In this Section, we provide brief descriptions of the methods for THz generation and detection required to understand the different techniques used for characterisation of THz waveguides in Subsections 2.3.1 and 2.3.2. Terahertz sources and detectors used in this thesis for characterisation of dielectric waveguides are based on

photoconductive antennas. Therefore, only terahertz generation and detection techniques based on photoconductive antennas are discussed in detail here. A comprehensive review of different types of THz emitters and detectors can be found in Lee (2009) and Sakai (2005).

Terahertz radiation is either broadband, with the temporal shape of a single-cycle field pulse, or continuous-wave (CW), with the temporal shape of a sinusoidal field pulse as shown in Fig. 2.2. There are different techniques available for generation and detection of broadband and CW THz radiation. Here we do not group the generation and detection techniques based on pulse shape. We follow the proposed division scheme by Lee (2009), where THz generation and detection is grouped based on operational concepts.

2.2.1 Terahertz sources

There are three main techniques for the generation of terahertz radiation. The first technique is based on the exploitation of a non-linear medium with a second order non-linearity. Materials such as non-linear crystals (e.g. ZnTe, LiNbO₃, and InP) and semiconductors such as diodes can be used for generating THz radiation. The incident electromagnetic wave (femtosecond laser pulse, optical beats, or microwave) undergoes non-linear frequency conversion as a result of a non-linear medium and generates broadband or CW THz radiation. Optical rectification and difference frequency generation are second order nonlinear optical processes, which lead to a THz photon at frequency ω_T by interaction of two optical photons at frequencies ω_1 and ω_2 within a nonlinear crystal. Different methods of THz generation using a non-linear medium are shown in Fig. 2.2.

The second method used for generation of THz radiation is to exploit accelerating electrons and time-varying currents. Photoconductive (PC) antennas, electron accelerators, backward wave oscillators, and free-electron lasers can be used to generate broadband or CW THz radiation as shown in Fig. 2.3. A PC antenna consists of two metal electrodes deposited on a semiconductor substrate. An optical laser pulse or optical beats (mixing two laser beams with different frequencies), illuminating the gap between the electrodes, generates photocarriers, and a static bias field accelerates the free carriers. Consequently, broadband or CW THz radiation is generated. Generation of broadband THz radiation exploiting PC antennas is described in more detail in Section 2.2.3.

Furthermore, electron accelerators, backward wave oscillators, and free-electron lasers can be used to accelerate electrons for THz generation. An electron accelerator accelerates

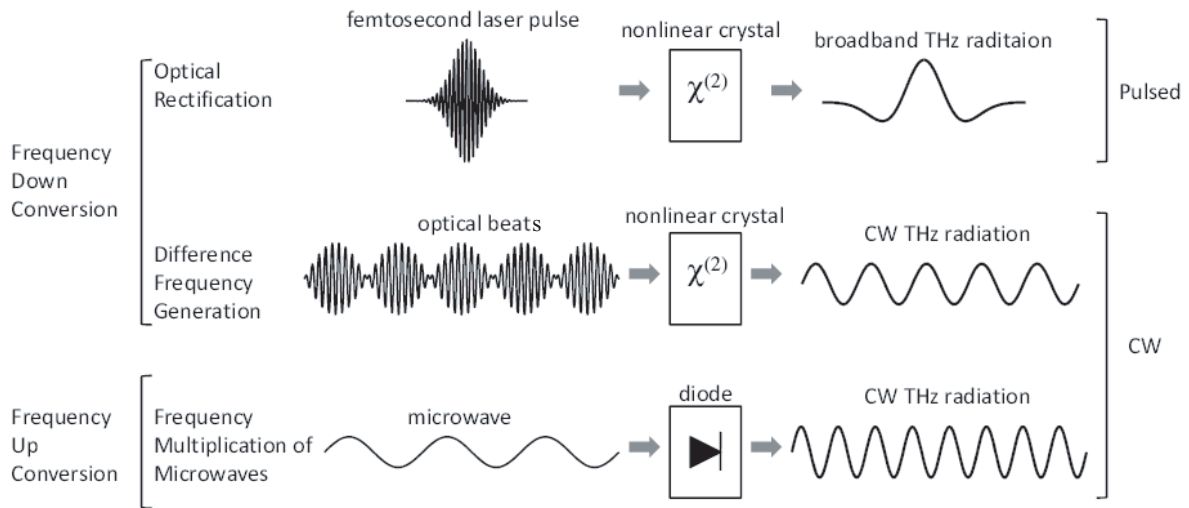


Figure 2.2. THz generation in non-linear media. Different generation techniques of broadband and CW THz radiation based on the exploitation of a non-linear medium. After Lee (2009).

electrons at relativistic speed either by smashing the electron bunch into a metal target or by bending the electrons within a magnetic field to generate broadband THz radiation. Ultrashort electron bunches are produced by triggering an electron source (e.g. photocathode electron guns or semiconductor surfaces) with femtosecond laser pulses. While, both backward wave oscillators (BWOs) and free-electron lasers (FELs) undulate an electron beam by a periodic structure (a BWO has a metal grating and a FEL consists of a magnet array) to generate CW THz radiation.

A THz laser is the third technique exploited for generating THz radiation. Several types of lasers have been developed for the THz region of the electromagnetic spectrum as shown in Fig. 2.4. For this purpose, a population-inverted two-level quantum system is required. Far infrared (IR) gas lasers, p-type germanium lasers, and quantum cascade lasers (QCLs) can be used to generate CW THz radiation. In IR gas lasers, the THz radiation is generated from the rotational transitions of the molecules (Lee 2009). The p-type germanium lasers and QCLs are solid state lasers, which rely on intraband transitions in semiconductors to generate THz radiation (Williams 2007, Lee 2009).

2.2.2 Terahertz detectors

Terahertz detection schemes are mainly divided into two main categories: coherent and incoherent detection schemes. The fundamental difference is that coherent detection

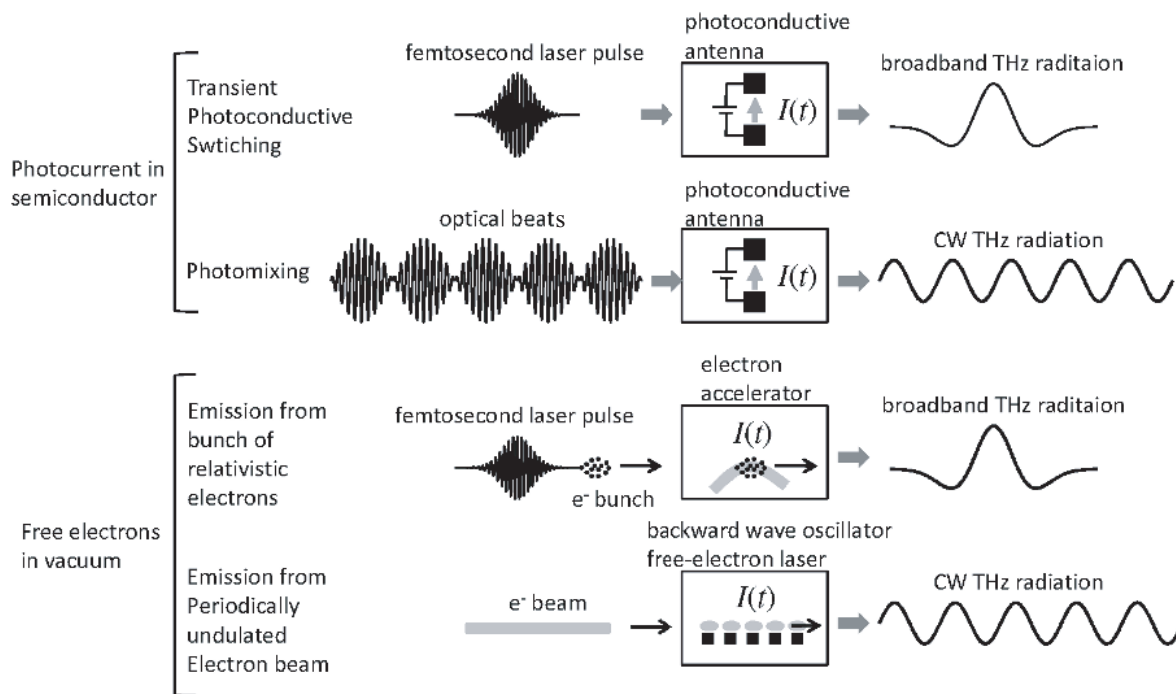


Figure 2.3. THz generation from accelerating electrons. Different generation techniques for broadband and CW THz radiation based on the exploitation of accelerating electrons and time-varying currents. After Lee (2009).

measures both the amplitude and phase of the electric field, while incoherent detection only measures the field intensity, i.e. amplitude. The coherent detectors use the same mechanisms and key components as THz emitters, in particular sharing the same light source, such as an optical laser.

Figure 2.5 illustrates the most commonly used coherent detection techniques. Non-linear crystals and photoconductive antennas are the main two devices employed for the detection of broadband THz radiation. A THz field induces birefringence in a non-linear optical crystal that is proportional to the field amplitude. Whereas, a THz field induces a current in the photoconductive gap of PC antenna, which is proportional to the THz field amplitude, when the PC antenna is not biased. In both cases the device is probed by a femtosecond laser pulse or by photomixed optical beats. Detection of broadband THz radiation exploiting PC antennas is described in more detail in Section 2.2.3.

A combined set-up of broadband THz generation and detection measures both the amplitude and phase of THz pulses in the time domain; this system is called THz time-domain

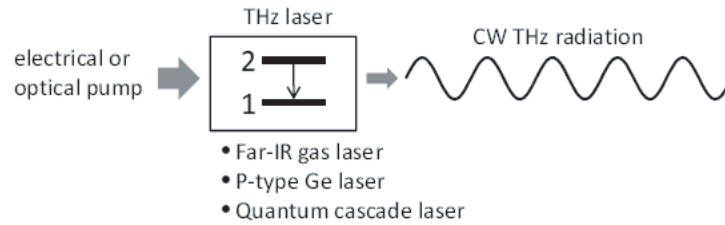


Figure 2.4. THz generation from lasers. Generation technique for CW THz radiation based on the lasers. After Lee (2009).

spectroscopy, in short THz-TDS (van Exter *et al.* 1989a, Dexheimer 2008). The absorption and dispersion coefficients can be determined after processing time domain pulses in frequency domain.

A PC antenna can also be used for the detection of CW THz radiation. The current induced in the photoconductive gap of a PC antenna has a sinusoidal dependence, when a photoconductive antenna is illuminated by CW THz radiation and probed using optical beats. This method is called photomixing and is used to measure CW THz radiation. Another detection technique employed for CW THz radiation is heterodyne detection. This method utilises a nonlinear device called a mixer, which down-converts the CW THz radiation to microwave frequencies. The amplitude of the attained signal is proportional to the THz amplitude. It should be noted that unlike other optical techniques, heterodyne detection is usually used to detect incoherent radiation.

Thermal detectors such as bolometers, Golay cells, and pyroelectric devices are commonly used as incoherent detectors. A radiation absorber attached to a heat sink is the common element of all thermal detectors. Radiation energy is recorded by a thermometer, which measures the temperature increase in the absorber. Each type of thermal detector employs different techniques to measure the temperature increase.

Bolometers utilise an electrical resistance thermometer made of a heavily doped semiconductor such as Si or Ge to measure the temperature of the radiation absorber. Usually for high detection sensitivity, bolometers operate at cryogenic temperature. Pyroelectric detectors employ a pyroelectric material as the radiation absorber in which temperature change gives rise to spontaneous electric polarisation (leading to dielectric constant variation). In a Golay cell, heat is transferred to a small volume of gas in a sealed chamber behind the absorber. The heat increases the pressure in the chamber. This deforms the membrane attached to the back of the chamber. Consequently, an optical reflectivity

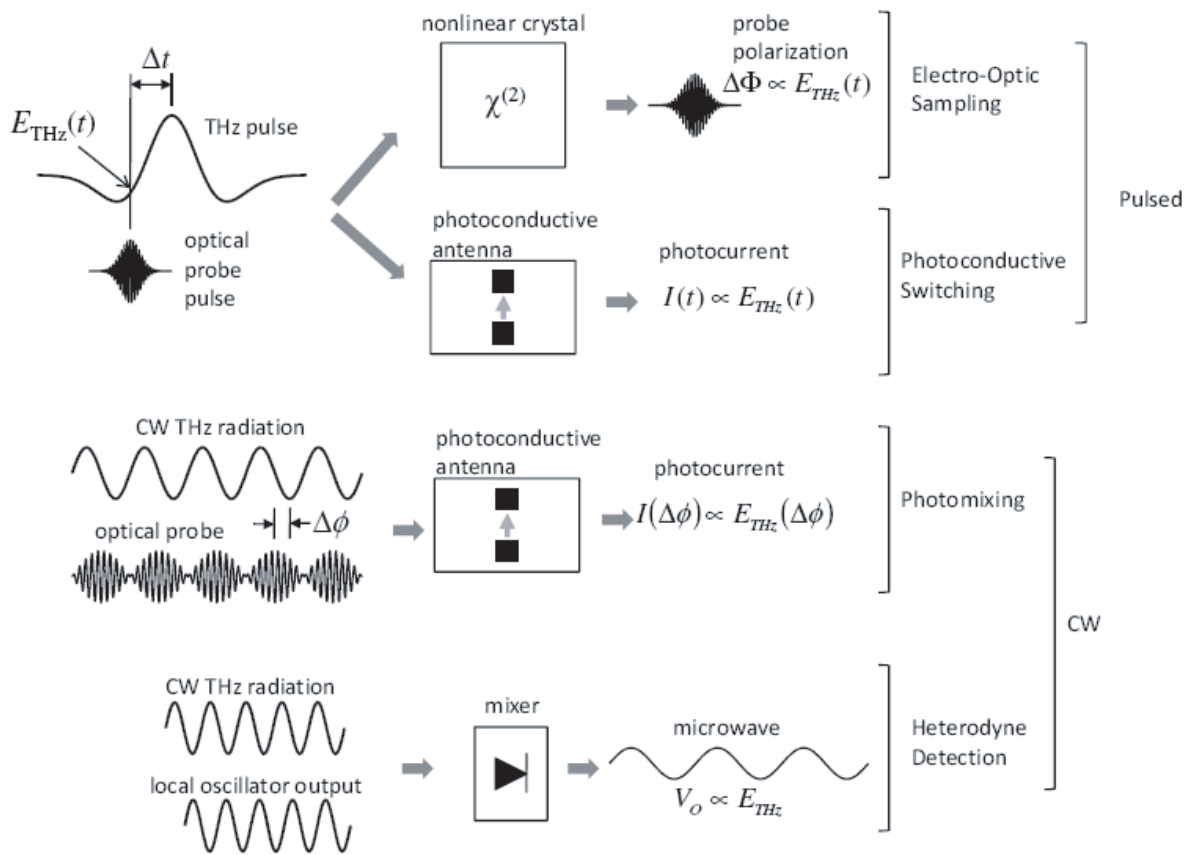


Figure 2.5. Coherent detection of THz radiation. Different detection techniques for broadband and CW THz radiation based on the exploitation of non-linear crystal, photoconductive antenna, and a nonlinear device (mixer). After Lee (2009).

measurement detects the membrane deformation. An advantage of such thermal detectors is that they respond to radiation over a very broad spectral range. However, since a radiation absorber must reach thermal equilibrium for a temperature measurement, its detection response is relatively slow (≈ 0.1 ms time constant at liquid helium temperature) compared with that of photon-detectors.

2.2.3 THz radiation generation and detection based on photoconductive antennas

A photoconductive (PC) antenna consists of at least two metal electrodes deposited on a semiconductor substrate, as shown in Fig. 2.6. When the gap between the electrodes is illuminated with femtosecond optical pulses (such as from a Ti:sapphire laser) with

photon energy greater than the band-gap of the semiconductor, free electrons are generated in the conduction band. The static bias field applied to the electrodes accelerates the free carriers. The accelerated carriers decay with a time constant determined by the carrier lifetime across the substrate, resulting in a pulsed photocurrent that emits a sub-picosecond electromagnetic pulse, i.e., a THz pulse. As shown in Fig. 2.6, the generated THz pulse is emitted from the substrate side. Since the size of the source is much smaller than the THz wavelength, the generated THz radiation is highly divergent. Therefore, a high-resistivity hyper-hemispherical lens is usually employed to collimate the THz radiation. Finally, beam shaping optics such as off-axis parabolic mirrors, hyper-hemispherical or -cylindrical lenses, and beam splitters can be used for guiding and manipulating the generated THz radiation.

In essence, the PC antenna operates as follows: The switch on-time depends on the laser pulse duration, and the switch off-time is determined by the carrier lifetime in the semiconductor substrate. The switching action in the PC antenna occurs on the sub-picosecond time scale in order to emit or detect THz radiation. Therefore, in addition to a short laser pulse duration, a short carrier lifetime is a vital property for ultrafast photoconductive switching. For this purpose a PC substrate with excellent properties of short carrier lifetime, high mobility, and high breakdown is required. Several photoconductive materials have been employed for PC switches: low-temperature grown gallium arsenide (LT-GaAs), radiation-damaged silicon-on-sapphire (RD-SOS), chromium-doped gallium arsenide (Cr-GaAs), indium phosphide (InP), and amorphous silicon. The characteristics of these ultrafast photoconductive materials is shown in Table 2.1. The most commonly

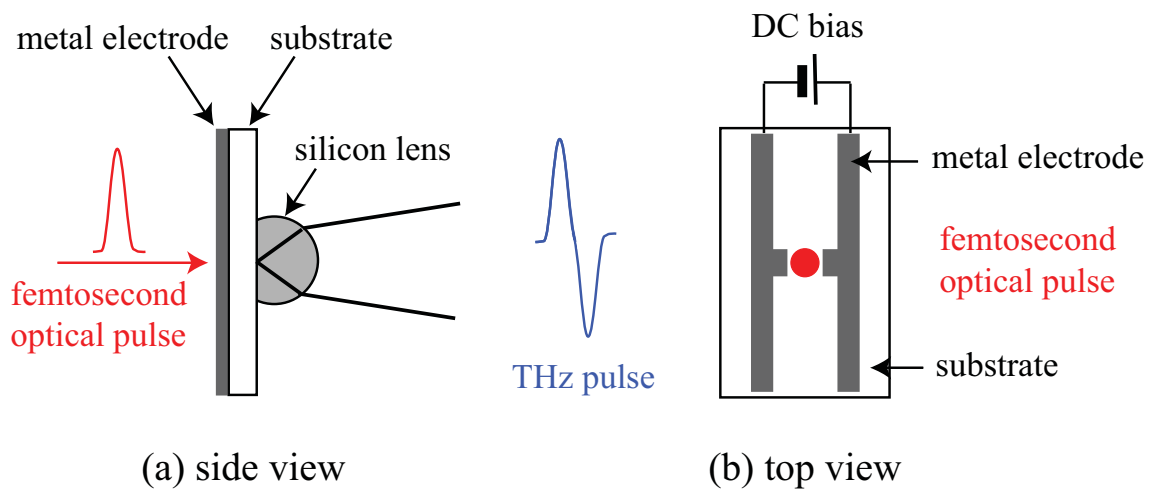


Figure 2.6. Generation of THz radiation from a PC antenna. Generation of a broadband THz pulse from a PC antenna pumped with a femtosecond optical pulse. After Sakai (2005).

Table 2.1. Characteristics of ultrafast photoconductive materials. This table indicates properties—carrier lifetime, mobility, resistivity and band-gap—of some ultrafast photoconductive materials. After Sakai (2005).

Photoconductive material	Carrier lifetime (ps)	Mobility ($\text{cm}^2/(\text{V}\cdot\text{s})$)	Resistivity ($\Omega\cdot\text{cm}$)	Band-gap (eV)
Cr-doped SI-GaAs	50-100	≈ 1000	10^7	1.43
LT-GaAs	0.3	150-200	10^6	1.43
SI-InP	50-100	≈ 1000	4×10^7	1.34
Ion-Implanted InP	2-4	200	$> 10^6$	1.34
RD-SOS	0.6	30	—	1.10
Amorphous SI	0.8-20	1	10^7	1.10

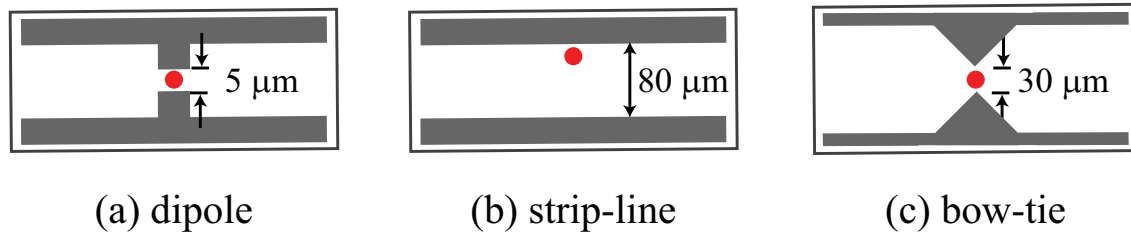


Figure 2.7. Schematic diagram of a dipole, strip-line and bow-tie PC switches. Schematic diagram of a dipole, strip-line and bow-tie photoconductive switches. The red dot represents the focused femtosecond optical pulse.

used materials for THz emitters and detectors are RD-SOS and LT-GaAs. The semiconductor substrate of PC antennas used for characterisation of THz waveguides in this thesis is LT-GaAs.

It should be noted that the power and bandwidth of a THz pulse emitted from a PC antenna depends not only on bias but also on its metal electrode structure. These electrodes are usually made of Gold-Germanium (AuGe), Nickel (Ni), and Gold (Au) metal layer. Figure 2.7 illustrates the commonly used electrode structures of PC switches: stripline, dipole, and bow-tie electrodes. Typical values of the dipole gap, strip-line and bow-tie separation are 5-10 μm , 30-100 μm , and 10-40 μm ; respectively. The electrode structures of the PC antennas employed in this thesis are discussed in Chapter 6.

The detection mechanism of the THz field using a PC antenna follows a similar principle to the generation mechanism. Figure 2.8 shows a schematic diagram of a time-resolved

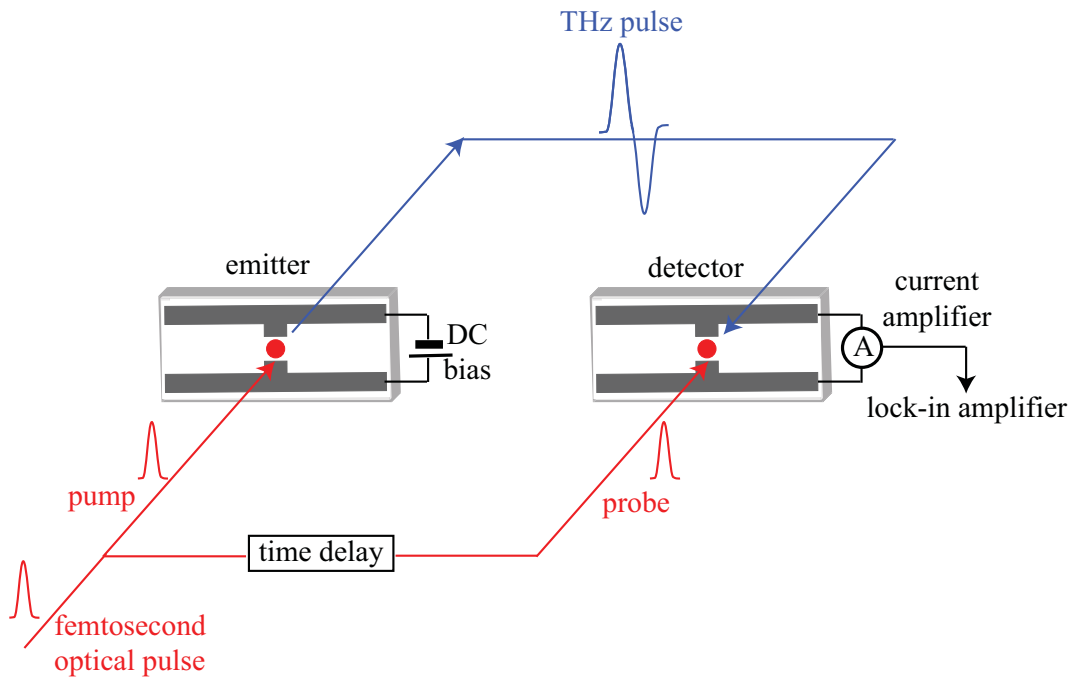


Figure 2.8. Detection of THz radiation from a PC antenna. Detection of a broadband THz pulse from a PC antenna probed with a femtosecond optical pulse. After Sakai (2005).

measurement of THz electric fields with a PC receiver. Note that no bias voltage is applied to the electrodes of a PC receiver. Instead, the THz electric field induces a photocurrent when the detector is illuminated by an optical probe pulse. The optical probe pulse is partially divided from the pump beam (used to generate the THz radiation at the emitter) by a beam splitter. The induced photocurrent is proportional to the THz field focused on the photoconductive gap. The THz pulse shape is mapped out in the time domain by measuring this current, while varying the time delay between the THz pulse and the optical probe. The photocurrent measured at the detector is usually amplified with a low-noise current amplifier and is fed to a lock-in amplifier. A Fourier analysis of the temporal profile of the received THz pulse reveals the amplitude and phase spectrum. This will be discussed in detail later in Section 3.3.

2.3 Terahertz waveguides

In well developed parts of the electromagnetic spectrum, optical and microwave waveguides have been exploited as sensing and imaging probes. Waveguides are key components of quantum-cascade lasers, to guide waves in the sub-wavelength regime (beyond

the diffraction limit), and to offer tight confinement of the electromagnetic waves to the structure beyond the Rayleigh range.

Analogously, waveguides can convey similar benefits to the THz spectrum. Nevertheless, the material selection for waveguides is one of the major barriers for expanding their number of applications. Metals that are suitable for microwave frequencies have high Ohmic losses, while polymers and glasses that work properly for infrared (IR) and optical frequencies have unacceptable frequency dependent absorption losses. Another major barrier that limits the application of waveguides in THz spectroscopy and communication systems is the group velocity dispersion. Consequently, different components of the THz spectrum travel with a different group velocity leading to distorted pulse shapes. Metal waveguides experience strong dispersion near the cut-off frequency of the guiding mode unless they support a transverse electric and magnetic (TEM) mode that has no cut-off frequency. Whereas, dielectric waveguides suffer mainly from waveguide dispersion. Although the dispersion can be tailored around a frequency, it is challenging to find a dielectric waveguide that offers almost zero dispersion for the entire broad spectrum of THz.

In spite of this, the benefits of having low-loss and -dispersion waveguides are countless for THz spectrum. The bulk optics used for manipulating the THz radiation in free space THz time-domain spectroscopy systems (TDS) can be then replaced by waveguides. This will open up new opportunities in further development of compact THz systems and consequently lab-on-chip systems. The diffraction limited spot-size can be reduced further and tight mode confinement can be achieved by exploiting the sub-wavelength featured fibres. This is beneficial for THz sensing applications specifically for the noninvasive and label-free molecular detection, and gas and liquid spectroscopy. A minute sample can be replaced in or at the vicinity of the waveguide where strong interaction with a THz pulse is achieved due to the existence of large power fraction of the guided mode. In much the same way that optical endoscopy has benefited from integration with MEMS devices (Xu *et al.* 2007), THz waveguides open up the possibility a means of coupling THz systems with MEMS in order to broaden the scope of biosensing applications. Other THz devices such as near-field scanning optical microscope, THz sources based on quantum-cascade lasers, imaging and communication technologies, which revolve around THz waveguides, will benefit in their functionalities.

Several classes of waveguides have been proposed in the literature for the THz spectrum in order to reduce frequency loss and dispersion. In this section we review THz waveguides.

We categorise the waveguides into two main groups: metallic and dielectric waveguides. We first review a number of metallic waveguides in terms of loss, dispersion and the proposed experimental methods for characterisation of the waveguides in Subsection 2.3.1. Then in Subsection 2.3.2, we conduct a thorough review of loss and dispersion values of dielectric waveguides and the employed experimental methods for characterisation of the waveguides.

2.3.1 Metallic waveguides

Metallic waveguides proposed for THz radiation guidance are mostly in essence the scaled-down versions of well-known guiding devices from microwave and radio frequencies. Electromagnetic waves at terahertz frequencies are not as dissipative in metallic components as they are for higher frequencies. Thus metallic structures still can be used for guidance in this regime. In this section we review waveguides with circular and rectangular cross-sections, parallel-plate waveguides, bare metal wires and slit metallic waveguides. Other metallic waveguide structures are proposed in the literature for THz radiation guidance such as sub-millimetre coaxial lines (Jeon and Grischkowsky 2004), one- and two-dimensional photonic crystals (Bingham and Grischkowsky 2007, Bingham and Grischkowsky 2008) and two-wire waveguides (Mbonye *et al.* 2009). These structures are not covered in detail here, since the main scope of this thesis is dielectric waveguides.

Circular (tube) and rectangular cross-section waveguides

Metallic waveguides with circular cross-section were one of the first experimental investigations conducted using quasi-optical methods to couple freely propagating THz pulses (McGowan *et al.* 1999). In 1999, McGowan *et al.* (1999) demonstrated that circular waveguides have lower loss ($\alpha = 0.7 \text{ cm}^{-1}$ at 1 THz) relative to coplanar and microstrip transmission lines ($\alpha = 14 \text{ cm}^{-1}$ and $\alpha = 18 \text{ cm}^{-1}$, respectively). This is mainly due to the fact that the propagating THz pulses experience only Ohmic losses due to the metallic body of circular waveguide, while they suffer from three different loss mechanisms when propagating via transmission lines; i.e. Ohmic losses due to metal strips, dielectric losses due to substrate, and radiative losses. However, THz pulses propagating through circular waveguide experience strong dispersion near the cut-off frequency associated with the fact that the transmitted THz pulse through these waveguides is stretched with the higher frequencies arriving earlier in time, i.e. a negative chirp. As an example, ≈ 1 ps duration

THz pulse after propagating 25 mm through a 280 μm diameter circular brass waveguide stretches to ≈ 40 ps (Gallot *et al.* 2000).

A year later, Gallot *et al.* (2000) demonstrated both theoretically and experimentally that rectangular metallic waveguides have similar losses as circular waveguides, for 0.65–3.5 THz bandwidth. Similarly, the pulses propagating through the waveguide only suffer from Ohmic losses of the metal walls. Rectangular waveguides also suffer from dispersion near the cut-off frequency in the same manner, i.e. the higher frequencies arrive earlier in time compared to lower frequencies, negative chirp. As an example, the input THz temporal pulse (with approximately 1 ps initial pulse duration) stretches to 13 ps wide for 25 mm long rectangular brass waveguides (Gallot *et al.* 2000).

The cross-section of circular and rectangular metallic waveguides are shown in Fig. 2.9(a). The dimensions of these waveguides—circular (240 μm) and rectangular (with 300 μm width)—are such that more than 25 modes can be excited, i.e. the cut-off frequency of modes falls into the THz spectrum (0.1–4 THz). For such a broad spectrum, many octaves, it is not possible to design a single mode metallic circular or rectangular cross-section waveguide. However, the modes excitation also depends on the the polarisation, the shape, and the phase front of the source, in this case THz pulses. The linearly polarised incoming THz pulse significantly couples only into three (TE_{11} , TE_{12} , and TM_{11}) and two (TE_{10} and TM_{12}) modes of the circular and rectangular waveguides, respectively (Gallot *et al.* 2000). This reduces significantly the number of the modes than can be excited inside these waveguides. Consequently, a single mode propagation can be achieved from 0.7 to 4 THz for the rectangular waveguide with a 250 $\mu\text{m} \times 125 \mu\text{m}$ cross-section.

A standard optoelectronic THz time domain spectroscopic (THz-TDS) setup, shown in Fig. 2.9(b), is used to characterise the circular and rectangular metallic waveguides proposed by McGowan *et al.* (1999) and Gallot *et al.* (2000). The setup is composed of an optoelectronic transmitter and receiver with terahertz beam shaping and steering optics, along with a pair of plano-spherical and cylindrical lenses for coupling the terahertz field inside the circular and rectangular waveguides, respectively. The THz pulse generated from a standard setup is linearly polarised leading to a higher coupling of THz pulse into the rectangular waveguide where the polarisation of the dominant mode is also linear.

Parallel-plate waveguides

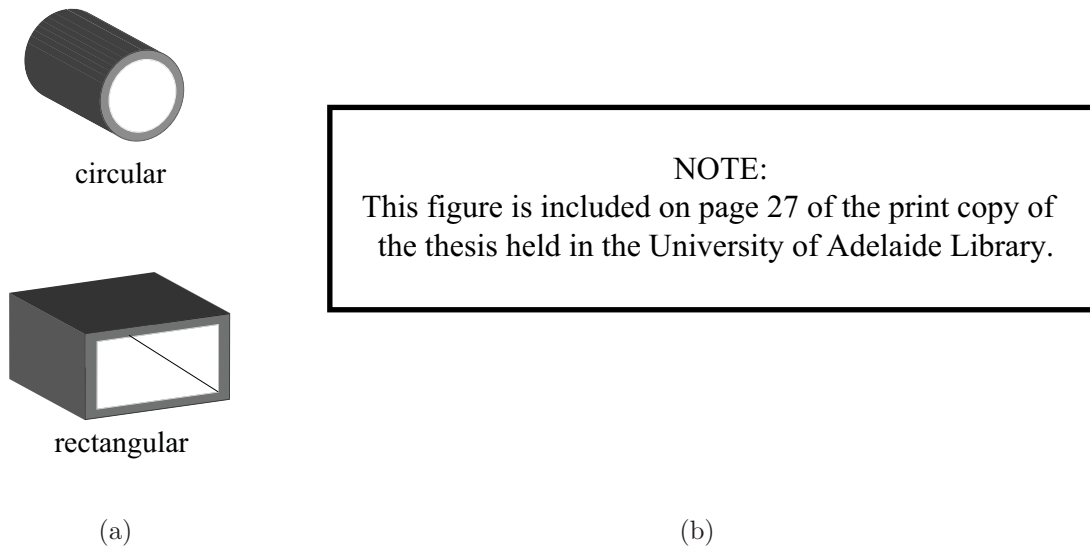


Figure 2.9. Circular and rectangular cross-section metallic waveguides. (a)- The cross-section of circular and rectangular metallic waveguides. (b)- Schematic of the optoelectronic THz-TDS system used for characterisation of circular and rectangular waveguides. After Mendis (2001).

In 2001, Mendis and Grischkowsky (2001b) reported undistorted propagation of sub-picosecond THz pulses in a parallel-plate copper waveguide. The guiding structure consists of two parallel conducting plates positioned close together (108 μm gap in between the plates) as shown in Fig. 2.10(a). The structure supports single TEM (Transverse ElectroMagnetic) mode propagation, which is the lowest order TM mode: TM_0 . The TEM mode has no cut-off frequency. Thus, unlike the circular and rectangular metallic waveguides that suffer from extreme broadening of THz pulse near the cut-off frequencies, parallel-plate waveguide has no group-velocity dispersion (Mendis 2001). Moreover, the electric field of a parallel-plate waveguide is linearly polarised and perpendicular to the plates. This facilitates the coupling of linearly polarised THz pulses into the structure.

An attenuation constant less than 0.3 cm^{-1} and almost no pulse broadening (zero dispersion) is observed for a parallel-plate waveguide within the bandwidth from 0.1 to 4 THz (Mendis and Grischkowsky 2001b). The Ohmic losses due to the finite conductivity of the plates and divergence losses due to beam spreading in the unguided direction are the main loss mechanisms in these waveguides. Thereafter, the first demonstration of a physically flexible THz parallel-plate interconnect with minimal pulse distortion and loss

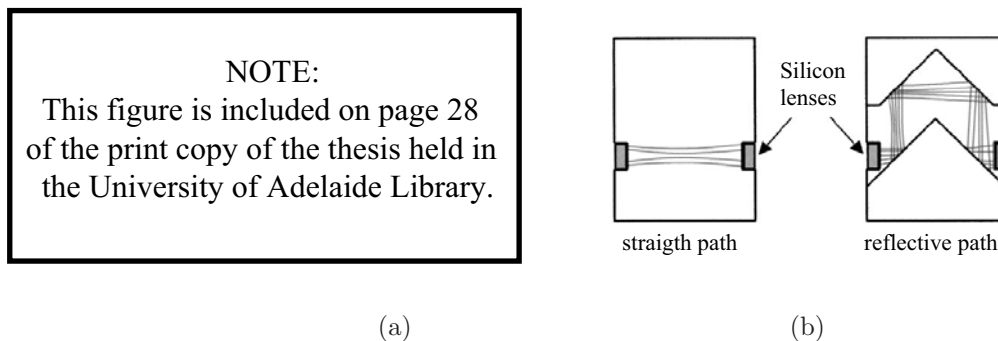


Figure 2.10. Parallel-plate waveguide and interconnect. (a)- The cross-section of a parallel-plate waveguides and hypo-cylindrical silicon lens used for coupling the THz pulse into the waveguides. After Mendis (2001). (b)- Schematic of a two dimensional straight path and reflective path interconnect layer using parallel-plate waveguide. After Coleman and Grischkowsky (2003).

is reported (Mendis and Grischkowsky 2001a). Subsequently, sharp bends with minimal mode distortion is reported by including quasi-optical mirrors in parallel-plate interconnect (Coleman and Grischkowsky 2003). The schematic of a straight path and reflective path interconnect layer using parallel-plate waveguide is illustrated in Fig. 2.10(b). Because of almost zero dispersion and low-loss characteristics of parallel-plate waveguide, this waveguide has also been used in applications such as sensing, imaging, and signal processing (Mendis and Mittleman 2009a).

The TE_1 mode is the second higher order mode that can be excited in parallel-plate waveguide if the polarisation of the incoming beam is parallel to the plates. However, this mode suffers from high distortions and filtering effects by virtue of the cut-off frequency. Recently, Mendis and Mittleman (2009a) demonstrated that it is possible to modify the design of a parallel-plate waveguide in such a way that undesirable effects caused by the second higher order mode, TE_1 , can be suppressed. Increasing the separation of the plates more than 25 times ($108 \mu\text{m}$ to 5mm), lowers the cut-off frequency of TE_1 mode, which is inversely proportional to the plate separation height, to around 0.03THz . Thus the group-velocity dispersion and filtering problems caused by TE_1 mode near the cut-off frequency falls out of the required guiding window, $0.2\text{--}1 \text{THz}$ (Mendis and Mittleman 2009a, Mendis and Mittleman 2009b). Moreover, increasing the plate separation reduces the TE_1 Ohmic loss even lower than that of the TEM mode. Also, due to the nature of field components of TE_1 mode, the divergence losses can be mitigated for by introducing a slight curvature to the plates or a transverse concavity (Mendis and Mittleman 2009b).

The coupling efficiency of a linearly polarised THz beam into both TEM and TE_1 modes is high (almost 100% for TE_1), since the electric field of both modes are also linearly polarised. However, they cannot be both excited at the same time unless the waveguide is positioned at an angle. The TE_1 mode is excited if the input beam is polarised parallel to the plates, while the TEM mode is excited when the input beam is polarised perpendicular to the plates. The selection of which mode to excite in parallel-plate waveguides depends on the application. As an example, TE_1 mode can be exploited for excitation of a simple resonant cavity integrated with a parallel-plate waveguide, which cannot be excited by the TEM mode.

To conclude, in parallel-plate waveguides, the TEM mode can be excited if the polarisation of the incoming beam is perpendicular to the plates. The TEM mode has no cut-off frequency thus the propagating pulse has almost zero dispersion. However, the plates offer a one-dimensional confinement, and the structure suffers from divergence losses along the unguided direction. Whereas, TE_1 mode is excited if the polarisation of the incoming beam is parallel with the plates. The cut-off frequency of this mode is inversely proportional to the plate separation. Thus increasing the plate separation reduces the cut-off frequency beyond the lower limit of the THz spectrum reducing the undesired dispersion effect. Due to TE_1 mode nature, introducing a slight curvature to the plates lessens the divergence losses. However, the propagating mode in such a wide plate separation is not tightly confined to the structure and it is almost propagating in the air.

A similar THz-TDS experimental setup used for circular and rectangular metallic waveguides, shown in Fig. 2.9(b), has been used for the loss and dispersion characterisation of parallel-plate waveguides and the interconnects discussed above. A pair of hypercylindrical silicon lens, shown in Fig. 2.10(a), are used for coupling the THz pulse into and out of the waveguides.

Bare metal wires

The bare metal wire, also known as a Sommerfeld wire, is a single cylindrical conductor (wire). Electromagnetic waves propagate as weakly guided radial surface waves along an infinitely long wire of circular cross-section, due to the finite conductivity of the metal and are called surface plasmon waves. Only the principle mode, a radially symmetric transverse magnetic wave (TM_{01}), travels along the wire and has remarkably low loss and low group velocity dispersion (King and Wiltse 1962) whereas all other modes have high attenuation, which makes the wire effectively single mode. The guided surface-wave and

the single wire are called respectively the Sommerfeld wave and the Sommerfeld wire, because Sommerfeld found the first rigorous solution of Maxwell's equations, for wave propagation on a single wire (Jeon *et al.* 2005, Wächter *et al.* 2005).

Wang and Mittleman (2004) were first to observe the propagation of THz pulses on the bare metal wire. Their interest in metal wires was inspired from their investigations of the propagation of THz pulses on optical antennas in near-field scanning optical microscopy. They demonstrated that the guided mode in a bare metal wire is similar to the TEM mode of a coaxial waveguide, i.e. it has a radial distribution. Calculation shows that, at the surface of the wire, the magnitude of the E_z component of the electric field is usually at least two orders of magnitude smaller than that of the E_r component (King and Wiltse 1962). Therefore, the observed field distribution, by Wang and Mittleman (2004), is similar to the TEM mode. In comparison to other metallic waveguides, the exposed metal surface area to propagating THz pulses is reduced leading to lower Ohmic losses. As an example, a 0.9 mm diameter stainless steel wire has an attenuation constant less than 0.03 cm^{-1} and almost zero dispersion from 0.25 to 0.75 THz (Wang and Mittleman 2004).

The mode propagating along a single-wire largely extends into the surrounding air. The wire acts as a rail for the guiding mode, which is analogous to optical nanowires discussed in Chapter 3. As an example less than 22% of the guided mode power is within the area not exceeding one wavelength around the wire (Wächter *et al.* 2007). This makes the coupling in between the wires simple, i.e. the THz pulses can be coupled into a wire if it is positioned in the extended field of another wire. Low loss and almost zero dispersion characteristics of the wire leads to realisation of a THz Y-splitter, a 90° output directing structure, and the first THz endoscope (Wang and Mittleman 2004).

Figure 2.11 shows the setup used by Wang and Mittleman (2004) for their experiment. In this setup the THz pulses are not directly coupled onto the waveguide. A second wire (input coupler) is used to couple the field onto the main wire (waveguide). The input coupler acts as a scatterer and a small portion of the scattered THz field is coupled to the waveguide (Wang and Mittleman 2004).

Following the observation by Wang and Mittleman (2004), Jeon *et al.* (2005) also demonstrated an experimental and theoretical study of Sommerfeld wave propagation on single metal wires with improved coupling efficiency. The field distribution of the fundamental mode on a Sommerfeld wire is radial. Therefore the THz beam generated from the standard TDS system, where the generated THz pulse is linearly polarised, is not appropriate for maximum coupling onto the wire due to poor spatial overlap. Jeon *et al.* (2005) have

demonstrated that by employing a specially designed THz PC transmitter switch, with two concentric electrodes instead of two parallel ones as shown in Fig. 2.12(a), generates radially polarised THz pulses. This improves the coupling efficiency onto the metal wire compared to the scattering method because of the better spatial overlap of THz pulses and the propagating mode. The schematic diagram of the experimental set-up used by Jeon *et al.* (2005) is shown in Fig. 2.12(c). In this experiment, the metal wire is directly positioned on the transmitter and detector chips for the measurement. No lenses are used for coupling onto the waveguide. Different lengths of wire are used for characterisation of the waveguide. An attenuation constant less than 0.003 cm^{-1} and almost zero dispersion is achieved for a 0.52 mm diameter copper wire in the 0.1–0.4 THz range (Wang and Mittleman 2004).

Wächter *et al.* (2005) improved the measurement technique employed for characterisation of the Sommerfeld wire. As shown in Fig. 2.13, they employed a photoconductive probe-tip to investigate the THz transmission characteristics (frequency-dependent attenuation and dispersion parameters) of Sommerfeld waves. The advantage of this method compared to previous measurement techniques is that one single long wire can be used instead of different lengths of the same wire for characterisation. The probe-tip moves freely along the wire and samples the propagating mode at the different positions on the wire. This measurement technique is only viable for characterisation of waveguides that have field extending outside the waveguide.

NOTE:
This figure is included on page 31 of the print copy of
the thesis held in the University of Adelaide Library.

Figure 2.11. Bare metal wire experimental setup. A coplanar transmission line composed of aluminum metal lines lithographically fabricated on a silicon-on-sapphire substrate. After Wang and Mittleman (2004).

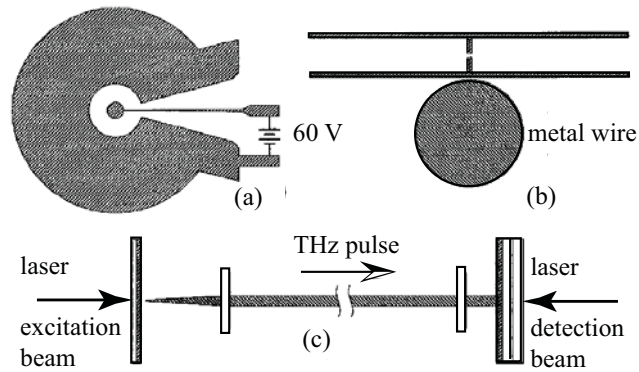


Figure 2.12. Sommerfeld wire experimental set-up I. The schematic diagram of (a)- the transmitter chip, (b)- the detector chip and output face of wire, and (c)- the arrangement of the experimental set-up. After Jeon *et al.* (2005). The specially designed transmitter chip improves the coupling efficiency onto the metal wire and allows positioning of the wire directly on the transmitter.

NOTE:
This figure is included on page 32 of the print copy of the thesis held in the University of Adelaide Library.

Figure 2.13. Sommerfeld wire experimental set-up II. The schematic diagram of the cross-section of the experimental setup. After Wächter *et al.* (2005). The probe-tip is kept in a fixed position, while all other components are moving freely with motorised translation stages.

Despite its superior transmission behavior, the bare metal wire suffers from radiation losses. Any perturbation to the structure, e.g. bending, and even at the vicinity of the wire (within the region of extended field) leads to high radiation losses due to the loose confinement of the mode to the structure. On the other hand the field extension into the air enables easy coupling in between the wires and better interaction of the field with the sample in sensing applications. Coating the wire with a dielectric is an approach to improve the confinement. However, for the THz spectrum, the dielectric coating introduces frequency dependent loss to the propagating mode (Wächter *et al.* 2005).

Metallic slit waveguides

There is a trade-off between strong mode confinement and low attenuation characteristics in metallic waveguides. Metal wires have lower conductivity losses compared to parallel-plate waveguides. However, the propagating mode is loosely confined to the metal wire and extends all around the wire. Instead, parallel-plate waveguides has one-dimensional confinement in virtue of the plates and suffers from divergence loss on the other dimension.

Wächter *et al.* (2007) proposed metallic slit waveguide for the guidance of THz radiation to increase the field confinement to the waveguide. The structure is made up of two planar slabs ($20 \text{ mm} \times 300 \text{ }\mu\text{m}$) located at a $d = 270 \text{ }\mu\text{m}$ apart from each other, as is shown in Fig. 2.14(a). Compared with the bare metal wire, the electromagnetic fields are more confined to slit waveguide. As an example, at THz frequencies, more than 50% of guided mode power is within the area not exceeding one wavelength around the slit waveguide, while this number is less than 22% for bare metal wire (Wächter *et al.* 2007). However, the attenuation loss of slit waveguides is higher than metal wires. The propagating mode in a slit waveguide is in contact with larger metal area compared to that of a metal wire leading to higher attenuation losses for the slit waveguide. On the contrary, the conducting loss, the dominating loss mechanism in metallic waveguides, of a slit waveguide is lower than a parallel-plate waveguide due to the less metal and mode contact. The attenuation constant of a slit waveguide made from silicon wafer coated with Ti and Au is less than 0.07 cm^{-1} in the frequency range 0.1–1 THz (Wächter *et al.* 2007).

The THz experimental set-up used to characterise a split waveguide is shown in Fig. 2.14(b). A photoconductive antenna array, which covers the input port of the waveguide, is employed for generation of linearly polarised THz pulses (Wächter *et al.* 2007). The antenna consists of two sets of 14 interconnected low temperature grown GaAs based photoconductive switches with $11 \text{ }\mu\text{m}$ gaps. The large effective area of the antenna ($290 \times 318 \text{ }\mu\text{m}^2$) allows direct coupling of THz pulses into the waveguide without utilizing a collimating silicon lens. A photoconductive probe-tip placed at a few micron distance from the waveguide is used to sample THz pulses (Wächter *et al.* 2007). This detection technique can be employed if and only if the waveguide mode expands to the surrounding medium, where the probe-tip can be positioned for sampling purposes.

Remarks: Four different metallic structures have been reviewed in this subsection. Metallic waveguides with circular and rectangular cross-sections: the propagating mode (TE and/or TM modes) is tightly confined in the structure (metallic walls) leading to high losses due to finite conductivity of the metals in THz frequencies. Moreover, the

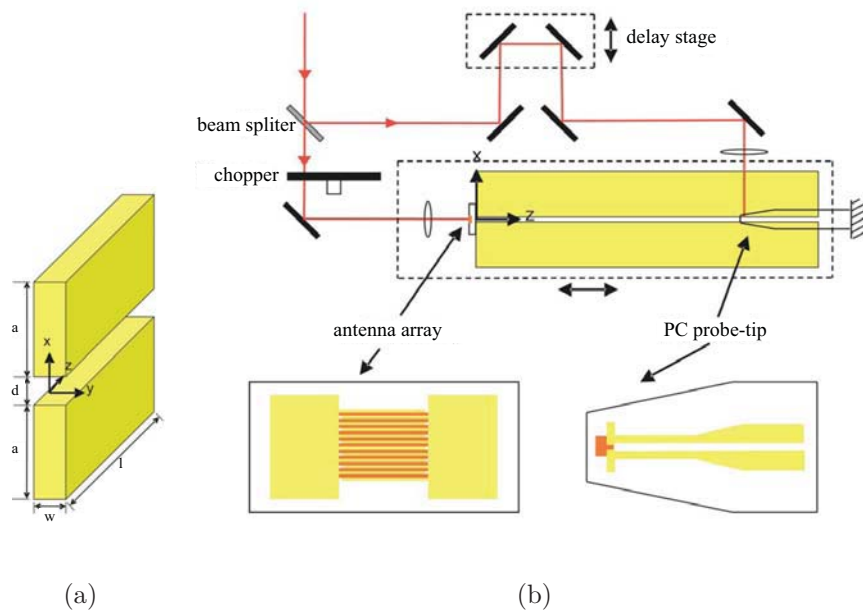


Figure 2.14. Metallic slit waveguide experimental set-up. (a)- Waveguide structure. (b)- Schematic diagram of the THz-TDS experimental set-up. A photoconductive antenna array, consists of two sets of 14 interdigitated electrodes, and a photoconductive dipole antenna (probe-tip) are used for the generation and detection of THz pulses, respectively. After Wächter *et al.* (2007).

propagating mode inside these metallic waveguides suffers from high dispersion near the cut-off frequency of the mode leading to a negative chirp. Parallel-plate waveguides: the propagating mode (TEM) is still confined in between the plates in one direction with lower attenuation constant compared to circular and rectangular metallic waveguides. In addition to lower loss, these waveguides offer dispersion free propagation. Bare metal wire: the conducting (Ohmic) loss is reduced considerably since the wire acts as a rail for the guided mode (TM_{01}). The mode is loosely confined to the wire and is expanded to the surrounding medium (air) resulting in low-loss and dispersion free propagation of THz pulses. Metallic slit waveguide: the THz pulses still propagate in air with a higher confinement to the waveguide compared to metal wire and nearly no dispersion. Although the confinement leads to higher loss for the slit waveguide compared to metal wire, the slit waveguide loss is still lower than that of a parallel-plate, circular, and rectangular waveguides. A summary of all the key parameters discussed for the above metallic waveguides is presented in Table 2.2.

2.3.2 Dielectric Waveguides

Dielectric waveguides, are also known as fibres if they have circular cross-sections and are mostly used at higher frequencies, such as infrared and optical frequencies, where metallic waveguides are dissipative. In this section we review the dielectric waveguides proposed in the literature for THz guidance. The dielectric waveguides can be divided into two main categories: hollow-core and solid-core waveguides/fibres. The loss, dispersion, and experimental set-up used for characterisation are discussed for each dielectric waveguide.

Hollow-core waveguides/fibres

Guiding the mode through the hollow core is the common feature of waveguides in this sub-section. In general, the guiding mechanisms in all-dielectric hollow-core waveguides are via formation either photonic band-gap or Von-Neumann-Wigner quasi-bound states (Benabid *et al.* 2009, Rowland 2010). In the former guiding mechanism, the cladding does not support modes for certain ranges of frequency so the guided modes stay in the core. Fibres such as microstructured⁴ band-gap fibres (Knight *et al.* 1996, Knight *et al.* 1998), and Bragg fibres (Temelkuran *et al.* 2002, Katagiri *et al.* 2004) are the two well known examples of this group in optics. While in the latter guiding mechanism, there is a low overlap between the core guided modes and cladding modes by virtue of low density of states in the cladding, which leads to the confinement of the mode in the core. Kagomé (Couny *et al.* 2006, Argyros and Pla 2007) and square (Couny *et al.* 2008, Argyros *et al.* 2008) lattice hollow-core microstructured fibres, in which the guiding mechanism is due to the antiresonance effect of the lattice, are the well known examples of this group. Extensive detail of guiding mechanisms in hollow-core fibres can be found in Rowland (2010).

For the THz frequency range, the material absorption of hollow-core waveguides is low since THz radiation is mainly concentrated in the air-core. However, as we observe for each waveguide below, the dimension of these waveguides are in the order of a few millimetres. Generally, we also observe that for such a broad THz spectrum these waveguides are narrow-band, i.e. the transmission is limited to a selected frequency bands due to the guiding mechanisms.

Hollow pipe waveguides

⁴Fibres with micrometre-scale air holes running along their length are called microstructured fibres.

Metallic waveguides with circular cross-section were one of the early non-planar waveguides purposed for THz guidance. These waveguides had low transmission efficiency, strong dispersion near the cut-off frequencies, and were rigid. In 2003 Hidaka *et al.* (2003) proposed hollow terahertz waveguide made of ferroelectric poly vinylidene fluoride (PVDF), a flexible polymer.

The dielectric constant of PVDF is a frequency dependent and has a resonance frequency in terahertz range. The dielectric constant of the PVDF becomes negative for frequencies larger than 0.3 THz. This results in an imaginary refractive index like metals. With an imaginary refractive index, the material shows complete reflection like metals (close to unity) for the both TM and TE polarisations from 1 to 2 THz (Hidaka *et al.* 2000, Hidaka *et al.* 2005). Compared to metals such as Cu, the reflectivity of TM polarisation for PVDF is even higher in this frequency range. This leads to a three times larger transmission coefficient for an 8 mm bore diameter (larger than the wavelength), 120 μm thickness and 30 cm long PVDF pipe compared to that of a similar Ni-Cu pipe. The attenuation constants were, respectively, about 1.5 m^{-1} and 5 m^{-1} , for PVDF and metal pipe waveguides. Due to the large bore diameter the hollow pipe waveguides suffer from multimode propagation.

The PVDF and Ni-Cu waveguides were prepared by rolling the PVDF and Ni-Cu sheets and inserting them into a acrylic support pipes (Hidaka *et al.* 2005). For the loss measurement of waveguides, a broadband THz radiation is generated by a non-linear optical crystal—magnesium oxide doped lithium niobate ($\text{MgO}:\text{LiNbO}_3$)—pumped by a Q-switched Nd:YAG laser⁵. A Si-bolometer in liquid He is used as the terahertz detector. The bolometer measures the amplitude of the THz pulse leading to only a loss measurement of the waveguide. A spatial aperture at the entrance of the waveguide was employed in order to ensure that only THz pulse transmitted via waveguide is detected Hidaka *et al.* (2003).

Recently, a polymer hollow pipe waveguide, i.e. a large air-core and one thin layer of dielectric material as cladding, consisting of a hollow pipe single polymer (frequency independent dielectric constant) ring as shown in Fig. 2.15(a) has been proposed for THz guidance (Lai *et al.* 2009, Chen and Chen 2010).

Unlike the metallic/PVDF pipes (discussed above and in the previous subsection), and hybrid-clad pipes (discussed next) where the guiding mechanism is due to highly reflective

⁵Nd:YAG lasers operate in both pulsed and continuous mode. When operated in the pulsed mode it is called a Q-switched Nd:YAG laser, since an optical switch is inserted in the laser cavity for this purpose.

mirrors, the guiding mechanisms in these polymer hollow pipes is based on an anti-resonance guiding mechanism. This waveguide can be viewed as a simplified Kagomé-lattice fiber (discussed later here) reduced to one layer of cladding, and the mode is guided based on the anti-resonance guiding mechanism (Gérôme *et al.* 2010).

Due to the large core diameter (9 mm larger than operating wavelength), these waveguides suffer from multimode propagation. Lai *et al.* (2009) have shown that with the single low index dielectric layer (0.5 mm thickness), an attenuation constant of less than 0.02 cm^{-1} with almost 200 GHz bandwidth is achievable. Commercially available Teflon tubes were used as pipe waveguide. The experimental set-up used for characterisation of the pipe waveguide is shown in Fig. 2.15(b). Two tunable continuous-wave Gunn oscillator modules with 0.32 to 0.46 THz and 0.405 to 0.52 THz frequency ranges and a Golay cell are used as the emitter and detector; respectively. Due to the large core diameter, the THz radiation is coupled directly into the structure from the parabolic mirror without a lens.

An average of 40 % coupling efficiency is reported for this guiding structure. The measured intensity after 3 metres propagation is very similar to the intensity of the fundamental mode, indicating that higher order modes disappear due to their high leakage losses (Lai *et al.* 2009). This polymer pipe waveguide is not flexible. Moreover, due to the large core size higher order modes are easily excited especially at bends or small discontinuities as for earlier hollow-core waveguides.

Hybrid-clad waveguides

Hollow-core waveguides with hybrid claddings are another category of THz waveguides proposed to lower the attenuation coefficient of the propagating modes, i.e. the loss. Here, hybrid-clad waveguides refer to structures with a minimum of two different cladding layers. Each cladding layer can be a simple material layer (e.g. dielectric coating) or a composite material layer, e.g. metamaterial (Yan and Mortensen 2009). Generally, each layer has special functional properties and contributes to the propagation of the mode. However, there are cases where the cladding layer acts only as the supporting base for the next layer (the first example of this group). A common layer employed in the hybrid-clad THz waveguide is a metal layer in virtue of its superior reflecting surface for TE modes.

Hollow-core metal coated waveguides are the first hybrid-clad waveguide proposed in the literature for guidance of THz radiation (Harrington *et al.* 2004, Ito *et al.* 2007). When the thickness of metal film is greater than the skin depth of the metal at terahertz, the hollow-core waveguides with an inner metal coating perform like metal waveguide with

NOTE:

This figure is included on page 38 of the print copy of the thesis held in the University of Adelaide Library.

Figure 2.15. Single dielectric ring (pipe) waveguide and the experimental set-up. (a)- The Teflon low-index pipe waveguide, where D and t represent core diameter and cladding thickness; respectively. (b)- The experimental set-up used for characterisation of low-index pipe waveguide. Two tunable continuous-wave Gunn oscillator modules with 320460 GHz and 405520 GHz frequency ranges are used as the THz emitter. The THz radiation is coupled into the structure with a pair of parabolic mirrors. A Golay cell is used as THz detector. After Lai *et al.* (2009).

circular cross-section (metal pipe). On the contrast of metal waveguides, these hollow-core waveguides are flexible and have smoother and homogeneous inner surface. This approach was adapted from InfraRed (IR) metal-coated hollow glass waveguides (Harrington 2000).

Hollow-core polycarbonate waveguide with a Cu inner coating (Harrington *et al.* 2004) and hollow-core glass waveguide with a silver coating (Ito *et al.* 2007) are the examples proposed for THz guidance. The deposited Cu and Ag layer thicknesses inside the tubes were respectively 0.5–0.7 μm , and 0.1–0.12 μm , which is greater than the skin depth of about 0.05 μm for Cu and 0.065 μm for Ag at THz frequencies. The bore (hollow-core) diameter of the hollow-core waveguide with Cu inner coating was relatively large (2–6.3 mm); therefore in order to have a flexible structure a polymer material with a smooth inner surface, nearly equal in roughness to silica glass, was chosen instead of glass capillaries. The hollow-core waveguide with Cu inner coating was fabricated by depositing Cu employing a liquid-phase chemical process. While, the hollow-core waveguide with Ag inner coating was fabricated by employing a silver mirror-plating technique. Both techniques are adapted from hollow core IR waveguides (Harrington 2000). The loss of this hollow-core waveguide was measured at three different frequencies (1.6, 1.9, and 2.5 THz) for three different bore diameters (2, 3, and 6.3 mm). The lowest loss was 0.9 m^{-1} at

1.9 THz ($\lambda = 158.3 \mu\text{m}$) for the 3 mm bore waveguide (Harrington *et al.* 2004). The losses were measured using a continuous-wave single-mode far IR gas laser as the source and a pyroelectric camera as the detector. The tunable IR laser ($42 \mu\text{m} < \lambda < 1020 \mu\text{m}$) used for generation of THz pulses is optically pumped using a CO₂ gas laser. The measured loss of hollow-core glass waveguide with Ag inner coating was around 1.9 m^{-1} at the 1.25–1.67 THz for the 1 mm bore diameter (Ito *et al.* 2007). A tuneable parametric oscillator with a MgO:LiNbO₃ crystal pumped by a Q-switched Nd:YAG laser was used as a terahertz source and a Si bolometer as a terahertz detector. A polymer lens was used to focus the beam into the waveguides.

In hollow-core metal waveguides the TE₁₁ mode is the dominant mode and is excited with the linearly polarised THz pulses. However, it is not the mode with lowest attenuation constant in the metal waveguides. The TE₀₁ mode has the lowest loss (attenuation constant) with a doughnut-shaped mode distribution which cannot be launched easily with linearly polarised THz pulses. In order to reduce the loss further, in these hybrid-clad waveguides, a dielectric coating is added. This coating lowers the attenuation constant of the TM modes and allows hybrid mode propagation. Thus the HE₁₁ mode becomes the dominant mode with lower attenuation constant (Bowden *et al.* 2008a, Matsuura and Takeda 2008, Tang *et al.* 2009). An important parameter in the design of dielectric coated hollow-core waveguides is the thickness of the dielectric coating, which determines whether the TE₀₁ or HE₁₁ mode has the lowest loss.

Bowden *et al.* (2007) demonstrated that in a silver/polystyrene (Ag/PS) coated hollow glass waveguide, a loss of 0.22 m^{-1} (0.95 dB/m) at 2.5 THz (119 μm) is obtained for the fundamental mode. The thickness of the deposited PS coating and the bore size of the waveguide were 8.2 μm and 2.2 mm, respectively. The metallic and dielectric coatings in the hollow-core waveguide were obtained using liquid-phase chemistry methods. The large bore size (2.2 mm) reduces attenuation and allows a very good coupling of the free-space beam in the structure. However, the large bore size results in excitation of higher order modes (Bowden *et al.* 2008b). A source and detector employed for the THz measurements were similar to the ones used for hollow-core polycarbonate waveguide with Cu inner coating described above. The THz pulse was focused into the waveguide using a high-density polyethylene lens (Bowden *et al.* 2007).

Matsuura and Takeda (2008) demonstrated that the loss in a polyethylene (PE)-loaded hollow glass tube with silver-deposited PE film, whose PE side faced the hollow-core (Ag/PE), was 0.32 m^{-1} (1.3 dB/m) at 2.5 THz (200 μm). The thickness of the deposited

PE coating and the bore size of the waveguide were 26 μm and 3 mm, respectively. The waveguide was fabricated by inserting an Ag/PE film into polycarbonate tube. The Ag film was deposited onto a strip of PE by sputter deposition. The measured loss for Ag/PE hollow-core waveguide was 3 dB lower than that of a similar hollow-core waveguide with a silver inner coating in the frequency region from 1.2 THz to 2 THz. The measurement was performed using a Fourier transform infrared spectrometer (FT-IR) with a Si bolometer as detector. The THz pulse was focused into the waveguide by a gold-coated off-axis mirror.

A drawback of introducing the dielectric layer in a metallic waveguide is that the dielectric coating introduces interference peaks, which limits the bandwidth of operation (Matsuura and Takeda 2008). Therefore the thickness of the dielectric coating should be designed so that the low loss transmission window is located in the desired frequency region. Another drawback of a dielectric coating is that the inner dielectric coating adds absorption losses. Therefore the dielectric materials with low absorption loss, i.e. $\kappa = 2\pi\alpha/\lambda$ less than 0.065 (Matsuura and Takeda 2008), should be selected in order to achieve lower losses in a hollow-core waveguide with inner dielectric coating compared to a metallic hollow-core waveguide.

Hollow-core microstructured band-gap fibres

Hollow-core microstructured band-gap fibres consist of a hollow-core surrounded by micron scale air holes in the cladding, which run the length of the fibre. The mode confines and propagates in the core when the cladding does not support the mode, i.e. the cladding forms a two-dimensional photonic crystal and the excited mode lies in the band-gap of the cladding. They were first proposed, developed and optimised for visible and infrared regime (Knight *et al.* 1996, Knight *et al.* 1998, Correa and Knight 2008). The scanning electron microscope image of an optical hollow-core microstructured band-gap fibre is shown in Fig. 2.16(a).

As is well known from optics, these fibres can suffer from high-confinement losses⁶ due to the finite number of air-holes composing the cladding lattice (Geng *et al.* 2008a) and scattering loss due surface roughness at the dielectric-air interface (Roberts *et al.* 2005). The leakage can be suppressed by incorporating sufficient concentric rings of air-holes

⁶Confinement loss for axial mode propagation is the loss of power through the transverse structure, which is also known as leakage loss.

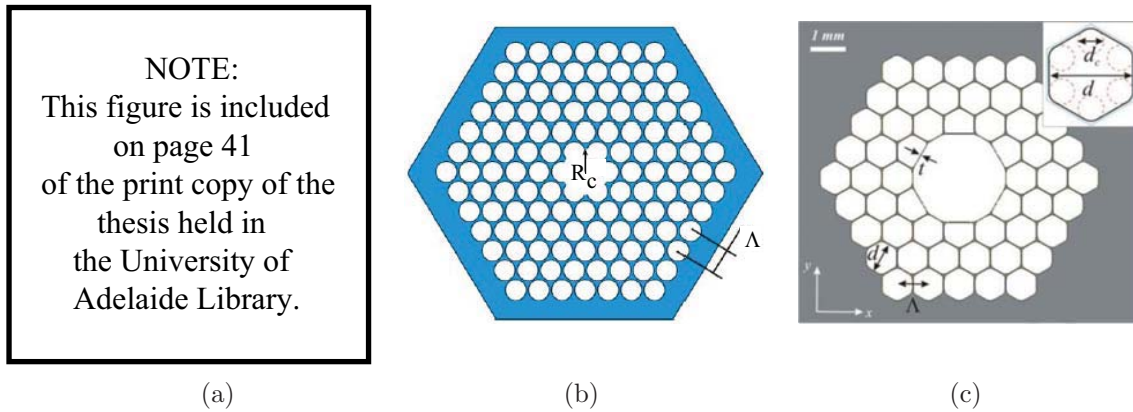


Figure 2.16. Hollow-core microstructured band-gap fibre. (a)- The scanning electron microscope image of optical photonic band-gap fibre. After Correa and Knight (2008). (b) and (c)- The cross-sections of the analysed THz hollow core photonic band-gap fibre. After Geng *et al.* (2008a) and Vincetti (2009a).

around the core or by increasing the ratio of the cladding air-hole diameter to the hole-to-hole spacing pitch (d/Λ). Though, the higher the number of concentric air-hole rings, the more difficult the process of fabrication becomes. The scattering losses, which are inversely proportional to the operating wavelength, can be suppressed to a certain degree by controlling the fibre fabrication parameters.

The concept of hollow-core microstructured band-gap fibres has been expanded to THz frequencies (Geng *et al.* 2008a, Geng *et al.* 2008b, Ren *et al.* 2008, Vincetti 2009a). The advantage of using these fibres for THz are: firstly, like all other hollow-core fibres most of the electromagnetic field propagates in the air core (which is transparent medium for THz); and secondly, at THz frequencies (longer wavelength compared to invisible and optics) scattering losses are low and do not significantly affect the overall loss mechanism (Vincetti and Polemi 2009).

Geng *et al.* (2008a) analysed waveguides composed of two-dimensional triangular arrangement of air-holes in the cladding with larger diameter-to-pitch ratio ($d/\Lambda = 0.93$ and 0.96) and a seven-unit-cell air core, as shown in Fig. 2.16(b). The hollow core radius (R_c) of the waveguides were chosen equal to the hole-to-hole spacing pitch ($\Lambda = 292 \mu\text{m}$) in the cladding to guarantee a single mode propagation. HDPE was considered as the host material of the waveguides due to its low absorption coefficient at THz. The band-gap width calculated for $d/\Lambda = 0.93$ and $d/\Lambda = 0.96$ waveguides was respectively 0.11 THz ($1.42\text{--}1.53 \text{ THz}$) and 0.24 THz ($1.54\text{--}1.78 \text{ THz}$). The evaluation indicated that the leakage losses for these waveguides were negligible in comparison to the absorption losses

rising from material absorption HDPE. The lowest value of the leakage and absorption losses for the waveguide with $d/\Lambda = 0.93$ were respectively reported $3.0 \times 10^{-5} \text{ cm}^{-1}$ at 1.5 THz and 0.0224 cm^{-1} at 1.53 THz, and for the waveguide with $d/\Lambda = 0.96$ were respectively reported $3.5 \times 10^{-6} \text{ cm}^{-1}$ at 1.69 THz and 0.0141 cm^{-1} at 1.75 THz. The dispersion analysis reveals that the dispersion curve of the waveguides change rapidly from -4 to 1 ps/THz/cm in the bandgap with a smother slope for the waveguide with $d/\Lambda = 0.96$ around the centre (GDV = 0).

A hollow-core microstructured band-gap fibre with the cross-section shown in Fig. 2.16(c) (this theoretical structure has sharp corners rounded off based on real fabricated fibre structures in the optical regime) was also analysed for THz guidance (Geng *et al.* 2008b, Ren *et al.* 2008, Vincetti 2009a). Geng *et al.* (2008b) stated leakage and absorption loss values of respectively 1.1×10^{-5} and 0.0006 cm^{-1} at 1.68 THz, for a 19-unit-cell air core ($R_c = 225 \text{ }\mu\text{m}$) and 4 layers of hexagonal air-holes ($d = 539 \text{ }\mu\text{m}$, $\Lambda = 550 \text{ }\mu\text{m}$, and $t = 5.5 \text{ }\mu\text{m}$) with rounded corners as cladding of the HDPE waveguide. Vincetti (2009a) theoretically showed that just three concentric rings of air-holes in the cladding were enough for a THz hollow-core microstructured bang-gap fibre to have negligible leakage loss compared with cladding material absorption loss. They have demonstrated theoretically that the propagation loss is two decades lower than the absorption losses of the bulk material for the THz band-gap fibre ($R_c = 2.7 \text{ mm}$, $d = 882 \text{ }\mu\text{m}$, $\Lambda = 900 \text{ }\mu\text{m}$, and $t = 9 \text{ }\mu\text{m}$). Loss values less than 0.01 cm^{-1} and dispersion values less than 2 ps/nm/km are obtained for a Teflon and HDPE microstructured band-gap fibre over the frequency range of 0.895–1.145 and 0.82–1.02 THz, respectively. Also a periodic arrangement of square holes with rectangular air-core and round corners in the cladding was analysed, where a phase index birefringence of 10^{-3} was reported (Ren *et al.* 2008).

In a nutshell, the numerical results discussed above indicate that for larger diameter-to-pitch ratio and core diameters, lower transmission loss and lower group velocity dispersion can be achieved in plastic hollow-core microstructured band-gap fibres. The confinement loss is negligible for these waveguides; it is more than two orders of magnitude lower than the absorption loss. The losses and dispersion are strongly frequency dependent, i.e. they have small values around the centre of the band-gap and the values increase on approaching the boundaries of the band-gap. The operational bandwidth of these waveguides is defined by the band-gap width. Although they can be tuned to operate in a different frequency band, the bandwidth is extremely narrow compared to the THz spectrum, moreover, they have large diameter. As an example, three concentric rings for

the cladding and two omitted concentric rings to form the hollow core, lead to a 10 mm diameter for THz hollow-core photonic band-gap fibre. The waveguide diameter indicates that these fibres are inflexible and not a proper guiding structure for integrated THz devices. Additionally, these fibres suffer from multimode propagation due to their large core size. Decreasing the core diameter increases the leakage from the core which leads to higher absorption losses. To reduce the leakage more layers of cladding are required, which adds to the waveguide diameter. The coupling coefficient is also very low in these fibres due to the closeness of the propagation constant of the fundamental mode and higher order modes. To the best of our knowledge so far, there has been no fabrication and experiment reported in the literature on THz hollow-core microstructured band-gap fibres.

Hollow-core multilayer band-gap waveguides (Bragg fibre)

Multilayer dielectric band-gap waveguides, well known as Bragg fibres in optics, consist of a hollow-core surrounded with concentric cylindrically-periodic (CP) structure. The CP waveguide confines the mode in the core by band-gap effects (Temelkuran *et al.* 2002, Katagiri *et al.* 2004, Rowland 2010). So far at the optical regime, there are three types of hollow-core Bragg fibres. The first one is the omnidirectional Bragg fibre, made up of combination of either glass or polymer materials with very large index variation between concentric cladding layers as shown in Fig. 2.17(a). The second type is ring-structured Bragg fibre, made up of single material with alternating circular rings of air-holes, which behave like the low-index layers of an omnidirectional Bragg fibre, as shown in Fig. 2.17(b). Finally, the third type is the cob/spider-web structured Bragg fibre made up of layers of single material and air, where a certain number of supporting strips, called struts, are used to keep the structure together, as shown in Fig. 2.17(c). All the three types of Bragg fibres have also been explored for THz (Skorobogatiy and Dupuis 2007, Yu *et al.* 2007, Ponseca *et al.* 2008).

A hollow-core multilayer band-gap waveguide featuring concentric cylindrically-periodic layers (PVDF and polycarbonate polymers) was theoretically studied for THz guidance (Skorobogatiy and Dupuis 2007). Two fabrication techniques were proposed for these waveguides: consecutive deposition of polymer layers by solvent evaporation on the inside of a rotating polymer tube, and co-rolling and solidification of the two polymer films. The second approach can employ drawing to achieve the desired diameter. Moreover, an extra manufacturing step either during or after drawing is needed for activating

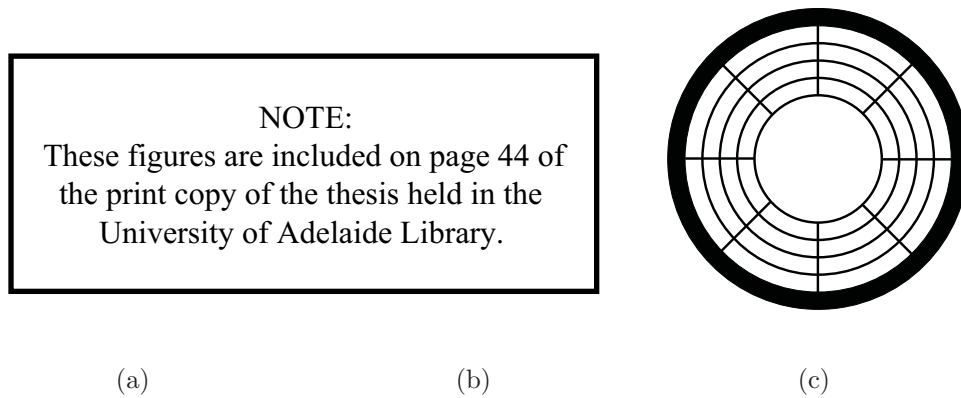


Figure 2.17. THz Bragg fibres. (a)- Concentric cylindrically-periodic Bragg fibre with a large variation in index between the cladding layers. After Yu *et al.* (2007). (b)- The microscope image of a ring structured Bragg fibre. After Ponceca *et al.* (2008). In contrast to omnidirectional Bragg fibre, the ring structured Bragg fibre is made up of single material and variation in index between the cladding layers is achieved by including alternating circular rings of air-holes. (c)- Cob/spider-web structured Bragg fibre. After Yu *et al.* (2007) and Rowland (2010). These Bragg fibres are also made up of a single host material (concentric layers of material and air), and struts are used to keep the structure together.

PVDF polymer. Theoretical loss values less than 0.02 cm^{-1} for $1 < \omega < 3 \text{ THz}$ was presented for a 1 mm core diameter and 31 layers ($\approx 50 \mu\text{m}$ thickness) of PVDF/PC reflector. In such a broad frequency window, the hollow-core multilayer band-gap waveguide guides THz pulses not only in the band-gap regime, but also outside the gap. The structure also acts as a metamaterial waveguide with a sub-wavelength reflector period, a single PC, or a PVDF tube at THz range. No experimental characterisation of the hollow-core multilayer band-gap waveguide is reported.

For a hollow-core multilayer band-gap waveguide, it is difficult to find two materials with sufficient index contrast⁷, similar thermal and mechanical properties, as well as a compatible processing techniques in realising the structure. Thus, hollow-core band-gap waveguides made of single material (i.e. ring and spider-web structured band-gap waveguides) are more favourable. Absorption losses less than $1.8 \times 10^{-5} \text{ cm}^{-1}$ in the frequency range 1.5–4.3 THz was theoretically calculated and reported for a hollow-core HDPE spider-web structured band-gap waveguide for 8 mm core radius, 25/500 μm thickness

⁷The relative size of the band-gap is proportional to the relative index contrast of materials.

of material/air layers, and 3 alternating layers for cladding (Yu *et al.* 2007). Like microstructured band-gap waveguides, the confinement loss ($3.8 \times 10^{-12} \text{ cm}^{-1}$ at 3.6 THz) of spider-web structured band-gap waveguide is negligible. Extrusion techniques have been proposed for fabrication of these waveguides; however, no experimental characterisation is reported.

Guiding of THz pulses in both the hollow-core and the microstructured cladding were observed in a PMMA ring structured Bragg waveguide (Ponseca *et al.* 2008). The preforms were prepared by drilling the hole pattern into a 7 cm diameter of PMMA rod and drawn to 6 mm diameter waveguides. Two waveguides with the following parameters were characterised: waveguide 1 (6.3 mm outer diameter, 69 μm hole diameter, 93 μm between the holes in the same ring and 105 μm between the holes in adjacent ring) and waveguide 2 (5.6 mm outer diameter, 65 μm hole diameter, 86 μm between the holes in the same ring and 93 μm between the holes in adjacent ring). The experimental set-up used for characterisation of THz Bragg fibre is shown in Fig. 2.18. A mode-locked Ti:sapphire laser is used to pump the n-type bulk Indium-Arsenide (InAs) emitter under a 1 T magnetic field⁸, while the detector is a bow-tie type photoconductive antenna.

Transmission bands of 0.8–1.4 THz for waveguide 1 and 1.0–1.6 THz for waveguide 2, which were in good agreement with the expected band-gap location were observed. The total propagation loss due to the both pulses, guided in the core by virtue of the band-gap effect and guided in the cladding by virtue of total internal reflection, was estimated to be 1.3 and 1.1 cm^{-1} for waveguides 1 and 2, respectively. Due to separation of two guided pulses (20 ps), the loss for individual pulses was also estimated. The minimum absorption loss of the pulse guided in the hollow core was estimated to be 0.44 cm^{-1} at 1.0 THz for waveguide 1 and 0.2 cm^{-1} at 1.3 THz for waveguide 2.

These multilayer band-gap waveguides allow low loss propagation of THz pulses in the band-gap regime, which is narrow compared to the broad spectrum of THz. The loss and dispersion of these waveguides increases as the frequency approached to the edges of the bands. The guidance in these waveguides is not limited to the gap region. Depending on the cladding design and material, these waveguides act as hollow-core microstructured

⁸It has been shown that the generation of THz radiation from specific semiconductors (such as InAs, GaAs and InSb) is enhanced by applying the external magnetic field. It has also been demonstrated that InAs is the most efficient emitter in the presence of a magnetic field (Zhang *et al.* 1993, Sakai 2005).

NOTE:
This figure is included on page 46 of the print copy of
the thesis held in the University of Adelaide Library.

Figure 2.18. Bragg fibre experimental set-up. The schematic diagram of the experimental setup used for characterisation of Bragg fibre. An n-type bulk Indium-Arsenide (InAs) emitter and a bow-tie type photoconductive antenna is used for the generation and detection of THz radiation. After Ponseca *et al.* (2008).

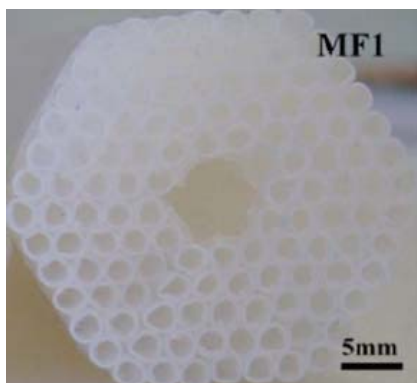
fibres guiding in the band-gap regime, a metamaterial fibre with a sub-wavelength reflector period, a tube waveguide, or microstructured fibre guiding based on total internal reflection.

Direct scaling up of the optical dimensions results in large THz waveguide dimensions (6-10 mm in diameter), making them potentially very inflexible. Such structures also suffer from high losses especially at bends or discontinuities, due to coupling of propagating mode TE_{01} to the lossy TM_{11} degenerate mode⁹. Although addition of an external metal coating might improve the radiation losses (Llombart *et al.* 2009), the narrow bandwidth (resulting in high losses and dispersion at the edges of the bandwidth) and rigidity of the waveguides are the two main disadvantages of these waveguides.

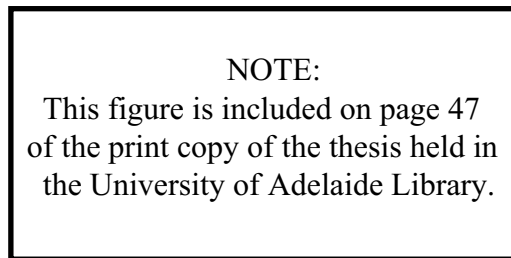
Kagomé hollow-core microstructured fibres

The hollow-core microstructured fibre proposed by Lu *et al.* (2008c) is—as the name suggests—composed of a central hollow core and a cladding layer formed by periodic arrangements of Teflon tubes. The Teflon tubes are chosen for this purpose since the THz absorption coefficient of Teflon is low, i.e. less than 3 cm^{-1} for 0.2–3 THz (Fischer 2005),

⁹Degenerate modes are the modes that have identical cut-off frequency, e.g. TE_{0n} and TM_{1n} in circular cross-section waveguides.



(a)



(b)

Figure 2.19. Hollow-core microstructured Kagomé fibres. (a) THz hollow-core microstructure fibre proposed by Lu *et al.* (2008c). (b) Scanning electron microscope image of the optical Kagomé fibre by Couny *et al.* (2006).

and also these tubes are commercially available in different inner and outer diameters. As shown in Fig. 2.19(a), the Teflon tubes are bound together in triangular lattice and the seven central tubes (the central tube and the six tubes in the first layer) are removed to create the hollow core. The guiding mechanism in this fibre is similar to the Kagomé-lattice optical fibre, shown in Fig. 2.19(b), (Couny *et al.* 2006, Argyros and Pla 2007, Vincetti 2009b), where the guided modes confined in the hollow-core are prevented from efficiently coupling to the cladding due to the anti-resonance effect of the Kagomé lattice. The guiding mechanism in these fibres is by virtue of the formation of Von-Neumann-Wigner quasi-bound states and the cladding does not support photonic band-gaps (Benabid *et al.* 2009).

A low attenuation constant less than 0.01 cm^{-1} is experimentally achieved at 0.770 THz for hollow-core microstructured fibres made up of seven cladding rings (Lu *et al.* 2008c) as shown in Fig. 2.19(a). The waveguide was fabricated by stacking commercially available Teflon tubes. The attained structure was suitable for the guidance of THz pulses, and no further drawing steps were required. For the characterisation of the waveguide proposed by Lu *et al.* (2008c), a broadband pulse source is used for generation of THz radiation, but no detail is provided as to the type of THz source used. A Martin-Puplett polarising interferometer¹⁰ (Lambert and Richards 1978) together with a bolometer are employed

¹⁰Interferometry is the technique of measuring the properties of waves by studying the pattern of interference created by their superposition.

on the detection side. Due to the large core sizes no lenses were required for coupling into the waveguide.

Theoretical investigations of these waveguides reveal that the transmission spectrum exhibits an alternation of low loss and high loss bands. The minimum loss in each low loss region depends on tube diameter (d), while the frequency ranges of low loss and dispersion is depend on the thickness (t) of the tubes (Vincetti 2009b). Increasing the tube diameter reduces the minimum loss about of one order of magnitude, flattens the dispersion, and increases the core and total diameter of the waveguide. While, decreasing the thickness of the tubes leads to a wider transmission band. As an example, for a waveguide obtained by removing the seven innermost Teflon tubes ($d = 2.8$ mm and $t = 44$ μm) loss lower than 0.002 m^{-1} and dispersion coefficient lower than 0.03 ps/nm/km are calculated over a frequency range from 1.3 to 3 THz (Vincetti 2009b).

Kagomé-lattice waveguides offer a wider transmission band compared to Bragg waveguides. Similar to Bragg waveguides the leakage loss for Kagomé lattice waveguides (even with one ring of tubes as cladding) are negligible compared to absorption loss, except where the frequencies coincide with cut-off frequencies. The dispersion curve is S-shaped and it increases at the edges of the transmission band due to the anticrossing with cladding modes at the resonance frequencies.

A drawback of Kagomé waveguides is that they have diameters of the order of a few tens of millimetres. As an example for the seven ring microstructure fibre proposed by Lu *et al.* (2008c), the total fibre diameter ranges from 18 to 35 mm for the commercially available Teflon tubes with the outer/inner diameters of 1.68/2.08 mm, and 0.81/1.11 mm. It should be noted that the diameter of the fibre is greater than 10 mm even when a single layer of cladding is used. Thus, these waveguides are not flexible. Another disadvantage of these fibres is that they are multimode due to the large core diameters. It has been shown that reducing the core size leads to single mode propagation at the expense of high fundamental mode propagation losses and dispersion. It should be noted that single-mode propagation can be obtained to some extent by controlling the launch condition (Vincetti 2010). A third disadvantage of these waveguides is that the loss and dispersion curves contain irregular small perturbations in the low loss regions (in between two dominant perturbations that define the transmission band) due to the weak coupling between core modes and cladding modes (Vincetti 2009b).

Remarks An advantage of hollow-core waveguides is that the THz pulses propagate mainly in the hollow core and only small fraction of it propagates in the material resulting to low absorption losses. These waveguides can be tailored to offer low-loss and dispersion in the required transmission band. Another advantage of these waveguides is that they are suitable for sensing applications, i.e. the sample under test can be located in the core where a better interaction of the field and sample can occur compared to free-space propagation systems.

In spite of the above advantages, generally the hollow-core waveguides have in transmission window by virtue of the resonance or band-gap effects. Therefore, they only offer low-loss and dispersion for the designed narrow window and are not suitable to guide a broad THz spectrum. Another drawback of these waveguides is that their dimension is in the order of a few millimetres. Thus, commonly they are inflexible. Reducing the core diameter leads to an increase in the absorption loss.

A summary of all the key parameters discussed for the above hollow-core waveguides is presented in Table 2.3.

Solid-core waveguides/fibres

The guiding mechanism of solid-core waveguides/fibres, where the effective refractive index of the core is higher than that of the cladding, is based on well-known total internal reflection. These solid-core waveguides suffer from material absorption since most of the mode is guided within a dielectric medium and there is no known low loss dielectric material in THz. Therefore, the material choice and waveguide structure have a great impact on the fibre performance, not only on transmission loss but also on dispersion.

Air-clad dielectric waveguides with sub-wavelength core

Plastic ribbon waveguide (Mendis and Grischkowsky 2000) and sapphire fibre (Jamison *et al.* 2000) are the first two dielectric waveguides proposed by Oklahoma State University research group. As the names indicate, these structures were made of up respectively sapphire with the diameters of 150, 250 and 325 μm and high-density polyethylene slabs with the thicknesses of 120 and 150 μm . The structures offer lower absorption loss than the bulk material loss, less than 6 cm^{-1} for the frequencies less than 2.5 THz and less than 1 cm^{-1} over the frequency range 0.1 to 3.5 THz for sapphire fibre and ribbon waveguide, respectively. This occurs by virtue of the sub-wavelength dimension of the waveguides, where the propagating mode is not tightly confined to the waveguide and expands to

the air. The THz temporal pulse is negatively and positively chirped after propagating through sapphire and plastic ribbon waveguides, respectively. The absorption losses of these waveguides are much lower than those of coplanar waveguides discussed earlier in this section. Nevertheless, the achieved losses are not comparable to those of parallel-plate waveguide, bare metal wire, and recently developed dielectric waveguides discussed later in this Section. A similar THz-TDS system, shown in Fig. 2.9(b) for characterisation of metallic waveguides (optoelectrical emitter and detector, and steering optics), was employed for characterisation of sapphire and plastic ribbon waveguides. Silicon hyper-hemispherical and plano-cylindrical lenses were used to couple the energy into and out of sapphire and plastic ribbon waveguides, respectively.

In 2006, Chen *et al.* (2006), from Taiwan University, reported loss values less than 0.01 cm^{-1} near 0.3 THz in a polyethylene sub-wavelength air-clad waveguide. An air-clad fibre with a core diameter of $200 \mu\text{m}$ is used to guide the THz radiation. Compared to sapphire waveguide, proposed earlier in the literature, this waveguide only has different host material and is analysed at low frequencies where the waveguide dimension is smaller than the operating wavelengths ($830\text{--}970 \mu\text{m}$). As we later show in Chapter 3, the sub-wavelength dimension pushes a large portion of the transmitted power is in the air-clad, which is transparent for THz frequencies leaving a small portion of it in the low loss plastic material. Therefore, the loss averaged in the transverse plane reduces dramatically. The concept used by Chen *et al.* (2006) is similar to the concept developed in optics; i.e. optical nanowires (Tong *et al.* 2003). More details on optical nanowires and the expansion of the concept to the THz region will be discussed in Chapter 3.

The schematic of the THz experimental set-up used for the loss measurement of the sub-wavelength fibre is shown in Fig. 2.20. A photonic transmitter¹¹ excited by an optical femtosecond laser pulse and an Si bolometer is used for the generation and detection of THz radiation. A special fibre coupler made from paper is used to hold the fibre and a metal cone is employed at the end of the fibre to prevent scattered waves from being detected.

The sub-wavelength air-clad waveguides are flexible due to their sub-wavelength dimension (a few hundred microns). The extension of the propagating mode in the air allows coupling via surface contact and straightforward interaction of the mode with the surrounding environment leading to practical applications in sensing. For examples, these waveguides

¹¹Printed circuit antenna on an ultrafast photoconductive material (LT-GaAs), which generates quasi-CW narrow-band THz radiation (Shi *et al.* 2002, Tien *et al.* 2004).

NOTE:
This figure is included on page 51 of the print copy of
the thesis held in the University of Adelaide Library.

Figure 2.20. Sub-wavelength air-clad dielectric fibre experimental arrangement. Schematic of the THz TDS experimental setup. A photonic transmitter excited by an optical femtosecond laser pulse and an Si bolometer is used for the generation and detection of THz radiation. After Chen *et al.* (2006).

have been utilised as straight THz tip sensors for spectroscopy (You *et al.* 2009, You *et al.* 2010), THz directional couplers (Chen *et al.* 2009) and as waveguide based THz endoscopes in interferometric imaging (Lu *et al.* 2008b, Lu *et al.* 2008a).

In spite of that, one disadvantage of these sub-wavelength air-clad waveguides with low power fraction in the core is that they suffer from high losses due to any perturbation (e.g. bends) to the structure. This occurs due to the weak confinement of the mode to the waveguide compared to waveguides with strong confinement of the field in the core (e.g. conventional core/clad fibres, and hollow-core band-gap waveguides).

Solid-core microstructured waveguides

The guiding mechanism of a solid-core microstructured waveguide, also known as a solid-core photonic crystal fibre (PCF), is achieved by total internal reflection, while in PCFs with low index cores, e.g. air-core, it is achieved by the photonic band-gap effect. Han *et al.* (2002) were the first to realise, fabricate, and experimentally demonstrate the loss and dispersion of solid-core microstructured waveguides in the THz spectrum. As shown in Fig. 2.21(a), the structure is fabricated from high-density polyethylene (HDPE) tubes and a filament that represent respectively the cladding and core. A relatively low loss (less than 0.5 cm^{-1}) and low dispersion (average group velocity of 2 ps/THz/cm at 0.4 THz) is attained within the bandwidth of $0.1\text{--}3 \text{ THz}$ (Han *et al.* 2002). An identical experimental

arrangement employed for metallic waveguides, shown in Fig. 2.9(b), is used for characterisation of the PCFs. The THz pulse was generated employing optical rectification method and was detected by a photoconductive antenna.

The attenuation of a guided mode of the solid-core PCF depends on the field confinement in the core and the core material absorption. It has been shown that the main contribution of the transmission loss is the material absorption loss (Han *et al.* 2002). Consequently, the attenuation can be reduced by using material with lower loss or lower refractive index in the THz regime. Goto *et al.* (2004) have demonstrated that fabricating a similar solid-core PCF from polytetrafluorethylene, commonly known as Teflon, reduces the solid-core PCF loss further to less than 0.12 cm^{-1} for 0.1–1.3 THz. This is due to relatively a low refractive index of Teflon ($n = 1.46$) compared to that of HDPE ($n = 1.53$) (Birch *et al.* 1981), which leads to a lower confinement of THz radiation into the solid-core and consequently lower loss. The experimental set-up employed for the characterisation of the Teflon PCF is shown in Fig. 2.21(b). The broadband terahertz radiation is generated by employing an In-As semiconductor pumped by a mode-locked Ti:sapphire laser under a 2.5 T magnetic field. An Si-bolometer is employed for the detection of THz field intensity.

Nielsen *et al.* (2009) improve the loss of solid-core microstructured waveguides further to less than 0.1 cm^{-1} for 0.35–0.65 THz by using cyclic olefin copolymer, COC and commercially known as TOPAS, as the host material. The THz dielectric properties of COC is demonstrated in this thesis in Chapter 3. The photographs of two different solid-core microstructured waveguides fabricated from COC are shown in Fig. 2.22(a). These COC waveguides have S-shaped dispersion curves with absolute dispersion parameter β_2 values less than $1 \text{ ps}^2/\text{THz}/\text{cm}$ for 0.4–1.4 THz and zero dispersion between 0.5–0.6 THz.

Unlike previous characterisation setups discussed so far, these COC microstructured waveguides are characterised in a reflection based THz time domain spectroscopy system. Two photoconductive antennas are used for generation and detection of broadband THz pulses. In order to have a constant in- and out-coupling of the THz pulses during loss measurements, a reflection arrangement is considered as shown in Fig. 2.22(b). A metallic reflector is positioned at the back end facet of the waveguide for this purpose and the waveguide is also cleaved from this end for loss measurements. A COC beam splitter is used to separate the reflected THz beam from the incoming beam. A COC hyper-hemispherical lens is employed for coupling in and out of the PFC instead of silicon lenses.

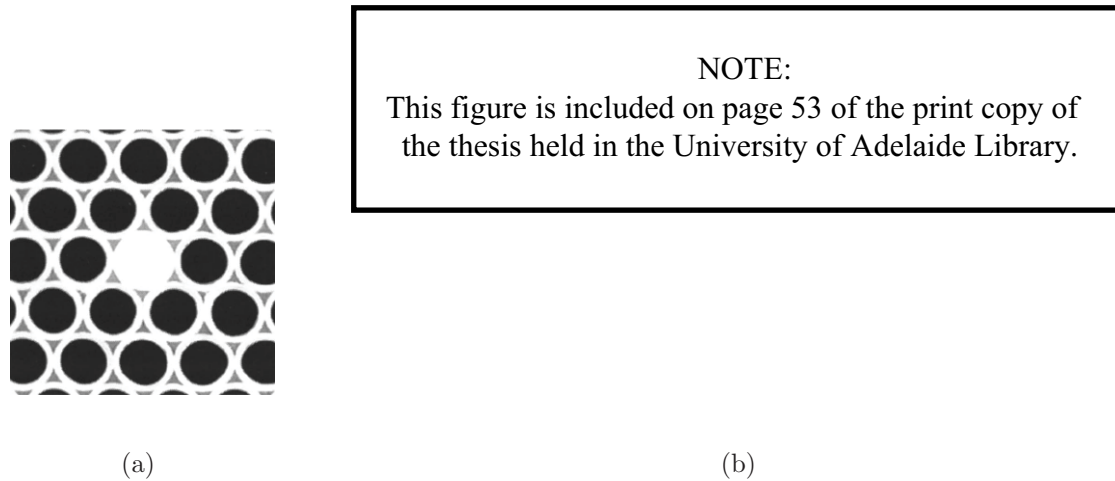


Figure 2.21. Solid-core microstructured fibre and the experimental arrangement I. (a)- Optical micrograph of a solid-core photonic crystal fiber. After Han *et al.* (2002). (b)- An undoped Indium-Arsenide (InAs) emitter and a liquid-He cooled Si-bolometer are used for the generation and detection of THz radiation. A silicon hyper-hemispherical lens is used to couple the THz radiation into the Teflon PCF. After Goto *et al.* (2004).

Compared to air-core microstructured waveguides, the solid-core microstructured waveguides has a broader transition bandwidth since the guiding mechanism is based on total internal reflection and not based on antiresonance or band-gap effects. Thus these waveguides are better suited for the broadband THz guidance. Although the COC solid-core microstructured waveguides can be bent (90-degree bend) by heating the waveguide, generally they are rigid due to their large dimension (a few millimetres).

Waveguides with a low index discontinuity in the core

Nagel *et al.* (2006b) have proposed low index discontinuity waveguides in order to improve the confinement of the THz radiation, which is the disadvantage of sub-wavelength fibre and metal wire. In that work, Nagel *et al.* (2006b) have transferred the concept proposed by Almeida *et al.* (2004) for integrated optical devices to THz range. Almeida *et al.* (2004) showed theoretically and experimentally that a high-index dielectric single-mode rectangular waveguide split along the axis of wave propagation enhances and confines a substantial fraction of power in the low-index split region as shown in Fig. 2.23(b). The

NOTE:
This figure is included on page 54 of the print copy of
the thesis held in the University of Adelaide Library.

Figure 2.22. Solid-core microstructured fibre and experimental arrangement II. (a)- The photographs of two different solid-core PFC fabricated from COC. (b)- The reflection arrangement considered for constant in- and out-coupling of the THz signal during loss measurements. After Nielsen *et al.* (2009).

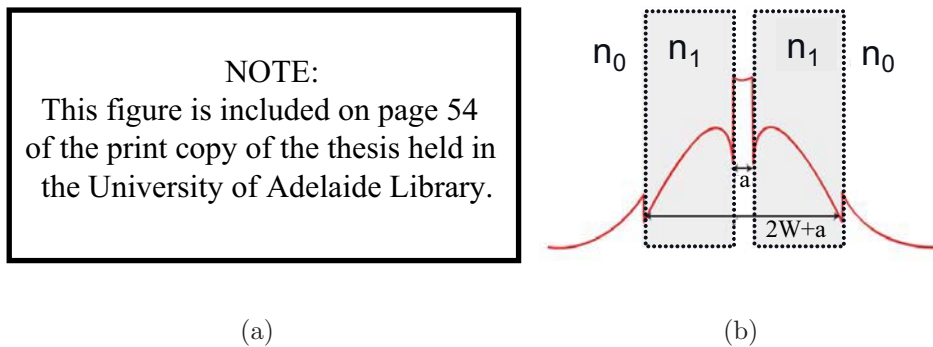


Figure 2.23. Schematic of a dielectric slit rectangular and tube waveguides, and electric field enhancement. (a)- Geometries of a slit rectangular waveguide (SRW) and a tube waveguide (TW). After Nagel *et al.* (2006b). (b)- Electric field enhancement within low-index discontinuity.

concept has been expanded to THz by Nagel *et al.* (2006b) and the attenuation, dispersion and single-mode confinement properties for two structures, a split rectangular waveguide and a tube waveguide shown in Fig. 2.23(a), are investigated. The mode confinement in the virtually lossless low-index air gap reduces THz transmission losses compared to that of the same structure without the split and increases the confinement of the mode compared to bare metal wires (Nagel *et al.* 2006b). The concept of the field enhancement within the low-index discontinuity, which is the core concept of the porous fibres proposed in this thesis, is explained in more detail in Chapter 4.

For a tube waveguide composed of fused silica, loss values less than 0.7 cm^{-1} are measured for the frequency range of 0.4-0.6 THz (Nagel *et al.* 2006b). The measured effective permeability ($\epsilon_{\text{eff}} = n_{\text{eff}}^2$) for the tube waveguide varies from 2 to 4 over the frequency range of 0.3–0.7 THz. The numerically calculated loss and effective relative permeability of a slit rectangular waveguide made of high resistivity silicon are less than 0.01 cm^{-1} and 2, respectively, for 0.5–0.9 THz. For characterisation of tube waveguide, two identical photoconductive antennas embedded in a parallel-plate waveguide are used for the generation and detection of broadband THz radiation. The parallel-plate waveguide serves as the output and input port of the emitter and detector. The tube waveguide is aligned at a distance of a few micrometers to the parallel-plate waveguide port. The components used in this system and the measurement techniques have been described in more detail in (Nagel *et al.* 2006b, Nagel *et al.* 2006a).

Remarks The guiding mechanism in the solid-core dielectric waveguides is based on total internal reflection. These waveguides suffer from material absorption losses. This loss can be reduced if the dimension of the core is chosen smaller than the operating wavelengths, since the higher portion of the mode power propagated in the air-clad with almost zero loss. However, this reduces the confinement of the mode to the waveguide. A method proposed to increase the confinement was to introducing a sub-wavelength discontinuity in the waveguide. The absorption loss can also be reduced if low loss dielectric materials such as COC are used. However, the waveguides achieved are rigid due to their dimension. A summary of all the key parameters discussed for the above hollow-core waveguides is presented in Table 2.4.

2.4 Chapter Summary

In this chapter, different methods of terahertz generation and detection are reviewed. The physics underpinning the generation and detection THz radiation based on photoconductive antennas/switches are also discussed, since the PC antennas are employed for generation and detection of THz radiation in this thesis.

Then we have reviewed different THz non-planar waveguide structures in the terms of loss, dispersion and proposed experimental arrangements. We have divided the waveguide solutions into two main categories: metallic and dielectric. Metallic waveguides suffer from

Ohmic losses due to their finite conductivity. The metallic waveguide has higher propagation loss if the mode is confined within the structure (circular and rectangular waveguides) and the loss decreases as the mode gets less confined to the structure (bare metal wire). On the other hand the radiation losses due to any perturbation increases when the mode is loosely bound to the structure. An advantage of using metallic waveguides such as parallel-plate waveguides and bare metal wires is that these structures have a broadband undistorted wave propagation at THz spectrum, i.e. almost zero dispersion. We have compared the main points discussed in this chapter on metallic waveguides in Table 2.2.

The dielectric waveguide solutions proposed in the literature have been categorised into two main groups: hollow-core and solid-core waveguides. The material absorption is almost zero for hollow-core waveguides since the THz radiation is mainly confined in the air-core. The confined mode in the core makes them a good candidate for sensing application. However, the dimension of these waveguides is in the order of a few millimetres. This dimension leads to rigid and large waveguides, which are not practical for the integrated THz devices. Another drawback of these waveguides is that their low-loss and low-dispersion behaviours are limited to a transmission window, which is narrow compared to the THz spectrum. A third drawback of these kind of waveguides is the multimode operation due to the large core sizes. Although reducing the core size eliminates higher order modes, it increases the attenuation of the fundamental mode (Vincetti 2010). On the other hand, THz radiation propagating in the solid-core dielectric waveguides suffers from material absorption. There are two solutions proposed to decrease the loss value of a solid-core waveguide: firstly, utilizing the waveguide structures from low loss dielectric materials such as COC. Secondly, pushing most of the propagating mode into the air by either decreasing the waveguide dimension (sub-wavelength air-clad waveguides) or introducing a discontinuity (low-index discontinuity waveguide). In order to summarise the dielectric waveguides discussed here, we have also prepared two tables one for hollow-core dielectric waveguides and the other for solid-core dielectric waveguides, Tables 2.3 and 2.4 respectively. A schematic or photograph of each waveguide and the geometrical details are also included.

In the following chapter we investigate THz sub-wavelength fibre, named *microwire* in this work, for low-loss terahertz transmission. We first examine the dielectric properties of some host materials for fibres, i.e. four glasses and two polymers. Then we evaluate the affect of using these materials on the normalised field distribution, power fraction, effective area, loss and dispersion properties of THz sub-wavelength fibres.


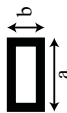

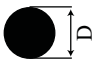
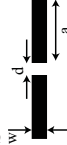
Waveguide	Dimensions	Material	$\alpha_{\text{eff}} [\text{cm}^{-1}]$	Dispersion	Remarks	References
Circular 	$D = 240 \mu\text{m}, l = 24 \text{ mm}$	stainless steel	< 1	$1 \text{ ps} \rightarrow 20 \text{ ps}$	mode: TE ₁₁ , TE ₁₂ , TM ₁₁	McGowan <i>et al.</i> (1999)
	$D = 280 \mu\text{m}, l = 25 \text{ mm}$	brass	$0.8 < f < 3.5 \text{ THz}$	$1 \text{ ps} \rightarrow 40 \text{ ps}$	$f_c = 0.75 \text{ THz}$ for TE ₁₁ strong dispersion due to f_c	Gallot <i>et al.</i> (2000)
Rectangular 	$250 \times 125 \mu\text{m}^2, l = 25 \text{ mm}$	brass	-	$1 \text{ ps} \rightarrow 13 \text{ ps}$	mode: TE ₁₀ $f_c = 0.6 \text{ THz}$ strong dispersion due to f_c	Gallot <i>et al.</i> (2000)
Parallel-plate 	$b = 108 \mu\text{m}, l = 24.4 \text{ mm}$	copper	< 0.3	almost zero	mode: TEM, no f_c	Mendis and Grischkowsky (2001a)
	$b = 500 \mu\text{m}, l = 25 \text{ mm}$	aluminum	$0.2 < f < 1 \text{ THz}$	almost zero	mode: TEM, no f_c	Mendis and Grischkowsky (2001b)
	$b = 500 \mu\text{m}, l = 25 \text{ mm}$	aluminum	$0.35 < f < 1 \text{ THz}$	$0.8 \text{ ps} \rightarrow 150 \text{ ps}$	mode: TE ₁ , $f_c = 0.3 \text{ THz}$	Mendis and Mittleman (2009b)
	$b = 5 \text{ mm}, l = 25 \text{ mm}$	aluminum	< 0.004	almost zero	mode: TEM, no f_c	Mendis and Mittleman (2009a)
	$b = 5 \text{ mm}, l = 25 \text{ mm}$	aluminum	$f < 1 \text{ THz}$	almost zero	mode: TE ₁ , $f_c = 0.03 \text{ THz}$	
Wire 	$D = 0.9 \text{ mm}$	stainless steel	< 0.03	almost zero	mode: Sommerfeld wave (axial surface-wave) TM ₀₁	Wang and Mittleman (2004)
	$D = 0.52 \text{ mm},$ $l = 20, 64 \text{ \& } 104 \text{ cm}$	copper	$f < 0.75 \text{ THz}$	almost zero	specially designed antenna for better coupling in	Jeon <i>et al.</i> (2005)
	$D = 50 \mu\text{m}, l = 1 - 25 \text{ cm}$	copper	$f < 0.4 \text{ THz}$	almost zero	freely positioned probe-tip for detection	Wächter <i>et al.</i> (2005)
Slit 	$d = 270 \mu\text{m}$	Si wafer coated with Ti & Au	< 0.02	$< 0.02 < f < 1 \text{ THz}$	mode: TEM	Wächter <i>et al.</i> (2007)
	$w = 300 \mu\text{m}$ $a = 20 \text{ mm}$					

Table 2.2. Summary of key parameters of THz metallic waveguides.

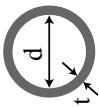
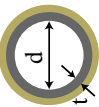
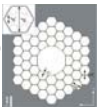

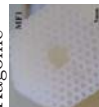
Waveguide	Dimensions	Material	α_{eff} [cm^{-1}]	Remarks	References
Pipe 	$d = 8 \text{ mm}$, $t = 0.12 \text{ mm}$, $l = 30 \text{ cm}$	PVDF	$0.015(\text{ave})$ $f < 2 \text{ THz}$	3 times lower than Ni-Cu pipe	Hidaka <i>et al.</i> (2005)
Hybrid clad 	$d = 9 \text{ mm}$, $t = 0.5 \text{ mm}$, $l = 3 \text{ m}$	Teflon	< 0.02 $f < 0.53 \text{ THz}$ $\approx 8 \times 10^{-4}$ $f = 0.4 \text{ THz}$	mode: HE_{11} 200-300 GHz bandwidth	Lai <i>et al.</i> (2009)
Microstructured band-gap 	$t = 10 \mu\text{m}$, $d = 2.2 \text{ cm}$, $l = 30 - 90 \text{ cm}$	Ag/PS coated	< 0.002 $f = 2.5 \text{ THz}$	mode: TE_{01} or TE_{11} thickness of the coating determines the lowest loss mode	Bowden <i>et al.</i> (2008b)
Bragg 	$t = 26 \mu\text{m}$, $d = 3 \text{ mm}$, $l = 30 \text{ \& } 100 \text{ cm}$	Ag/PE coated	$< 4 \times 10^{-3}$ (1.2 < $f < 2 \text{ THz}$) $\approx 3.2 \times 10^{-3}$ $f =$ 1.5 THz	3dB lower than Ag pipe	Matsuura and Takeda (2008)
	$\Lambda = 900 \mu\text{m}$, $d = 882 \mu\text{m}$, $t = 9 \mu\text{m}$, $R_c = 2.7 \text{ mm}$	Teflon HDPE	< 0.01 (0.895 < $f < 1.45 \text{ THz}$) ≈ 0.005 $f = 1 \text{ THz}$ < 0.01 (0.82 < $f < 1.02 \text{ THz}$) ≈ 0.0035 $f = 1 \text{ THz}$	only theoretical results reported mode: HE_{11} (multimode) dispersion: $< 2 \text{ ps/mm/km}$ confinement loss: 0.1 dB/m narrow transmission bandwidth	Vincetti (2009a)
	$D_{\text{core}} = 670 \mu\text{m}$, $l < 1.5 \text{ cm}$ $D_{\text{fibre}} = 6.3 \text{ \& } 5.6 \text{ mm}$ $D_{\text{hole}} = 69 \text{ \& } 65 \mu\text{m}$ $\Lambda_{\text{sampling}} = 93 \text{ \& } 86 \mu\text{m}$ $\Lambda_{\text{adjacentring}} = 105 \text{ \& } 93 \mu\text{m}$	PMMA	1.3(ave) $f < 1.4 \text{ THz}$ ≈ 0.4 $f = 1 \text{ THz}$ 1.1(ave) $f < 1.6 \text{ THz}$ ≈ 0.2 $f = 1.3 \text{ THz}$	mode: HE_{11} (TEM) ave: average loss values THz radiation propagates both in the core and cladding	Ponseca <i>et al.</i> (2008)
Kagomé 	$D_{\text{core}} = 1 \text{ mm}$, $l = 1 \text{ m}$ 31 layers of PVD/PC t of each layer $\approx 50 \mu\text{m}$	PVDF & PC	< 0.02 (1 < $\omega < 3 \text{ THz}$)	only theoretical results reported mode: HE_{11} (TEM) different guiding mechanisms	Skorobogatiy and Dupuis (2007)
	$D_{\text{core}} = 16, 20 \text{ \& } 30 \text{ mm}$, $d_{\text{air}} = 0.5, 0.7 \text{ \& } 2.25 \text{ mm}$, $d_{\text{material}} = 25, 70 \text{ \& } 150 \mu\text{m}$, $l = 28 \text{ cm}$	HDPE	$< 2 \times 10^{-5}$ (0.3 < $f < 4.3 \text{ THz}$) $\approx 2 \times 10^{-6}$ $f = 3.34 \text{ THz}$	only theoretical results reported mode: TE_{01} the frequency range is covered by three different waveguides	Yu <i>et al.</i> (2007)
	$D_{\text{core}} = 5.5 \text{ mm}$, $l = 20 \text{ cm}$, Teflon tubes In/out diameters: 1.68/2.08 mm	Teflon tubes	< 0.01 ($f = 0.77 \text{ THz}$)	mode: HE_{11} (multimode) $d \propto$ minimum loss $t \propto$ bandwidth	Lu <i>et al.</i> (2008c) Vincetti (2009b)

Table 2.3. Summary of key parameters of THz hollow-core dielectric waveguides.


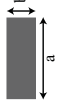

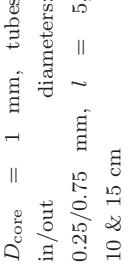
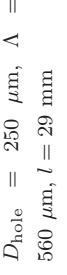
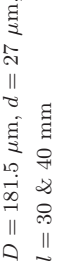
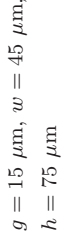
Waveguide	Dimensions	Material	α_{eff} [cm^{-1}]	Dispersion	Remarks	References
Air-clad 	$D = 150, 250$ & $325 \mu\text{m}$, $l = 7.3, 7.8$ & 8.3 mm $D = 200 \mu\text{m}$, $l = 6, 13, 17.5 \text{ cm}$	sapphire PE	< 6 ($f < 2.5 \text{ THz}$) < 0.01 $f < 0.35 \text{ THz}$	$0.6 \text{ ps} \rightarrow 10\text{-}13 \text{ ps}$ no value reported	mode: HE ₁₁ different regimes of guidance in the transmission band	Jamison <i>et al.</i> (2000) Chen <i>et al.</i> (2006)
	$b = 150$ & $120 \mu\text{m}$, $a = 2 \text{ cm}$, $l = 10$ & 20 mm	HDPE	< 1 ($0.1 < f < 3.5 \text{ THz}$)	$1 \text{ ps} \rightarrow 20, 40 \text{ ps}$	mode: TM ₀ (TEM)	Mendis and Grischkowsky (2000)
Microstructured 	$D_{\text{core}} = 500 \mu\text{m}$, tubes in/out diameters: $0.5/0.55 \text{ mm}$, $l = 2 \text{ cm}$	HDPE	< 0.5 ($0.1 < f < 3 \text{ THz}$) ≈ 0.2 ($f = 1 \text{ THz}$)	$0.8 \text{ ps} \rightarrow 5 \text{ ps}$ ≈ 14 ($f = 0.25 \text{ THz}$) ≈ 2 ($f = 0.4 \text{ THz}$) ≈ 0 ($f = 0.5 \text{ THz}$) ≈ -0.3 ($f > 0.6 \text{ THz}$)	mode: HE ₁₁ dispersions are in ps/THz/cm	Han <i>et al.</i> (2002)
	$D_{\text{core}} = 1 \text{ mm}$, tubes in/out diameters: $0.25/0.75 \text{ mm}$, $l = 5, 10$ & 15 cm	Teflon	< 0.12 ($0.1 < f < 1.3 \text{ THz}$)	no value reported	mode: HE ₁₁ (TEM) knife-edge measurements to test the confinement of THz radiation	Goto <i>et al.</i> (2004)
	$D_{\text{hole}} = 250 \mu\text{m}$, $A = 560 \mu\text{m}$, $l = 29 \text{ mm}$	COC	< 0.1 ($0.35 < f < 0.65 \text{ THz}$) ≈ 0.02 ($f = 0.6 \text{ THz}$)	< 1 ($0.4 < f < 1.4 \text{ THz}$) ≈ 0 ($0.5 < f < 0.6 \text{ THz}$)	mode: HE ₁₁ (TEM) dispersion parameter β_2 are in ps/THz/cm	Nielsen <i>et al.</i> (2009)
Low index discontinuity 	$D = 181.5 \mu\text{m}$, $d = 27 \mu\text{m}$, $l = 30$ & 40 mm	silica	< 0.7 ($0.4 < f < 0.6 \text{ THz}$)	$2 < \epsilon_{\text{eff}} < 4$ $(0.3 < f < 0.7 \text{ THz})$	mode: HE ₁₁	Nagel <i>et al.</i> (2006b)
	$g = 15 \mu\text{m}$, $w = 45 \mu\text{m}$, $h = 75 \mu\text{m}$	high resistivity silicon	< 0.01 ($0.5 < f < 0.9 \text{ THz}$)	$1 < \epsilon_{\text{eff}} < 2$ $(0.5 < f < 0.9 \text{ THz})$	mode: quasi TE (analogous to TM mode in slab waveguides) only theoretical results reported	Nagel <i>et al.</i> (2006b)

Table 2.4. Summary of THz solid-core dielectric waveguides.

THz microwires

THIS chapter explores the use of microwires for low-loss terahertz transmission. Microwires, which are air-clad wire waveguides with diameters smaller than the operating wavelength (a few μm), have an enhanced evanescent field in the cladding that, as shown here, can result in a low loss waveguide structure for the terahertz (T-ray) frequency regime. Based on our experimental data for the bulk material absorption of four glasses (F2, SF6, SF57 and bismuth) and two polymers (PMMA and COC), we evaluate normalised field distribution, power fraction, and effective area of microwires. Signal degradation, loss and dispersion, of microwires are also evaluated. It is shown that the effective loss of straight microwires is the main loss mechanism and approaches to the same order of loss ($< 0.01 \text{ cm}^{-1}$), regardless of material used.

3.1 Introduction

Several terahertz waveguide structures based on concepts arising from either electronics or photonics have been reviewed in Chapter 2. One of the dielectric waveguide structures proposed was plastic fibres by Chen *et al.* (2006). This was the solution that initially inspired this thesis. The concept of THz guided propagation in plastic fibers proposed by Chen *et al.* (2006) is similar to the concept of optical nanowire (Tong *et al.* 2003). Optical nanowires are filaments of dielectric media whose tailorable sub-wavelength dimensions, in the order of nm, allow a substantial fraction of the guided light (wavelength of 1-1.5 μm) to propagate outside the structure. As a result, in this regime, there exists an enhanced evanescent field outside the nanowire. Such an enhanced evanescent field behaviour occurs for micrometre diameter fibres in the THz band ($\lambda = 30\text{-}3000 \mu\text{m}$ or $f = 0.1\text{-}10 \text{ THz}$). Therefore we coin the term *microwires* for these type of waveguides used in the terahertz regime (Atakaramians *et al.* 2006b).

3.1.1 Objective and framework

In this chapter, nanowires and related concepts are discussed in Section 3.2. In Section 3.3 the measured dielectric properties (absorption coefficient and refractive index) of the bulk material of four soft glasses, two polymers and a diamond sample are examined. The bulk material dielectric properties are required for investigation of THz microwires in the next section. In Section 3.4, by solving the full vectorial Maxwell's equations for a simple rod geometry and using the measured bulk loss coefficients from Section 3.3, we demonstrate the normalised field distribution, and power fraction of microwires made of soft glass and polymer materials. Section 3.5 focuses on signal degradation mechanisms in microwires. Different loss mechanisms (effective material loss, bend loss, and surface roughness) for THz microwires are discussed in Section 3.5.1, while the dispersion properties of microwires are investigated in Section 3.5.2.

3.2 Optical Nanowires

In recent years there has been significant interest in both metallic and dielectric optical nanowires. The guiding mechanisms of electromagnetic waves in metallic and dielectric nanowires are different, as described below. However, in both cases the electromagnetic field is substantially located outside the wire. In metallic wires, electromagnetic waves

NOTE:
This figure is included on page 63 of the print copy of
the thesis held in the University of Adelaide Library.

Figure 3.1. Optical nanowires. (a)- A scanning electron microscope image of a bent 280 nm silica nanowire. (b)- An optical microscope image of launching light via a 390 nm diameter taper wire into a 450 nm diameter silica nanowire. After Tong *et al.* (2003).

propagate as weakly guided surface waves (Sommerfeld 1952, Stratton 1941), while, in dielectric wires the electromagnetic waves is weakly confined to the waveguide with an enhanced evanescent field in the air (Tong *et al.* 2003). The guiding properties of the modes in metallic wires are modeled under the framework of the Sommerfeld equations, while in dielectric wires they are calculated by the well known vectorial Maxwell's equations. The diameter of these waveguides are much smaller than the optical wavelength, i.e. in the order of nanometers as shown in Fig. 3.1(a).

The dielectric nanowire, which is also called an air-clad wire waveguide has a sub-wavelength diameter core, possesses interesting properties such as enhanced evanescent fields and tight light confinement—however, its low-loss optical waveguiding is restricted by sidewall smoothness and diameter uniformity, especially when the diameter of the waveguide is very small (Tong *et al.* 2003). It is known that as the diameter of the nanowire decreases below the scale of the wavelength of light, loss increases dramatically as a result of the frozen-in surface roughness (Ebendorff-Heidepriem *et al.* 2004, Ebendorff-Heidepriem *et al.* 2009). An advantage of using nanowires is that coupling between wires can be achieved via surface contact as shown in Fig. 3.1(b). This technique as we see later in Chapter 6 is also employed for coupling in/out of THz pulses from waveguides that have substantial power in the air.

A question we raise here is: “Is it possible to apply this concept to the terahertz regime?” Or in other words: “Is the use of the nanowire concept a possible way to reduce the loss via moving a significant portion of the guided mode *outside* the highly absorbing material (core)?” If yes, under what parameter conditions?

To answer these questions, first in the following section we investigate the dielectric properties of the bulk materials (four soft glasses, two polymers and a diamond sample) in THz. The bulk material properties are later employed in Sections 3.4 and 3.5 to investigate and compare different parameters (field distribution, power fraction, loss and dispersion) of THz microwires made up of these materials.

3.3 Dielectric properties of the bulk materials in THz

In this section we present the results of loss and refractive index measurements (dielectric properties) for four glasses (F2, SF6, SF57 and bismuth), two polymers (polymethyl methacrylate commonly called PMMA and cyclic olefin copolymer called COC and also known as TOPAS), and a diamond sample in the terahertz regime. The choice of glass and polymer materials is based on the relevant fabrication facilities available in CoEP (Centre of Expertise in Photonics). The COC billet used in this thesis has been provided from the Department of Photonics Engineering, Technical University of Denmark. It should be noted that there was no prospect within this project to fabricate all diamond waveguides. However, diamond samples have been considered in this chapter for comparison purposes.

The glass materials used have composition of heavy metal oxides such as PbO and Bi₂O₃. The concentration of the PbO in the F2, SF6, and SF57 glasses and the Bi₂O₃ in the bismuth glass are shown in Table 3.1. Other main components of the glasses are SiO₂ and B₂O₃. The F2, SF6, and SF57 glasses are supplied by Schott-AG (SCHOTT Accessed: February 2010) and the bismuth glass is supplied by Asahi Glass (AGC Accessed: February 2010). The supplied bismuth glass has a similar composition to BI-3 glass (Sugimoto *et al.* 1999). The references in Table 3.1 are the sources of these concentration values¹².

Some glass and polymer samples in the billet form are shown in Fig. 3.2(a). The billets are cylindrical with 3 cm diameter and 5 cm height. The diameter of these billets is much larger than the spot-size of the THz beam. However, these glass billets are very thick for THz spectroscopy measurements. The THz signal is very weak and noisy after

¹²The concentration value for SF57 is obtained by direct measurement using Energy Dispersive X-ray (EDX) spectroscopy in-house by Dr Heike Ebendorff-Heidepriem.

Table 3.1. Composition of heavy metal oxide glasses. The Table indicates the PbO concentrations in F2, SF6, and SF57 and the Bi₂O₃ concentration in the bismuth glass. Other main components of the glasses are SiO₂ and B₂O₃.

Glass	PbO	Bi ₂ O ₃	Reference
F2	19 mol. %	—	Long and Brueck (1999)
SF6	40 mol. %	—	Long and Brueck (1999)
SF57	43 mol. %	—	—
bismuth	—	43 mol. %	Sugimoto <i>et al.</i> (1999)

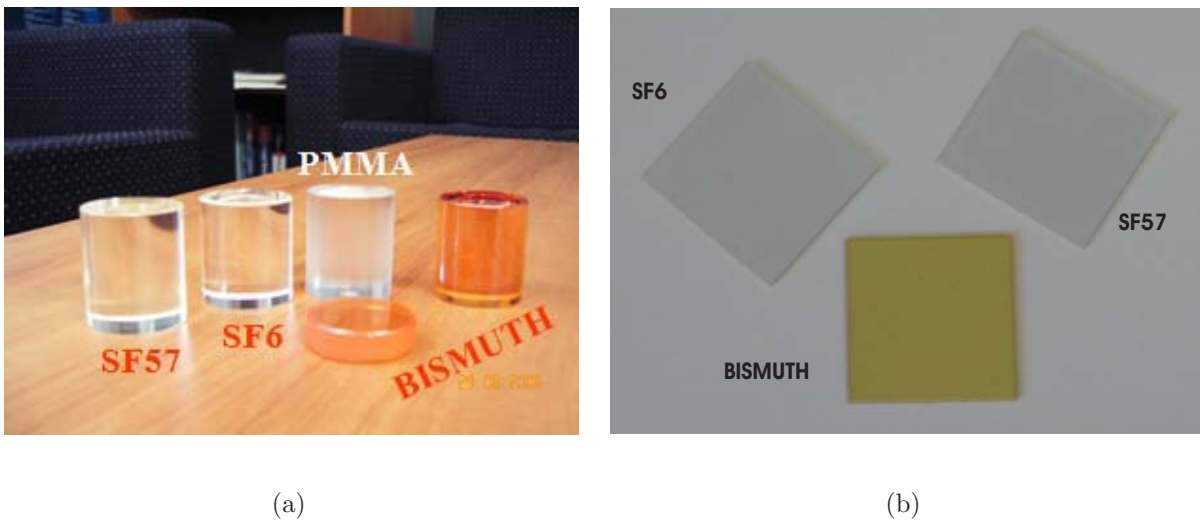


Figure 3.2. Glass and polymer samples. (a)- Glass and polymer samples in billet format. (b)- Prepared samples for THz spectroscopy. Both sides polished with 0.5 mm thickness of SF6, bismuth, and SF57.

traveling through such thicknesses. Therefore, we choose to prepare thin samples for THz spectroscopy measurements. The prepared samples are well polished on both sides with a cross-section of 2 cm × 2 cm and a 0.5 mm thickness. Fig. 3.2(b) shows the prepared samples of SF6, SF57 and bismuth for THz spectroscopy. It is worth mentioning that for F2 and polymer samples, we use existing billets with 16 mm and 35 mm heights, respectively. These materials have lower absorption coefficient (loss) at THz frequencies, thus there was no need for special preparation (very thin) of these samples.

To measure the refractive indices and absorption coefficient of bulk materials, we use a commercially available THz time-domain spectrometer, Picometrix T-Ray 2000TM shown in Fig. 3.3 (PICOMETRIX Accessed: July 2010, Mittleman 2003). The system consists of

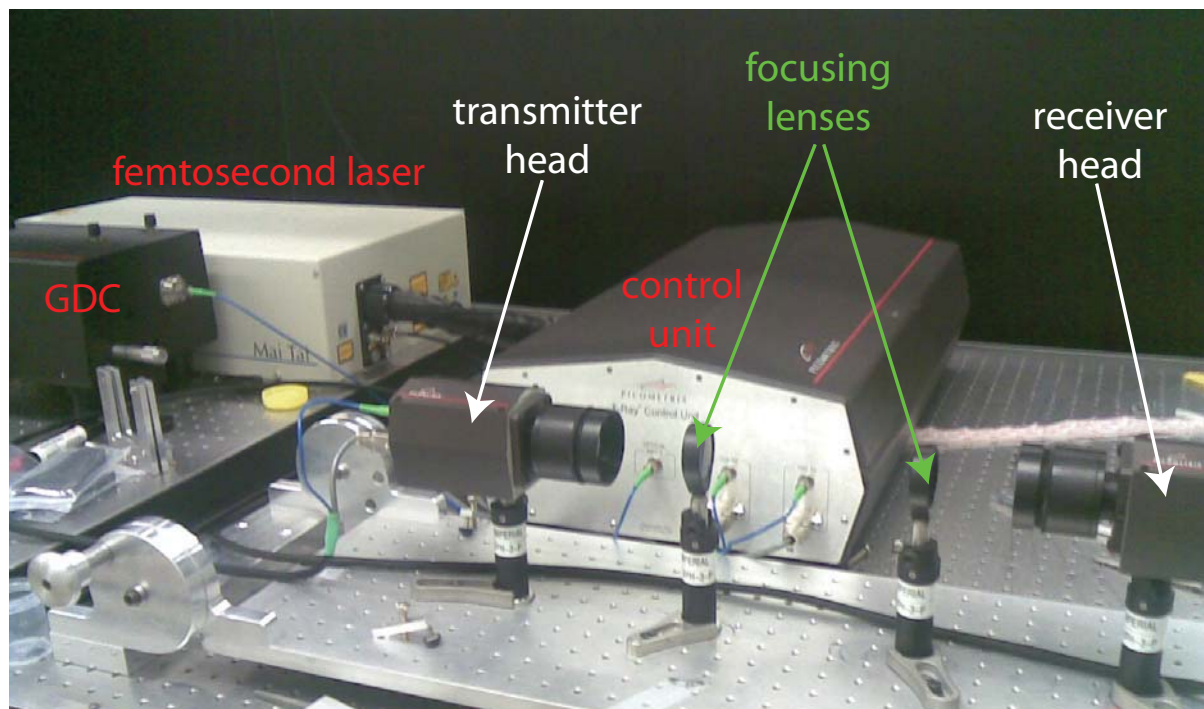


Figure 3.3. T-Ray 2000™ system. The system consists of 5 major components: femtosecond laser, grating dispersion compensator (GDC), control unit, transmitter and receiver heads, and computer (not shown in figure) for data acquisition. There is also a pair of silicon lenses for focusing THz radiation on the sample.

5 major components: a femtosecond laser, grating dispersion compensator (GDC), control unit, T-ray transmitter and receiver heads, and computer for data acquisition. The laser is a Mai-Tai femtosecond laser with a pulse width of less than 100 fs, central frequency of 800 nm and a repetition rate of 80 MHz. The terahertz transmitter and receiver modules are integrated into the two fibre coupled heads, which gives flexibility for positioning the heads. The GDC creates negative group velocity dispersion (GVD) for compensation of the optical pulse compression by the fibre optic components. The control unit contains optics splitter, optical delay rail and rapid scanner, motion control electronics, and power supplies.

To conduct the THz spectroscopy of the samples, the transmitter and receiver heads are positioned in a direct line of sight. The generated THz beam is collimated with a 38.1 mm beam width. It should be noted that there is a silicon lens integrated in the head, which collimates the beam. In order to focus the beam on the sample, another silicon lens with 38.1 mm diameter and 76.2 mm focal length is used. The measured spot size at the focal point is around 0.6 mm. The sample is placed at the focal point. An identical arrangement

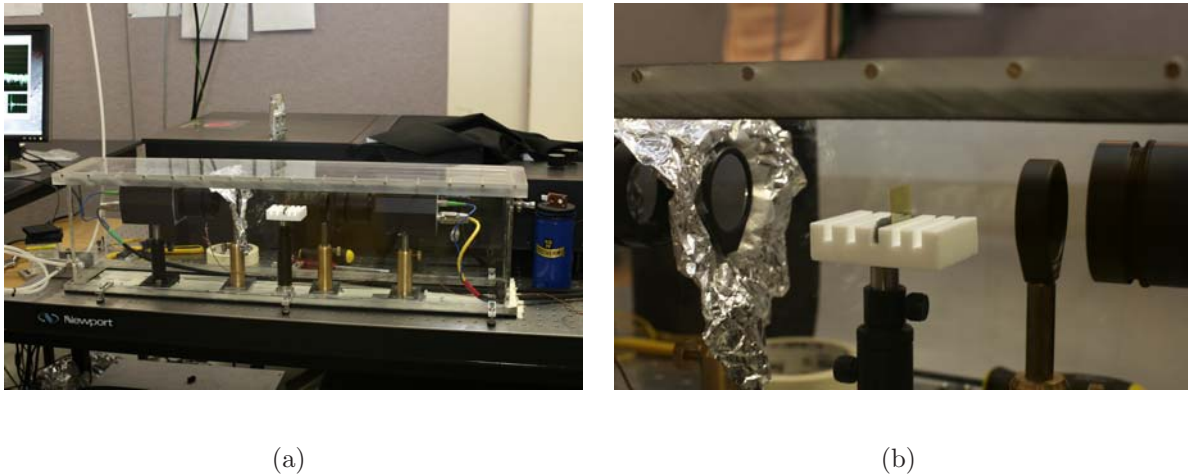


Figure 3.4. Experimental setup. The experimental setup in National Adelaide T-ray Facilities. (a)- Picometrix T-Ray 2000™ with a perspex box around the heads. (b)- The close up of the experimental setup showing the focusing silicon lenses, the sample holder, and the bismuth sample. The aluminum foil is used to block any stray beams reaching the detector.

is considered for the detection side. A perspex box is put around the transceiver heads, lenses, and the sample as shown in Fig. 3.4(a) and is purged with nitrogen. In this way the absorption dips and distortion in the signal due to water vapour molecules (van Exter *et al.* 1989b, Rønne *et al.* 1999) are suppressed. Figure 3.4(b) shows a close up the focusing silicon lenses, the sample holder, and the bismuth sample.

The absorption coefficients and refractive indices are obtained by comparing the sample pulse with a reference pulse propagating through free-space (i.e. a nitrogen purged medium or commonly called dry air). The pulse propagating through the set up, when the sample is present, is called the sample pulse and when there is no sample it is called the reference pulse. The measured quantity is the complex electric field, i.e. amplitude and phase. Assuming single mode propagation, the measured electric field after propagating through a sample of thickness l can be written in the frequency domain as:

$$E_{\text{sam}}(\omega) = E_0 T_1 T_2 \exp(-\alpha l/2) \exp(-j\beta_0 n l) \quad (3.1)$$

where, E_0 and $E_{\text{sam}}(\omega)$ are the complex electric fields at angular frequency ω before the sample and after passing through the sample, respectively; β_0 is the free space phase/propagation constant; α is the power absorption coefficient; and n the refractive index of the sample. Here, T_1 and T_2 are the total transmission coefficients that take

into account the reflections at the entrance and exit faces of sample, respectively. These transmission coefficients for a normal incidence are given by the Fresnel equation (Pedrotti and Pedrotti 1993). It should be noted that transmission coefficients are a function of frequency, since the refractive index is dependent on frequency. In the case of measurements conducted here, where the refractive index of the free-space is considered unity, these coefficients are as follows:

$$T_1 = \frac{2n(\omega)}{n(\omega) + 1} \quad (3.2)$$

$$T_2 = \frac{2}{n(\omega) + 1}. \quad (3.3)$$

As mentioned earlier, the reference pulse—measured electric field when no sample is present—is also required for evaluation of absorption coefficient and refractive index. The reference pulse through vacuum ($n = 1$, $\alpha = 0$) of the same length as the sample is given by:

$$E_{\text{ref}}(\omega) = E_0 \exp(-j\beta_0 l). \quad (3.4)$$

Dividing electric fields of sample and reference pulses in Eqns. 3.1 and 3.4 results in a frequency dependent complex ratio as follows:

$$\frac{E_{\text{sam}}(\omega)}{E_{\text{ref}}(\omega)} \equiv A \exp(i\varphi) = \frac{4n(\omega)}{(n(\omega) + 1)^2} \exp(-\alpha l/2) \exp(-j\beta_0(n - 1)l). \quad (3.5)$$

The refractive index and power absorption coefficient can be extracted from the phase and amplitude of Eqn. 3.5 as:

$$n(\omega) = 1 + \frac{\varphi}{\beta_0 l} \quad (3.6)$$

$$\alpha(\omega) = -\frac{2}{l} \ln \left(\frac{(n(\omega) + 1)^2}{4n(\omega)} A \right). \quad (3.7)$$

To measure the dielectric properties of each glass and polymer bulk sample, we conduct 12 scans; 6 reference pulses and 6 sample pulses. The scan sequence is three reference pulses, six sample pulses and then three reference pulses again. From the comparison of

the first and second set of measured reference pulses we are able to estimate if there is a change in the signal level due to laser drift during the measurements. In such cases the data is discarded and the experiment is repeated. Figure 3.5(a) shows an example (bismuth glass sample) of measured THz reference and sample pulses by the Picometrix T-Ray 2000TM. The temporal shape of the averaged reference pulse is shown in blue while the temporal shape of the averaged sample pulse is shown in red. By comparing two pulses in the time domain, the dielectric properties of the sample can be revealed. The time delay of the pulse is due to the higher index of refraction of the sample, and the attenuation of the peak amplitude is due to the absorption. The refractive index and the attenuation are calculated as a function of frequency from the phase (Eqns. 3.6) and amplitude (Eqns. 3.7) of the recorded pulse. The sample used here for the demonstration is bismuth glass. Figure 3.5(b) shows the spectral amplitude of the THz reference and sample pulses in blue and red respectively. This is obtained by taking the Fourier transform of the averaged reference and samples pulses. The image shows that the bandwidth is reduced from 2.5 THz for the reference pulse to 0.75 THz due to high absorption coefficient of the sample at the higher frequencies. Figures 3.5(c) and (d) show the refractive index and power absorption coefficient evaluated from the frequency dependent amplitudes and phases of the sample and reference pulses ratio. It should be noted that the error, which is the standard deviation of amplitudes and phases resulted from the 6 measurements, in refractive index and absorption coefficient is less than 0.5% for the bismuth glass measurements shown in Fig. 3.5.

We choose to use very thin samples (500 μm thickness) in order to increase the dynamic range of measurements. The dynamic range of a measurement is obtained by normalising the recorded frequency spectrum to the noise floor¹³ of the experiment. In the transmittance measurements the dynamic range of the THz signal determines the largest detectable absorption coefficient, which is inversely proportional to the sample thickness (Jepsen and Fischer 2005). However, for the thin samples there are artifacts caused by multiple reflections in the sample from the sample interfaces, which becomes more pronounced when the thickness of the sample decreases. These artifacts, called etalon effects, occur at the interfaces of the sample and air according to the Fresnel equation, resulting in constructive and destructive interference with the main signal (Fischer 2005). This etalon effect leads to an oscillatory feature in the data as can be seen in Figs. 3.5(c) and (d).

¹³Noise floor is the spectrum of the recorded THz signal when the THz beam is completely blocked.

The calculated absorption coefficient and refractive indices from the measured reference and sample pulses are shown in Figs. 3.6(a) and 3.6(b), respectively. Individually, the refractive index of each glass sample is significantly higher than the refractive index of the polymer and diamond samples. The SF6, SF57 and bismuth glasses show effective refractive index equal or greater than silicon, i.e. $n = 3.41$ for 0.2-2.8 THz (Fischer 2005). As we will see in the following section, the high refractive index results in a tighter confinement of the terahertz radiation into the waveguide. However, the absorption coefficients of these glasses are high and increase exponentially as a function of frequency compared to silicon, where the absorption coefficient of silicon is almost flat function of frequency, i.e. $\alpha = 0.5 \text{ cm}^{-1}$ for 0.2-2.8 THz (Fischer 2005). The F2 glass has refractive index and absorption coefficient lower than those from other glasses. Diamond and PMMA samples have similar absorption coefficient and lower than that of soft glasses, while COC sample has the lowest absorption coefficient among the measured materials. The refractive index of diamond is higher compared to that of the polymers samples (≈ 1.5 -1.6). The error, defined as the standard deviation of the 6 measurements, calculated in refractive index and absorption coefficient is less than 1% in total for all the measurements. It should be noted that the colour scheme chosen for each material is kept consistent through-out this chapter.

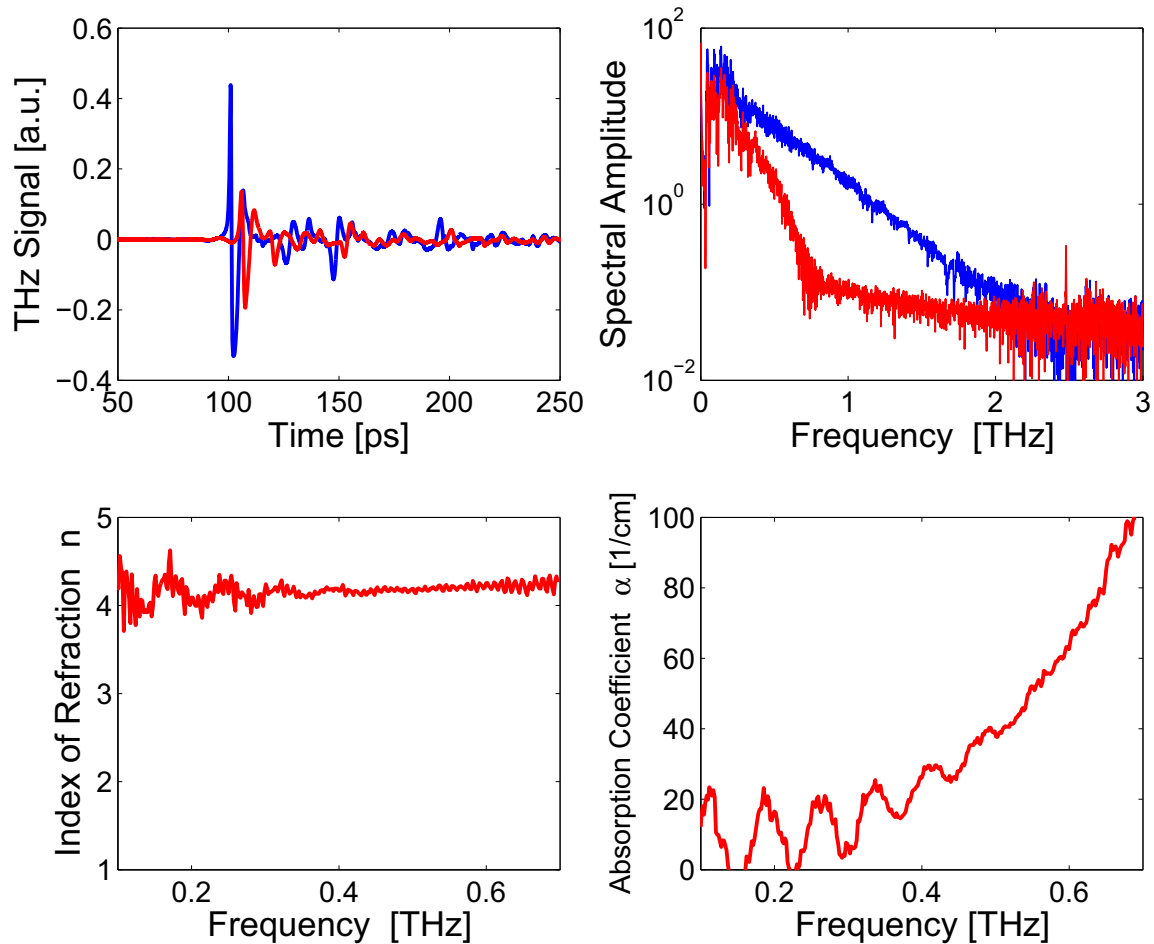


Figure 3.5. Determination of the THz dielectric properties from reference and sample pulses.

(a) The temporal shape of the reference and sample pulses in blue and red respectively. The sample used in this example is bismuth glass. The comparison of two pulses reveals the dielectric properties of the sample: the time delay of the pulse is due to the higher index of refraction, the attenuation of the peak amplitude is due to the absorption. (b) Spectral amplitude of the THz reference and sample pulses in blue and red respectively. The bandwidth is clearly reduced due to the high absorption coefficient of the sample at higher frequencies. (c) The refractive index and (d) the power absorption coefficient evaluated from the frequency dependent amplitudes and phases of the sample to reference pulse ratio.

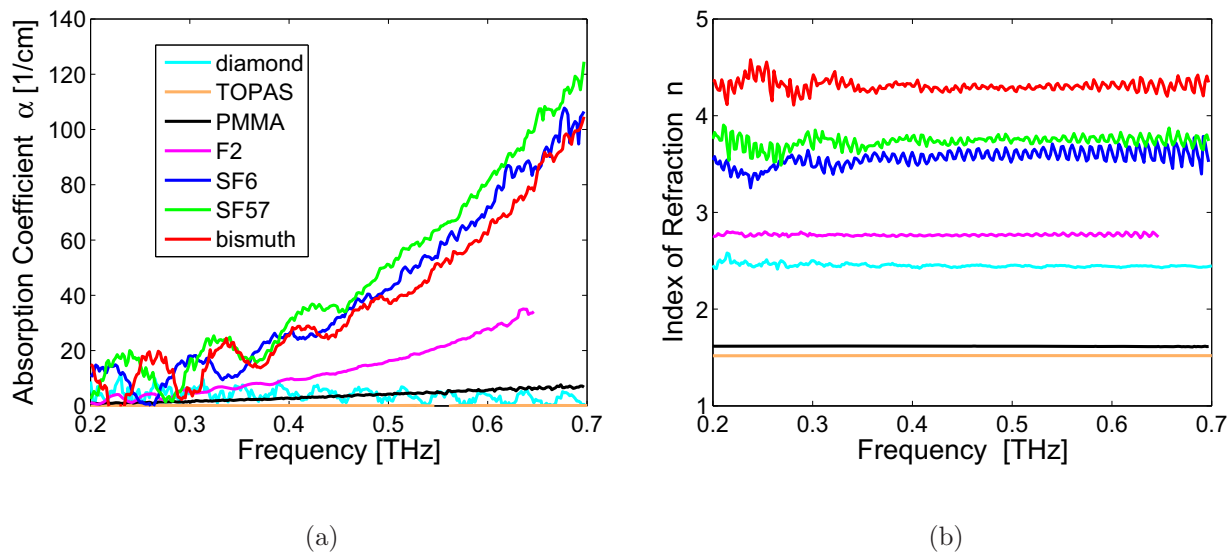


Figure 3.6. Dielectric properties of the glass and polymer materials. (a)- Absorption coefficients and (b)- the refractive indices of the bulk materials (PMMA, F2, SF6, SF57 and bismuth) measured with a THz time domain spectrometer. Note that the inset in Fig. 3.6(a) indicates the materials for both Figs. 3.6(a) and 3.6(b).

It is worth highlighting that although the THz microwire and porous fibre measurements presented in this thesis are not carried out in a true vacuum, all the measurements of bulk materials in this section are carried out in dry air (purged with nitrogen) to reduce the effect of water lines in the THz spectrum. Therefore in the following chapters of this thesis the dielectric properties measured in the normal environment, not in dry air, is considered.

To conclude, among of the materials that can be extruded to form fibres and considered here, polymers have lower loss (absorption coefficient) in comparison with the glass samples. Thus polymers are one of the most promising materials among the ones we studied for fibre fabrication. In the following sections we investigate the effect of polymer and glass materials on THz microwires in the terahertz frequency range.

3.4 Microwires

The terahertz (T-ray) spectrum has a wavelength range from 30 to 3000 μm . As a result, the enhanced evanescent field phenomenon—observed in optical nanowires with $D \ll \lambda_{\text{optic}}$ —occurs in a dielectric fibre of a few micrometers in diameter, depending on

the material used. Thus we use the term *microwire* to describe dielectric fibres with micrometre scale diameter in terahertz frequencies that possesses optical nanowire-like properties. It should be noted that the nanowire has two operating regimes—tight and loose confinement. We are interested in the loose confinement regime, where $D \ll \lambda_{\text{optic}}$ and most of the propagating mode is outside the wire, for THz radiation guidance.

It is straight-forward to calculate analytically the propagation constant of the modes propagating in a microwire. We assume that the structure has a circular cross-section, an infinite air cladding, and a step-index profile. It is also assumed that the wire is uniform in diameter and has a smooth sidewall. Moreover, we consider that the refractive index of air is equal to unity and the permeabilities of both media (core and clad) are equal to that of free-space. Thus solving the vectorial Maxwell's equation in cylindrical coordinates for the microwire structure results in the following eigenvalue equation for the hybrid modes (Snyder and Love 2000, Okamoto 2000, Balanis 1989):

$$\left[\frac{J'_n(u)}{uJ_n(u)} + \frac{K'_n(w)}{wK_n(w)} \right] \left[\frac{J'_n(u)}{uJ_n(u)} + \left(\frac{1}{n_1} \right)^2 \frac{K'_n(w)}{wK_n(w)} \right] = n_1^2 \left(\frac{1}{u^2} + \frac{1}{w^2} \right) \left[\frac{1}{u^2} + \left(\frac{1}{n_1} \right)^2 \frac{1}{w^2} \right] \quad (3.8)$$

where, J_n is the Bessel function of the first kind, and K_n is the modified Bessel function of the second kind. Here, u and w are normalised transverse wave numbers in the dielectric and air region, respectively; calculated as follows:

$$u = a\sqrt{\beta_0^2 n_1^2 - \beta^2} \quad (3.9)$$

$$w = a\sqrt{\beta^2 - \beta_0^2} \quad (3.10)$$

where, a is the microwire radius, β_0 is the free space propagating constant, and β is the propagation constant of the hybrid mode that is calculated by solving Eqn. 3.8. Having the propagation constant of the modes, one can easily calculate the electromagnetic fields in the dielectric (core) and in the air (cladding) using the approach reported in Snyder and Love (2000) and Okamoto (2000). For convenience, the electromagnetic field equations can be found in Appendix A.

In the following sub-sections of this and the next sections, we calculate and discuss the fundamental propagating mode, normalised electric and magnetic field distributions, and

the power fraction outside and inside microwires. The material and dielectric properties discussed in Section 3.3 are considered for these calculations.

3.4.1 Electric and magnetic field distributions

For this purpose, we first evaluate the propagation constant of the hybrid modes using Eqn. 3.8. As mentioned earlier for THz microwires the THz dielectric properties of materials are used. Then all the three components of the electric and magnetic fields are calculated in the core and the cladding region using equations in Appendix A.

As can be seen from the equations in Appendix A, there exist two polarisations for the fundamental mode (HE₁₁), which is determined by the variable ψ . The field distribution patterns are the same for both polarisations with a 90° rotation, i.e. the modes are degenerate for this perfect circular waveguide. The two polarisations are achieved by considering $\psi = 0$ and $\psi = 90^\circ$. Figure 3.7 shows the normalised electric field components of the two polarisation of the fundamental mode (HE₁₁) of a 200 μm diameter PMMA microwire. The images in the first row represent the normalised electric field components when $\psi = 0$ while the images in the second row represent the normalised electric field components when $\psi = 90^\circ$.

Figure 3.8 shows the normalised magnetic fields components of the two polarisations of the fundamental mode (HE₁₁) of 200 μm diameter PMMA microwire. The images in the first row represent the normalised electric field components when $\psi = 0$, while the images in the second row represent the normalised electric field components when $\psi = 90^\circ$. The electric and magnetic fields are normalised by using the convention described in Snyder and Love (2000), where both normalised electric and magnetic fields are achieved by dividing the fields to the square root of the total power in the relevant mode. The normalised electric and magnetic fields of the j -th propagating mode in the microwire are as follows:

$$\hat{E}_j = \frac{\vec{E}_j}{\sqrt{N_j}} \quad (3.11)$$

$$\hat{H}_j = \frac{\vec{H}_j}{\sqrt{N_j}} \quad (3.12)$$

where \vec{E}_j and \vec{H}_j are the electric and magnetic fields of the j -th propagating mode, \hat{E}_j and \hat{H}_j are the normalised electric and magnetic fields of the j -th propagating mode, N_j is the total power of the j -th mode calculated from the following equation:

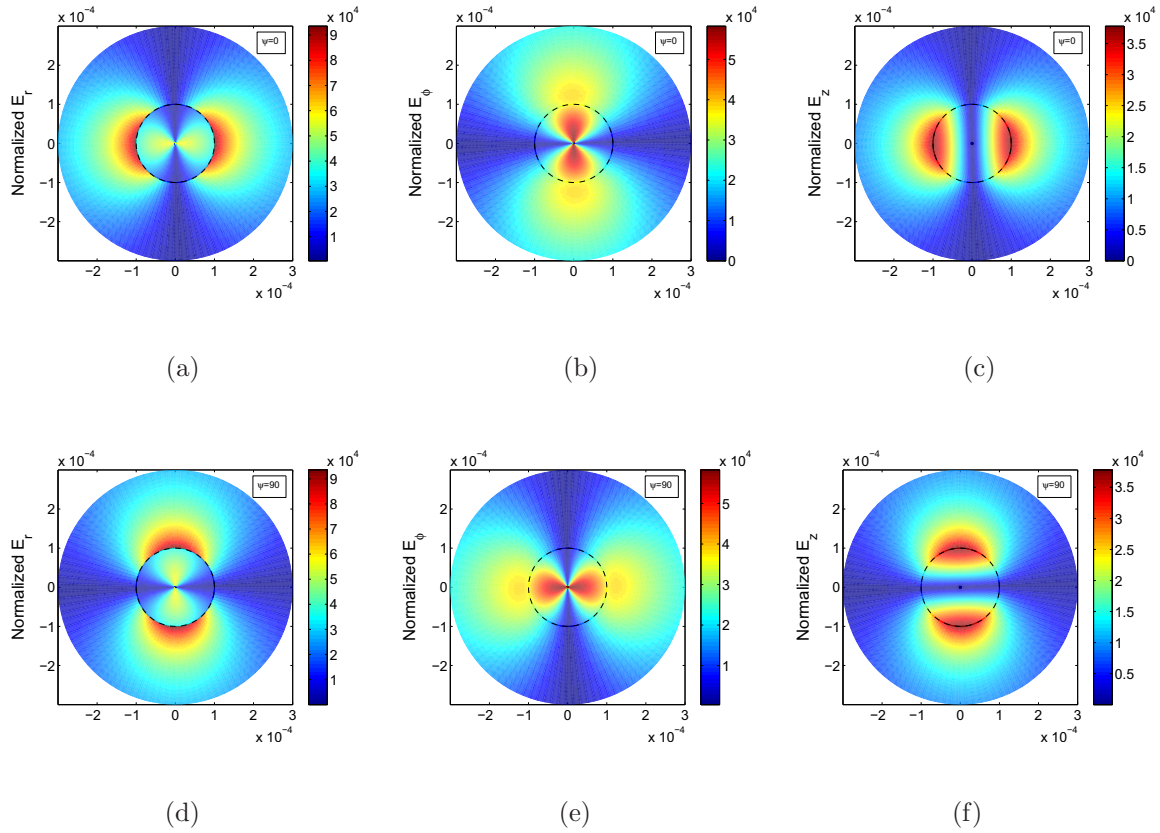


Figure 3.7. Normalised electric fields of the fundamental mode. The normalised electric fields components of the two polarisation of the fundamental mode (HE_{11}) of a $200 \mu\text{m}$ PMMA microwire at the $f = 0.5 \text{ THz}$ or $\lambda = 600 \mu\text{m}$. (a)- E_r , (b)- E_ϕ , and (c)- E_z are the normalised electric field components when $\psi = 0$ while (d)- E_r , (e)- E_ϕ , and (f)- E_z are the normalised electric field components when $\psi = 90^\circ$. The black dashed line shows the core and clad interface of the microwire.

$$N_j = \frac{1}{2} \left| \int_{A_\infty} \vec{E}_j \times \vec{H}_j^* \cdot d\vec{A} \right| = \frac{1}{2} \left| \int_{A_\infty} \vec{E}_j^* \times \vec{H}_j \cdot d\vec{A} \right|. \quad (3.13)$$

Where A_∞ is the finite cross-section, $*$ denotes the complex conjugate, and $d\vec{A} = \hat{z}dA$ is the element of integration across the cross-section of the fibre. In this case since we are dealing with the fundamental mode, then $j = 1$. This is the convention used for the normalisation of the fields throughout the thesis.

Figure 3.9 shows the normalised z -component of the Poynting vector, $S_z = \frac{1}{2} \vec{E}_j \times \vec{H}_j^* \cdot \hat{z}$, of the two polarisations of the fundamental mode (HE_{11}) of a $200 \mu\text{m}$ diameter PMMA microwire. It should be noted that the 90° rotation between the two polarisations of the fundamental mode is clearly visible in the normalised z -component of the Poynting vector. However, as the microwire diameter increases to the order of a wavelength or

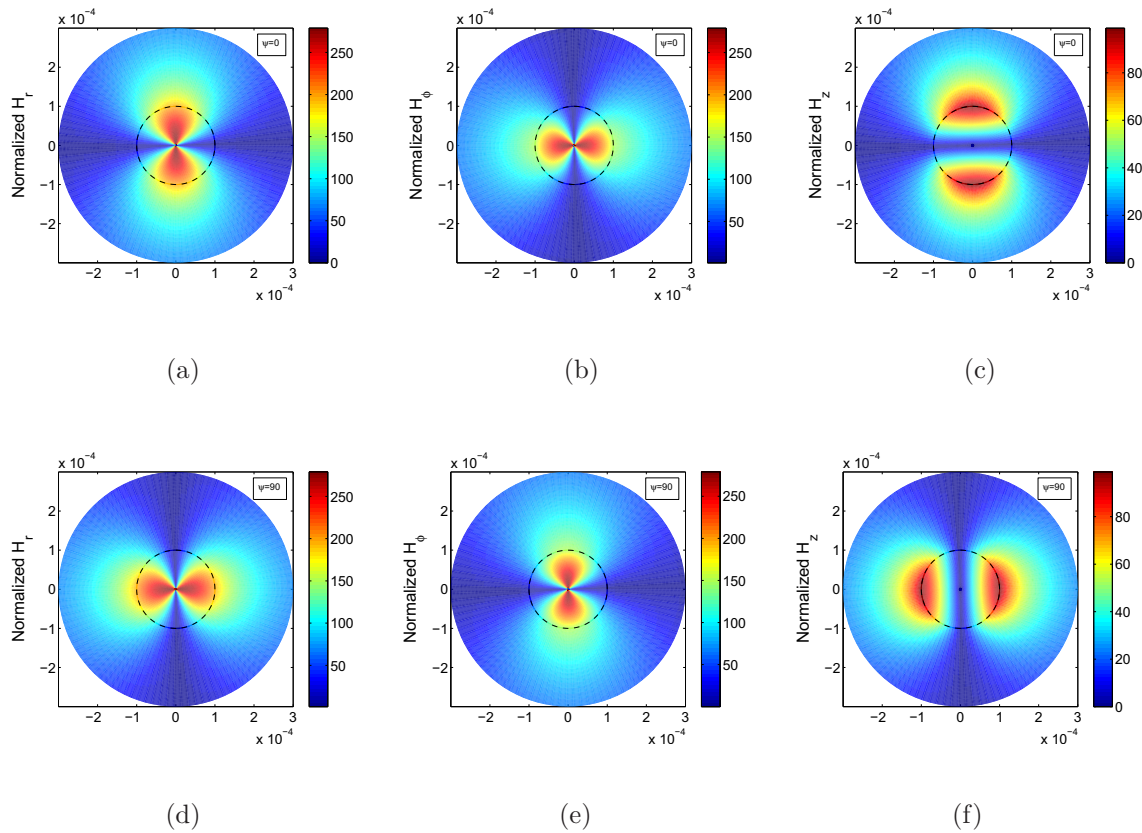


Figure 3.8. Normalised magnetic fields of the fundamental mode. The normalised magnetic field components of the two polarisations of the fundamental mode (HE_{11}) of a $200 \mu\text{m}$ PMMA microwire at the $f = 0.5 \text{ THz}$ or $\lambda = 600 \mu\text{m}$. (a)- H_r , (b)- H_ϕ , and (c)- H_z are the normalised magnetic field components when $\psi = 0$ while (d)- H_r , (e)- H_ϕ , and (f)- H_z are the normalised magnetic field components when $\psi = 90^\circ$. The black dashed line shows the core and clad interface of the microwire.

larger, this difference diminishes and becomes less noticeable between the two polarisation of normalised z -component of the Poynting vector. As an example the z -component of the Poynting vector of a microwire with diameter of $600 \mu\text{m}$ (at $f = 0.5 \text{ THz}$ or $\lambda = 600 \mu\text{m}$) is shown in Fig. 3.10. As we see next, this is due to the fact that E_r component of electric field becomes more confined to the core. This leads to almost similar normalised z -component of the Poynting vector for both polarisations.

The behaviour of the field vectors on the boundaries between two media are governed by the *boundary conditions*. The boundary conditions are thoroughly explained in electromagnetics text books, e.g. Balanis (1989). Given that the core and clad media are dielectric, finite conductivity media, the interface between the core and clad of microwire

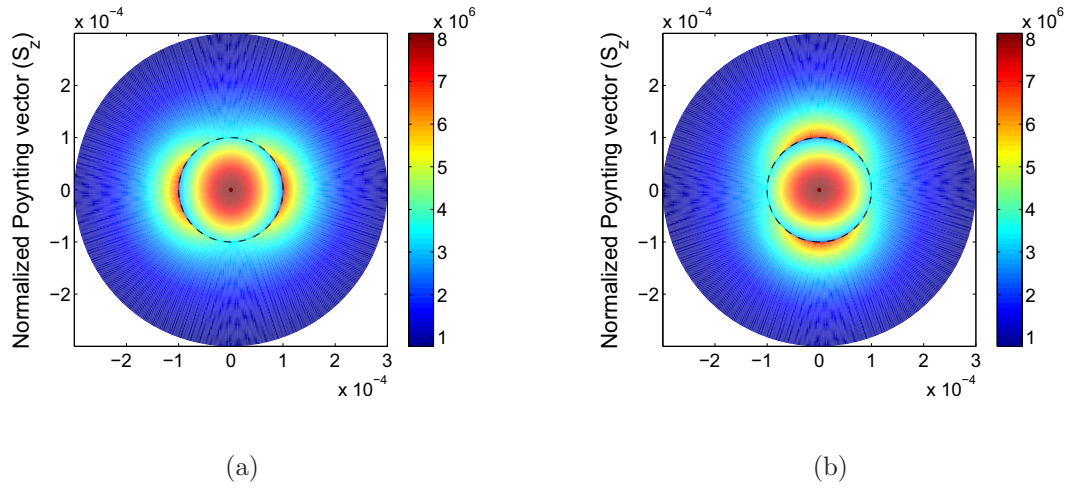


Figure 3.9. Normalised Poynting vector distribution of the fundamental mode. The Poynting vector distribution of the two polarisations of the fundamental mode (HE_{11}) of a $200 \mu\text{m}$ PMMA microwire at $f = 0.5 \text{ THz}$ or $\lambda = 600 \mu\text{m}$: (a)- $\psi = 0$ and (b)- $\psi = 90^\circ$. The black dashed line shows the core and clad interface of the microwire.

is an interface with no charges or sources. Thus the boundary conditions on this surface are as follows:

$$\hat{n} \times (\vec{E}_2 - \vec{E}_1) = 0 \quad (3.14)$$

$$\hat{n} \times (\vec{H}_2 - \vec{H}_1) = 0 \quad (3.15)$$

$$\hat{n} \cdot (\vec{D}_2 - \vec{D}_1) = 0, \Rightarrow \epsilon_2 \vec{E}_{2n} = \epsilon_1 \vec{E}_{1n} \quad (3.16)$$

$$\hat{n} \cdot (\vec{B}_2 - \vec{B}_1) = 0, \Rightarrow \vec{H}_{2n} = \vec{H}_{1n} \quad (3.17)$$

where media 1 and 2 are the core and clad medium and \hat{n} is the normal unit vector pointing from medium 1 to 2. Equations 3.14 and 3.15 state that the tangential components of the electric and magnetic fields across the interface of core and clad are continuous. Equations 3.16 and 3.17 state that the normal components of the electric and magnetic flux densities across the interface of core and clad are continuous. This leads to a discontinuity in the normal component of the electric field across the interface and this discontinuity is proportional to the refractive indices ratio of the two media. While, the normal component of the magnetic field across the core-clad interface is continuous since $\mu_2 = \mu_1 = \mu_0$, for microwire. In a nutshell, all the components of the electric and magnetic field are continuous across the core-clad interface except E_r component of the electric field.

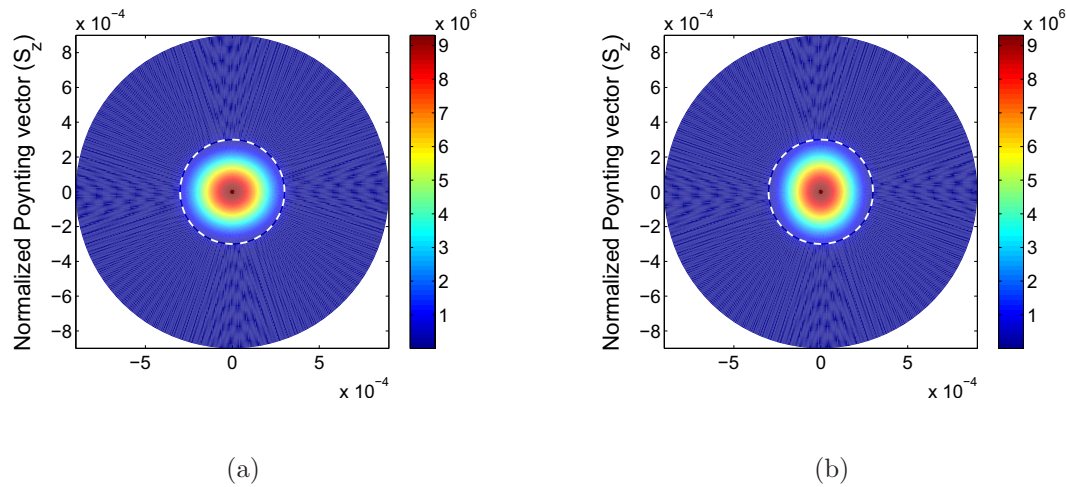


Figure 3.10. Normalised Poynting vector distribution of the fundamental mode. The Poynting vector distribution of the two polarisations of the fundamental mode (HE_{11}) of a $600 \mu\text{m}$ PMMA microwire at $f = 0.5 \text{ THz}$ or $\lambda = 600 \mu\text{m}$: (a)- $\psi = 0$ and (b)- $\psi = 90^\circ$. The white dashed lines show the core and clad interface of the microwire.

The calculated normalised electric and magnetic field distributions in Figs. 3.7 and 3.8 also confirm that all the components of the electric and magnetic fields are continuous on the core-clad interface except the ones in Figs. 3.7(a) and 3.7(d). These two fields are the radial components of the two different polarisations of the electric field, which are perpendicular to the core-clad interface. Since these components are the strongest field components they influence the z -component of the Poynting vector, S_z . This enhancement of the power distribution can be seen clearly in Fig. 3.9 for both polarisations. In the microwire case, where the second medium (cladding) is air, Eqn. 3.16 is simplified as follows:

$$\vec{E}_{2n} = \epsilon_1 \vec{E}_{1n}. \quad (3.18)$$

This indicates that the electric field is enhanced in the cladding for a microwire. It also points out that the enhanced electric field is proportional to the refractive index of the core and the electric field amplitude inside the core close to the interface. Figure 3.11(a) shows the normalised E_r component of the electric field at the xz -plane, $\phi = 0$, for PMMA microwires with two different diameters: $241 \mu\text{m}$ and $289 \mu\text{m}$. The core material of both microwires is the same, however the amplitude of the electric field component at the core-clad interface is different. This results in a stronger enhancement for the microwire with the small diameter, as the electric field is stronger at the interface. It should be

noted that both diameters are still sub-wavelength ($\lambda = 600 \mu\text{m}$, $f = 0.5 \text{ THz}$). As the diameter increases the enhancement becomes less pronounced. For a conventional optical fibre (core diameter larger than operating wavelength) the modal power is confined close to the core centre and the enhancement is inconspicuous. Moreover, usually there is a small variation in refractive index profile of conventional fibre, i.e. $n_{\text{core}} \cong n_{\text{clad}}$. Therefore the modes of conventional fibre are usually evaluated using weakly guiding approximation. In this approximation method, the modes are computed from the solution of scalar wave equations, rather than the vectorial form (Snyder and Love 2000).

Figure 3.11(b) shows the effect of different materials, i.e. different values of ϵ_1 , on the enhancement of the electric field. The diameter of the microwires are chosen in a way that they have the same electric field amplitude at the interface of the core-clad in the core. The enhancement of the fields in the clad region is proportional to the refractive indices of the material measured and depicted in Fig. 3.6(b). The bismuth glass microwire has the highest refractive index resulting in the largest enhancement, whereas the COC microwire has the lowest refractive index resulting in the smallest enhancement. The enhancement of the field at the interface is beneficial where strong interaction of the field and sample is required, such as in sensing applications.

3.4.2 Power fraction and effective area

In order to observe the effects of microwire diameter variations on the fundamental mode distribution, we study the power fraction in the clad and the effective mode area of microwires in this sub-section. The power fraction specifies the ratio of power in the cladding to the total power, while the effective mode area specifies the power distribution across the cross-sectional area of the fibre; as explained below.

The power fraction leads us to more information of the power distribution in the radial direction, i.e the fraction of the total power is in the core and clad region. The power fraction in air (clad region) is calculated by using the following formula (Snyder and Love 2000):

$$P_F = \frac{P_{\text{air}}}{P_{\text{total}}} = \frac{\int_{A_{\text{clad}}} S_z dA}{\int_{A_{\infty}} S_z dA} = \frac{\int_a^{\infty} \int_0^{2\pi} S_{z2} r dr d\phi}{\int_0^a \int_0^{2\pi} S_{z1} r dr d\phi + \int_a^{\infty} \int_0^{2\pi} S_{z2} r dr d\phi} \quad (3.19)$$

where, a represents the diameter of the microwire, and S_{z1} and S_{z2} are the z -components of the Poynting vectors inside (core region) and outside (clad region) the microwire,

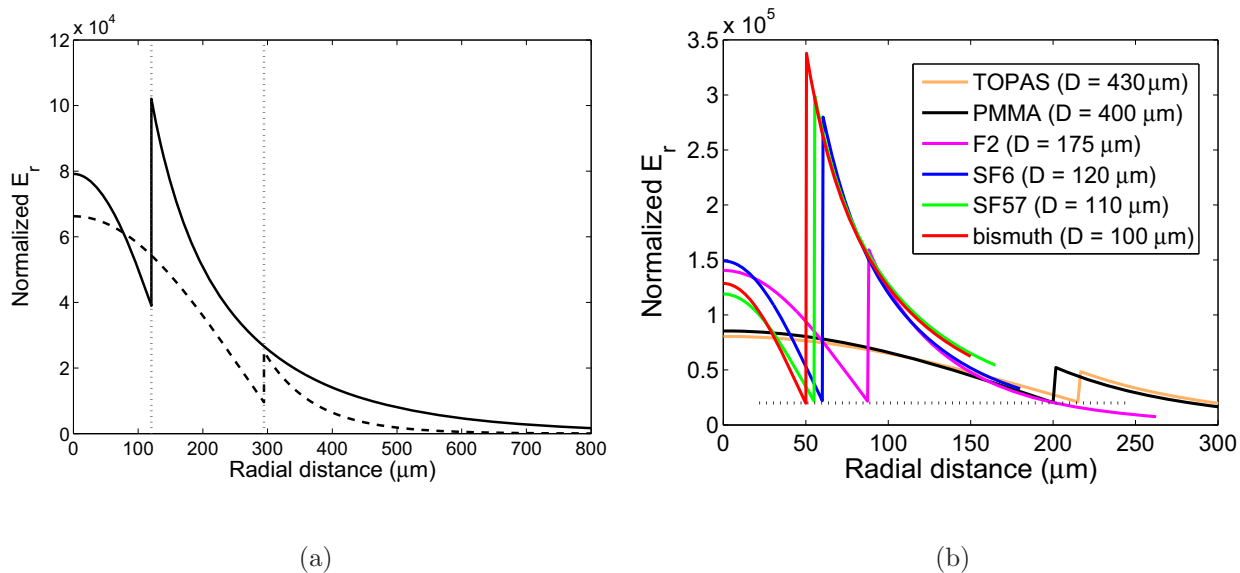


Figure 3.11. Enhancement of the electric field in the lower refractive index medium. Normalised E_r component of the electric field in the xz -plane ($\phi = 0$) for the first polarisation of the fundamental mode at $f = 0.5$ THz ($\lambda = 600 \mu\text{m}$): (a)- for two different diameters of a PMMA microwire (241 μm and 289 μm). The vertical dotted lines represent core-clad interfaces. (b)- for microwires made up of different materials (COC, PMMA, F2, SF6, SF57, and bismuth). The diameters of the microwires are chosen such that they have the same electric field amplitude at the interface of the core-clad in the core. The dotted line denotes the interface.

respectively. Figure 3.12(a) shows the power fraction outside the microwires made up of glasses (F2, SF6, SF56 and bismuth) and polymers (COC and PMMA) as a function of diameter variations. For large diameters, in the order of operating wavelength $\lambda = 600 \mu\text{m}$ ($f = 0.5$ THz), the power fraction in air is very close to zero. This indicates that most of the power is residing in the core of the microwire, since the power fraction in the core is $\frac{P_{\text{core}}}{P_{\text{total}}} = 1 - \frac{P_{\text{air}}}{P_{\text{total}}}$. Decreasing the diameters to less than the operating wavelength results in an increase in the power fraction in air. This indicates that most of the mode power penetrates the clad region as the diameter decreases, eventually converging to unity. At this point most of the mode power is in air and the mode is weakly confined to the structure. It should be noted that both the diameter where the fibres enter the microwire operating regime (the power fraction in the air increases) and the slope of the convergence of the power fraction to unity strongly depends on the refractive index of the material.

The effective mode area—effective area (A_{eff})—is a quantitative measure of the area which a waveguide or fibre mode effectively covers in the transverse dimensions. In other words,

it defines the power distribution across the cross-sectional area of the fibre and is related to the fibre structure and the refractive index profile. The scalar effective mode area is defined as (Agrawal 2001):

$$A_{\text{eff}}^{\text{S}} = \frac{\left(\int_{A_{\infty}} |F(x, y)|^2 dA \right)^2}{\int_{A_{\infty}} |F(x, y)|^4 dA} \quad (3.20)$$

where, $F(x, y)$ is the transverse distribution of the electric field of the fundamental mode. In the case of the weakly guided approximation, i.e. the propagation constant is obtained from the scalar wave equations and the square of the electric field is proportional to the power distribution, Eqn. 3.20 is valid. However, for the modal distribution obtained from the vectorial form of Maxwell's equation, Eqn. 3.20 is modified to vectorial effective mode area as follows (Afshar V. and Monro 2009):

$$A_{\text{eff}}^{\text{V}} = \frac{\left| \int_{A_{\infty}} S_z dA \right|^2}{\int_{A_{\infty}} |S_z|^2 dA} \quad (3.21)$$

where, the z -component of the Poynting vector is used instead of the field distribution. In this thesis we are dealing with complex inhomogeneous sub-wavelength waveguide structures, thus we use the vectorial form of Maxwell's equations for calculating propagating modes in the fibres. Therefore, Eqn. 3.21 is always used to compute the $A_{\text{eff}} = A_{\text{eff}}^{\text{V}}$ throughout this thesis, unless otherwise stated.

Figure 3.12(b) shows the effective area of microwires made up of COC, PMMA, F2, SF6, SF57, and bismuth. The A_{eff} values initially decline until they reach a minimum, as the microwire diameter is reduced to less than the operating wavelength ($\lambda = 600 \mu\text{m}$). The minimum point on the A_{eff} curves indicate the lowest achievable effective mode area for the fundamental mode. Decreasing the diameter further results in an increase in the A_{eff} curves with a much steeper slope. This happens as a result of pushing most of the power distribution into the air region by decreasing the diameter.

In order to have a gain insight into understanding of the differences of the two effective area definitions, $A_{\text{eff}}^{\text{S}}$ and $A_{\text{eff}}^{\text{V}}$, we depict both of them together for a PMMA microwire in Fig. 3.13(a). The cyan and black lines represent $A_{\text{eff}}^{\text{S}}$ and $A_{\text{eff}}^{\text{V}}$, respectively. There is a clear difference between the curves especially close to the minimum point.

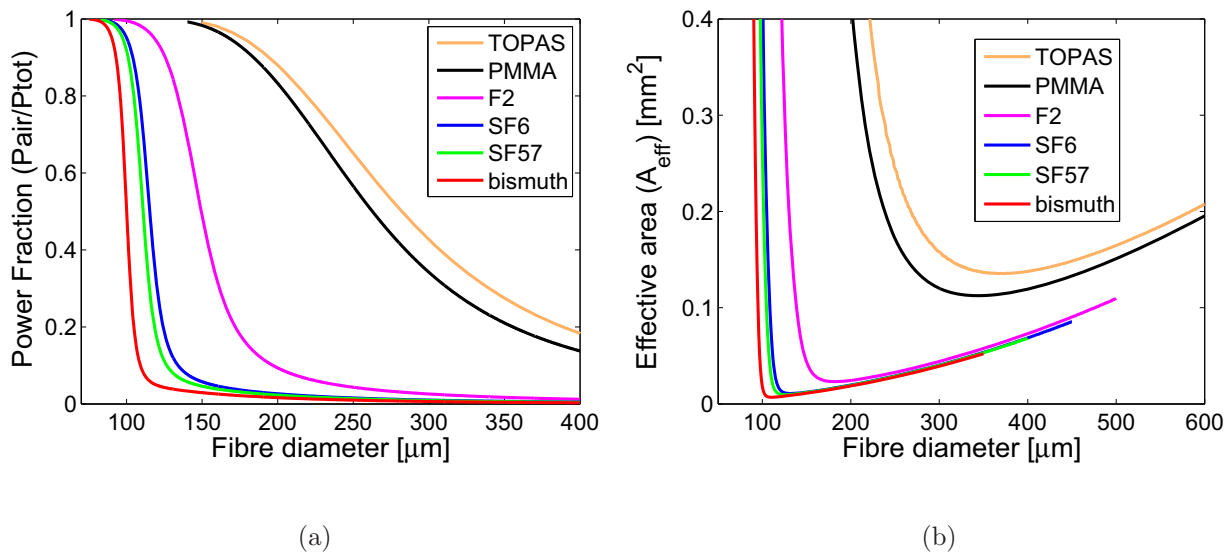


Figure 3.12. Power fraction and effective area of microwires. (a)- Power fraction in the air for microwires made up of COC, PMMA, F2, SF6, SF57, and bismuth versus the fibre diameter at $f = 0.5$ THz ($\lambda = 600 \mu\text{m}$). (b)- Effective area for microwires made up of COC, PMMA, F2, SF6, SF57, and bismuth microwires versus the diameter at $f = 0.5$ THz ($\lambda = 600 \mu\text{m}$).

The black horizontal dashed line in Fig. 3.13(a) represents an $A_{\text{eff}}^{\text{V}} = A_{\text{eff}} = 0.19 \text{ mm}^2$. For this A_{eff} value, there exist two different diameters, 241 and 589 μm . Although these two diameters have the same A_{eff} values, as shown in Fig. 3.11(a) their field distribution is different. In the next section, the bend loss associated to these two points will be discussed. It will be shown that although these two points have identical effective areas, they experience different bend loss values.

Figure 3.13(b) shows A_{eff} and the geometrical area of a PMMA microwire. The former identifies the area in which most of the transverse power of the fundamental is located, while the latter shows the physical area of the core. For larger diameter values the A_{eff} of the microwire is smaller compared to the core area values. This indicates that most of the mode power is confined in the core of the microwire. However, these values approach and cross each other as the diameter continues to decrease. As the diameter of the microwire decreases, the power fraction in the cladding increases resulting into larger A_{eff} values compared to geometrical area. Relying only on the A_{eff} curve does not give us much explanation about the mode confinement since two modes can have completely different field distribution with identical A_{eff} values. As we will see in the next section, another

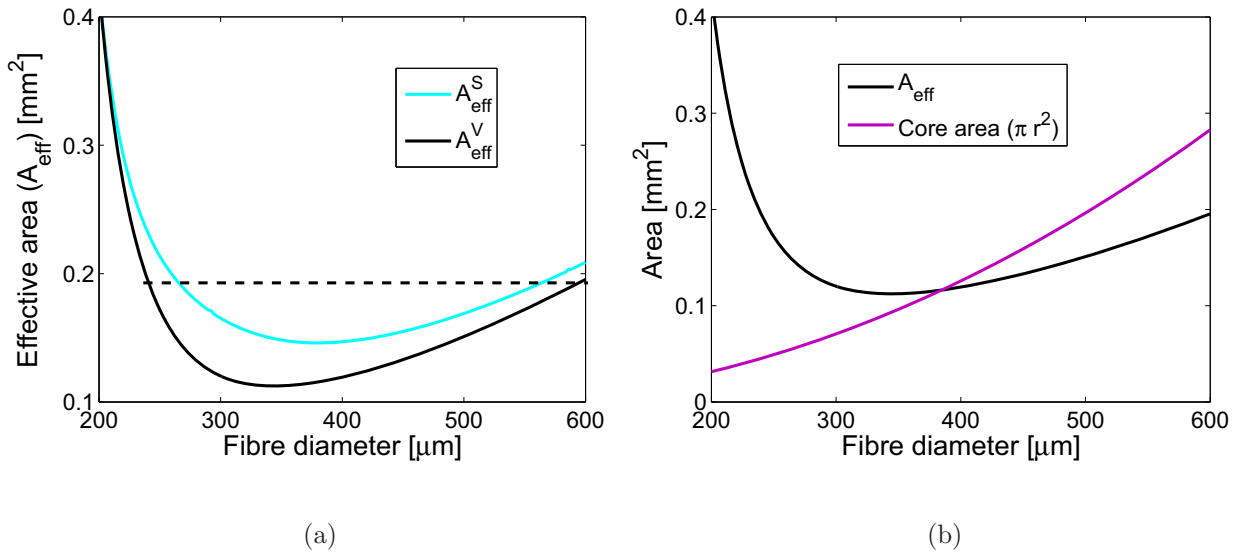


Figure 3.13. Scalar and vectorial effective area of a PMMA microwire. (a)- Diameter variation effects on the scalar and vectorial effective area, cyan and black respectively represent $A_{\text{eff}}^{\text{S}}$ and $A_{\text{eff}}^{\text{V}}$, for a PMMA microwire at $f = 0.5$ THz ($\lambda = 600 \mu\text{m}$). (b)- Effective area ($A_{\text{eff}}^{\text{V}}$) and geometrical core area of the PMMA microwire versus diameter variations at $f = 0.5$ THz ($\lambda = 600 \mu\text{m}$).

parameter, as namely the ratio of effective area and core area is a much better parameter for confinement comparison.

3.5 Signal degradation in THz microwire

Signal attenuation, also known as waveguide/fibre losses, is one of the most important parameters for THz fibres. It determines the practical length of waveguiding systems, which is at the present of the order of a few metres (Lai *et al.* 2009, Mendis and Mittleman 2009a). Of equal importance is signal dispersion. The dispersion mechanism causes the signal pulses to broaden as they travel along the fibre. In this section we focus on these signal degradation mechanisms. In part 3.5.1 we discuss the main loss mechanisms in THz microwires, which are effective material loss, bend loss and scattering losses due to surface roughness. Then in part 3.5.2 we discuss the signal distortion arising from material dispersion, waveguide dispersion, also known as group velocity dispersion, and modal dispersion.

3.5.1 Loss mechanisms

In the ideal case, where the waveguide material is non-absorbing, the mode will propagate indefinitely on an infinitely long uniform fibre. In reality due to the lack of such an ideal non-absorbing material, i.e. no low loss solution available for guiding the mode, this never happens. Thus one of the most important waveguide parameters is the measure of power loss during the transmission of the signals. Waveguide losses, especially in dielectric waveguides and fibres, are due to several effects such as material absorption, impurity absorption, confinement and scattering effects. In this section we mainly focus on the fibre material loss as the main mechanism of fibre losses. The ultimate goal of having low loss THz waveguide structures is to be able to transmit the THz pulse to points where there is no direct access in applications such as endoscopy. Hence this necessitates of having flexible waveguide structures that can easily bend around the corners, leading to another loss mechanism known as *bending loss*.

In this section we mainly focus on these two main loss mechanisms for THz microwires, material and bend losses. We also briefly explain losses due to the surface roughness, which is a limiting factor in achieving a minimum loss for optical photonic crystal fibres (Roberts *et al.* 2005).

Effective material loss

The material absorption (α_m) is caused by the molecules of the basic waveguide material, either glass or plastic. These losses represent a fundamental minimum to the attainable loss and in conventional fibres and can be overcome only by changing the waveguide material. In the optical regime, the loss depends on the impurities of the glass and there are ultra-pure glasses that have low material absorption. However, the terahertz regime is lacking such materials for proper waveguiding, therefore reducing the fractional power inside the dielectric core—the microwire operating regime—is a way of improving the material absorption (Chen *et al.* 2006).

The loss modal fields experience by propagating along a THz microwire with α_m material absorption coefficient, is called *effective material loss* and is calculated here. It should be noted that this calculation is valid only when the power lost per wavelength along the waveguide is small compared to the power flowing along the waveguide, i.e. the waveguide is slight absorbing waveguide (Elsasser 1949, Snyder and Love 2000). Therefore the electric and magnetic fields can be approximated by the fields calculated from non-absorbing ($\alpha_m = 0$) waveguides. The law of conservation of power/energy states that in a region V

characterised by μ , ϵ , σ , and enclosed by the surface S the total amount of power/energy is conserved over time. The energy conservation equation derived from Maxwell's equations in electromagnetics is as follows (Balanis 1989):

$$\iint_S (\vec{E} \times \vec{H}^*) \cdot \vec{ds} + \iiint_V \vec{H} \cdot (\vec{M}_i + \vec{M}_d) dv + \iiint_V \vec{E} \cdot (\vec{J}_i + \vec{J}_c + \vec{J}_d) dv = 0 \quad (3.22)$$

where, \vec{E} and \vec{H} are electric and magnetic field intensities, \vec{J}_i and \vec{M}_i electric and magnetic sources, \vec{J}_d and \vec{M}_d are electric and magnetic displacement current densities, and \vec{J}_c is the conduction current within the volume V .

For calculation of the effective material loss of a microwire (i.e. lossy dielectric rod) we consider a cylindrical volume, as indicated by the dashed line in Fig. 3.14, which has the same axis as the waveguide. Therefore the two caps of cylinder are perpendicular to the microwire z -axis. These caps expand to infinity. Taking into account that in a microwire there is no electric and magnetic sources, and displacement current densities the equation is simplified as:

$$\iint_S (\vec{E} \times \vec{H}^*) \cdot \vec{ds} = - \iiint_V \vec{E} \cdot \vec{J}_c dv = -\sigma \iiint_V |E|^2 dv \quad (3.23)$$

where, σ is the conductivity. Considering there is no power perpendicular to the microwire at large distances and assuming $\sigma = 0$ outside the dielectric waveguide, Eqn. 3.23 in the limit ($\Delta z \rightarrow \infty$) is simplified as (Elsasser 1949, Snyder and Love 2000):

$$\frac{d}{dz} \iint_{S_{\text{cap}}} S_z ds = \frac{d}{dz} P = - \iiint_V \sigma |E|^2 ds \quad (3.24)$$

where, S_z is z -component of the Pointing vector and represents the power in the modal field, P . Thus the term dP represents the power lost from modal field due to the absorption over the differential length dz . In a lossy medium that has complex profile (permittivity/refractive index)¹⁴ the Maxwell-Ampère equation can be written as (Balanis 1989):

¹⁴Complex permittivity : $\epsilon = \epsilon^r - j\epsilon^i$, complex refractive index: $n = n^r + jn^i$, and the equations relating these two quantities are $\epsilon^r = \epsilon_0((n^r)^2 - j(n^i)^2)$ and $\epsilon^i = 2\epsilon_0 n^r n^i$ where, r and i stands for real and imaginary components, respectively (Snyder and Love 2000).

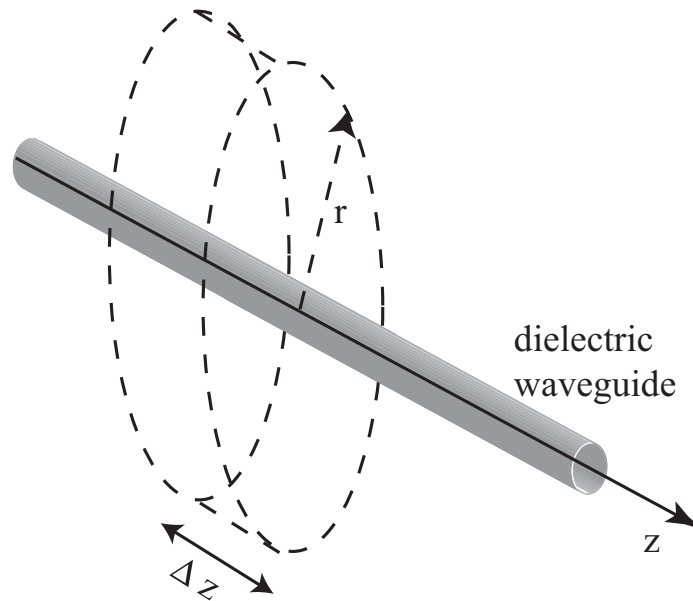


Figure 3.14. Dielectric waveguide. This figure shows a microwire, dielectric waveguide with circular cross-section. The microwire is along the z -axis. The dashed cylinder with the volume V enclosed by the surface S , represents the volume over which the law of energy/power conservation is applied. The cylinder has the same axis as the microwire and the radius of the region, r , expands to infinity.

$$\begin{aligned}
 \nabla \times \vec{H} &= \vec{J}_i + \vec{J}_c + j\omega(\epsilon^r - j\epsilon^i)\vec{E} \\
 &= \vec{J}_i + \sigma\vec{E} + \omega\epsilon^i\vec{E} + j\omega\epsilon^r\vec{E} \\
 &= \vec{J}_i + \sigma_e\vec{E} + j\omega\epsilon^r\vec{E}
 \end{aligned} \tag{3.25}$$

where, σ_e represent the total conductivity of the medium, i.e. the summation of static field, and alternating field conductivities. Thus for a dielectric waveguide in the time variant fields, the total conductivity is equal to alternating field conductivity:

$$\sigma_e = \omega\epsilon^i = 2k \left(\frac{\epsilon_0}{\mu_0} \right)^{1/2} n^r n^i \tag{3.26}$$

where, ω is the angular frequency and k is the free-space wave number. A second expression is obtained from power attenuation along the waveguide. In this case, we assume that power absorption coefficient is zero in cladding and is α_m in the core. The power attenuation of the fundamental mode over a differential distance of dz is determined from

the following equation (Snyder and Love 2000):

$$dP = -\alpha_{\text{eff}} P_0 \exp(-\alpha_{\text{eff}} z). \quad (3.27)$$

If we equate Eqns. 3.24 and 3.27 and replace σ from the Eqn. 3.26, we obtain the effective material loss/power attenuation coefficient for the waveguide as follows:

$$\alpha_{\text{eff}} = 2k \left(\frac{\epsilon_0}{\mu_0} \right)^{1/2} \frac{\int_0^a \int_0^{2\pi} n^r n^i |E|^2 r dr d\phi}{\left| \int_0^a \int_0^{2\pi} S_{z1} r dr d\phi + \int_a^\infty \int_0^{2\pi} S_{z2} r dr d\phi \right|}. \quad (3.28)$$

The calculated effective material loss is accurate if the fields in Eqn. 3.28 are obtained from the eigenvalue equation of an absorbing/lossy waveguide. However, as stated earlier for slightly absorbing waveguides (e.g. the microwire operating regime) the fields in the Eqn. 3.28 can be approximated by the fields obtained from Eqn. 3.8.

The calculated effective material loss of microwires made up of glasses and polymers are shown in Fig. 3.15(a). As the diameter of the microwires approaches the operating wavelength ($\lambda = 600 \mu\text{m}$), the upper limit of the effective loss approaches the bulk material loss, which is presented by dashed lines in Fig. 3.15(a). For diameters larger than the operating wavelength all the mode power is in the core of the fibre, therefore the effective loss of the fundamental mode is the same as the material loss. For fibre diameters well below the THz operating wavelength (THz microwire operating regime), the effective loss of all fibres approaches the same loss value. In order to have a clear view of this phenomena, Fig. 3.15(b) shows the enlargement of effective loss for small diameters. Regardless of material used, the effective loss of all microwires drops to less than 0.01 cm^{-1} . Each microwire reaches to the same order of loss values at different diameters due to the differences of the THz dielectric properties (refractive index and absorption coefficient). It should be noted that the trend of the effective material loss of a COC microwire is very similar to that of a PMMA microwire. The effective material loss curve for a COC microwire is lower (almost zero) than for a PMMA microwire. The bulk material absorption of the COC is 0.1 cm^{-1} at $f = 0.5 \text{ THz}$, which is more than an order of magnitude less than that of the PMMA. The curve is not shown in Fig. 3.15(a) to avoid the overcrowding at lower loss values.

It should be noted that the effective loss peaks at the point where the effective area of the microwire has the minimum value. At this point the effective material loss of the microwire is even higher than the pure bulk material loss due to the E_z component of the

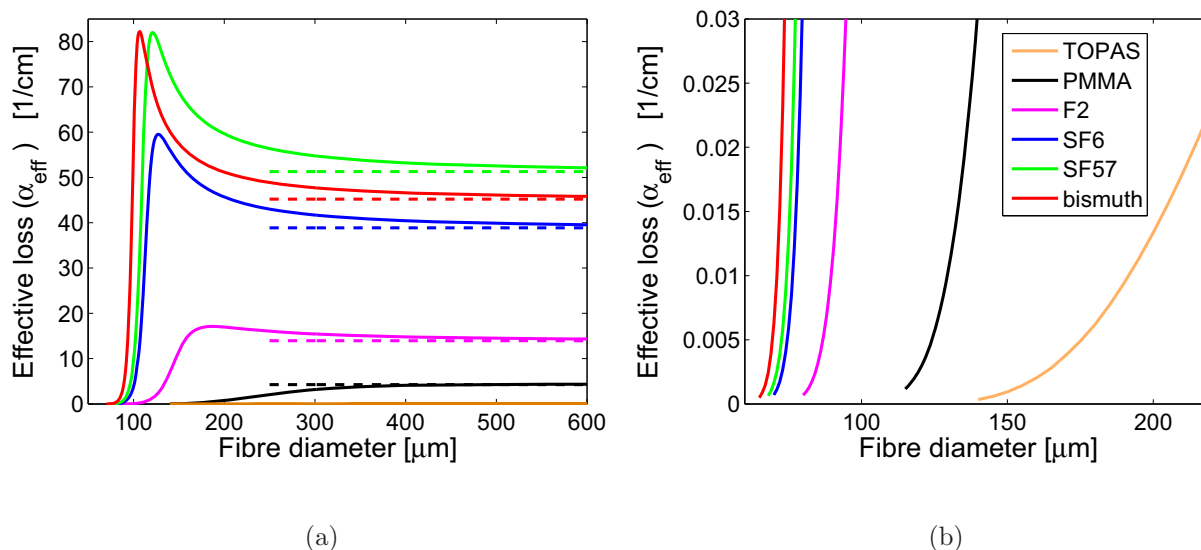


Figure 3.15. Effective loss of COC, PMMA, F2, SF6, SF57 and bismuth microwires. (a)- Effective loss of microwires made up of COC, PMMA, F2, SF6, SF57 and bismuth materials versus core diameter at $f = 0.5$ THz ($\lambda = 600 \mu\text{m}$). Dashed lines represent the bulk material loss at $f = 0.5$ THz ($\lambda = 600 \mu\text{m}$). (b)- Magnification of the lower limit of the effective loss curves of microwires shown in Fig. 3.15(a). Note that the inset in Fig. 3.15(b) indicates the materials for both Figs. 3.15(a) and 3.15(b).

fundamental mode. To clarify this further, the effective material loss of the microwires shown in Fig. 3.15(a) are calculated and shown in Fig. 3.16(a) by just considering the transverse components of the electric field, i.e. $|E|^2 = |E_t|^2$ in Eqn. 3.28. The upper and lower limits of the graphs overlap exactly the upper and lower limits of graphs shown in Fig. 3.15. However, the transition between these limits is gradual, without any peak in between. This is usually the case for the weakly guided approximation, where the fundamental mode is considered to be just polarised in the transverse plane.

For the case where vectorial form of Maxwell's equations is solved to find the fundamental propagating mode of a microwire, the electric and magnetic fields are no longer transverse. Therefore, the z -component of the electric field should also be considered in the numerator of Eqn. 3.28 to accurately calculate the effective loss. Figure 3.16(b) shows the contribution of the E_z component on the effective loss of microwires, i.e. $|E|^2 = |E_z|^2$ in Eqn. 3.28. For the small and large microwire diameters, where more than 90% of the power is in the clad or in the core, the effective loss due to the contribution of the E_z is almost zero. However, for diameters in between these two extremes this value peaks, particularly where the effective area is minimum. The contribution of the E_z component

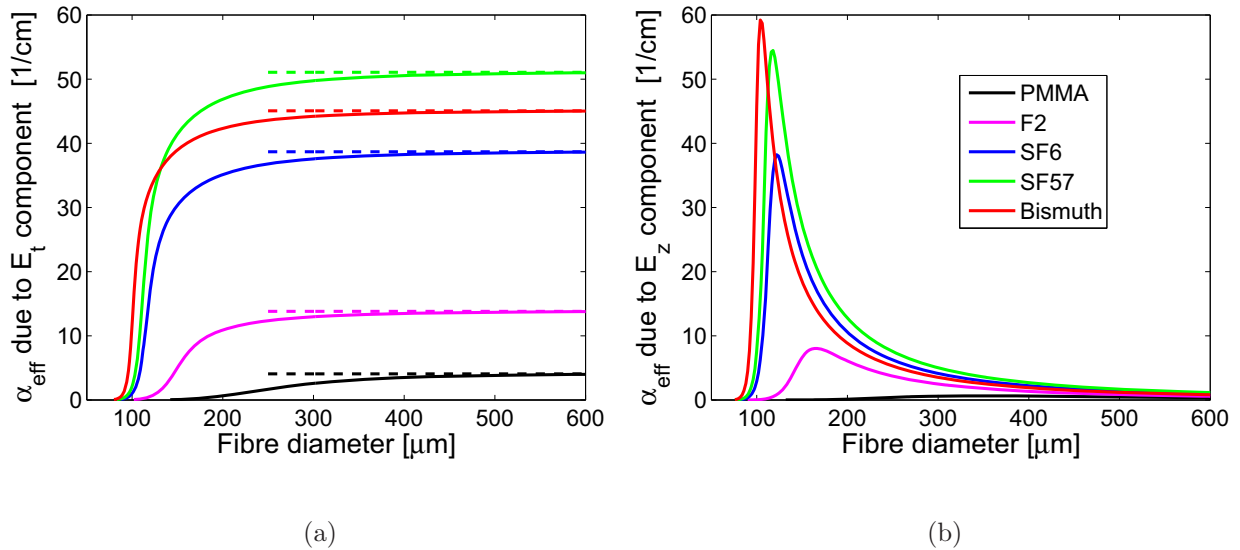


Figure 3.16. Contribution of transverse- and z -components of electric field on α_{eff} . The effect of (a)- transverse E_t -component, and (b) z -component of the electric field on effective loss of microwires made up of PMMA, F2, SF6, SF57 and bismuth materials versus fibre diameter at $f = 0.5$ THz ($\lambda = 600$ μm). Dashed lines represent the bulk material loss at $f = 0.5$ THz ($\lambda = 600$ μm). Note that the inset in Fig. 3.16(b) indicates the materials for both Figs. 3.16(a) and 3.16(b).

to the effective loss is more pronounced for those materials that have a high index of refraction and absorption coefficient. This is consistent with Eqn. 3.28, where effective loss is a function of the refractive index (n_1) and absorption coefficient (α_m). Thus the effect of the E_z component on the effective loss is negligible for microwires made up of COC and PMMA while it is significant for a bismuth microwire.

Bend loss

Radiative losses occur whenever the fibre undergoes a bend of finite radius curvature. The fibres can be subjected to two kinds of bends, macroscopic and microscopic bends. If the radius of the bend is larger than the fibre diameter, it is known as a macroscopic bend and the loss due to this bending is called *macro-bending loss* or simply *bending loss*. While, if the bends are random in the order of micrometer along the axis they are known as microscopic bends and the loss due to this bending is called *micro-bending loss* (Keiser 1991). For sufficiently small microbends, the amplitude of the bend is equivalent to a form of surface roughness (Snyder and Love 2000). As we will see later in Subsection 3.5.1 the

losses due to surface roughness scattering are negligible for the THz microwire. Therefore, in this thesis we only discuss the macrobending losses of the microwires in detail.

Qualitatively the bend loss can be defined as the continual loss of radiation that occurs along any curved section of a fibre and is related to the inability of the tail of the mode to successfully navigate the bend. For a mode propagating along a curved trajectory, the local velocity along the phase fronts of the mode must decrease on the inside of the bend and increase on the outside of the bend in order to maintain a constant angular velocity across the mode. At a certain distance from the centre of the fibre, the mode tail would have to move faster than the speed of the light. Since this is not possible the optical energy in the mode tail beyond this point radiates away (Baggett *et al.* 2003).

The power attenuation of the fundamental mode after traveling a length of L of a bent fibre with a constant radius of R , is determined from the following equation (Sumetsky *et al.* 2004):

$$\frac{P_L}{P_0} = \exp(-\alpha_{\text{bend}}L) \quad (3.29)$$

where, P_0 and P_L are the powers at the beginning and at the end of the bend. The power attenuation coefficient, α_{bend} , can be calculated by the asymptotic formula (Snyder and Love 2000):

$$\alpha_{\text{bend}} = \frac{u^2}{2v^2w^{(3/2)}K_1^2(w)} \left(\frac{\pi}{aR}\right)^2 \exp\left[-\frac{4w^3}{3v^2} \left(1 - \frac{1}{n_1^2}\right) \frac{R}{a}\right], \quad (3.30)$$

where, K_n is the modified Bessel function of the second kind. The parameters u and w are defined by Eqns. 3.9 and 3.10, respectively. The parameter v is the waveguide parameter, and is defined as follows (Snyder and Love 2000):

$$v = a\beta_0\sqrt{n_1^2 - 1}. \quad (3.31)$$

Equation 3.30 is derived using the weak guided approximation. As stated by Sumetsky *et al.* (2004), for the strong guiding mode, i.e. the HE_{11} mode in nanowires, the strong exponential dependence in Eqn. 3.30 is asymptotically accurate if the propagation constant is calculated from Eqn. 3.8. Therefore, this also is going to be valid for the nanowire counterpart that we call the microwire, considered in this thesis. It has also

been shown that the prefactor term (coefficient) in Eqn. 3.30 is accurate within a factor of one (± 1) (Sumetsky *et al.* 2004). Therefore this equation can still be used for bend losses calculation of microwires.

Figure 3.17(a) shows the calculated bend loss for a COC, PMMA, F2, SF6, SF56 and bismuth microwires. The bend loss due to three different bend radii—100 m solid lines, 60 m dashed lines and 40 m dotted lines—are calculated for each microwire at $f = 0.5$ THz ($\lambda = 600 \mu\text{m}$) as a function of diameter. The bend radii are chosen a few tens of metres so that the effect of effective material and bend losses can separately be monitored on the total loss, discussed in the next subsection. The bend loss increases and becomes larger than the material loss, shown in Fig. 3.15(b), as the diameter of the microwire decreases. By moving towards the microwire regime (Fig. 3.15(b)), the field becomes less confined to the fibre core. Therefore, the fraction of the power in the evanescent tail becomes larger than that of the conventional fibre, which leads to more radiation loss even for a large radius of curvature.

The bend loss increases as the radius of curvature decreases. At a certain radius, the bend loss of the fundamental mode becomes equal to 3 dB per loop, i.e. half of the power in the fundamental mode is lost by traveling through the bend. This radius of curvature is known as critical bend radius, R_c . For bends tighter than the critical radius, the bend loss increases dramatically and little power is transmitted through the bend (Snyder and Love 2000). The critical bend radius for the microwires are shown in Fig. 3.17(b). The exponential increase observed by decreasing the diameter of the microwire is strongly dependent on the refractive index of the material. The large values of critical bend radius (order of a few metres) for the lower diameters of microwires, where the effective loss is less than 0.01 cm^{-1} , indicates that these fibres can not be bent too tightly.

Before moving to the next loss mechanism, it is worth investigating the relation between A_{eff} and bend loss curves. In order to do so, the bend loss of a PMMA microwire as a function of diameter, for 5 cm (solid line) and 10 cm (dashed line) bend radii curvatures are compared in Fig. 3.18(a). Small bend radii are chosen deliberately to show the amount of bend loss a microwire undergoes if the bend radius is of the order of a few centimeters. The two vertical dotted lines represent the two microwire diameters, $241 \mu\text{m}$ and $289 \mu\text{m}$. As shown in Fig. 3.13(a), these two diameters have the same effective areas, however as shown in Fig. 3.11(a) the mode distribution of these two diameters is very different. The difference in the mode distributions effect the amount of power residing in the tail of the mode thus results in different bend loss values as seen in Fig. 3.18(a). Although the

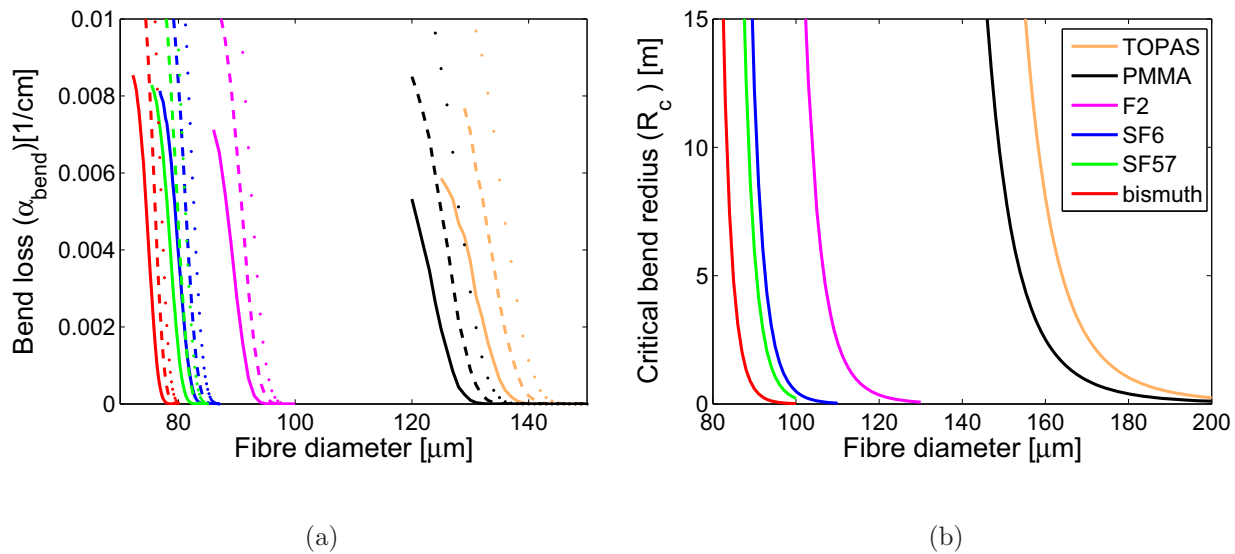


Figure 3.17. Bend loss and critical bend radius of microwires. (a) Bend loss of microwires made up of COC, PMMA, F2, SF6, SF56 and bismuth versus fibre diameter, for three different bend radii at $f = 0.5$ THz ($\lambda = 600 \mu\text{m}$). For each microwire the solid line, dashed line and dotted line represent bend loss due the 100 m, 60 m, and 40 m bend radii. (b) Critical bend radius of microwires made up of COC, PMMA, F2, SF6, SF56 and bismuth versus fibre diameter at $f = 0.5$ THz ($\lambda = 600 \mu\text{m}$). Note that the inset in Fig. 3.17(b) indicates the materials for both Figs. 3.17(a) and 3.17(b).

effective area gives information about the propagating mode area, it is not possible to compare the bend loss values of two fibres based on effective area unless both points are located either after or before the minimum of the effective area curve. We have normalised the effective area of the fibre to its geometrical area of the core, as shown in Fig. 3.18(b), in order to obtain a quantitative curve. There are no two points that have identical A_{eff} values on this normalised effective area curve. This curve increases as the diameter of the microwire decreases. The normalised effective area curve, shown in Fig. 3.18(b), represents that the smaller the ratio of effective core area to fibre geometrical area is, the more confined the mode to the structure is, which ensures lower radiation loss at bending.

Scattering loss

In addition to the loss mechanisms mentioned above, the presence of a glass-air interface in fibres introduces a further mechanism of loss so-called scattering loss, scattering of the guided modes to non-guided modes. This is due to the inherent roughness of the glass interface (Jäckle and Kawasaki 1995, Roberts *et al.* 2005). The roughness forming

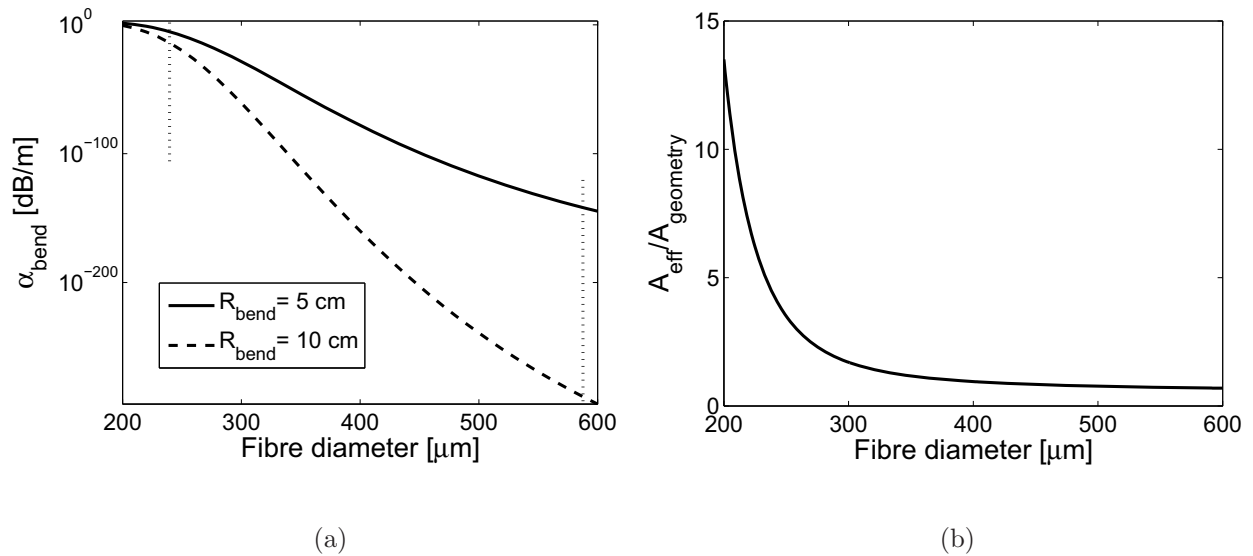


Figure 3.18. Correlation of the bend loss and effective area. (a) Bend loss of a PMMA microwire versus fibre diameter, for 5 cm (solid line) and 10 cm (dashed line) bend radii curvature at $f = 0.5 \text{ THz}$ ($\lambda = 600 \mu\text{m}$). The vertical dotted lines are representing diameters of 241 μm and 589 μm . (b) Effective area of PMMA microwire normalised to the geometrical area of the core.

process on the fibre surface happens during the fibre drawing process at the glass transition temperature. The surface of a liquid in thermal equilibrium is not flat due to the thermal excitation of surface capillary waves. Such fluctuations exist on the surface of molten glass and become frozen-in during the fiber drawing. Atomic force microscopy measurements of surface roughness demonstrate that nanowires, hollow-core fibers and fire-polished glass samples exhibit root-mean-square surface roughness amplitudes of 0.1-0.5 nm (Ebendorff-Heidepriem *et al.* 2009). The scattering loss due to surface roughness is a limiting factor in achieving a minimum loss in these fibres at optical regime, 1550 nm wavelength (Roberts *et al.* 2005, Ebendorff-Heidepriem *et al.* 2009). The computed and measured scattering loss due to surface roughness by Roberts *et al.* (2005) indicates that nature of this loss is a weak function of wavelength ($\frac{1}{\lambda}$). It also indicates that the scattering due to surface roughness has a non Rayleigh character, since the Rayleigh scattering has a $\frac{1}{\lambda^4}$ dependence.

In the THz range, the ratio of wavelength to the height of the surface roughness perturbation is much larger (nearly a thousand times) than that in the optical range. Thus for THz microwires, the surface roughness loss would be substantially less ($\lambda_{\text{THz}} \gg \lambda_{\text{optical}} \rightarrow \frac{1}{\lambda_{\text{THz}}} \ll \frac{1}{\lambda_{\text{optical}}}$) and can be ignored compared to other dominant loss mechanisms, effective

material and bend losses. Therefore we have neglected the loss due to surface roughness for the THz waveguides in this thesis.

Total loss

In this section, we sum up the two loss mechanisms (effective material and bend losses) to have a tangible understanding of the effect of each of the losses. Figure 3.5.1 shows the total loss that a microwire can undergo when it is bent with 100 m, 60 m, and 40 m bend radii. The total loss is calculated by adding up the effective material and bend losses, i.e. the losses presented in Figs. 3.15(b) and 3.17(a). The bend losses start dominating as we get to the low effective material loss, microwire operating regime. The diameter related to the minimum of the total loss shown in Fig. 3.5.1 of a bent microwire is the turning point of the dominant loss mechanism. The total loss is mainly due to effective material loss for the large diameters while for small diameters is mainly due to the bend losses. The value and position of the minimum achievable total loss depends on the bend radius. As an example for a PMMA microwire with the bend radius of 40 m, the minimum achievable loss value is calculated as 0.0014 cm^{-1} and the diameter of the microwire at this point is $129 \mu\text{m}$. While for the bend radius of 100 m the minimum achievable loss is 0.0008 cm^{-1} and the diameter of the microwire at this point is $124 \mu\text{m}$. Such a large bend radii (order of a few tens of metres) indicates that in order to benefit from low loss propagation in microwires, i.e. less than 0.01 cm^{-1} , the structure should be kept absolutely straight. As long as the bend radius is larger than 100 m, which is almost a straight fibre, the total loss of the structure will still be less than 0.01 cm^{-1} . The same behaviour occurs for microwires made up of glass materials.

Figure 3.20(a) shows the comparison of our theoretically calculated effective material loss values with the theoretically calculated and experimentally measured loss values proposed by Chen *et al.* (2006). For our calculations we consider the same parameters as stated in (Chen *et al.* 2006), i.e. $200 \mu\text{m}$ fibre diameter, 1.5 material refractive index and 1 cm^{-1} material absorption coefficient. Our calculated result is slightly lower than the results proposed by Chen *et al.* (2006). We attribute this to the slight bending of the fibre under test. Considering a gentle bend, as for example bend radii of 50 m and 100 m, significantly increases the total loss the microwire undergoes, as can be seen in Fig. 3.20(b). This indicates that any slight bend along the microwire significantly effects the loss values.

The comparison of the theoretical and experimental loss measurements shown in Fig. 3.20 also indicates that loss due to surface roughness does not play a major role in the total loss

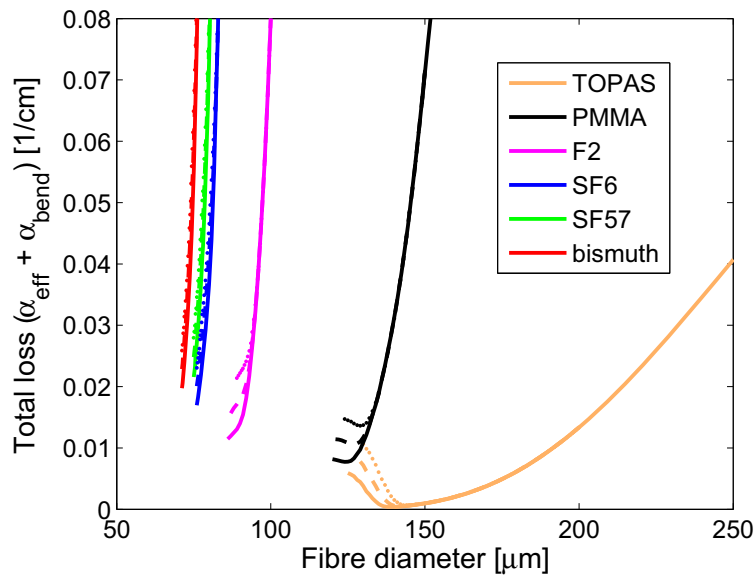


Figure 3.19. Total loss: effective material and bend losses. This figure illustrates the total loss calculated theoretically for THz microwires. Here the total loss is the addition of effective material loss and bend loss. The total loss is calculated for three bend radii at $f = 0.5$ THz ($\lambda = 600 \mu\text{m}$) for each microwire material. Solid lines, dashed lines and dotted lines represent the total loss of microwires when the bend radii is 100 m, 60 m, and 40 m, respectively.

mechanism. The results also indicate that microwires enable low loss guiding mechanism for THz regime provided that the structure is kept straight or undergoes just a gentle bend. Therefore, these fibres have the potential of being used as short tip sensors in the THz regime. For examples, these fibres have been used as straight THz tip sensors (You *et al.* 2009, You *et al.* 2010), THz directional couplers (Chen *et al.* 2009), and in THz reflective imaging (Lu *et al.* 2008b, Lu *et al.* 2008a).

3.5.2 Dispersion mechanisms

Dispersion is the other mechanism that leads to signal degradation in broadband applications. This occurs when the propagation constant of the guided modes varies with frequency (wavelength). The frequency dependency of the propagation constant might arise from refractive index variation of the host material (material dispersion) or/and waveguide (waveguide dispersion) with frequency. This frequency dependence characteristics results in pulse spreading even when different components of the spectrum propagate along the same path. The signal distortion due to this fact is known as group velocity

NOTE:
This figure is included on page 96 of the print copy of
the thesis held in the University of Adelaide Library.

Figure 3.20. Comparison of our results with Chen et al. (2006). (a) Solid line represents our calculated effective loss based on parameters stated in Chen *et al.* (2006). The dashed line and squares represent the theoretically calculated and experimentally measured loss values, by Chen *et al.* (2006), respectively.

dispersion (GVD). It is also known as chromatic dispersion (Buck 2004) or intramodal dispersion (Keiser 1991). An additional degradation mechanism in transmission is associated with polarisation effects, leading to polarisation mode dispersion. This is very important for single-mode fibres and may lead to unacceptable pulse broadening, even with the absence of chromatic dispersion.

Other pulse-broadening mechanisms are associated with mode dependent propagation delays in multi-mode fibres, which is known as modal dispersion (Buck 2004) or intermodal dispersion (Keiser 1991). In THz microwires we usually focus on the low loss operating regime, where the fibres are operating in their single-mode operating regime. Thus in this section, we discuss the main causes for chromatic/intramodal dispersion—material dispersion and waveguide dispersion—and polarisation mode dispersion, which are the dispersions a single-mode fibre may undergo.

Material dispersion

Material dispersion arises from the variation of the refractive index of the core material of fibres as a function of frequency (wavelength). This causes a frequency dependence of the

group velocity of the mode; i.e. pulse spreading occurs when different frequencies travel through the fibre.

To calculate material dispersion, we consider a plane wave propagation in an infinite dielectric medium. The propagation constant is thus obtained by:

$$\beta = \frac{2\pi n}{\lambda}, \quad (3.32)$$

where n is the refractive index of the medium and is a function of frequency (wavelength). Thus the group velocity, the velocity at which the energy in a pulse travels in the medium is:

$$\nu_g = \partial\omega/\partial\beta, \quad (3.33)$$

and subsequently the material dispersion is:

$$D = \frac{1}{L} \frac{\partial\tau_g}{\partial\lambda}, \quad (3.34)$$

where, τ_g is the group delay and L is the distance traveled by the pulse along the fibre. The group delay can be calculated from the following equation:

$$\tau_g = L/\nu_g = L \frac{\partial\beta}{\partial\omega}. \quad (3.35)$$

Figure 3.21 shows the material dispersion of the polymer and glass materials used in this chapter. The material dispersion is calculated by fitting a third order polynomial curve to the measured refractive index of materials in THz region shown in Fig. 3.6(b). As expected from the almost flat refractive index values, the material dispersion of the bulk material is negligible ($< 10^{-10}$) in the THz range. The units used for dispersion in the optical regime are ps/km/nm, where the length of the fibre and the operating wavelength are in the order of kilometers and nanometers, respectively. If we adjust that for the THz range where the length of the fibre is in the order or less than a metre and the operating wavelength is in the order of micrometers, the dispersion units will be in ps/m/ μm . In this thesis, the units used for dispersion are ps/m/ μm . The conversion ratio between ps/km/nm and ps/m/ μm is unity, since the factors for converting the km to m (10^3) and nm to μm (10^{-3}) cancel each other out.

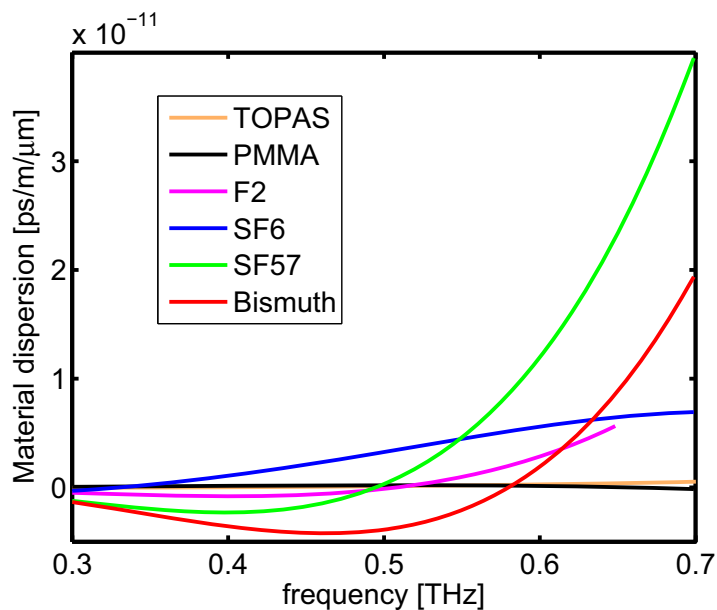


Figure 3.21. Material dispersion of the polymer and glass samples. The bulk material dispersion of COC, PMMA, F2, SF6, SF57 and bismuth versus frequency.

Waveguide dispersion

This dispersive phenomena is due to the presence of a waveguide structure. This occurs in addition to the material dispersion discussed above. Waveguide dispersion contributes to the overall pulse broadening by either adding to or subtracting from the material dispersion. As a result, the waveguide offers flexibility in controlling the amount of dispersion though appropriate index profile design. The waveguide dispersion indicates that the effective refractive index of the propagating mode is a function of frequency (wavelength). The material dispersion of materials used for waveguides in this thesis is almost zero, i.e. the refractive index of hosting material is a flat function of frequency and the waveguide dispersion is dependent only to the shape/structure of the waveguide.

Let us first consider the phase velocity and group velocity. For the time-harmonic HE_{11} mode propagating through a microwire, the propagation (phase) constant of the mode is equal to:

$$\beta_{\text{eff}} = \frac{2\pi n_{\text{eff}}}{\lambda_0} = \frac{\omega}{\nu_p} = \frac{\omega n_{\text{eff}}}{c}, \quad (3.36)$$

where n_{eff} is the effective refractive index of the fundamental mode and ν_p is known as the phase velocity of the mode. Once the propagation constant of the mode is known the phase velocity (ν_p) can be calculated from Eqn. 3.36. As discussed earlier the group

(energy) velocity, ν_g , represents the velocity with which the wave energy is transported. It is also interpreted as the propagation of a group of waves whose frequencies are distributed over an infinitesimally small bandwidth centered around frequency w . The group velocity can be calculated from the following equation once the propagation constant is evaluated:

$$\nu_g = \frac{\partial \omega}{\partial \beta_{\text{eff}}}. \quad (3.37)$$

Anomalous dispersion can cause the group velocity to be faster than the speed of light but the phase velocity can be equal to but not exceed the speed of light (Withayachumnankul *et al.* 2010). The product of group velocity and phase velocity is always equal to

$$\nu_g \nu_p = C^2 = \frac{1}{\mu_0 \epsilon_0}. \quad (3.38)$$

The effective refractive index (n_{eff}) of the fundamental mode (HE_{11}) of two PMMA microwires (200 μm and 280 μm diameters) and two bismuth microwires (90 μm and 120 μm diameters) are shown in Figs. 3.22(a) and 3.22(b). The effective refractive index of microwires is a function of frequency and the changes in n_{eff} of bismuth microwires are more pronounced due to the high bulk material refractive index nature of bismuth glass. For the waveguide dispersion analysis we decided to consider two examples of the seven materials discussed so far: one polymer (PMMA) and one glass (bismuth). They both have the highest refractive index in their category.

The phase velocity (ν_p) and group velocity (ν_g) of all four microwires are shown in Figs. 3.22(c) and 3.22(d), respectively. The velocities are normalised to the speed of light in free space for easier comparison. The phase velocities of microwires are proportional to the inverse of n_{eff} . For low frequencies, where the dimensions of the fibres are less than the operating wavelength and almost all the power is in the air, the phase velocity approaches unity and decreases as the frequency increases. The decrease for bismuth microwires is faster compared to that of the PMMA microwires due to the high bulk material refractive index of bismuth. Similarly the group velocity approaches unity at low frequencies. By increasing the frequency, eventually the group velocity approaches to that of the bulk material. The group velocity of the bulk materials is shown with dotted lines in Fig. 3.22(d). The group velocity drops to lower than that of the bulk material with a minimum point around 0.67 THz for the 280 μm diameter PMMA microwire and 0.44 THz and 0.58 THz for the 90 μm and 120 μm diameter bismuth microwires, respectively. As we will see later, these minima correspond to zero dispersion points.

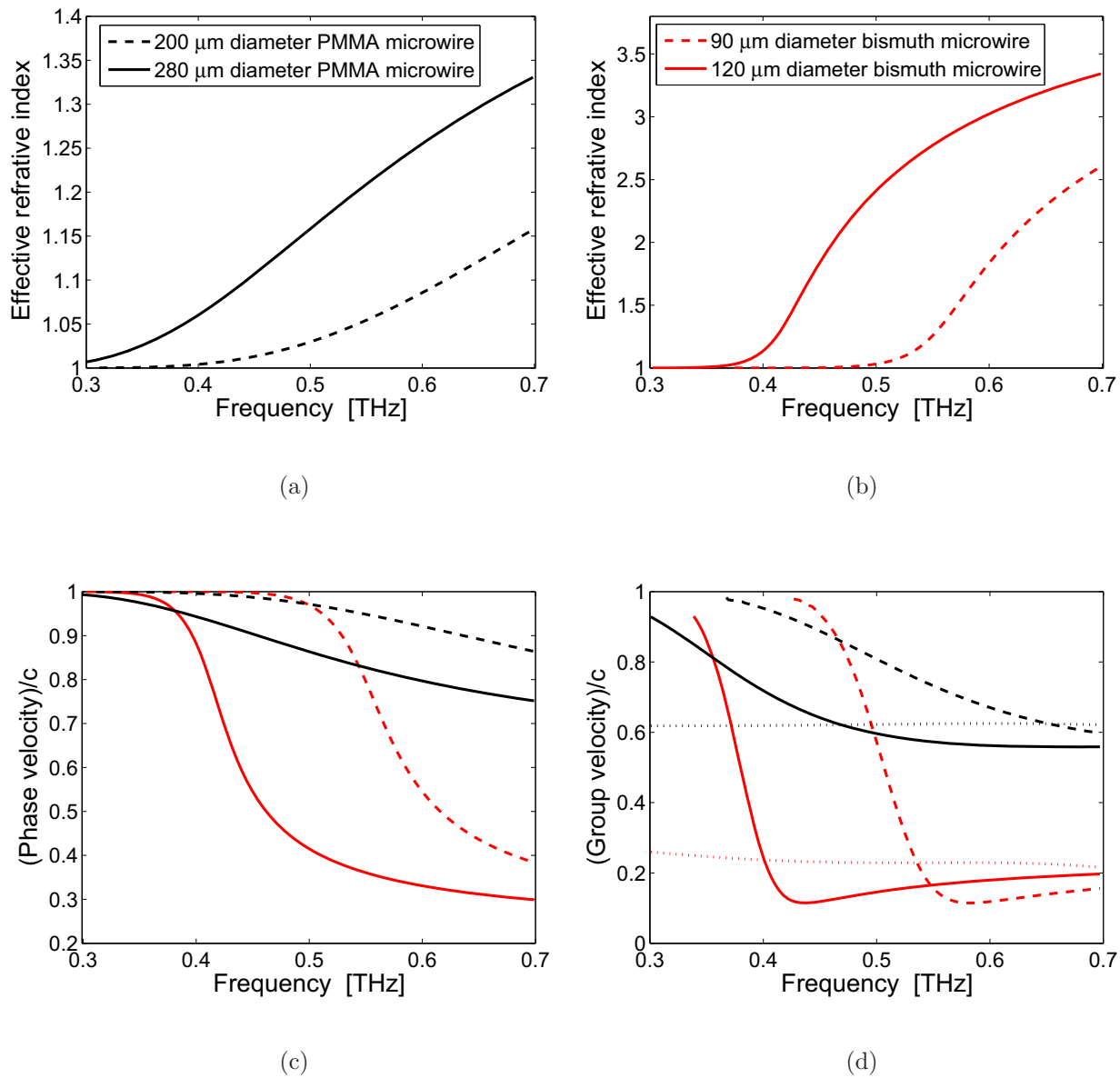


Figure 3.22. Effective refractive indices, phase velocity and group velocity of PMMA and bismuth microwires. The effective refractive indices of (a) 200 μm (black dashed line) and 280 μm (black line) diameters PMMA microwires and (b) 90 μm (red dashed line) and 120 μm (red line) diameters bismuth microwires. (c) The phase velocity of all the four microwires as a function of frequency. (d) The group velocity of all the four microwires as a function of frequency. The black and red dotted lines represent the group velocities of bulk PMMA and bismuth materials, respectively.

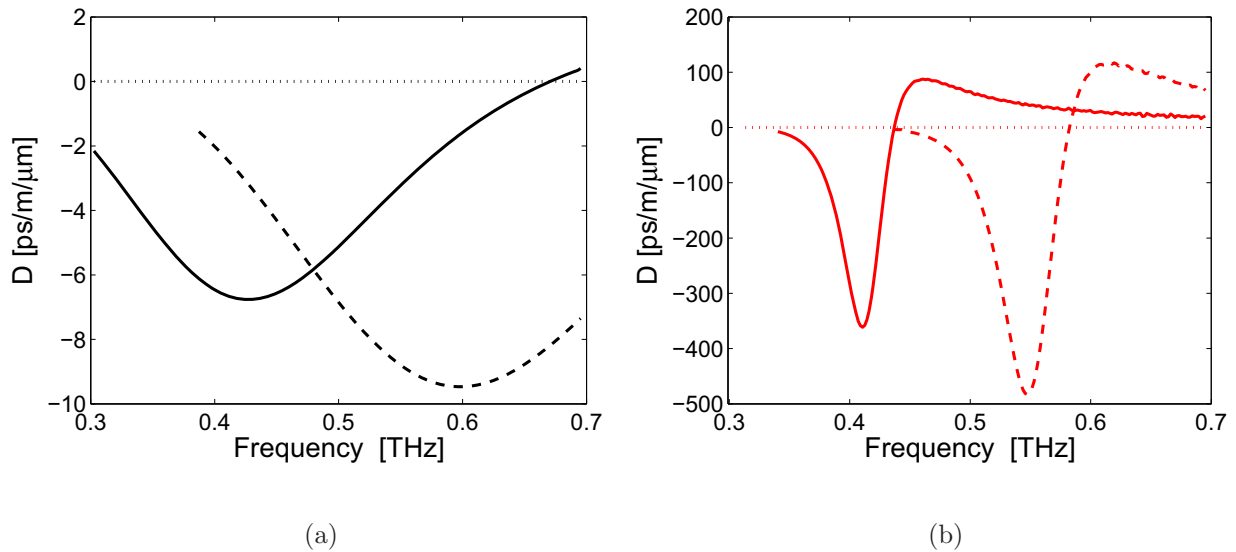


Figure 3.23. Waveguide dispersion of PMMA and bismuth microwires. The waveguide dispersion of (a) 200 μm (black dashed line) and 280 μm (black line) diameter PMMA microwires and (b) 90 μm (red dashed line) and 120 μm (red line) diameter bismuth microwires at THz frequencies.

The slopes of the group velocity curves indicate that different components of the spectrum propagate at different group velocities. This leads to signal distortion known as waveguide dispersion. The waveguide dispersion can be evaluated from group velocity by using Eqn. 3.34. The waveguide dispersion of the PMMA and bismuth microwires are shown in Figs. 3.23(a) and 3.23(b), respectively. The curves indicate that a terahertz pulse propagating along a microwire encounters normal dispersion (negative dispersion) at lower frequencies, corresponding to a decrease in the group velocity curve. They also indicate that the same terahertz pulse encounters anomalous dispersion (positive dispersion), corresponding to an increase in the group velocity curve after the minimum point, at higher frequencies. The normal dispersion corresponds to a positive chirp in the time domain, while anomalous dispersion corresponds to a negative chirp in the time domain. It should be noted that for each microwire there is a zero dispersion point, which corresponds to the minima on the group velocity curves.

It should be noted that the PMMA microwire waveguide dispersion (Fig. 3.23(a)) changes gradually and is much lower than that of bismuth microwire (Fig. 3.23(b)). This is expected due to the flat curves of effective refractive index, group and phase velocities of the PMMA microwire compared to that of bismuth microwire.

Polarisation mode dispersion

Additional degradation in transmission is associated with birefringence, which can arise from structural and environmental perturbations. The linearly polarised electric field of fundamental mode has the same propagation constants for two orthogonal polarisations provided that microwire has circular cross-section with no perturbation along the length of the fibre. However, in reality the fabricated fibres do not have the circular cross-section and may have bends and deformation along the fibre, which results in different group velocities between the two principal orthogonal states of polarisation. This is also dependent on mechanical stresses arising from temperature variations. Therefore the difference between the propagation constants for two orthogonal polarisations leads to pulse broadening through polarisation mode dispersion. It is well known from optics that the solution to this problem is the use of polarisation maintaining (PM) fibres, which introduce modal birefringence into the fibre (Noda *et al.* 1986). Modal birefringence arises from effective refractive index differences between x and y polarisation modes, $|n_x - n_y|$. Modal birefringence can be introduced using either mechanical stress in the cladding (Noda *et al.* 1986) or/and asymmetry in the core/cladding geometry of the fibres (Suzuki *et al.* 2001). Thus a mode launched onto one of the principle axes of a PM fibre remains in this polarisation in the presence of any environmental perturbations. The study of polarisation-related dispersion in fibres involves many methods of analysis and characterisation, which is beyond the scope of this thesis. However, in this thesis later in Subsection 4.4.3, we will investigate the modal birefringence of porous fibres, $|n_x - n_y|$ as a function of frequency and we will compare the results to those for an ideal microwire.

3.6 Chapter Summary

In this chapter, we used the concept of optical nanowires in the terahertz frequency range to achieve low loss terahertz waveguides. The THz dielectric characteristics of bulk materials—four glasses (F2, SF6, SF57 and bismuth), two polymers (COC and PMMA), and a diamond—have been measured. The normalised field distribution, power fraction, effective area, and signal degradation (loss and dispersion) of microwires have been studied thoroughly. It has been shown that in the microwire operating regime most of the power is outside the core (in the air-clad region). This reduces the effective material loss of microwires, while makes them susceptible to any gentle curvature.

We have demonstrated that the main limiting loss mechanism for terahertz microwires is the effective material loss, provided that microwires are used for applications without fibre bending. We have also shown that in the microwire operating regime ($D \ll \lambda_{T\text{-ray}}$) the effective loss of all microwires approaches to similar loss values (less than 0.01 cm^{-1}) regardless of the material used. The diameter at which the low loss is achieved depends on the bulk material dielectric properties.

Another dominant loss mechanism for bend microwires is bend loss. The small diameter of the microwire, compared to the operating wavelength, results in less confinement of the field to the structure and therefore increased loss due to bends. Rigid and straight microwires are promising solutions for low loss terahertz transmission.

We have also demonstrated that material dispersion of polymers and soft glasses represented in this chapter is negligible due to their almost flat loss dielectric profile at THz. As a result, the waveguide dispersion of THz waveguides is only dependent on the design, i.e. the effective refractive index profile. Moreover, polymer microwires have much lower dispersion waveguide values (more than one order of magnitude lower) compared to glass microwires. This is due to the low dielectric profile of polymer waveguides in THz compared to that of the glass microwires.

The following chapter shows how we can improve the mode confinement to the microwire with introducing sub-wavelength air-holes in the core of the air-clad waveguide. As we will see these sub-wavelength air-holes not only improve the confinement, but also reduce the signal degradation (loss and dispersion) in the THz waveguide. From this point onward in this thesis, we mainly focus on the THz waveguides made up of polymers, since we have shown in this chapter that these materials are more transparent (lower loss and lower dispersion) for THz radiation compared to glasses.

THz porous fibres: concept and modelling

IN this Chapter a novel class of optical waveguide with a porous transverse cross-section that is created by arranging sub-wavelength air-holes within the core of the waveguide is proposed. These waveguides can offer a combination of low transmission loss and high mode confinement in the THz regime by exploiting the enhancement of the guided mode field that occurs within these sub-wavelength holes. We evaluate the properties of these porous fibres and quantitatively compare their performance relative to that of a microwire (solid core air cladded fibre). For similar loss values, porous fibres enable improved light confinement and reduced distortion (loss and dispersion) of a broadband pulse compared to microwires. We also demonstrate for the first time that introducing asymmetrical sub-wavelength air-holes in the core of porous fibres leads to a birefringence $|n_x - n_y| \approx 0.026$. This opens up the potential for realisation of novel polarisation preserving fibres in the terahertz regime.

4.1 Introduction

The guiding mechanism that operates in a microwire, as discussed in detail in Chapter 3, is based on total internal reflection. In this waveguide low loss is achieved when almost all the field propagates in the medium surrounding the structure. This medium is usually air, where the losses are greatly reduced for THz radiation. In other words, the structure acts as a rail for guiding THz radiation, rather than as pipe in which the field is confined in the structure. This, however, results in weak confinement of the guided field within the structure and makes the guided field susceptible to any small perturbation on the surface or vicinity of the structure. Any perturbation causes a large portion of the guided power to couple into radiation modes. Furthermore, as a result of weak confinement, the guided modes within these structures suffer strong bend loss as discussed in Section 3.5. In order to produce practical waveguide structures for THz, it is critical to find a means of improving the mode confinement while retaining the reduction in material loss. For THz, this is associated with locating most of the guided field in air.

An approach to improve field confinement in the THz waveguides has been demonstrated by Nagel *et al.* (2006b) as discussed earlier in Subsection 2.3.2. They have shown that a low index discontinuity in dielectric waveguides (such as split rectangular and tube waveguides) has increased field in the low-index central region and reduced field in the air-clad surrounding region, resulting in increased confinement. Initially the concept was proposed by Almeida *et al.* (2004) for integrated optical devices and then has been expanded to THz and optical waveguides (Nagel *et al.* 2006b, Wiederhecher *et al.* 2007, Monro 2007).

4.1.1 Objective and framework

In this Chapter, we propose a novel class of waveguides, *porous fibres*, based on introducing sub-wavelength low index discontinuities. In Section 4.2, we discuss the concept of the field enhancement within a low-index discontinuity in waveguides. Then in Section 4.3, we expand this concept to an array of sub-wavelength air-holes in the core of the fibre. We also discuss the simulation method, and convergence and symmetry techniques used in simulation for characterisation of porous fibres. Then we theoretically investigate the effective material loss and the confinement of THz propagation as a function of fibre porosity and diameter, and compare it with those of THz microwires in Section 4.4. We demonstrate that for similar loss values, the porous fibre leads to better confinement than

the microwire. In the same Section, we demonstrate that porous fibres provide a significant improvement in the group velocity (ν_g) and consequently group velocity dispersion (GVD) in comparison to THz microwires. We also propose new designs of porous fibres, introducing asymmetrical discontinuities, which lead to a strong birefringence reducing distortion due to polarisation mode dispersion.

Because of the low loss properties of polymers in the THz regime, polymethyl methacrylate (PMMA) and cyclic olefin copolymer (COC, also known as TOPAS) are considered as the host material for the waveguides in this chapter. Note that PMMA is considered as the host material in Sections 4.3, and Subsections 4.4.1 and 4.4.2, and COC in Subsection 4.4.3. Due to the availability of PMMA billets, the initial analysis, fabrication and experimental results are carried out for PMMA fibres. Then later on, it is expanded to COC fibres.

4.2 Sub-wavelength air-hole in a dielectric waveguide

At any interface between two materials with no surface charge, the normal component of the electric flux density (displacement electric field) is continuous, as shown in Eqn. 3.16, with respect to boundary conditions. By Eqn. 3.18, this leads to a discontinuity in the electric-field strength; i.e., the electric-field is enhanced on the low refractive index side. The strength of the enhanced electric field depends on the square of the ratio of refractive indices and the electric field strength at the high index side. As a result, a higher enhanced electric field is formed at a low-index interface discontinuity. As discussed in detail in Subsection 3.4.1 and shown in Fig. 3.11, the enhancement phenomena is noticeable at the core-clad interface of microwires and is negligible at the core-clad interface of conventional fibres (diameter much larger than operating wavelength).

The enhancement phenomena occurs, at any discontinuity (not just at core-clad interface) in a dielectric waveguide. As an example, for a hollow core air-clad PMMA fibre, the enhanced electric field is shown in Fig. 4.1. The fibre core diameter is $1600 \mu\text{m}$ and the fibre core-clad interface is shown with a vertical dashed line. This is a multimode fibre at $f = 0.5 \text{ THz}$ or $\lambda = 600 \mu\text{m}$. The normalised electric field of the fundamental mode is shown in Fig. 4.1 for three different bore (the central air-hole) diameters of 900 , 300 , and $100 \mu\text{m}$. In order to be able to compare the three curves, we normalise each electric field by its maximum. The enhanced electric field at both bore-core and core-clad interfaces rapidly decays away. This is clearly noticeable for the enhanced fields at all the core-clad

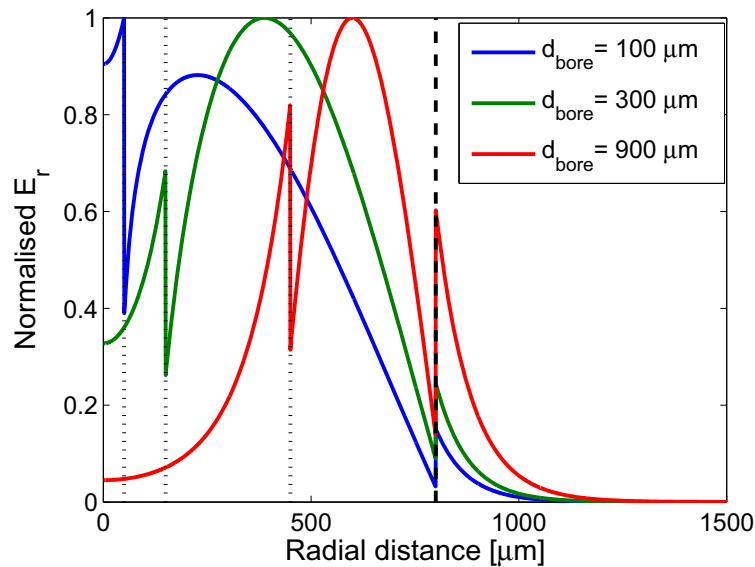


Figure 4.1. The electric field enhancement inside the central bore of a hollow core fibre.

The normalised electric field of a hollow core THz fibre for 100, 300, and 900 μm bore and 1600 μm core diameters at $f = 0.5$ THz ($\lambda = 600$ μm). The enhanced electric field on the bore-core interface decay rapidly for the bore diameter of 900 μm , shown in red. As the bore diameter decreases to the order of operating wavelength the decay of the evanescent field becomes minimised and localised in the bore. The vertical dashed line represents the core-clad interface, while the vertical dotted lines represent the bore-core interface.

interfaces and also for the bore-core interface of the fibre with 900 μm bore diameter. The decay of the evanescent field within the bore decreases and becomes localised as the bore diameter decreases to less than the operating wavelength (Wiederhecher *et al.* 2007, Monro 2007). The green and blue curves in Fig. 4.1 have a bore diameter of 300 and 100 μm respectively, which is less than operating wavelength, $\lambda = 600$ μm . For these bore diameters the enhanced evanescent field decays gradually and gets localised in the bore.

Nagel *et al.* (2006b) have demonstrated the effect of a central air-hole on a THz slab waveguide and THz fibre, shown in Fig. 2.23(a). They perform a thorough discussion of the effect of hole and core sizes on the power fraction localised in the discontinuity and in the fibre material. Their results indicate that the air discontinuity in a dielectric slab waveguide can trap 55% of the mode power in the vicinity of the gap between the two slabs, and a sub-wavelength air-hole in a fibre can trap 26% of the power in the sub-wavelength discontinuity. Nagel *et al.* (2006b) have also shown that introducing the discontinuity lowers the loss and dispersion of the propagating mode compared to

that of the same waveguide without a discontinuity. Also later, Zhao *et al.* (2008) have theoretically discussed the effect of material, core, and bore diameter changes on the power distribution, field distribution, and field enhancement in a THz hollow-core fibre.

In practice, the slab waveguide is difficult to handle because it needs a structure to keep the slabs together. This interferes with the propagating mode. A single sub-wavelength air-hole in the fibre cannot reduce the loss substantially since a large portion of the power of the guiding mode is still propagating inside the material. Moreover, reducing the dimension of the waveguides forces more power in the clad region and reduces the mode confinement, as we have seen in Chapter 3.

In the next section, we propose a novel class of waveguide for THz, based on introducing sub-wavelength low index discontinuities within the core of an air-clad fibres. Instead of having one sub-wavelength air-hole in the core, we consider a pattern of sub-wavelength air-holes in the core, and show that this leads to a better confinement of the field to the structure while still allowing THz propagation in the sub-wavelength air-holes.

4.3 Concept of THz porous fibre

In the optical regime, elongated void regions have previously been used in photonic crystals to improve the transmission efficiency simply by reducing the material (Wang 2002). Here in this work, we consider a fibre, *porous fibre*, with sub-wavelength holes in the core. This enables localisation and enhancement of the guided mode within the holes, which consequently as we see in this Chapter improves the confinement and signal degradation (loss and dispersion).

Porous fibres in this study are created by including a distribution of sub-wavelength air-holes within the *core* of an air-clad fibre. A typical example is shown in Fig. 4.2(a). The distribution, shape, and size of the holes determine the porosity of the structure, which is defined as the fraction of the air holes to core area. The arrangement of the holes within the core of porous fibre can be based on different varieties of lattice structures. The structure shown in Fig. 4.2(a) has a triangular lattice of circular holes with radii of 20 μm and a core radius of 200 μm , which results in a porosity of 37%.

In order to reduce the effective material loss in a porous fibre, we need to be able to access high porosity values. Therefore, we chose a triangular lattice for circular air-holes, which leads to higher porosity values when compared to a rectangular lattice. Theoretically, the

maximum achievable porosity for a porous fibre with a rectangular air-hole arrangement is $\frac{\pi}{4} \cong 0.785$, while for a triangular air-hole arrangement it is $\frac{\pi}{2\sqrt{3}} \cong 0.9$. The sparse porosity value (37%) in Fig. 4.2, is only chosen for purposes of clarity for displaying the concept in this section.

To find the propagation constant and field distributions for the porous fibres, we solve the full vectorial form of Maxwell's equations since, for the sub-wavelength scales considered here, a scalar approximation gives inaccurate results (Zheltikov 2005). Full-vectorial analytical solutions only exist for extremely simple waveguide designs such as, e.g. a circular core embedded in an infinite cladding (Balanis 1989, Snyder and Love 2000). Full-vector analytical solutions cannot be found in general for complex waveguide structures such as THz porous fibres and microstructured fibres. Thus, a numerical approach can provide a powerful alternative for the design and study of their guiding properties. Eigenmode analyses are typically performed with solvers based on the finite-difference method (FDM) or the finite-element method (FEM). Both approaches can provide a highly accurate solution for the propagation constant, cut-off frequency, confinement loss and birefringent properties of waveguides. For micro- or nano-structured fibres, such eigenmode solvers have been applied especially for photonic crystal fibres and have been compared in terms of usefulness and limitation (Zhu and Brown 2002, Saitoh and Koshiba 2005, Ademgil and Haxha 2008).

In this thesis, we use the FEM method instantiated in the commercial FEM package COMSOL 3.2 and 3.5. The geometry can be created and analysed using the COMSOL GUI interface like all other FEM software. One can also run the code scripts from MATLAB. The latter offers the flexibility of combining MATLAB commands for post processing. In this work, we run the code script from MATLAB and the code is included in the Appendix B.

The eigenvalue problem is formed by applying variational equations¹⁵ to each of the 2D finite-elements used to discretize the waveguide profile as shown in Fig. 4.3(b) (COMSOL Accessed: February 2010, Itoh 1989). The propagation constants, field distributions, and power distributions of guiding modes are calculated by applying proper boundary

¹⁵In the FEM, instead of partial differential equations with boundary conditions, variational expressions are applied to each of the elements. The method of weighted residual is used to project Maxwell's equations into a form suitable for numerical simulations, which leads to variation method upon which the FEM is based (Itoh 1989).

conditions. From there, we are able to calculate other parameters such as effective area, power fraction, effective material loss, and dispersion.

The concept of field enhancement within low-index discontinuity (as explained in Sections 3.4 and 4.2) is demonstrated in Fig. 4.2(b), which shows the normalised z -component of the Poynting vector ($S_z = \frac{1}{2} \vec{E} \times \vec{H} \cdot \hat{z}$) profile of the fundamental mode of the porous fibre along the arrow shown in Fig. 4.2(a). The refractive index profile along the same axis is also shown, demonstrating where the sub-wavelength air-holes are located. The refractive indices $n_1 = 1.6$ and $n_0 = 1$ refer to material (PMMA) and air refractive indices at $f = 0.5$ THz ($\lambda = 600 \mu\text{m}$), respectively. The normal component of electric field and as a result the power intensity (S_z) is enhanced at the each air-material interface and stays localised in the sub-wavelength air-holes, where the refractive index is n_0 . This phenomenon occurs for all the sub-wavelength air-holes in the structure as can be seen in Fig. 4.2(c). Since the enhancement coefficient of the normal component of electric field at each interface is constant, n_1^2 , the intensity of the localised power intensity (S_z) depends on the location of the sub-wavelength air-hole position. The closer the sub-wavelength air-hole to the center of the fibre, where the electric field intensity is stronger, the stronger the localised power intensity. Therefore the envelope of the intensified profile of the power has the similar profile pattern of the air-clad fibre without sub-wavelength holes. For the chosen porous fibre dimensions, the power profile envelope has a Gaussian shape, as shown in Fig. 4.2(d). The effect of these sub-wavelength air-holes on the fibre parameters—power fraction, effective area, effective material loss, and dispersion—is analysed later in this chapter.

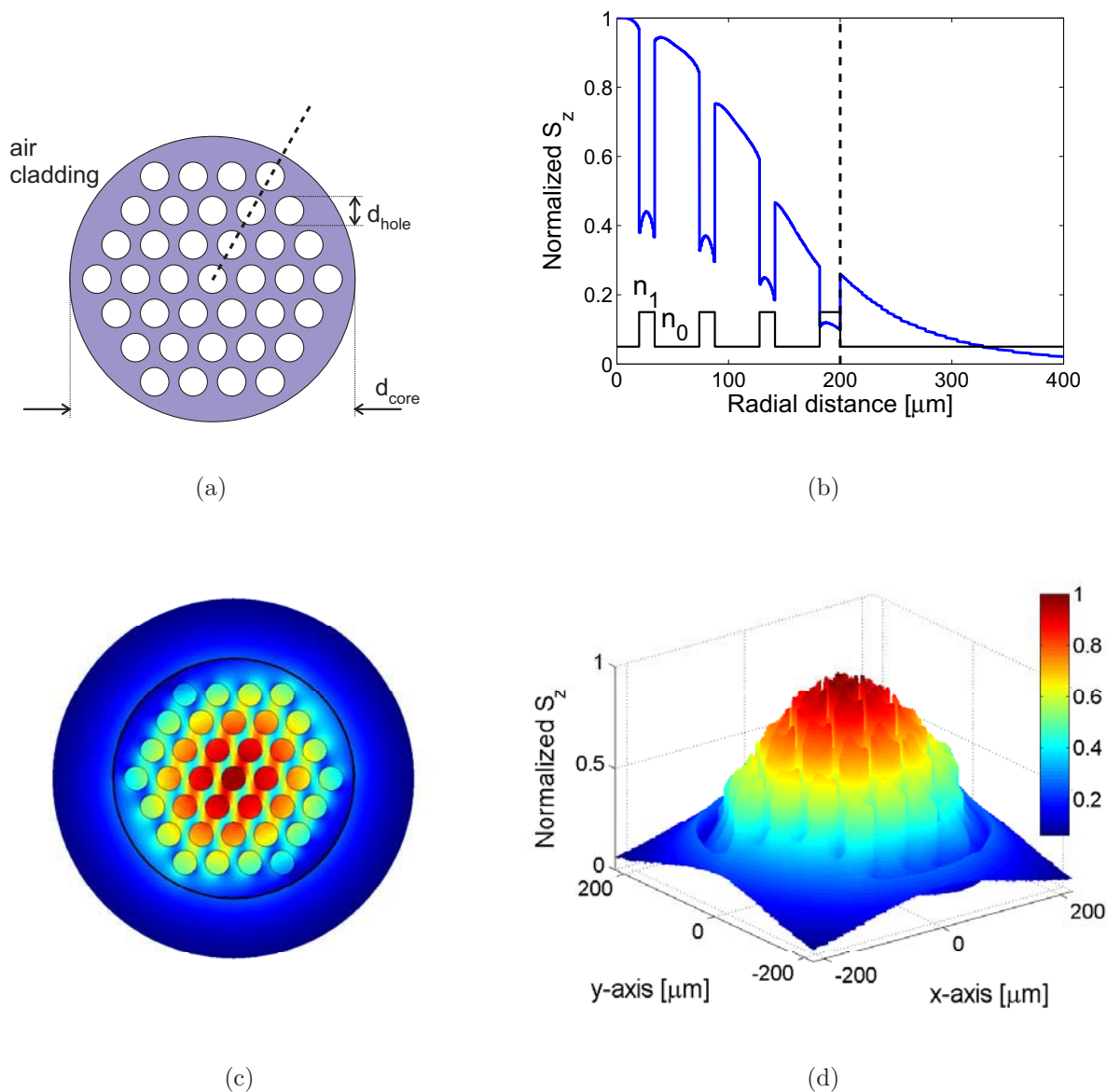


Figure 4.2. Power profile distribution of a porous fibre with triangular lattice. (a) Cross-section and geometrical definitions of the triangular lattice porous fibre. (b) The normalised z -component of the Poynting vector, S_z , profile along the dashed line shown in (a), of the fundamental mode of a polymer porous fibre with core radius of $d_{\text{core}}/2 = 200 \mu\text{m}$, hole radii of $d_{\text{hole}}/2 = 20 \mu\text{m}$ and 37% porosity at $f = 0.5 \text{ THz}$ ($\lambda = 600 \mu\text{m}$). The vertical dashed line represents the core to cladding interface and the lower solid line represents the refractive index profile. (c) 2D and (d) 3D view of the normalised S_z of the porous fibre. Note that S_z is normalised by its maximum and the colour bar shows the normalised S_z .

Convergence and symmetry

After creating the solution region, which includes the fibre geometry and a finite square cladding (more than 10 times larger than fibre diameter) with proper boundary conditions as shown in Fig. 4.3(a), the region is discretised into finite number of elements also known as a *mesh*. Although the element sizes are proportional to the dimension of each sub-region, they can be set manually in the code script. The finite element discretisation of the fibre geometry shown in Fig. 4.2(a) is illustrated in Fig. 4.3(b). The red lines represent the fibre geometry except the outer red circle. This is added intentionally to create a region around the fibre where the mesh density is high. Hence, this allows the fast decaying evanescent fields to be mapped with higher precision. A close up of the mesh for sub-wavelength air-holes and core of the fibre is also shown in Fig. 4.3(b). The propagation constants of propagating modes are obtained from the eigenvalue equation, which is formed by applying variational equations to each of these finite-elements. The normalised power distributions of the two polarisations of the fundamental mode are calculated and shown in Figs. 4.3(c) and 4.3(d). The transverse electric field vector is shown by black arrows on each figure. The arrows also indicate the direction in which the enhancement of the electric field occurs in the air-holes.

The mesh density in the sub-regions and the dimension of the finite boundary of the solution region are the two parameters that require attention. Setting these values high increases the computational time and requires large memory. However, setting these values low creates uncertainty in the evaluated propagation constant, which affects the other waveguide parameters. Thus we conduct convergence tests to find the optimum values for the mesh density and the length of the solution region. Before targeting the convergence tests (Fig. 4.6), first we simplify the solution region.

The solution region can be simplified further, i.e. due to the symmetry of the structure and the field distributions only a quarter of the entire region needs to be simulated. In order to do so, specific boundary conditions are required. These boundaries—perfect electric conductor (PEC) and perfect magnetic conductor (PMC)—act as a *mirror*. It has to be ensured that these boundary conditions, reproduce correctly all field components of the mode. In order to obtain both polarisations of the fundamental mode, we have to alternate the PMC and PEC boundaries and compile the code twice.

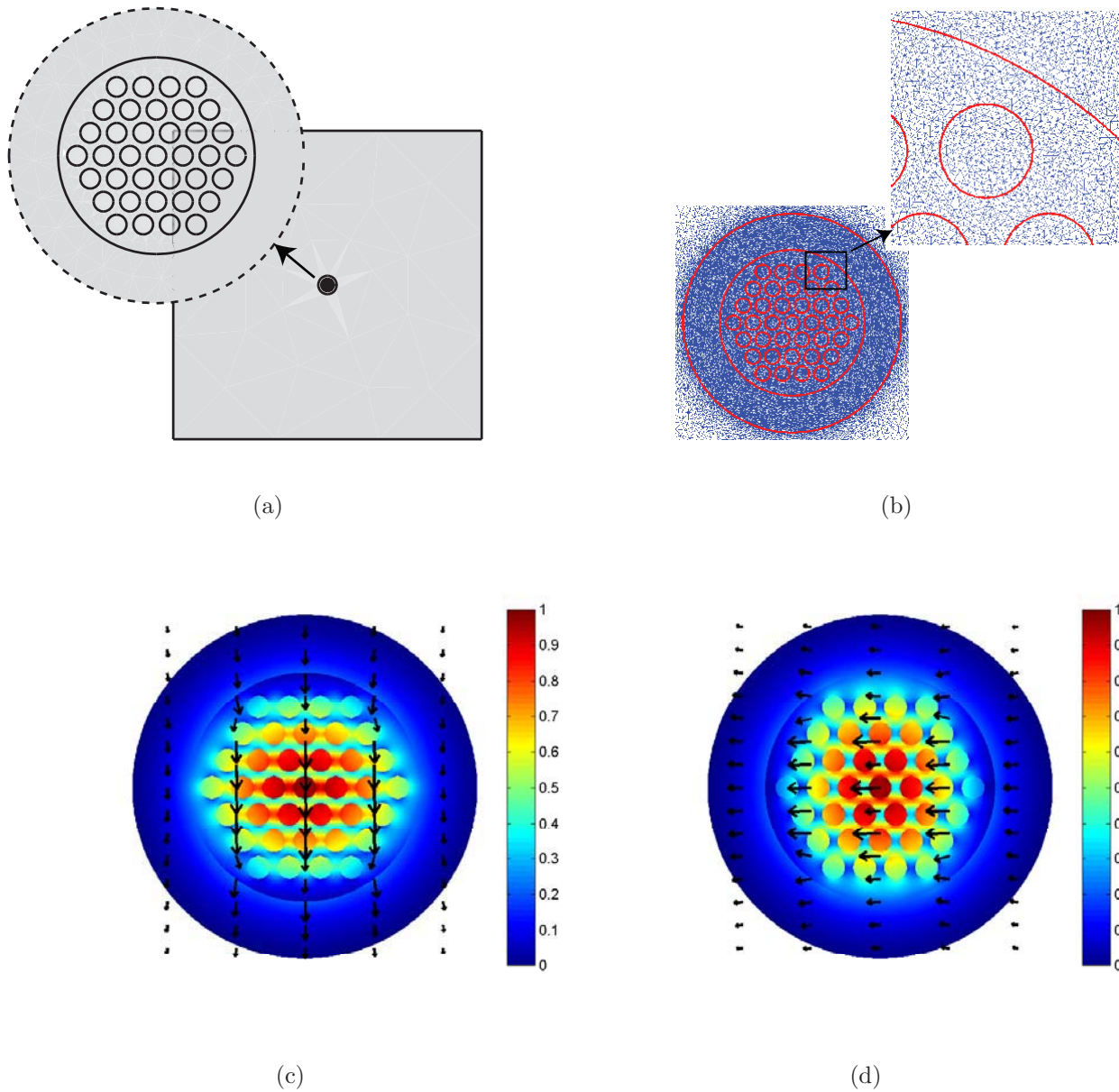


Figure 4.3. Numerical simulation steps of the full geometry of a PMMA porous fibre. (a) Solution region/domain, (b) discretisation of the solution region, (c) and (d) the normalised z -component of the Poynting vector for both polarisations, of the fundamental mode of a polymer porous fibre with core radius of $200 \mu\text{m}$, hole radii of $20 \mu\text{m}$ and 37% porosity at $f = 0.5 \text{ THz}$ ($\lambda = 600 \mu\text{m}$). Note that S_z is normalised by its maximum. The outer red circle in part (b) is added intentionally to increase the mesh density in the vicinity of the fibre. The black arrows in parts (c) and (d) represent the transverse electric field vector.

Generally, an electromagnetic problem may have three types of planar symmetry (Milligan 2005, Golestanirad *et al.* 2009): geometric, electric and magnetic. The type of symmetry depends on the geometric properties of the structure and the excitation sources. In the case of just geometrical symmetry, where the excitation sources and consequently the field distributions are not symmetrical, no simplification can be applied. In the case of electric symmetry, not only does the geometric symmetry hold but also additional requirements are met by the sources so that the tangential component of electric field and the normal component of magnetic field disappear at the symmetry plane, allowing us to replace it by a PEC plane. In a similar way, in the case of magnetic symmetry the source distribution assures that the tangential component of magnetic field and the normal component of electric field vanish on the symmetry plane and so allow replacing it with a PMC plane. Figures 4.4(a) and 4.4(b) show the electric and magnetic field distribution for one of the polarisations of the fundamental mode of a porous fibre shown in Fig. 4.2(a). The PEC and PMC planes are indicated with red and blue lines, respectively. Where the PEC plane is placed, there are no tangential components of electric field and normal components of magnetic field. In a similar way, where the PMC plane is placed, there are neither normal components of electric field nor tangential components of magnetic field.

Figure 4.5(a) shows the quarter-plane of the solution region with appropriate boundary conditions we employ for simulation of the porous fibre. Employing a quarter of the solution region enables us to expand the solution region and increase the mesh density further if requires as shown in Fig. 4.5(b). High mesh densities (e.g. 179816 elements for a 600 μm diameter porous fibre with 65% porosity) are essential for analysing porous fibres with high porosity. Figs. 4.5(c) and 4.5(d) illustrate the normalised power distributions of the two polarisations of the fundamental mode calculated via simulating quarter of the fibre. The transverse electric field vector is shown by black arrows on each figure. These results are identical to the ones shown in Figs. 4.3(c) and 4.3(d). The calculated effective refractive index for both full and a quarter plane is 1.108. As mentioned earlier, both polarisations of the fundamental mode are compiled in one go when the full structure is employed. While, for quarter of the structure it requires us to compile the code twice, since the direction of the electric and magnetic fields are different for each polarisation consequently requiring different boundary conditions.

We have also conducted a convergence test to find out the optimal parameters for the above simulation. The most important parameter is the length of the solution region. Figure 4.6(a) shows the effect of a solution region length change on the effective refractive

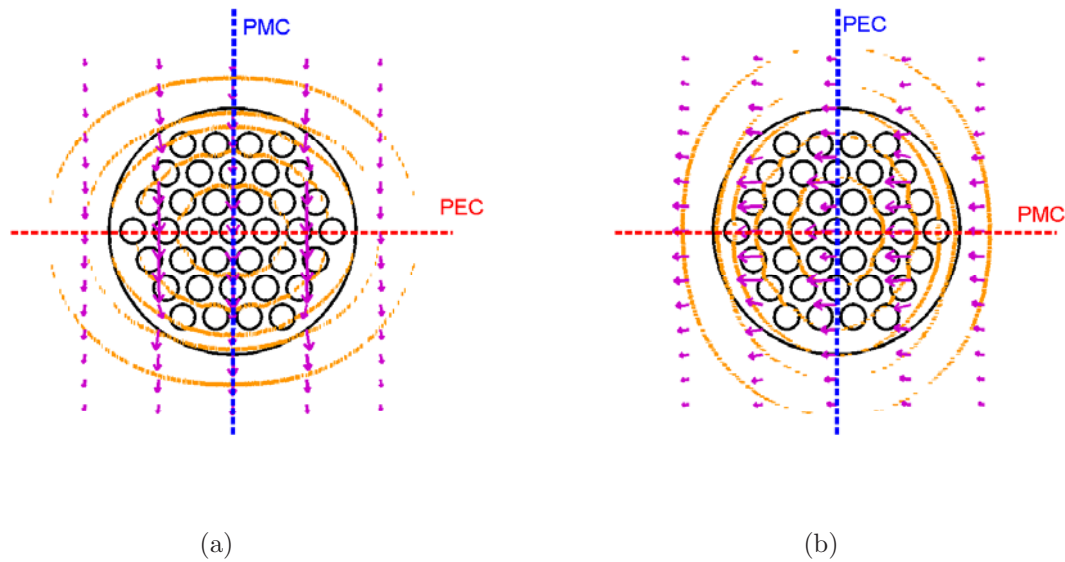


Figure 4.4. Electric and magnetic field distributions of the fundamental mode. The electric field arrows (purple) and magnetic field contours (orange) for the two polarisations of the fundamental mode of a polymer porous fibre with core radius of $d_{\text{core}}/2 = 200 \mu\text{m}$, hole radii of $d_{\text{hole}}/2 = 20 \mu\text{m}$ and 37% porosity at $f = 0.5 \text{ THz}$ ($\lambda = 600 \mu\text{m}$) are shown in parts (a) and (b). The blue and red dashed lines represent the perfect electric conductor (PEC) and perfect magnetic conductor (PMC) planes.

index of porous fibre, shown in Fig. 4.5(a). The length changes from two times to more than 12 times of the fibre radius. At $f = 0.5 \text{ THz}$ ($\lambda = 600 \mu\text{m}$) the curve converges for values greater than $600 \mu\text{m}$. The value is dependent on the operating frequency, and fibre dimension and porosity; e.g. for low frequencies ($f < 0.2 \text{ THz}$) and porosity values greater than 60%, the n_{eff} starts converging around 1.4 mm for a PMMA fibre. The solution region length depends inversely on frequency, i.e. for higher frequencies the length is shorter compared to that of lower frequencies. Therefore, for the rest of the simulations in this thesis we set the solution region length to 2 mm, which is larger than the maximum length required for low frequencies ($f < 0.2 \text{ THz}$). Figures 4.6(b), 4.6(c), and 4.6(d) show the effect of the solution region dimension on power fraction, effective loss, and effective area; respectively. Obviously the error propagates through these parameters via n_{eff} . These parameters, for porous fibre, will be discussed in detail in the following sections.

The second important parameter for convergence testing is the mesh density of the solution region, specifically in the core and sub-wavelength sub-regions. In these simulations, meshing plays a major role in the solution process. Setting the mesh value too fine results

in a huge amount of data, consequently requiring large memory and longer simulation time. The mesh density can be fine tuned by specifying the maximum mesh size. This can be carried out locally to make sure that the mesh is finer on certain sub-domains, i.e. core and sub-wavelength air-holes of porous fibre. This setting is important for porous fibres with high porosity values. As a rule of thumb, we make sure that there are at least three nodes in very narrow domains, e.g. the domain in between the air-hole and core of a porous fibre with porosity higher than 60%. This means that for each domain we relatively set the maximum element/mesh size.

Figure 4.7(a) illustrates the effect of maximum finite-element or mesh size on the effective refractive index of the porous fibre shown in Fig. 4.5(a). Changing the maximum element size from 2 to 25 μm in both core and air-holes introduces a relative error of only $1.6 \times 10^{-4}\%$, while it saves 10 minutes in simulation time. Since setting values higher than 10 μm does not affect the calculated results, one can conclude that the maximum element size considered by COMSOL for this simulation is around 10 μm . This maximum element size suffices for this specific porosity. However, in our simulations we consider different maximum element sizes for core and air-hole regions. Note that 0.5 μm and 2 μm are the maximum element sizes considered for the core and air-holes of porous fibre, respectively. The effect of the maximum finite-element or mesh size on power fraction, effective loss, and effective area is shown in Figs. 4.7(b), 4.7(c), and 4.7(d); respectively. The relative error for each case is also shown on the figure.

With the above region parameters—different mesh densities employed in regions and proper solution region length—the calculated propagation constant (i.e. effective refractive index) of the fibre is accurate to five significant figures and all other parameters—power fraction, effective material loss, and effective area—are accurate to three significant figures in this thesis. The convergence parameters are always adjusted to have the mentioned accuracy and always a quarter of the fibre is simulated due to the structure and field symmetries. Throughout this thesis we consider the above parameters for the solution region and maximum mesh size unless stated otherwise.

Another approach for minimizing the computation time is to include a PML (perfectly matched layer) on the boundaries of the simulation region. Since with the chosen parameters we are able to achieve convergence with an acceptable time frame and within the computational power of our computers, we do not exploit the PML.

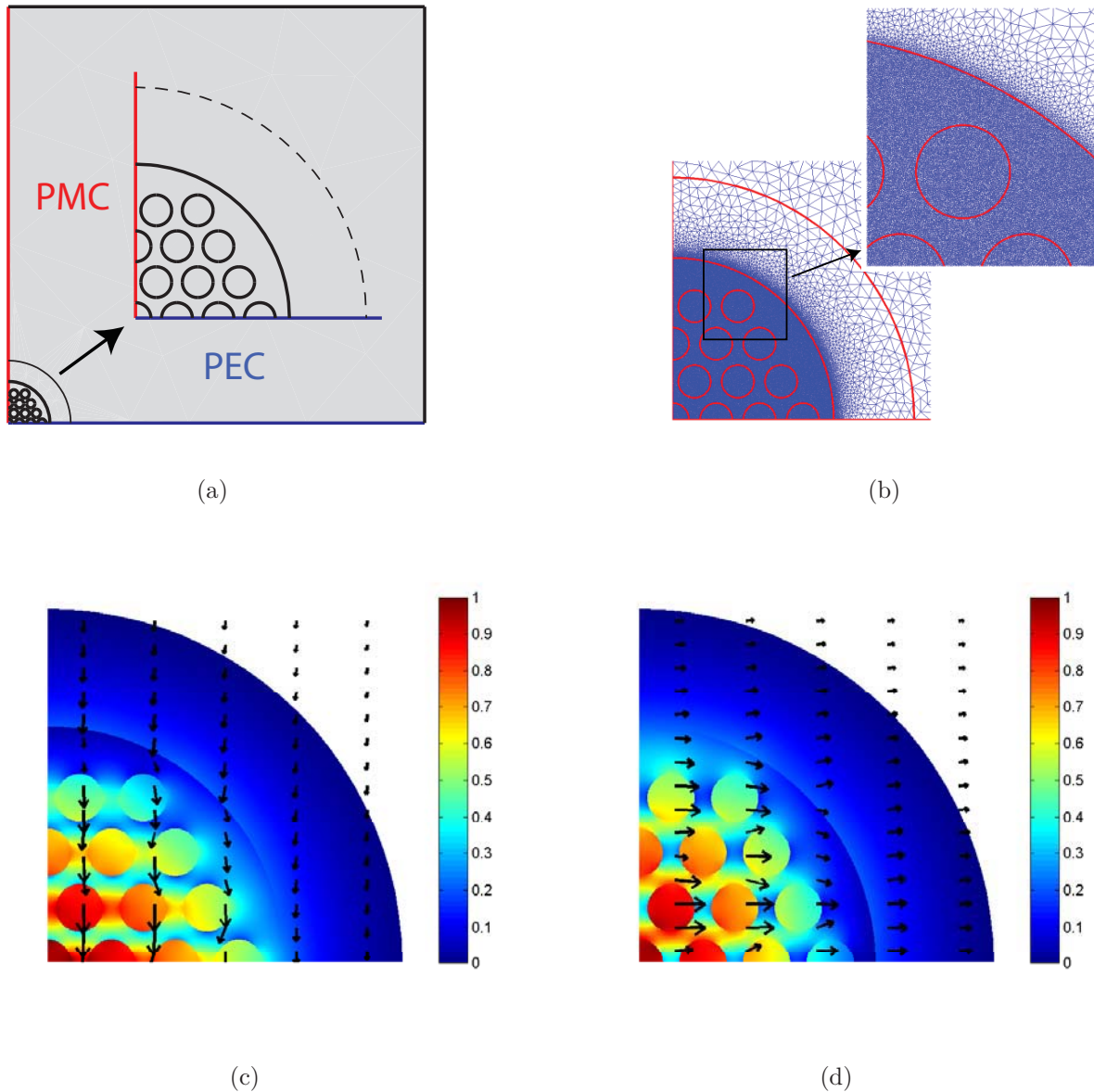


Figure 4.5. Numerical simulation steps of a quarter geometry of a PMMA porous fibre. (a) Solution region/domain, (b) discretisation of the solution region, (c) and (d) the normalised z -component of the Poynting vector for both polarisations, of the fundamental mode of a polymer porous fibre with core radius of $200 \mu\text{m}$, hole radii of $20 \mu\text{m}$ and 37% porosity at $f = 0.5 \text{ THz}$ ($\lambda = 600 \mu\text{m}$). Note that S_z is normalised by its maximum. The dashed curve in part (a) and the outer red curve in part (b) are added intentionally to increase the mesh density in the vicinity of the fibre. The black arrows in parts (c) and (d) represent the transverse electric field vector.

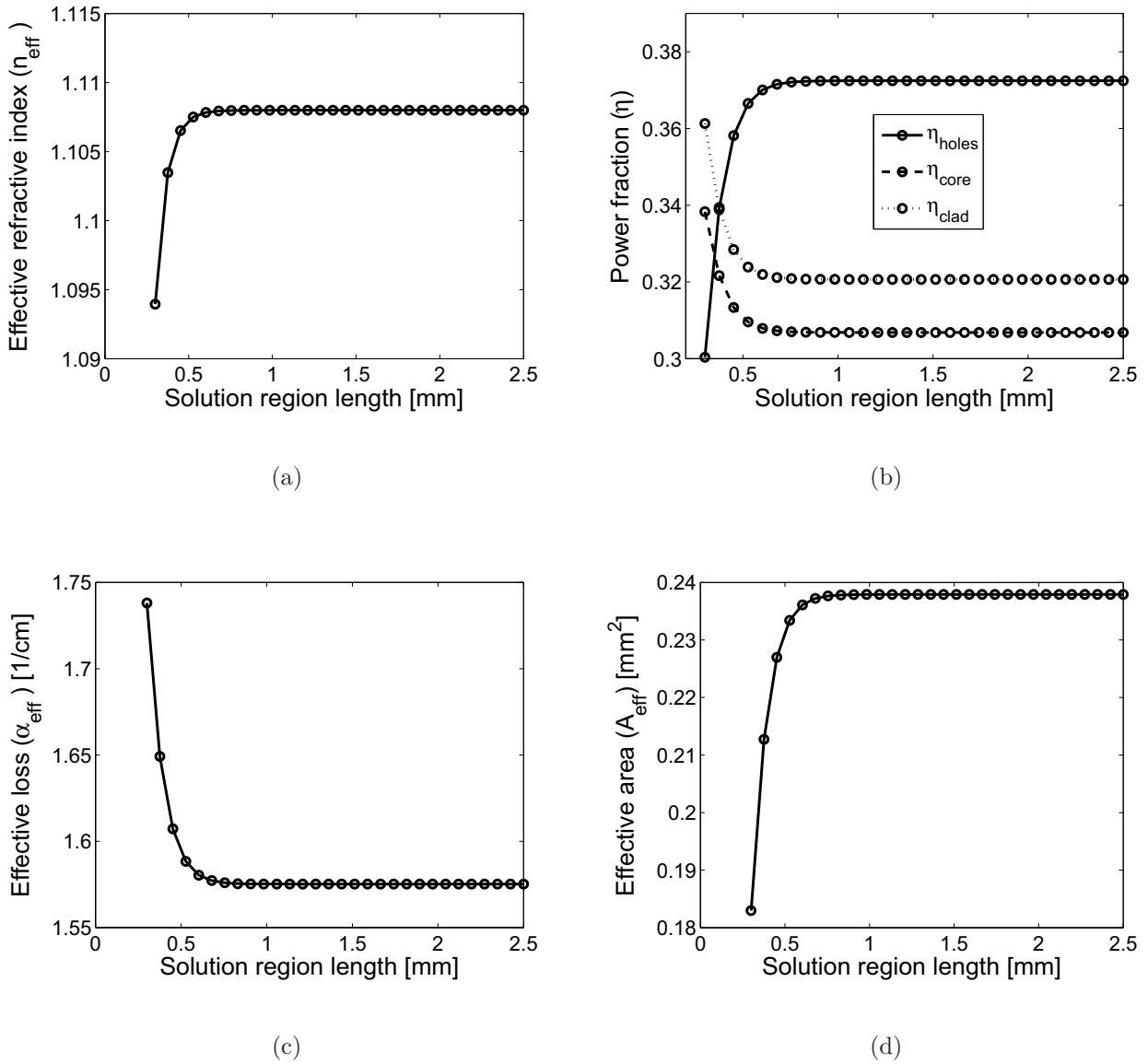


Figure 4.6. Impact of the solution region dimension on the porous fibre parameters. The impact of the solution region dimension on (a) effective refractive index, (b) power fraction, (c) effective material loss, and (d) effective area of the fundamental mode of a PMMA porous fibre is illustrated. The porous fibre geometrical dimensions are: core radius 200 μm , and air-holes radii 20 μm . The simulations are carried out at $f = 0.5$ THz ($\lambda = 600$ μm).

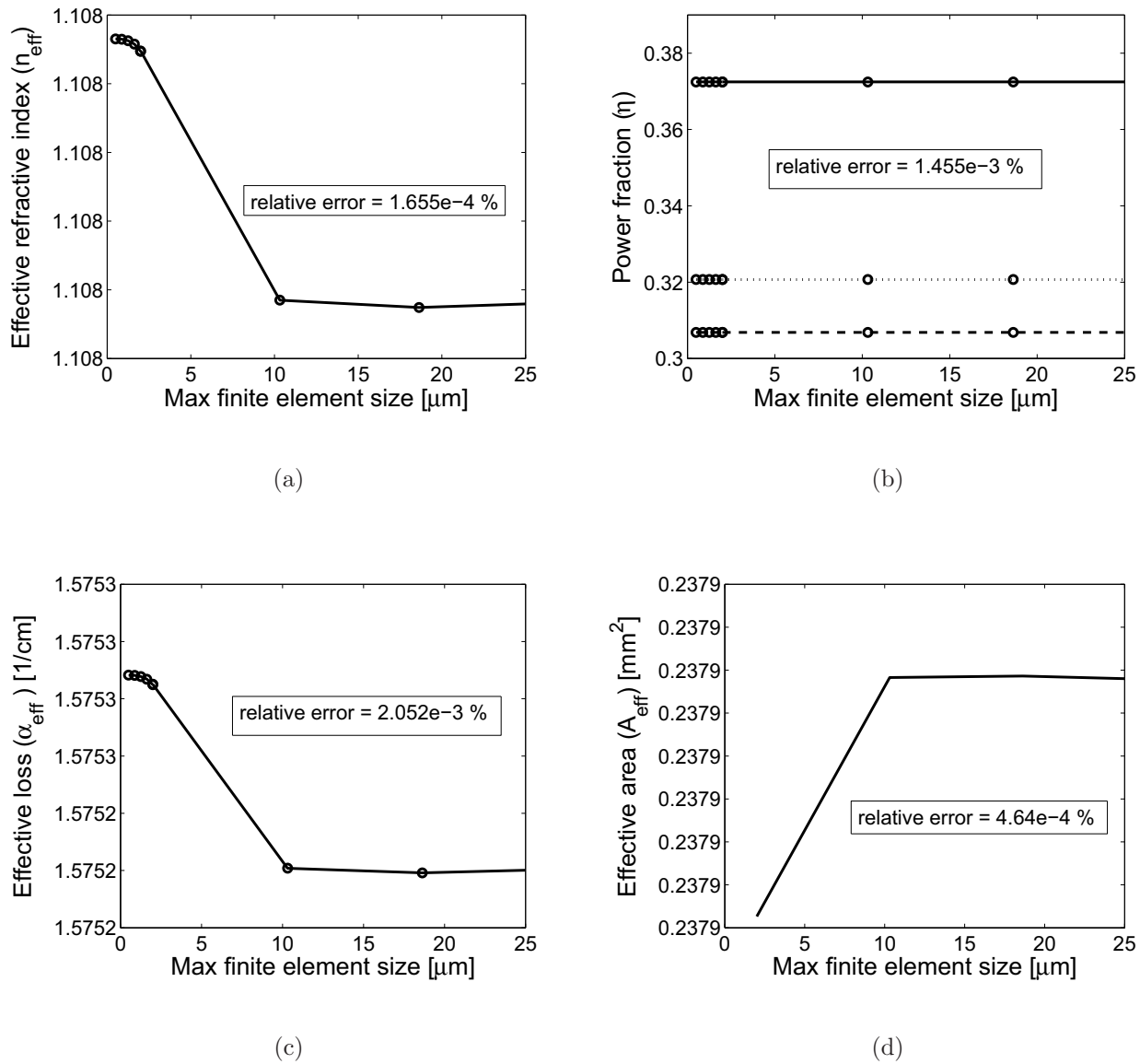


Figure 4.7. Impact of the finite-element dimensions on the porous fibre parameters. The impact of the finite-element dimensions in the core and air-holes on (a) effective refractive index, (b) power fraction, (c) effective material loss, and (d) effective area of the fundamental mode of a PMMA porous fibre, is illustrated. The porous fibre geometrical dimensions are: core radius $200\ \mu\text{m}$, and air-holes radii $20\ \mu\text{m}$. The simulations are carried out at $f = 0.5\ \text{THz}$ ($\lambda = 600\ \mu\text{m}$). The relative error, between the first and last values, is shown on each graph.

4.4 THz characteristics of porous fibre

In this section we investigate THz characteristics of porous fibres. We evaluate power fraction, effective area, effective material loss, fraction of power loss due to bending, and dispersion of the porous fibre with different porosity values. We also compare the results with those of a THz microwire, described in detail in Chapter 3. In the first two Subsections 4.4.1 and 4.4.2, PMMA is used as the host material of the porous fibres, while in the Subsection 4.4.3, COC is used. As we will see in the next two chapters, both PMMA and COC porous fibres are fabricated and characterised accordingly. Therefore, in this section both materials are used for theoretical calculations. Results for two the host materials are plotted separately to avoid cluttering the graphs, for greater clarity.

4.4.1 Power fraction and effective area

In this sub-section power fraction and effective area of three PMMA porous fibres and a microwire is calculated and compared. The porous fibres considered have different porosity values: 61%, 70%, and 74%. All the fibres are characterised at $f = 0.5$ THz ($\lambda = 600 \mu\text{m}$). At this frequency the dielectric parameters of the PMMA are $n = 1.6$ and $\alpha_m = 4.2 \text{ cm}^{-1}$. The propagation constants of porous fibres are evaluated using COMSOL, while the propagation constant of the microwire is evaluated analytically as described in Chapter 3.

The effective refractive indices of three porous fibres—61% (black line), 70% (green line) and 74% (blue line)— and a microwire (red line) as a function of core diameter are shown in Fig. 4.8. In order to maintain the porosity value for each porous fibre while the diameter changes, we keep the ratio of the air-holes to core diameter constant (0.1, 0.8 and 0.05 for 61%, 70% and 74% porosity respectively), i.e. all the dimensions of the fibre are scaled. It should be noted that for every porosity value there is an upper limit for the core diameter, where the effective refractive index curve stops in Fig. 4.8, beyond which the material between the sub-wavelength air-holes begins to act as an array of independent sub-wavelength fibres. The core diameter at which this occurs depends on the porosity of the fibre, i.e. for higher porosity values the limit is larger, indicating that the structure stays in the porous fibre regime for a wider range of diameters. Therefore, no data is shown beyond this limit in this and the following figures.

The effective refractive index of porous fibres are much lowered compared to that of a microwire for the same core diameter. This is expected since less material is residing in the

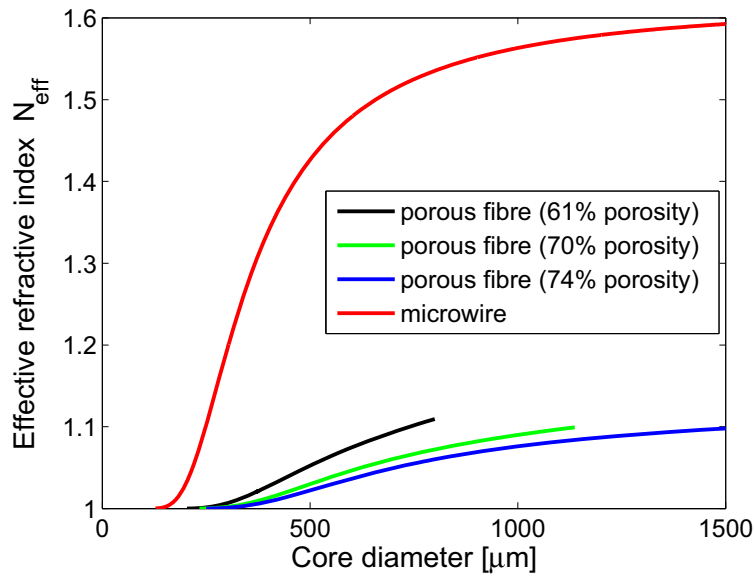


Figure 4.8. Effective refractive index of three porous fibres and a microwire as a function of core diameter. Effective refractive index (n_{eff}) versus fibre diameter of a THz microwire (red lines) and porous fibres of 61% (black lines), 70% (green lines) and 74% (blue lines) porosity at $f = 0.5$ THz ($\lambda = 600 \mu\text{m}$).

core of the porous fibre compared to the microwire for the same core diameter. Increasing the porosity value of the porous fibre lowers the effective refractive index curve further. Nevertheless, a question arises here: “What happens to the mode power distribution and effective area of the fibre?”

As discussed in Subsection 3.4.2, the power fraction leads to more information of the power distribution in the fibre. For convenience we consider three different regions within a porous fibre; sub-wavelength air-holes (region I), solid core material (region II), and the air cladding (region III). Therefore the fraction of the guided mode power (η) that is located within each region is defined as:

$$\eta_x = \frac{P_x}{P_{\text{total}}} = \frac{\int_{A_x} S_z dA}{\int_{A_\infty} S_z dA}, \quad (4.1)$$

where, S_z is the z -component of the Poynting vector, the subscript $x = \{\text{I, II, III}\}$ represents each region, $dA = r dr d\phi$, and A_∞ and A_x are the infinite and region x cross-sections, respectively. For porous fibres analysed with COMSOL, A_∞ is the solution region cross-section. Fig. 4.9 shows the power fraction versus fibre diameter of three porous fibres with fixed porosities—61% (black lines), 70% (green lines) and 74% (blue

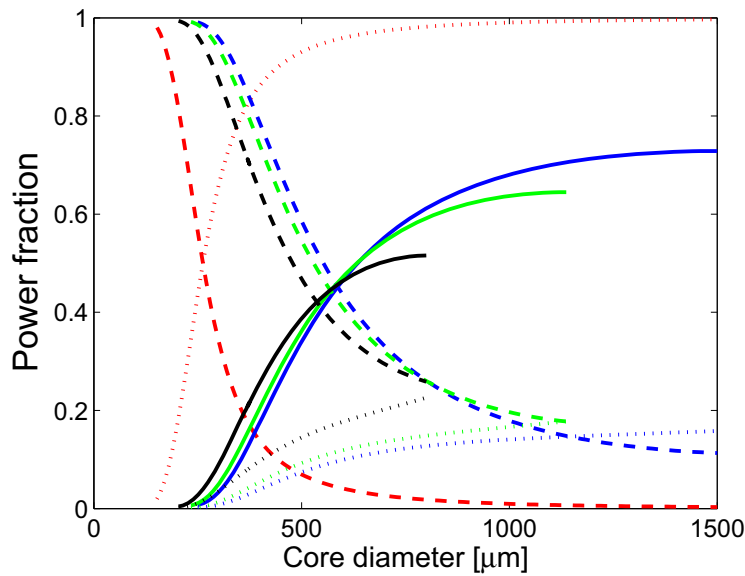


Figure 4.9. Power fraction of three porous fibres and a microwire as a function of core diameter. Power fraction in the air holes (solid lines), core material (dotted lines) and air-clad (dashed lines) versus fibre diameter of a THz microwire (red lines) and porous fibres of 61% (black lines), 70% (green lines) and 74% (blue lines) porosity at $f = 0.5$ THz ($\lambda = 600 \mu\text{m}$).

lines)—at $f = 0.5$ THz ($\lambda = 600 \mu\text{m}$). The solid, dashed and dotted lines demonstrate the power fraction in the regions I, II, and III, respectively. For comparison, the power fraction in the air-clad (dashed line) and solid core (dotted line) of a THz microwire have also been evaluated and sketched in red in Fig. 4.9.

For large fibre diameters ($d_{\text{core}} \geq \lambda$), most of the guided power of the THz microwire is located in the solid core, while the power fraction residing in the sub-wavelength air-hole region (solid black, green, and blue lines in Fig. 4.9) of the porous fibre is dominant. The diameter increase in the porous fibre does not have a significant effect on the power fraction in the core material, η_{II} , (dotted blue, green, and black lines in Fig. 4.9), while there is a considerable change in η_{I} and η_{III} . As an example, for a porous fibre with 74% porosity, η_{II} changes from 0.1% to 16%, while η_{I} changes from 0.1% to 73%, and η_{III} changes from 99.8% to 11%, as the diameter increases from 250-1500 μm . This means that by increasing the fibre diameter most of the power in the air-clad region is transferred to the sub-wavelength air-holes. This is an advantage over the THz microwire, in which increasing the diameter increases the power fraction in the solid-core of the fibre, resulting

into lower material loss in the porous fibre compared to the THz microwire. This is more evident in Fig. 4.11 and is discussed later on.

Unsurprisingly, for sub-wavelength diameters ($d_{\text{core}} \ll \lambda$), porous fibres and THz microwire have a similar behavior, i.e. the power fraction in the core of both waveguides (η_{I} and η_{II} for porous fibres) decreases as the diameter decreases and most of the power is transferred to the air-clad region. However, the influence of the small percentage of the power residing in the sub-wavelength air-holes of the porous fibre (η_{I}), is noticeable in the loss values as will be shown in the next subsection.

The effective areas, (A_{eff}), of the three porous fibres and microwire are shown in Fig. 4.10. The effective area—which is the mode area in the transverse dimensions—is calculated from Eqn. 3.21. The effective area of porous fibres are higher than that of the microwire for the same core diameter. This result is expected due to the lower effective refractive index of these porous fibres compared to microwire as shown in Fig. 4.8. The mode power is expanded more in the air region consequently A_{eff} increases as the refractive index of the fibre decreases. This indicates that if a porous fibre and a microwire with identical core diameters are bent, the porous fibre will experience higher bend losses. However, as we will see in the next sub-section, a porous fibre and microwire with identical diameters do not have the same effective loss values. It is inappropriate to compare these fibre bend losses while their effective losses differ. Therefore, as shown later the effective area curves can be plotted as a function of effective loss to reveal more compatible information for comparison of the fibres.

4.4.2 Loss and confinement

There are two major loss mechanisms to be considered for these fibre structures: effective material loss and bend loss, as discussed in Section 3.5.1. The effective material loss (α_{eff}) is a measure of the loss that a guided mode with a certain mode field distribution experiences when it propagates along a fibre with an inhomogeneous loss coefficient profile in the transverse direction. The effective material loss of a guided mode in porous fibre is evaluated from Eqn. 3.28, which is repeated here for convenience:

$$\alpha_{\text{eff}} = 2k \left(\frac{\epsilon_0}{\mu_0} \right)^{1/2} \frac{\int_0^a \int_0^{2\pi} n^r n^i |E|^2 r dr d\phi}{\left| \int_0^a \int_0^{2\pi} S_{z1} r dr d\phi + \int_a^\infty \int_0^{2\pi} S_{z2} r dr d\phi \right|}. \quad (4.2)$$

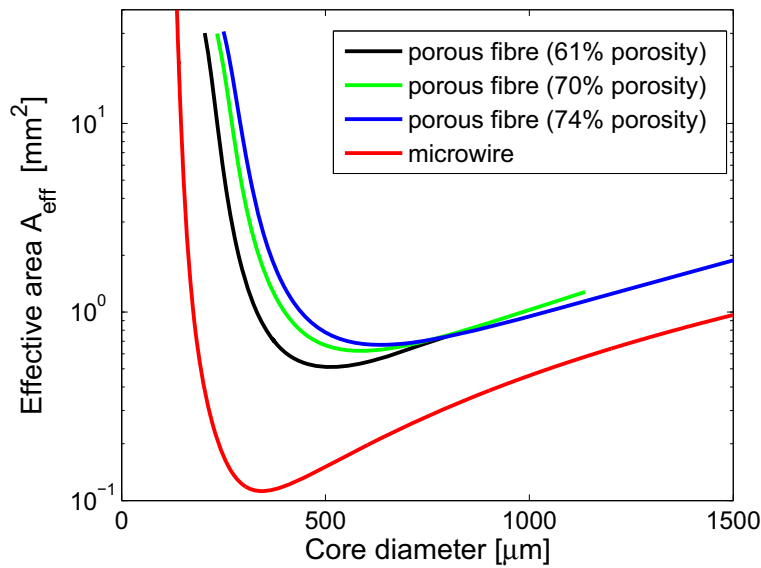


Figure 4.10. Effective area of three porous fibres and a microwire as a function of core diameter. Effective area (A_{eff}) versus fibre diameter of a THz microwire (red lines) and porous fibres of 61% (black lines), 70% (green lines) and 74% (blue lines) porosity at $f = 0.5$ THz ($\lambda = 600 \mu\text{m}$).

Since air is a transparent medium for THz (negligible absorption coefficient $\alpha_m = 0$), the integration in the numerator of the α_{eff} equation is performed only over the material part of the core. Figure 4.11 shows the effective material loss of porous fibres and a THz microwire at $f = 0.5$ THz ($\lambda = 600 \mu\text{m}$). Owing to porosity of the core, it is evident in Fig. 4.11 that for similar diameters the effective material loss of these fibres is less than that of the THz microwire. Moreover for porous fibres the effective material loss decreases as the porosity increases, since less material resides in the core. For sub-wavelength diameters ($d_{\text{core}} \ll \lambda$), the effective material loss declines to the same order for all the structures with different descending slopes. For porous fibres the loss starts declining from a lower loss value over a larger diameter range, indicating that the effective material loss of porous fibre is less sensitive to diameter variation when compared to that of THz microwires. This is more evident in Fig. 4.15 and is discussed later on.

As illustrated in Fig. 4.10 for identical diameter values, the effective area of a microwire is smaller than that of a porous fibre. This is due to the fact that for similar diameters the core refractive index of microwire is higher than that of the porous fibre. On the other hand the effective loss of a microwire is larger than that of a microwire for similar diameter values. In order to have a tangible understanding of these two parameters (α_{eff} and A_{eff}),

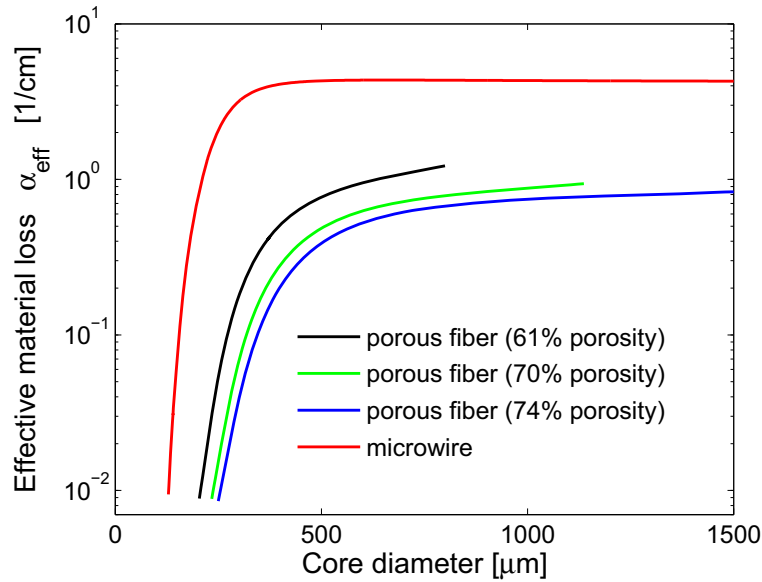


Figure 4.11. Effective material loss of three porous fibres and a microwire as a function of core diameter. Effective material loss versus fibre diameter of a THz microwire (red line) and porous fibres of 61% (black line), 70% (green line) and 74% (blue line) porosity at $f = 0.5$ THz ($\lambda = 600 \mu\text{m}$).

it is worthwhile to study the relationship in between. Figure 4.12 shows normalised effective area of three porous fibres and a microwire as a function of effective material loss. The effective area is normalised to the geometrical area of the fibres, πr_{core}^2 . The normalised effective area decreases as the porosity of porous fibre increases. For similar effective loss values, the microwire has a higher normalised effective area compared to that of the porous fibre. This indicates that the fundamental mode of the porous fibre is more confined to the structure compared to that of a microwire. Consequently we expect the bend loss of the microwire to be higher than that of the porous fibre for identical effective loss values. In order to have a physical understanding of this fact, we evaluate the fraction of the mode power lost as radiation in these fibres due to bending.

Pure bend loss is defined as the continual loss of radiation that occurs along any curved section of fibre and is related to the inability of the tail of the mode to successfully navigate the bend (Baggett *et al.* 2003). For a mode propagating along a curved trajectory, the local velocity along the phase fronts of the mode must decrease on the inside of the bend and increase on the outside of the bend in order to maintain a constant angular velocity across the mode. If we consider the guided mode propagation in the z direction around a bend in the x -plane, as shown in Fig. 4.13, at some distance towards the outer tail of

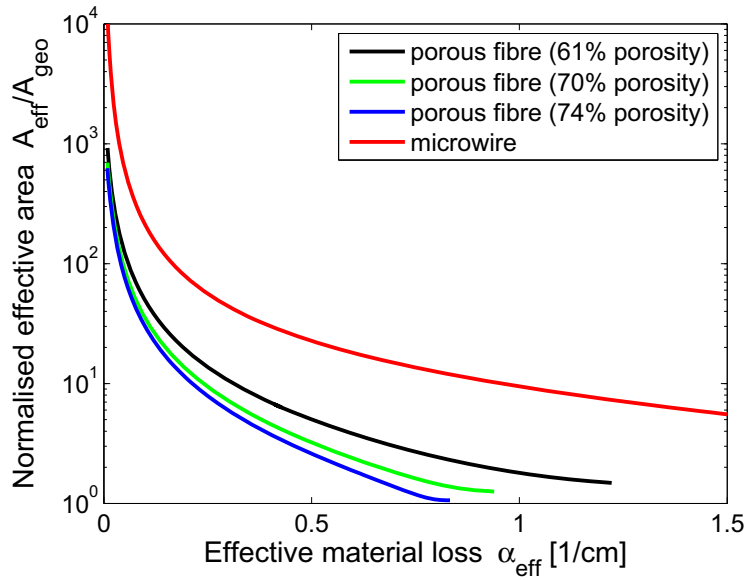


Figure 4.12. Normalised effective area versus effective material loss of three porous fibres and a microwire. Normalised effective area ($A_{\text{eff}}/A_{\text{geo}}$) versus effective material loss (α_{eff}) of a THz microwire (red lines) and porous fibres of 61% (black lines), 70% (green lines) and 74% (blue lines) porosity at $f = 0.5$ THz ($\lambda = 600 \mu\text{m}$).

the mode ($x = x_r$) the required phase velocity will exceed the local speed of light. This distance from the center of the fibre is evaluated for microstructured fibres by Baggett *et al.* (2003) and is equal to:

$$x_r = \left(\frac{\beta_b}{\beta_{\text{FSM}}} - 1 \right) R_o, \quad (4.3)$$

where R_o is the bend radius and β_b and β_{FSM} are the propagation constants of the mode of the bent fibre and the fundamental space-filling mode of the cladding¹⁶, respectively. For the air-clad fibres discussed in this thesis $\beta_{\text{FSM}} = k_0$, where $k_0 = 2\pi/\lambda$. Since the power beyond x_r is lost as radiation, the structure with more power in the tail beyond this point experiences higher bend loss.

Figure 4.14 shows the fraction of power beyond x_r , η_{rad} , for a porous fibre with a 74% porosity (solid lines) and a microwire (dashed lines) as a function of effective material loss for two bend radii, 20 cm and 50 cm. It is evident that if a porous fibre and a microwire

¹⁶The lowest-order cladding mode, which is often referred to as the fundamental space-filling mode for a photonic crystal structure, is evaluated by solving the wave equation for a single unit cell of the photonic crystal.

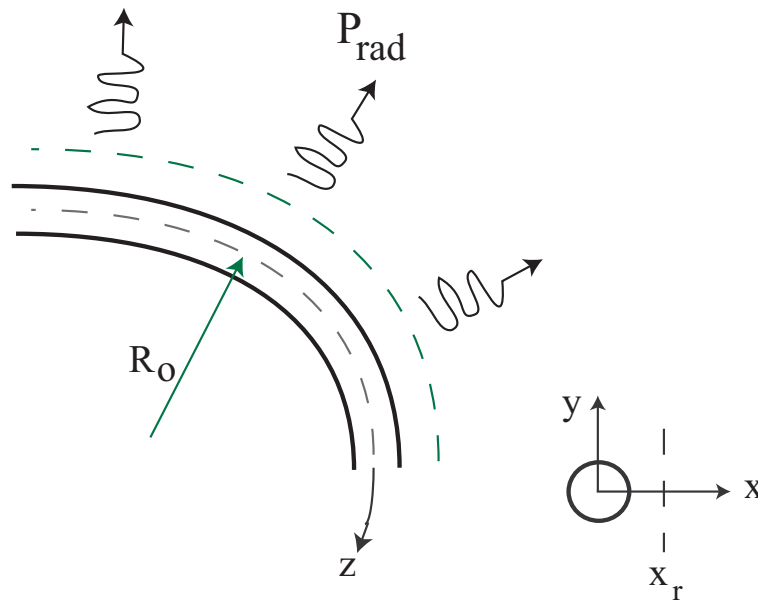


Figure 4.13. Sketch of a bent waveguide. A waveguide bend in the x -plane with a bend radius of R_0 .

with an identical effective loss value experience the same bend radius, the fraction of power lost as radiation for the porous fibre is lower than that of the microwire. This is due to the power fraction in the sub-wavelength air-holes of the porous fibre since the power in these holes is still in the air, but confined to the structure. It should be noted that as soon as x_r gets smaller than the core radius of porous fibre, the power radiated beyond x_r of the porous fibre approaches to that of the microwire. In summary, Fig. 4.14 indicates that for similar effective material loss values the mode is more confined to the porous fibre compared to microwire. The results are consistent with the outcomes of Fig. 4.12.

For the broad THz spectrum, it is also essential to investigate the frequency dependent loss for a porous fibre and microwire. The measured attenuation constant of bulk PMMA material, determined via THz-TDS in Section 3.3, is frequency dependent. Consequently this influences the loss that a propagating mode experiences at different frequencies leading to signal distortion. In order to compare the frequency dependence of the effective material loss of porous fibres and microwires, we evaluate the effective material loss variation versus frequency for a porous fibre with a 74% porosity and a THz microwire.

As shown in Fig. 4.15, a porous fibre of diameter $500 \mu\text{m}$ (black solid line) and microwire of diameter $320 \mu\text{m}$ (black dashed line) have the same order of effective material loss at $f = 0.2 \text{ THz}$ ($\alpha_{\text{eff}} < 0.01 \text{ cm}^{-1}$) and by increasing the frequency the loss in both of

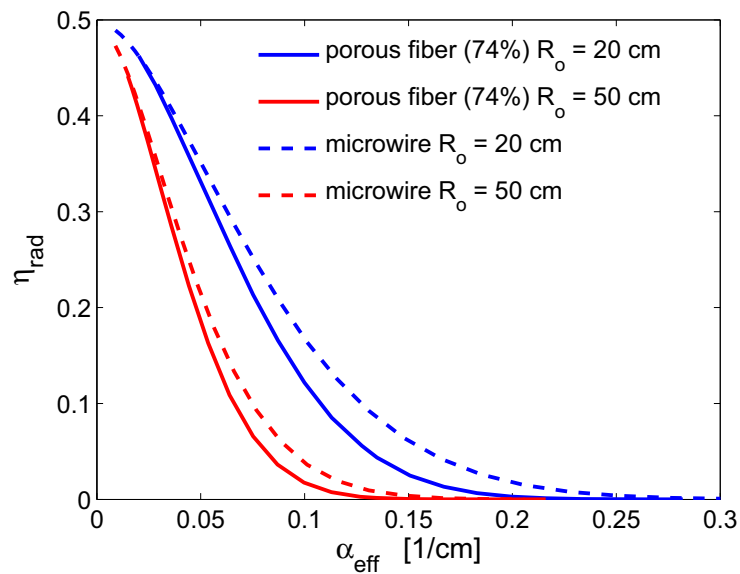


Figure 4.14. Fraction of power radiated for a porous fibre and microwire as a function of effective material loss for two different bend radii. Fraction of power beyond x_T lost as radiation in bends, η_{rad} , versus effective material loss of a THz microwire (dashed lines) and porous fibres of 74% porosity (solid lines) for two bend radii (20 cm and 50 cm) at $f = 0.5$ THz ($\lambda = 600 \mu\text{m}$).

them increases. However, the increase in α_{eff} of the porous fibre is less pronounced when compared to that of the microwire. For frequencies larger than 0.4 THz the effective material loss of the porous fibre is an order of magnitude lower than that of the microwire. This implies that the porous fibre causes less signal distortion of broad-spectrum pulses when compared to that of the THz microwire.

Additionally, Fig. 4.15 indicates that the porous fibre is less sensitive to diameter changes compared to the microwire. Increasing the core diameter by 20% (resulting in the red curves) changes the lower loss limit of the porous fibre to almost half an order of magnitude and the microwire to almost an order of magnitude. This is due to the fact that in porous fibres there is less material residing in the core compared to microwires. As the frequency increases, the curves for each waveguide merge. This occurs at 0.45 THz for the microwire and 0.7 THz for the porous fibre. Beyond this point, where most of the propagating mode is in the core of the waveguides, the diameter variation does not have significant effect on the effective loss. In summary, the diameter variations in the low frequency regime, where most of the power of the propagating mode is in the air-clad of the waveguide, have less influence on the effective loss of a porous fibre compared to a microwire.

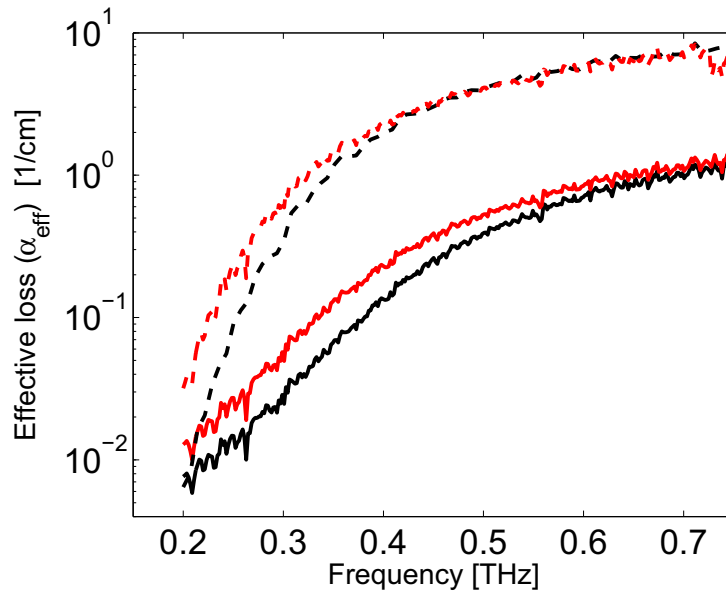


Figure 4.15. Signal degradation due to the frequency dependence of the host material loss for a porous fibre and microwire. Effective material loss versus frequency of a porous fibre with a 74% porosity (solid lines) with 500 μm (black), and 600 μm (red) diameters and a sub-wavelength fibre (dashed lines) with 320 μm (black), and 380 μm (red) diameters.

4.4.3 Dispersion

In this sub-section, we demonstrate that in addition to low loss and high confinement, porous fibres provide a significant improvement in group velocity dispersion in comparison to THz microwires. We also propose new designs of porous fibres by introducing asymmetrical discontinuities. This leads to porous fibres with a strong birefringence, which results in less distortion due to polarisation mode dispersion. Note that COC is considered as the host material of the waveguides studied in this subsection. With this consideration, both low loss polymer materials (PMMA and COC) used later on in fabrication are characterised theoretically in this section.

As stated in Section 4.3, porous fibres are air-clad fibres and have a pattern of sub-wavelength air-holes within the core. Field enhancement and localisation, occur within these sub-wavelength air-holes. In THz porous fibres, the discontinuities are chosen to be air; because firstly air is transparent at THz frequencies, has negligible loss, and secondly it gives the highest refractive index contrast, resulting in an increased enhancement of the field. In the early days of THz porous fibres, only circular air-holes were considered (Hassani *et al.* 2008a, Hassani *et al.* 2008b, Atakaramians *et al.* 2008e). However,

other geometries can also be introduced into the core of these fibres. As mentioned in Section 4.4.1, the degree of enhancement at the air-hole interface depends on the normal component of the electric field. Thus, in order to have well separated propagation constants for the two polarisations of the fundamental mode, we choose rectangular and slot-shaped sub-wavelength air-holes, where the sides of the rectangles align to the two polarisations. The advantage of introducing these air-hole geometries will be observed when the polarisation mode dispersion is discussed later in this sub-section. Figures 4.16 (a)-(c) show the three cross-sections of porous fibres considered here. The arrangement of the air-holes is chosen so that maximum porosity is achieved for each case. The two-dimensional view of the normalised z -component of the Poynting vector, S_z , at 0.4 THz of these porous fibres are demonstrated in Figs. 4.16 (d)-(f).

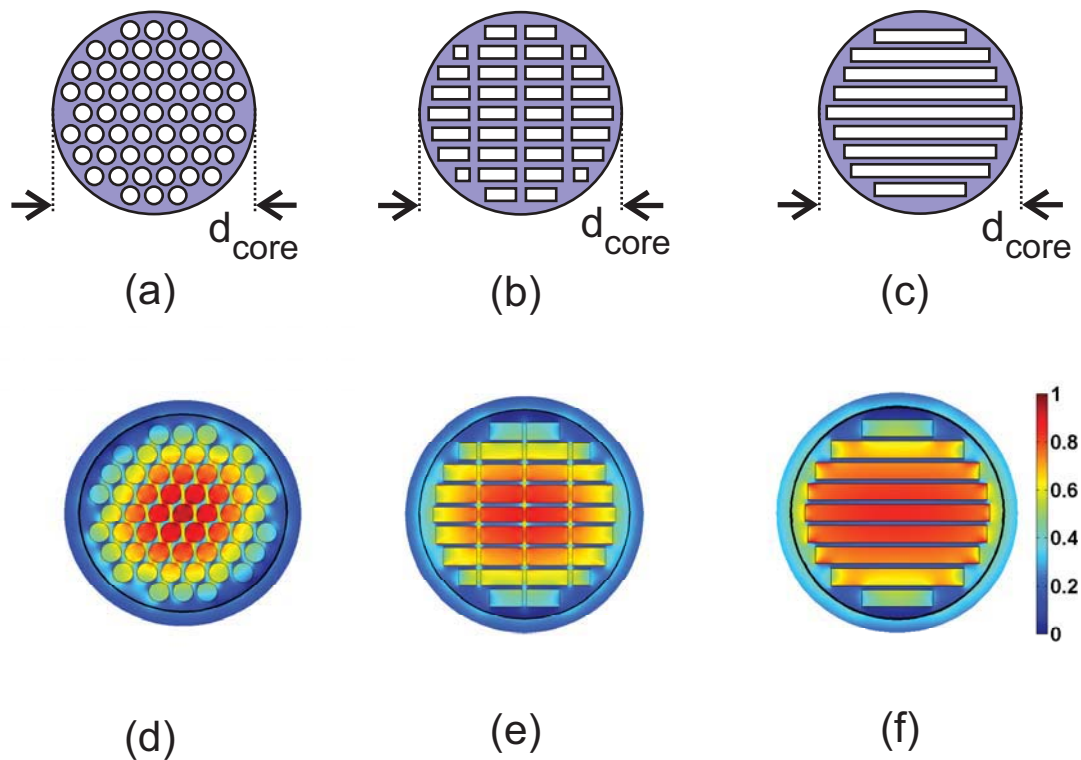


Figure 4.16. Different shapes of sub-wavelength air-holes in porous fibres and their normalised power distribution. Cross-section of porous fibres with (a) circular, (b) rectangular, and (c) slot shaped air-holes. The 2D view of normalised S_z for (d) circular shaped air-holes, 57% porosity and $d_{\text{core}} = 560 \mu\text{m}$, (e) rectangular shaped air-holes, 57% porosity and $d_{\text{core}} = 570 \mu\text{m}$, and (f) slot shaped air-holes, 61% porosity and $d_{\text{core}} = 600 \mu\text{m}$, at 0.4 THz ($\lambda = 750 \mu\text{m}$).

Prior to analysing the dispersion, we evaluate the effective material loss of these fibres and a microwire. This provides a tangible understanding of the effect of the fibre material,

COC, on the loss. Figure 4.17 compares the calculated effective material loss of the new designed porous fibres with rectangular and slot shaped air-holes to the porous fibres with circular shaped air-holes and a microwire. The THz dielectric properties of COC measured by THz TDS, Section 3.3, is used to calculate the porous fibre effective material loss. Note that in Fig. 4.17 the curves stop where the single mode operation ceases. As stated earlier, beyond this point the fibres either become multi-mode, or for the case of the porous fibres, the material begins to act as an array of independent sub-wavelength fibres. It should be noted that the bump in the effective loss spectra around 0.5 THz is from the spectral feature of COC bulk material.

The geometrical parameters of the fibres considered in this sub-section are as follows: a porous fibre with rectangular shaped air-holes, 57% porosity and $d_{\text{core}} = 570 \mu\text{m}$, a porous fibre with slot shaped air-holes, 61% porosity and $d_{\text{core}} = 600 \mu\text{m}$, a microwire with $d_{\text{core}} = 375 \mu\text{m}$, two porous fibres with circular shaped air-holes, 57% and 74% porosities and $d_{\text{core}} = 560 \mu\text{m}$ and $d_{\text{core}} = 760 \mu\text{m}$, respectively. The dimension of the fibres are chosen in a way that they have the same amount of loss at 0.2 THz, 0.007 cm^{-1} . Due to geometry, electric and magnetic symmetries of these structures only a quarter of geometry with proper boundary conditions (PEC and PMC) are simulated for all three structures.

The effective loss curves, illustrated in Fig. 4.17, indicate that porous fibres with different shaped air-holes but similar porosity values, 57%, have comparable loss values. This is expected as the effective material loss curve in porous fibre depends on the porosity and not the air-hole shapes. Also as shown in Fig. 4.17, the single mode operating bandwidth is lower for the porous fibres with rectangular and slot shaped air-holes.

Waveguide dispersion

Dispersion is one of the signal degradation mechanisms in broadband applications as indicated in Section 3.5. This occurs when the propagation constant of the guided modes varies with frequency. The frequency dependency of the propagation constant arises from refractive index variation of the host material (material dispersion) or/and waveguide structure (waveguide dispersion) with frequency. The material dispersion of both polymers discussed in this thesis is almost zero, shown in Fig. 3.21. This implies that the group velocity of these polymers is a constant function of frequency. The normalised group velocity of COC, bulk material, is shown in Fig. 4.18.

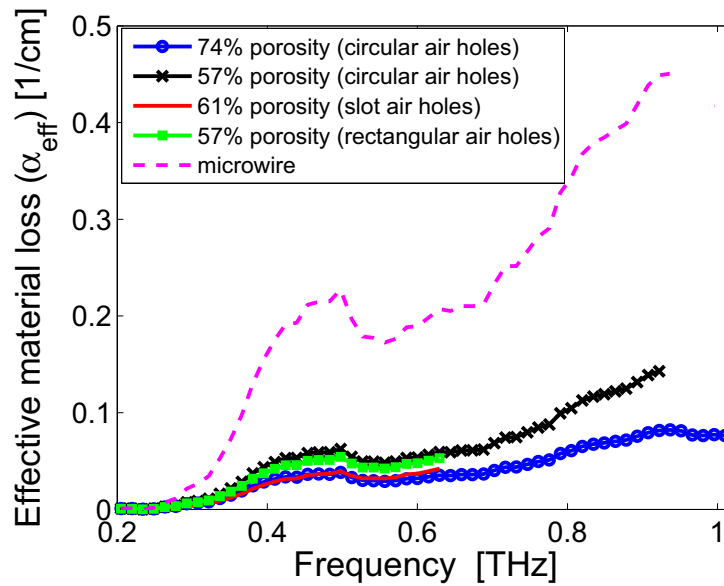


Figure 4.17. Effective material loss of porous fibres with symmetrical and asymmetrical shaped sub-wavelength air-holes. Effective material loss, α_{eff} , versus frequency of porous fibres with circular shaped air-holes and 74% porosity, and 57% porosity, porous fibres with rectangular and slot shaped air-holes and 57% porosity, and 61% porosity, respectively; and a microwire.

Although the material dispersion is almost zero, the waveguide dispersion of a microwire is not negligible as discussed in Subsection 3.5.2. Thus, it is presumed that porous fibres should also suffer from waveguide dispersion. Nevertheless, the question that arises here is: “Does the inclusion of sub-wavelength air-holes improve, i.e. reduce, the waveguide dispersion?”

In order to answer this question, the group velocity, $\nu_g = \partial\omega/\partial\beta_{\text{eff}}$, is calculated and compared for the porous fibres and a microwire. Figure 4.18 shows the group velocity normalised to the speed of light in free space as a function of frequency. For lower frequencies, where the dimension of the fibres is less than the operating wavelength and almost all the power is in the air, the group velocity of the propagating mode in all the structures approaches the velocity of light in free space. By increasing the frequency, the group velocity drops to that of the bulk COC for microwire with a turning point around 0.6 THz—corresponding to zero dispersion. While, the normalised group velocity curves drop very slowly and without a turning point to 0.9 and 0.83 for porous fibres with circular shaped air-holes and 71% and 56% porosity, respectively; and to 0.87 and 0.85 for porous fibres with slot and rectangular shaped air-holes and 61% and 56% porosity, respectively.

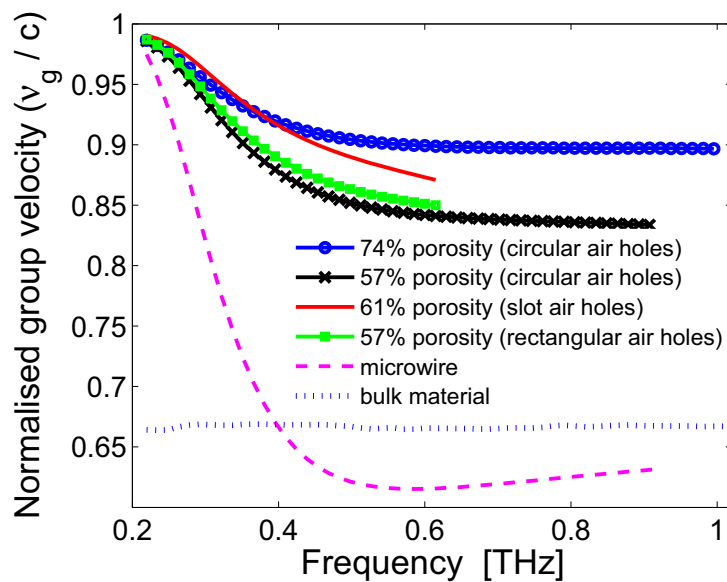


Figure 4.18. Normalised group velocity of four porous fibres (symmetrical and asymmetrical sub-wavelength air-holes) and a microwire. Normalised group velocity, waveguide dispersion, versus frequency of porous fibres with circular shaped air-holes and 74% porosity and 57% porosity, porous fibres with rectangular and slot shaped air-holes and 57% porosity and 61% porosity, respectively; and a microwire.

The group velocity of porous fibres, with circular shaped air-holes, plateaus after 0.5 THz indicating that all the frequency components propagate with constant ν_g , i.e. that dispersion is negligible. This is consistent with the n_{eff} variation with frequency, i.e. the n_{eff} curves reach a plateau at higher frequencies. Thus, a terahertz pulse propagating along a porous fibre encounters small normal dispersion at lower frequencies, corresponding to a positive chirp in the time domain, and zero dispersion at higher frequencies. In the case of microwires, Fig. 4.18, the THz pulse encounters strong normal and anomalous dispersion corresponding to a positive and a negative chirp in the time domain, respectively. Moreover, Fig. 4.18 indicates that group velocity (ν_g) can be controlled by choosing different porosities.

Polarisation mode dispersion

This dispersion is associated with birefringence in the fibre and occurs because of different group delays between the two polarisations of the fundamental mode. A solution to this problem is the use of polarisation maintaining (PM) fibres, which introduce deliberate modal birefringence into the fibre. Introducing deliberate asymmetry in the core/clad geometry of the fibre is a way of achieving the modal birefringence (Suzuki *et al.* 2001).

Maintaining the polarisation of the propagating field in THz waveguides makes these fibres a good substitute for free space THz propagation, where the polarisation of the field is preserved. These fibres have also potential applications in high-bit-rate communication systems, THz wave plates, and frequency filters (Scheller *et al.* 2010). Preservation of polarisation also opens up the possibility of allowing heterodyne detection (Karpowicz *et al.* 2008).

Figure 4.19 shows the modal birefringence, $|n_x - n_y|$ as a function of frequency of the porous fibres and microwire. As expected, for symmetrical fibres—i.e. the porous fibre with circular air-holes and microwire—the birefringence is zero as shown in Fig. 4.19. In contrast for porous fibres with slot and rectangular shaped air-holes, asymmetrical discontinuities in the x and y direction, there is a noticeable birefringence for the fundamental mode. The value of birefringence depends on the shape and arrangement of the holes; the porous fibres with slot and rectangular shaped air-holes proposed in here provides a birefringence of 0.026 and 0.015, respectively at 0.6 THz. These values are comparable to achieved high birefringences ≈ 0.021 at 0.3 THz (Cho *et al.* 2008) in THz solid-core microstructured fibres, and ≈ 0.025 at 1550 nm (Chen *et al.* 2004) in photonic crystals fibres, and are almost an order of magnitude higher than the birefringence achieved of ≈ 0.001 at 1 THz (Ren *et al.* 2008) in THz air-core microstructured Bragg fibres.

These high birefringence porous structures have lower single mode operating bandwidth relative to porous fibres with circular shaped air-holes, because there is a considerable amount of material between the air-holes and the edge of the core. It is also worth highlighting that for porous fibres, with circular shaped air-holes, the calculated birefringence is of the order of 10^{-5} , i.e. nearly zero. This nonphysical residual birefringence provides a guide to accuracy of the calculation that is discussed in detail in Section 4.3.

4.5 Chapter Summary

In this chapter, we have proposed a new fibre structure for the THz regime, a porous core fibre, based on a sub-wavelength low index discontinuity at the material-air interface. To begin with, we have considered a triangular pattern of circular holes within the core of the an air-clad fibre to explain the physics. We have shown that this leads to an improved confinement of the field to the structure while still allowing THz propagation in the sub-wavelength holes. We have investigated the loss (effective material loss) and the confinement of THz propagation as a function of fibre porosity and diameter and

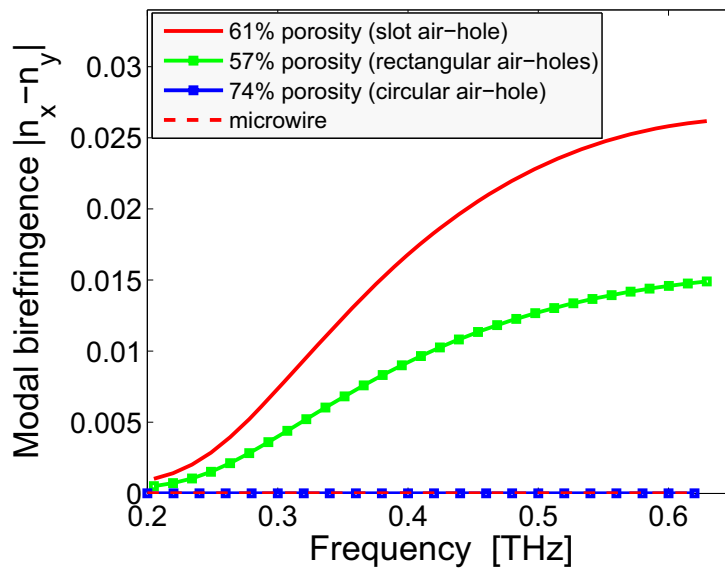


Figure 4.19. Modal birefringence of four porous fibres (symmetrical and asymmetrical sub-wavelength air-holes) and a microwire. Modal birefringence versus frequency of porous fibre with circular shaped air-holes and 74% porosity, porous fibres with rectangular and slot shaped air-holes with 57% porosity and 61% porosity, respectively; and a microwire.

compared them with those of a THz microwire. For similar loss values, it has been shown that the porous fibre leads to significantly better confinement than a microwire. It has also been shown that the loss of a porous fibre is a much flatter function of frequency and less sensitive to diameter variations. Thus, for applications with broadband pulses, porous fibre has reduced loss distortion compared to the THz microwire. As a result of strong localised field in the sub-wavelength air-holes, the porous fibre has potential application in THz gas and liquid spectroscopy. These results are supported independently (Hassani *et al.* 2008b, Hassani *et al.* 2008a).

We have proposed new designs for THz porous fibres, with asymmetrical discontinuities, for the first time in the literature (Atakaramians *et al.* 2008a). We have shown that the effective material loss and group velocity of porous fibres are independent of the air-hole geometry and a flatter function of frequency compared to microwires. We have also demonstrated that introducing asymmetrical, slot and rectangular shaped, sub-wavelength air-holes in the core of porous fibres leads to a birefringence ≈ 0.026 in the THz regime. Maintaining the polarisation of the propagating field in THz waveguides makes these fibres a good substitute for free space THz propagation, where the polarisation state of the THz field is always preserved.

The following Chapter focuses on the fabrication of polymer porous fibres. Despite all the advantages of porous fibre, the manufacturing process for this fibre is more challenging than the equivalent microwire, especially for higher porosity values. It is worth mentioning that the dimension of the holes (10-30 μm) and the core diameter (300-1000 μm) are larger than those of microstructured optical fibres manufactured for the visible and near infrared spectrum. Recent advances in fabrication of soft glass and polymer microstructured optical fibres with a large air fraction, and holes of 1-2 μm in diameter realised via the extrusion technique (Ebendorff-Heidepriem and Monro 2007, Ebendorff-Heidepriem *et al.* 2008), indicates that the fabrication of the proposed structures is feasible.

Porous fibres: design, fabrication and cleaving

THIS chapter describes the design and fabrication technique for THz polymer porous fibres. For the first time in the literature, highly porous polymer waveguides have been designed and fabricated by exploiting an extrusion technique. Two types of THz polymer porous fibres—spider-web and rectangular porous fibres—with 57% and 65% porosity have been designed and fabricated. Furthermore, three different cleaving techniques, based on the use of a semiconductor dicing saw, focused ion beam milling, and a 193 nm ultraviolet laser, have been exploited to cleave highly porous polymer fibres developed for guiding terahertz radiation. Regardless of the polymer material used for fabricating THz porous fibres, using a UV laser for cleaving and rotating the fibre during the process, provides smooth and reproducible cleaves across the entire fibre cross-section rapidly. Moreover, the cross-sections of the fabricated waveguides based on the structural information obtained from SEM images are modelled and are compared to those of the die exit cross-sections, i.e. designed cross-sections.

5.1 Introduction

In the previous Chapter, we have proposed and realised a novel class of THz waveguides, porous fibres, for guiding THz radiation. Our theoretical comparisons have shown that porous fibres allow low loss propagation and improved confinement of the field compared to microwires. We have also demonstrated that porous fibres have a smaller decrease in the group velocity, i.e. lower dispersion, relative to microwires. Furthermore, we have shown that these waveguides can be designed to maintain polarisation of the field by employing asymmetrical sub-wavelength air-holes. In order to confirm the above advantages experimentally, it requires to fabricate these waveguides. Thus, there arises the following questions:

- Is it possible to fabricate fibres with more than 50% porosity?
- Even if so, is it feasible to introduce asymmetric hole geometry to introduce birefringence?

Fortunately, the techniques used for fabrication of microstructured optical fibres (MOFs) pave the path for the fabrication of THz fibres. The fabrication technique for MOFs has usually two stages. The first stage is the fabrication of fibre preform, which is the scaled-up version of the fibre. In the second stage the fibre preforms are drawn into fibres. There are different techniques available for the fabrication of MOF preforms: stacking of capillary tubes, drilling holes in the bulk material, casting into a microstructured mold, and extrusion (Monro and Ebendorff-Heidepriem 2006). In general all four preform fabrication techniques can be utilised for the fabrication of THz microstructured fibres. As we indicate in Chapter 2, for THz hollow-core and solid-core microstructured fibres (Lu *et al.* 2008c, Han *et al.* 2002, Cho *et al.* 2008) the fibre preform by itself is suitable for THz guidance resulting to elimination of the second stage in fabrication process, i.e. the drawing process. For THz porous fibres with sub-wavelength dimensions and features, the two stage process is inevitable, i.e. the fibre preform needs to be drawn. This makes the porous fibre fabrication process challenging, i.e. preventing hole closure during the drawing process.

Figures 5.1(a)-(c) illustrate the cross-sections of porous fibre preforms fabricated utilizing stacking of capillary tubes, and casting into a mold proposed by Dupuis *et al.* (2009) and Dupuis *et al.* (2010). For the preform fabricated through a stacking technique, Fig. 5.1(a), the capillary tubes with inner and outer diameters of 4.25 and 5 mm are fabricated in-house by rolling a 100 μm PE film around a 5 mm inner diameter metal tube (Dupuis

et al. 2009). The fabricated thin-wall tubes are arranged in a two dimensional triangular lattice and are stacked together with a layer of PE film. Eventually the preform is drawn using self-pressurisation. For this purpose, first one end of the preform is sealed off, e.g. epoxy glue in this case, and then drawn to fibre. Trapping of air within the holes allows the pressure of the holes to build up and prevents the hole closure during the drawing process. There is the possibility of partial hole closure that can be prevented employing active-pressurisation¹⁷. The cross-section of the resultant porous fibre is shown in Fig. 5.1(d). A drawback of this approach is that the hole closure possibility is very high and the maximum achieved porosity so far is 8-18% (Dupuis *et al.* 2009). Moreover this method is only suitable for fabrication of porous fibre with the hexagonal array of circular air-holes.

Another technique employed for fabrication of porous fibres utilises casting of the preform into a structured mold. Two different approaches are considered for this purpose (Dupuis *et al.* 2010). In the first approach a composite preform is built by casting the desired material, in this case polyethylene (PE,) into a mold with polymer rods, in this case PMMA. The composite solid preform is pulled into fibre where the presence of PMMA rods prevents hole closure during the drawing process. Afterwards, the fibre segments are submerged into a solvent for several days to etch away the polymer material (PMMA) residing in holes. The fibres are also left to dry for several days. This technique is dubbed as the *sacrificial polymer technique*, since the PMMA rods are sacrificed to keep the holes open during the drawing process (Dupuis *et al.* 2009). The composite preform and the resultant fibre cross-sections are shown in Figs. 5.1(b) and (e). Although air-holes are preserved in this method, the fabrication process is very lengthy and the choice of material is limited in terms of dissolving solvent and melting temperature differences between the materials. Large melting temperature differences can result in material degradation. Moreover the maximum porosity achieved is 29-45%.

In the second approach, the fibre preform is constructed by casting PE into a glass mold (Dupuis *et al.* 2010). The glass rods are pulled out from the preform and any residual glass is etched away before pulling into fibre. Then the resultant PE preform is drawn down using active-pressurisation. The pressurisation is implemented not only to prevent the hole closure, but also to inflate the holes in order to increase the porosity. The fabricated preform and the resultant fibre cross-sections are shown in Figs. 5.1(c) and (f). A drawback of this approach is that the active-pressurisation severely deforms the fibre

¹⁷The holes are pressurised utilizing a controlled gas source.

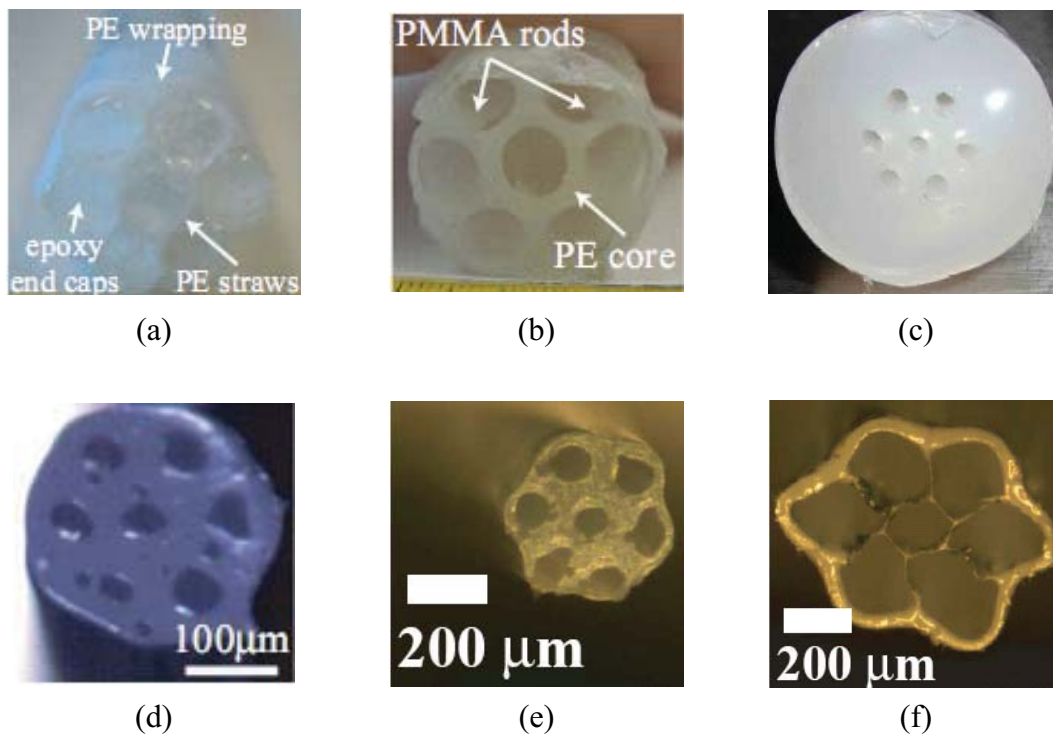


Figure 5.1. Cross-section of porous preforms and fibres fabricated employing stacking and structured molding approach. Cross-sections of porous fibre preforms fabricated based on (a) stacking technique, (b) structured molding based on sacrificial polymer technique, and (c) structured molding technique. Cross-sections of porous fibres pulled from preforms shown (d) in part (a), (e) in part (b), and (f) in part (c). After Dupuis *et al.* (2009) and Dupuis *et al.* (2010).

cross-section, shown in Figs. 5.1(f). It should be noted that high porosity is achieved due to inflation of the holes during the drawing process.

Drilling the hole pattern into a polymer preform (60-70 mm diameter) using a computer controlled mill, and drawing the preform down to fibre (6 mm diameter) is another technique utilised for fabrication of THz solid- and hollow-core microstructured polymer waveguides, Figs. 2.17(b) (Ponseca *et al.* 2008) and 2.22(a) (Nielsen *et al.* 2009). This technique is not suitable for the fabrication of THz porous fibres because the drilling process of the holes in the preform is very time consuming for a large number of holes. This method also has restricted maximum porosity due to the mechanical constraints of the hole size and the wall thickness between the holes (Barton *et al.* 2004). Furthermore the shape of the holes is limited to the circular shape.

Among all these methods, the extrusion technique is best suited for the fabrication of polymer porous fibre preforms. Because, firstly, MOFs made up of soft glass and polymer

with a large air fraction and holes of 1-2 μm in diameter have been successfully fabricated through the extrusion technique (Ebendorff-Heidepriem and Monro 2007), indicating that the fabrication process of THz porous fibre (with hundreds of microns in diameter and features in the tens of microns range) is easier to implement than the optical counterpart. Secondly, it has also been shown that it is possible to fabricate non-circular air-holes in microstructured optical fibres made up of polymer and soft glasses through the extrusion technique (Ebendorff-Heidepriem and Monro 2007, Ebendorff-Heidepriem *et al.* 2008), indicating that the fabrication of the proposed exotic structures are feasible.

Polymers are the common material being used for fabrication of the THz fibres due to their low material loss and dispersion characteristics in the THz regime. Cleaving of polymer MOFs is challenging due to their elasticity (Law *et al.* 2006b). They are easily squashed and deformed during cleaving process when conventional blades are used for this purpose. There are investigations conducted for optical fibres to improve the cleaving of low air-fraction MOFs. Law *et al.* (2006b) have demonstrated that heating up the cleaving blade and the fibre to 70-80°C improves the cleaved end-face of the optical MOFs. Canning *et al.* (2002) have shown that a 193 nm UV laser can be used for rapid cleaving and structuring of optical MOFs.

5.1.1 Objective and framework

In this chapter, in Section 5.2 we elaborate the fabrication process of highly porous THz fibres with symmetrical and asymmetrical sub-wavelength air-holes employing extrusion technique. We explain the fabrication process—including die design, preform, and fibre drawing conditions and procedures—for both polymethyl methacrylate (PMMA) and cyclic olefin copolymer (COC) porous fibres. In Section 5.3, we elucidate and compare different cleaving techniques employed for cleaving of these highly porous fibres. The cleaving parameters are adjusted based on the polymer material used, i.e. PMMA or COC. The final fibre cross-sections are very similar but not identical to the designed cross-sections. Therefore in Section 5.4, the theoretical values of the effective material loss and effective refractive index of the *ideal* and *real* porous fibres are compared to observe the effect of the structure deformation during the fabrication process.

5.2 Porous fibre fabrication based on extrusion

Here, we propose a novel fabrication method, based on the extrusion technique, for fabricating THz porous fibres. Exploiting this extrusion method, we fabricate preforms and fibres with porosities higher than 50%. These are the first highly porous polymer fibres fabricated for the guidance of THz radiation (Atakaramians *et al.* 2009c). The polymer materials used for the fabrication of porous fibres are polymethyl methacrylate (PMMA) and cyclic olefin copolymer (COC)¹⁸, whose THz dielectric properties are investigated in Chapter 3. The porous fibres are fabricated in a two-step process.

First the preforms with macroscopic scale (mm-scale) features are manufactured using the extrusion technique, which has been demonstrated to be not only viable for soft glasses (Ebendorff-Heidepriem and Monro 2007) but also for polymers (Ebendorff-Heidepriem *et al.* 2007). The preforms are extruded by heating up a bulk polymer/glass billet to a temperature where the material gets soft. Then the soft material is forced through an extrusion die using a ram extruder at a fixed speed. The die exit geometry determines the preform cross-section.

Figure 5.2 shows the images of the steps involved in the extrusion process. The extrusion billet, shown in Fig. 5.2(a), in conjunction with the die is placed inside a thick-walled stainless steel metal body. The billet is shielded from the metal body and ram by a thin-walled stainless steel sleeve, shown in Fig. 5.2(b), and a circular cap, shown in Fig. 5.2(c), respectively. Thus the metal body and ram can be retrieved and used for the next extrusion, which is vital specially when soft glass preforms are extruded. The whole structure is placed in a controlled heating furnace as shown in Fig. 5.2(d) and heated up. The heating process is conducted in three stages to prevent overshooting the melting temperature of the billet, which results in degradation. Then the soft material is pushed through the die in two steps. First, the speed is set higher (almost ten times) than the targeted value to fill the die and then the speed is reduced and kept constant during the extrusion process. The final speed depends on the die design and billet material. It should be noted that the sleeve, circular cap and die are cleaned before extrusion. The cleaning process is conducted in an ultrasonic bath. The extrusion pieces are first cleaned in the de-ionised water and detergent. Then they are rinsed with distilled water and methanol. An example of the extruded polymer preform is shown in Fig. 5.2(e).

¹⁸The COC billet used in this thesis is provided from the Department of Photonics Engineering, Technical University of Denmark.

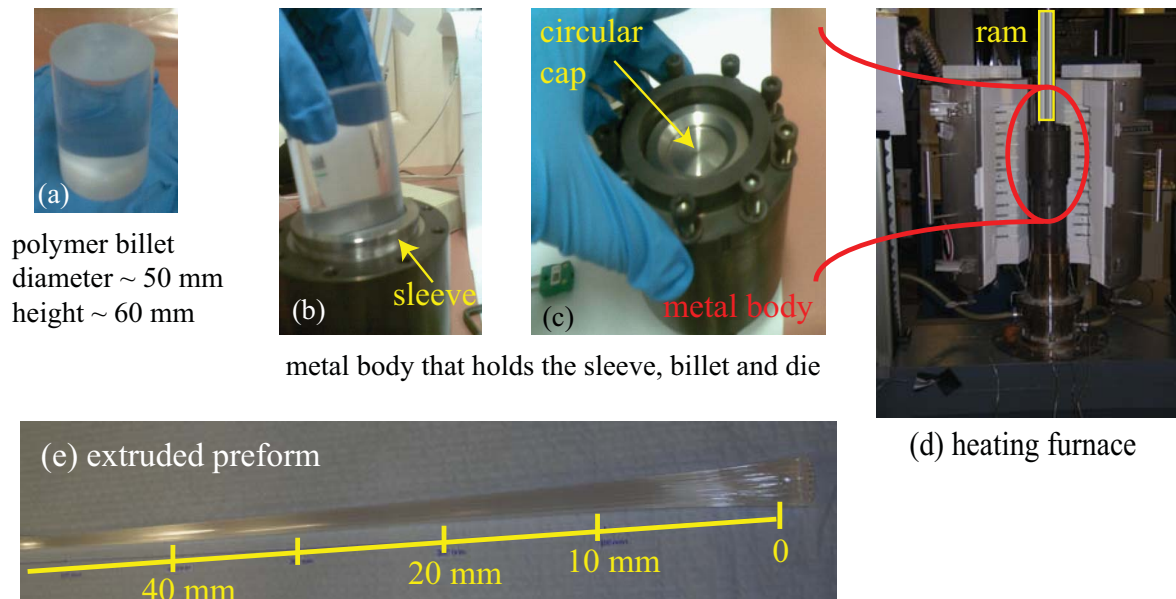


Figure 5.2. Preform extrusion process. (a) An example of a polymer billet. (b) and (c) show the stainless steel metal body which holds the sleeve, die, billet and the cap. (d) Heating furnace and the arrangement of the metal body in it. (e) An example of an extruded polymer preform.

The critical step in the porous fibre fabrication is the translation of the desired fibre structure, shown in Fig. 4.16(a) and (b), to the die exit structure. We develop the porous fibre die designs by combining the die manufacturing constraints and the porous fibre requirements (high porosity and sub-wavelength features) as discussed below. We start the die design with an hexagonal array of circular air-holes, which is one of the most studied and common arrangements of the air-holes in microstructured optical fibres. The cross-section of the die exit with hexagonal array of circular air-holes is shown in Fig. 5.3(a). The porosity achieved is limited to 47% due to extrusion die machining constraints, such as minimum wall thickness of 0.6 mm between the holes. In the fibre, the porosity will be even lower than the value given by the die exit due to thickening of the nodes between the air-holes (Ebendorff-Heidepriem *et al.* 2007).

Recent advances in the fibre preform extrusion and die design of microstructured fibres (Ebendorff-Heidepriem and Monro 2007) have allowed us to fabricate fibres with non-circular and sub-wavelength size air-holes (a few microns to hundreds of nanometre in size). This results in a thinner layer of material between non-circular air-holes in comparison to the circular air-holes, which increases the achievable porosity for the fibres.

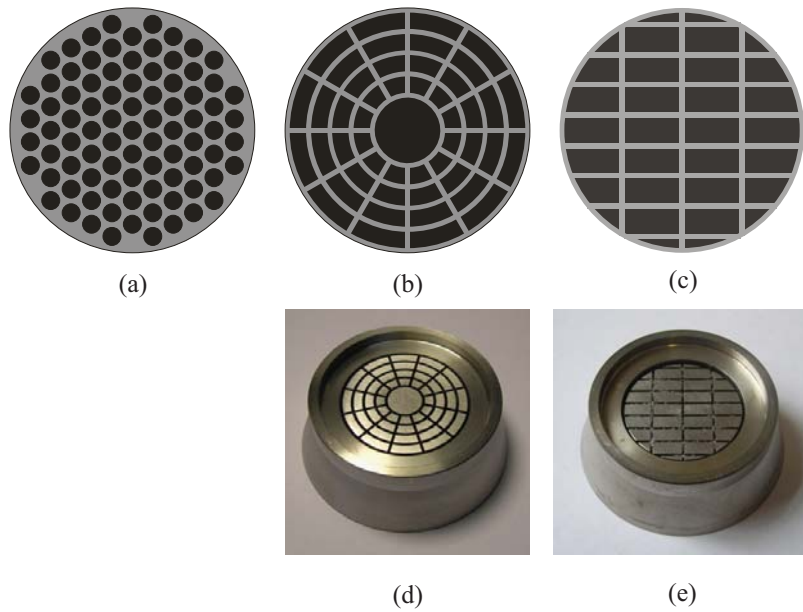


Figure 5.3. Designed die exit cross-sections. Designed die exit of the (a) hexagonal array of circular air-holes (b) spider-web and (c) rectangular porous structures cross-sections. The exit face of stainless steel extrusion dies (d) spider-web and (e) rectangular porous structures.

Thus adapting the new die design technique from optics opens up new opportunities in the design and fabrication of highly porous THz fibres.

We consider a die exit structure, shown in Fig. 5.3(b), for porous fibre with symmetrical sub-wavelength air-holes. Thin layers of material are employed in the design of this structure. This was initially designed for hollow-core Bragg fibre in optics. We use this design for THz porous fibres since it has high porosity and sub-wavelength scale holes. Due to the resemblance of the structure to a spider web, hereafter for simplicity this is called *spider-web design* and the porous fibre with spider-web shaped sub-wavelength air-holes is called a *spider-web porous fibre*. This design of spider-web porous fibre leads to a 67 % porosity. For the porous fibre with asymmetrical sub-wavelength air-holes, shown in Fig. 4.16(b), we design a die exit structure constructed from thin layers (0.6 mm) as shown in Fig. 5.3(c). Hereafter for simplicity, this design is called the *rectangular design* due to the shape of the holes and the porous fibre with rectangular shaped sub-wavelength air-holes is called the *rectangular porous fibre*. This particular design of the rectangular porous fibre leads to a 71 % porosity. We numerically have characterised the die exit designs to confirm the low-loss and low-dispersion guidance before fabricating the die, i.e. before fabrication of the die exit structure we modelled the designed structure to make sure they guide THz radiation and represent the THz guiding properties expected.

The modelling results of the spider-web and rectangular porous fibre die exit are shown in Section 5.4.

After the reassurance of the functionality of the designs, the dies are fabricated from stainless steel. The exit faces of the spider-web and rectangular dies are shown in Figs. 5.3(d) and 5.3(e), respectively. The die exit-face is the negative image of the die design, i.e. the voids in the design are replaced with the solid blocked pins to prevent material flow. The pins are affixed to a plate called the sieve. The plate has small feed holes in between the pins to allow material flow, hence it is called a sieve. The exit-face outer diameter of the dies shown in Fig. 5.3 are ≈ 44 mm.

To fabricate porous polymer preforms employing the designed dies, we first heat up the PMMA and COC billets to around 170-180 °C and 120-130 °C, respectively. Afterwards, the softened billet is pushed initially with 2 mm/min speed to fill the die with polymer and then as the polymer emerges from the die exit, the speed is reduced to 0.02 mm/min and is kept constant for the rest of extrusion process. The preform length depends on the billet size, die design, and degree of the tapering and bending that occurs. From a 50 mm diameter and 60 mm long polymer billet, a 2 m length of a highly porous preform is achieved.

The initial diameter of the preform is equal to the die exit-face (≈ 30 mm) and is buckled as shown in Figs. 5.4(a) and 5.4(b) for spider-web and rectangular porous fibres, respectively. The high speed of the ram at the beginning of the extrusion process introduces kinks in the first part of the polymer preform that emerges from the extrusion chamber. This happens due to the inherent elastic characteristics of polymer (Ebendorff-Heidepriem *et al.* 2007). Thus, the kinks settle down within the first 20–30 mm of the preform as the speed is lowered to the targeted low speed value, after the die is filled with softened polymer, as shown in Figs. 5.4(c) and 5.4(d), for spider-web and rectangular porous fibres.

The fibre preform is not uniform in terms of diameter, i.e. it has a somewhat tapered shape. The tension due to gravity effects on the extruded preform tapers the outer diameter of the preform. This initially undesired effect works out to our favour in this case. Due to the limitation of the die features (minimum 0.6 mm thickness), large diameter values (≈ 30 mm) are considered to achieve high porosity values. However, preforms with such a large diameters cannot be accommodated in the drawing tower. The tapering effect leads to smaller diameters (10–20 mm) throughout the preform. However, if needed an even (non-tapered) cross-section can be obtained if the extruded preform is submerged into a liquid such as water, which reduces the gravity effects.

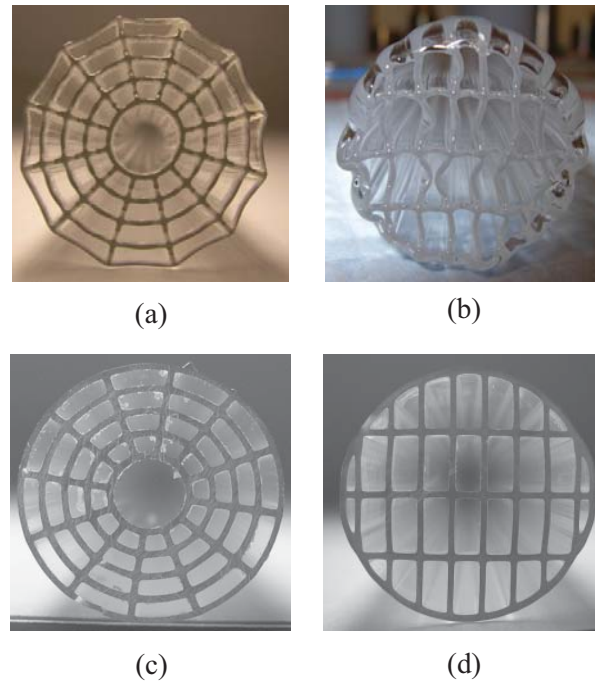


Figure 5.4. Photograph of the cross-sections of the extruded polymer porous preforms. The photograph of the cross-section of PMMA preforms: (a) spider-web and (b) rectangular porous preforms emerging from the die exit, (c) spider-web (12 mm diameter) and (d) rectangular (10 mm diameter) porous structures at the middle of the preform. The buckling in the cross-section of the polymer preforms settle to the design shape within the first 20–30 mm.

In the next step, the extruded preforms are drawn to form porous fibres. First, the fibre preform is cut into an appropriate length (≈ 180 mm) that can be housed in the drawing tower. Next, the voids in the preform are cleaned with a nitrogen gun and then in an ultrasonic bath with de-ionised water and detergent. Afterwards, the preforms are thoroughly rinsed with distilled water and are annealed at 80°C to remove the stress due to extrusion. A preform of 10–15 mm diameter and 180 mm length is drawn down to bands of more than 10 meters of fibres with outer diameters of a few hundreds of microns using a fibre drawing tower, shown in Fig. 5.5(a). For this purpose the fibre preform is suspended vertically and heated to temperatures higher than extrusion temperature. The lower part of the preform drops down due to the gravity after the right temperature is reached. This drop is followed with fibre. The structure of the preform is preserved during the drawing process provided that the temperature and initial pressure in the holes are adjusted correctly. The resultant fibre is wound on a drum. During the drawing

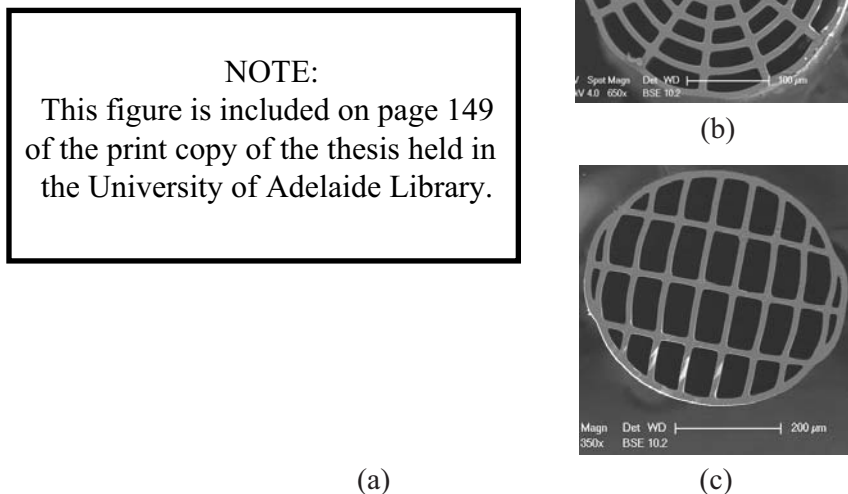


Figure 5.5. Fibre drawing tower and porous fibre cross-sections. (a) The fibre drawing tower in Centre of Expertise in Photonics (CoEP), at the University of Adelaide. The photograph taken by Heike Ebendorff-Heidepriem. scanning electron microscope (SEM) images showing the cross-sections of (b) spider-web and (c) rectangular polymer porous fibres, both cleaved using focused ion beam milling.

process, the diameter of fibre is monitored by two lasers and the temperature is adjusted accordingly to maintain the required diameter.

For the purpose of this work, a spider-web fibre preform of 12 mm diameter and 180 mm length is drawn down to two different outer diameters of 200-250 μm and 300-350 μm , whereas the rectangular fibre preform of 10 mm diameter and 180 mm length is drawn down to three different sets of outer diameters (350-400, 450-500, and 550-600 μm). As an example, the cross-section of the PMMA spider-web and rectangular porous fibres are shown in Figs. 5.5(b) and 5.5(c), respectively. These cross-sections are achieved by utilising focused ion beam milling. As we observe in the next section, cleaving of polymer porous fibres is not straight forward.

The porosity of the spider-web and rectangular porous fibres given by the die designs are 67% and 71%, respectively. Using scanning electron microscope (SEM) images shown in Figs. 5.5(b) and 5.5(c), the porosity of the fabricated fibres is measured to be 57% and 65%, respectively, which is smaller than the porosity given by the die design due to rounding of the corners and thickening of the struts. The effect of rounding of corners

and thickening of the struts on THz dielectric properties of porous fibres are investigated later in Section 5.4.

The advantage of using the extrusion technique for preform fabrication is that the preform structure itself has high porosity since it is the scaled up version of the final fibre structure. However, this is not achievable with the casting method proposed for preform fabrication, shown in Fig. 5.1(c). With such low porosity preforms, active-pressurisation should be employed during the drawing process to achieve a highly porous thin-walled structure. This process leads to deformation of the outer shape of the fibre as shown in Fig. 5.1(f). While for preforms fabricated via extrusion technique, shown in Fig. 5.5, the fibre cross-section is very well preserved and highly reproducible during the drawing process.

As indicated earlier, the cleaving process of such porous fibres is challenging. It is essential to have a reproducible cleaving technique in order to be able firstly to observe fabricated fibre cross-section without deforming during the cleaving process and secondly to conduct fibre loss measurement as we observe later in Chapter 6. Therefore, in the next section we discuss different cleaving methods exploited for cleaving of extremely porous polymer (PMMA and COC) fibres.

5.3 Cleaving of extremely porous polymer fibres

Two types of polymer porous fibres, spider-web and rectangular air-hole porous fibres, have been designed and fabricated in the previous section. The polymer is elastic compared to the glass, therefore unlike glass fibres that are brittle and break easily, polymer fibres are first deformed. Use of conventional cleaving blades for cleaving of polymer porous fibres, squashes and deforms fibre structure as shown in Figs. 5.6(a) and 5.6(b) for the spider-web and rectangular porous fibres, respectively. Moreover, as we will observe in the Chapter 6, the quality and repeatability of the cleaved end-face of the porous fibres introduces uncertainty in the loss measurements. To overcome this issue for loss measurements, either a rapid, reproducible and *in situ* cleaving method is required to conduct a cut-back based loss measurement or methods with no cleaving requirements are needed. The former approach is addressed in this section and the latter approach is discussed in Chapter 6.

To improve the cleaved end-face results of polymer optical fibres, the impact of different parameters such as magnitude of the stress due to the force (Griffith 1921), and crack depth (Dodds *et al.* 1991) have been studied. The process of cleaving becomes more

delicate when the polymer optical fibre has structures especially with high air-filling factor. For microstructured polymer optical fibres with relatively low air-fraction and thick walls, it has been shown by Law *et al.*, that heating up the cleaving blade and the fibre to 70-80°C improves the cleaved end-face of the optical fibres (Law *et al.* 2006a, Law *et al.* 2006b). However, we find that this approach does not improve the cleave quality for high air-fraction THz porous fibres. We have observed that the structure becomes deformed especially in the outer ring, because of high porosity and missing the outer solid region as in low air-fraction optical microstructured fibres, as shown in Figs. 5.6(c) and 5.6(d). Furthermore, the quality of the cleaved end-face of the porous fibres varies from cleave to cleave by using a conventional blade for cleaving, which as we observe later introduces significant variations in the coupling into these fibres as well as a large error in the loss measurements for such fibres. Furthermore, we observe that as long as the cleaving force is aligned with the struts of rectangular porous fibre, the achieved end-face of these fibres is better compared to the spider-web porous fibres. Hence it is important to develop a method for repeatable, high quality, and rapid cleaving of the porous fibres.

In this section, three different cleaving methods including a semiconductor dicing (SD) saw, focused ion beam (FIB) milling and a 193 nm ultraviolet (UV) laser, are investigated for cleaving of THz porous fibres. For each method, different parameters have been considered to find the optimum cleaving conditions (cleaving quality and time). The optimised cleaving parameters for each method are explained in corresponding sections. The cleaving techniques have been applied to the two THz porous fibres structures, spider-web and rectangular porous fibres, fabricated in-house. Furthermore, for each porous fibre structure, two different polymer materials, PMMA and COC, are investigated.

5.3.1 Semiconductor dicing (SD) saw

In this approach a silicon blade, with the width of 40-50 μm and exposure of 1.02-1.15 mm, was used to cleave the PMMA and COC porous fibres¹⁹. The dicing process is carried out in water and spindle rotation speed is 30000 rpm. The fibres need to be fixed firmly on a surface to prevent any damage and tearing during the dicing process. Typically, the fibres can be fixed firmly to a wafer frame with a dicing tape. However, there is a high possibility of damaging the fibre during the fixing and/or releasing process. Hence, we laid the fibres

¹⁹I have visited DSTO Edinburgh Adelaide, Australia to conduct these experiments. The assistance of the MicroEngineering staff in the development of the waveguide dicing procedure is gratefully acknowledged.

NOTE:

This figure is included on page 152 of the print copy of the thesis held in the University of Adelaide Library.

Figure 5.6. SEM images of cleaved end-face of PMMA porous fibres using a conventional blade and heating up the blade before hand. Cleaved end-face of the PMMA (a) spider-web and (b) rectangular porous fibres using conventional blades. Cleaved end-face of the PMMA (c) spider-web and (d) rectangular porous fibres using conventional blade and heating up the blade and fibre before cleaving. After Atakaramians *et al.* (2009d).

on a clear UV tape with 120 μm thickness. The tape has strong adhesive characteristics and there is no need to sandwich the fibre between the tape and substrate. To release the adhesive, the tape needs to be exposed to UV radiation for at least 5 minutes. The image of the semiconductor dicing saw used is shown in Fig. 5.7.

The SEM images of the resulting cross-section of the diced PMMA and COC spider-web and rectangular porous fibres are shown in Figs. 5.8(a)-5.8(d), respectively. As can be seen, for the PMMA porous fibres, the cross-section is well maintained. The end-face is chipped along the direction of the cleave, which is more pronounced for the spider-web porous fibre. Furthermore, the missing outer ring of spider-web porous fibre, Fig. 5.8(a), is where the blade touches the fibre and is due to the blade tearing the material. It is



Figure 5.7. Images of SD saw machine. The image of semiconductor dicing saw machine, DAD-2H/6 from DISCO, used for cleaving porous fibres.

worth highlighting that among all the cleaving trials there was no tearing off the outer ring for rectangular porous fibres. This shows that the mechanical stability of the rectangular porous fibre is better compared to that of the spider-web porous fibre.

For the COC porous fibres as seen in Figs. 5.8(c) and 5.8(d), the material has been smeared on the cleaved end-face due to the grinding action of the blade. The COC has a glass transition temperature²⁰ of 78°C, which is 20-30°C less than PMMA. Reducing the spindle rotation speed will lessen smearing of the structure. However, for such a soft polymer the friction between the material clogged in the blade's teeth and the fibre will result in smearing the cross-section regardless of the speed. Therefore, using the SD saw is not an appropriate cleaving option for COC porous fibres.

It takes on average of 30 s to cleave a porous fibre with 400 μm diameter and further 10 minutes exposure to UV radiation to remove the fibre from the tape without damaging the outer ring of the fibre. The UV radiation source used here, is an in-house built UV light box. As mentioned earlier the dicing process is carried out in water, this requires later annealing to remove water in the structure. While in principle the fibre end-tip can be polished to improve the facet quality, polishing is undesirable because it would contaminate the sub-wavelength air-holes within these porous fibres, which would lead to scattering loss. Moreover, these fibres are relatively fragile, and the extra handling of

²⁰Glass transition temperature (T_g) is the temperature at which the transformation of a glass-forming liquid into a glass occurs upon rapid cooling. The T_g is lower than the melting temperature.

NOTE:
This figure is included on page 154 of the print copy of
the thesis held in the University of Adelaide Library.

Figure 5.8. SEM images of SD saw cleaves. The SEM images of cleaved end-faces of fibres cleaved using a semiconductor dicing saw: (a) PMMA spider-web, (b) PMMA rectangular, (c) COC spider-web, and (d) COC rectangular air-hole porous fibres. After Atakaramians *et al.* (2009d).

the fibre during the polishing process is undesirable. Bearing in mind that a rapid and quick cleaving approach is essential not only for loss measurements, but also for any other practical applications of the fibres, using an SD saw is not the best cleaving option.

5.3.2 Focused ion beam (FIB) milling

In this method, gallium (Ga) ions are accelerated to an energy of 30 keV, and then focused onto a sample²¹. The image of the equipment used is shown in Fig. 5.9. The SEM images of the resulting cross-section of the FIB cleaved PMMA spider-web and rectangular porous fibres are shown in Figs. 5.10(a) and 5.10(b), respectively. Although this method provides fibres with undistorted end-face results, the cleaving time of a porous fibre with 400 μm diameter is about 17.5 hours with an ion beam current of 21 nA.



Figure 5.9. Images of FIB milling machine. Image of focused ion beam milling machine, Helios NanoLab 600 from FEI, used for cleaving porous fibres.

Using FIB milling for cleaving COC porous fibres failed due to the following reasons. Firstly, due to the lower glass transition temperature of COC, applying the same conditions bulge and deform the cross-section of the fibre as shown in Fig. 5.10(c). Secondly, decreasing the ion beam current to lower values such as 9.5 nA and 0.34 nA, takes 24 hours to cleave a quarter of the structure as shown in Fig. 5.10(d). With the FIB milling technique, there is a deposition of ions on the fibre tips. Further investigations are required to study the effects of deposited ions on the performance of the fibres. Moreover, there is a limitation in the length of the fibre. The fibre could be wound around a spool that fits in the machine, if longer lengths of fibre are required.

²¹We have conducted these cleaving experiments at Australian Microscopy and Microanalysis Research Facility (AMMRF) in Adelaide. The assistance of Mr Leonard Green, in carrying out the focused ion beam milling process is gratefully acknowledged.

NOTE:
This figure is included on page 156 of the print copy of
the thesis held in the University of Adelaide Library.

Figure 5.10. SEM images of FIB milling cleaves. The SEM images of cleaved end-faces of fibres using focused ion beam milling: PMMA (a) spider-web and (b) rectangular air-hole porous fibres, after Atakaramians *et al.* (2009c). Trial cleaves of COC rectangular air-hole porous fibre with an ion beam current of (c) 21 nA and (d) 0.34 nA. After Atakaramians *et al.* (2009d).

5.3.3 UV 193 nm laser

The cleaving experiments are carried out in collaboration with our colleagues at the Interdisciplinary Photonics Laboratories (iPL), School of Chemistry, University of Sydney, Australia²². Earlier work by Lippert and Dickinson (2003) showed the ablation of PMMA requires wavelengths less than 308 nm. At a wavelength of 193 nm, direct structuring of PMMA is possible while at most other wavelengths (248, 222, and 216 nm) significant melting and morphology changes of material are observed (Lippert and Dickinson 2003), (Canning *et al.* 2002). As developed by Canning *et al.* (2002), a 193 nm UV laser is now the standard and direct structuring tool for polymers. The cleaving process is based on ablation; however, increasing the wavelength reduces ablation and increases the possibility

²²I visited iPL to carry out these experiments. The assistance of Dr Kevin Cook and Prof John Canning in the development of the waveguide cleaving procedure is gratefully acknowledged.

of thermal damage. Here, we used a 193 nm UV laser to cleave the porous fibres. The UV laser cleaving has been used for comparatively low air-fraction microstructured polymer optical fibres with outer solid region (Canning *et al.* 2002). This is the first time that this method is used for cleaving of extremely porous polymer fibres, i.e. fibres that have no outer solid region (Atakaramians *et al.* 2009d).

In this method an Argon-Fluoride (ArF) exciplex laser with 0–200 Hz repetition rate, 0–100 mJ pulse energy, and a 20 ns pulse width is used. The laser central wavelength is 193 nm and the beam size is approximately 10 mm × 10 mm. For the laser cleaving, a cylindrical lens with the focal length of 15 cm is used to create a line focus perpendicular to the fibre. The focal spot-size of the beam after the lens is approximately a rectangle with dimensions 40 μm × 10 mm. Figure 5.11 shows the schematic of the setup used for porous fibres cleaving.

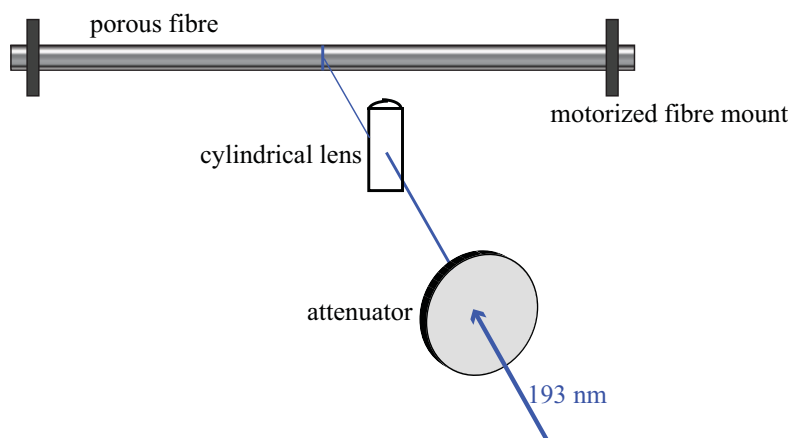


Figure 5.11. Schematic of the UV cleaving setup. The schematic setup used for UV cleaving of porous fibres. A cylindrical lens with the focal length of 15 cm is used to create a line focus on to the fibre. Two rotating, synchronised and motorised fibre mounts are used for holding the fibre.

The cleaving process of the PMMA and COC porous fibres are carried out at a 20 Hz and 40 Hz repetition rate, respectively. The average power of the laser at these repetition rates are respectively 25 mW and 68 mW, which corresponds to energy densities of 312 mJ/cm² and 425 mJ/cm². The fibre is held by two clamps 20 mm apart. The fibres are clamped with minimal tension, in order to prevent damage to the fibre due to clamping. The fibre is rotated 3.6°/sec during the cleaving process using two rotating, synchronised and motorised fibre mounts. This reduces the time need for cleaving to half compared to the case with no rotation. The amount of the time required for UV cleaving is determined by the laser intensity and repetition rate. With the above chosen parameters it takes

about an average 270 s and 210 s to cleave a PMMA and COC porous fibre with 400-500 μm outer diameters. The SEM images of the cross-sections of the UV cleaved PMMA and COC spider-web and rectangular porous fibres are shown in Figs. 5.12(a)-5.12(d), respectively. These images show that the UV laser cleaving leaves traces on the cleaved end-face in the direction of the beam due to ablation. Moreover, there is a clear axial difference between orthogonal struts of the rectangular porous fibre, one orientation is sunken relative to the other. Also it is noticeable that the nodes, where the struts cross in Figs. 5.12(b) and 5.12(d), seem to be more resistant to UV cleaving in case of rectangular porous fibre. This indicates that the energy dissipation at these nodes are high and also indicates that the mechanical stability of the rectangular porous fibre is higher compared to that of spider-web porous fibre. The end-face quality of the cleaves achieved by using a UV laser is relatively good, and is highly reproducible.

NOTE:
This figure is included on page 158 of the print copy of
the thesis held in the University of Adelaide Library.

Figure 5.12. SEM images of UV cleaves. The SEM images of cleaved end-faces of fibres cleaved using a UV laser: (a) PMMA spider-web, (b) PMMA rectangular, (c) COC spider-web, and (d) COC rectangular porous fibres. After Atakaramians *et al.* (2009d).

It is worth highlighting that rotating the fibres during the cleaving process not only reduces the cleaving time to almost half, but also results in a smoother end-face. Figs. 5.13(a) and 5.13(b) show the side view image of cleaved end-face of a COC spider-web porous fibre with and without rotation, respectively. A slightly-raised centre has been observed in the side view image of the fibre that has been rotated during the cleaving process, Fig. 5.13(a). The outer rings sit slightly lower compared to the centre since they have been exposed to UV radiation longer than the central part. However, for the case that the fibre has not been rotated during the cleaving process the end-face of the fibre is inclined at an angle, as shown in Fig. 5.13(b). This is attributed to the fibre relaxing asymmetrically as being cleaved from one side, causing the fibre to rise upwards toward the beam, resulting in an angled cleave. A slight blackening of the fibre end-face is also observed due to longer exposure of the fibre to the UV radiation during the cleaving process. This thermal build-up may be avoided by using lower repetition rates as reported in (Canning *et al.* 2002) however, it will come at the expense of increased cleave times. For the case when rotation is used, the centre of applied tension changes continuously during rotation, and results in a more even cleave with only a slight elevation toward the fibre centre as might be expected.

NOTE:

This figure is included on page 159 of the print copy of the thesis held in the University of Adelaide Library.

Figure 5.13. Side-view images of UV cleaves. The side view images of cleaved end-faces of a COC spider-web porous fibre cleaved using a UV laser: (a) with rotation, and (b) without rotation. After Atakaramians *et al.* (2009d).

The progression of the laser cleave of a COC spider-web porous is monitored by a CCD camera, in order to have a clear understanding of cleaving process of a non-rotating fibre. Fig. 5.14 shows the images at three different stages, beginning, in the middle and at the end of the cleaving process carried out at a 40 Hz repetition rate and 68 mW power.

Fig. 5.14(b) clearly shows the fibre inclination upwards toward the beam due to being cleaved from one side, resulting in an angled cleave.

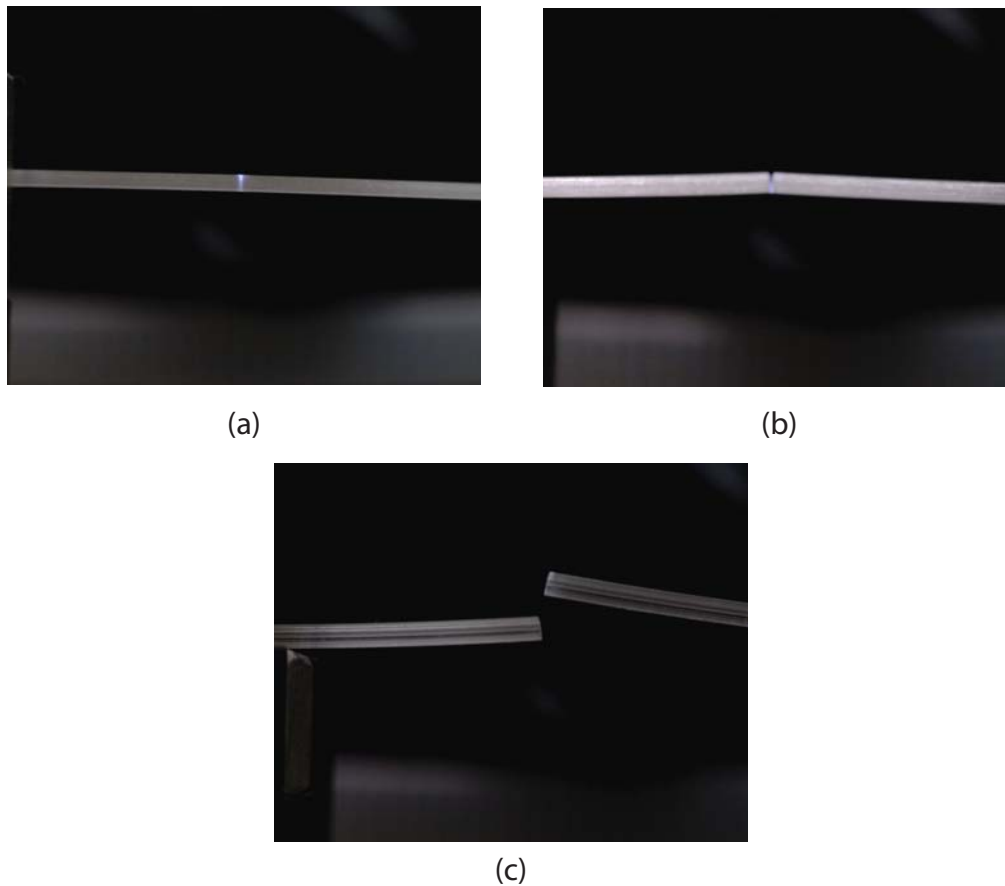


Figure 5.14. Progression of UV cleave. Progression of the UV laser cleaving process of a COC spider-web porous fibre monitored by CCD camera.

In the following section by exploiting the SEM images of PMMA and COC porous fibres, we investigate the effect of rounding of the corner and thickening of the struts on THz porous properties (effective material loss and effective refractive index).

5.4 Modelling of fabricated porous fibres

Comparison of the die designed cross-sections, Figs. 5.3(b) and 5.3(c), and the SEM images of the porous fibre cross-sections, Figs. 5.5(b) and 5.5(c), indicates that the porosity of the porous fibres differs from the die design. This occurs due to rounding of the corners and thickening of the polymer struts during extrusion and fibre drawing. The porosity of the spider-web and rectangular porous fibres given by the die design are 67% and

71%, respectively. While, the porosity calculated from SEM images of spider-web and rectangular porous fibres are reduced to 57% and 65%, respectively.

In order to observe the effect of the structure deformation on porous fibres performance, the THz properties, i.e. α_{eff} and n_{eff} , of the *ideal* and *real* porous fibres are theoretically modelled and compared in Fig. 5.15. For the *ideal* porous fibres, the die exit cross-sections, Figs. 5.3(b) and 5.3(c), are scaled down proportionally to the diameter of the fabricated porous fibre and used for numerical modeling. While, for the *real* porous fibres, the SEM images of the cross-sections of the fabricated porous fibres, Figs. 5.12(a)-(d), are used for numerical modeling. The SEM images taken from the different segments of a porous fibre after a draw, indicate that the porosity of the fibre is almost constant. That is, the deformation in the cross-section remains almost unchanged as the diameter of the fibre is changed (decreased or increased) during the drawing process. For each draw, an SEM image of fibre cross-section is imported to Matlab and is appropriately scaled.

The theoretical values of the effective material loss and effective refractive index of *ideal* and *real* PMMA porous fibres are compared in Figs. 5.15(a) and 5.15(b). For the *ideal* PMMA porous fibres, the die exit cross-sections of the spider-web and rectangular porous fibres are scaled down proportionally to a 350 μm outer diameter and used for numerical modeling. The resultant curves are displayed in dotted lines, spider-web porous fibre in red and the two x - and y -polarisations of rectangular porous fibre in blue and cyan. For comparison, the THz properties of a 300 μm diameter ideal circular shaped air-hole porous fibre with an hexagonal arrangement, shown in Fig. 5.3(a), is also evaluated and illustrated with a black dashed line. For this diameter, the effective material loss of the hexagonal array circular porous fibre at 0.3 THz is in the same order of magnitude compared with the spider-web porous fibre. For simplicity, the hexagonal array circular air-hole, spider-web, and rectangular porous fibres are respectively presented as fibre I, fibre II, and fibre III in Fig. 5.15.

For the *real* porous fibres, the SEM images of the cross-sections of the fabricated PMMA porous fibres, shown in Figs. 5.12(a) and 5.12(b), are used for numerical modeling. The resultant curves are displayed in solid lines, spider-web porous fibre in red and the two polarisations of rectangular porous fibre in blue and cyan. Unsurprisingly, the decrease in the porosity values of the fabricated fibres—due to rounding of the corners and thickening of the polymer struts—increases the value of the expected effective material loss and effective refractive index. Despite the increase, the characteristic values (α_{eff} and n_{eff}) for *real* spider-web and rectangular porous fibres are still lower than that of the *ideal*

hexagonal array circular air-hole porous fibre. This indicates that the porosity of fabricated spider-web and rectangular porous fibres is still higher than the ideal hexagonal circular air-hole porous fibres. The cross-section of real spider-web porous fibre is not circular. Therefore there is a slight difference between the α_{eff} and n_{eff} values of the two polarisations of fundamental mode. The curves for both polarisations are displayed in red solid lines in Figs. 5.15(a) and 5.15(b).

The deformation of the shape of rectangular porous fibre from an absolute circle to an ellipse with the major axis parallel with the short struts reduces the birefringence of the two polarisations of fundamental mode, as shown in Fig. 5.15(b). Higher birefringence could have been achieved if the major axis of the ellipse was parallel with the long side of rectangular holes.

Figures 5.15(c) and 5.15(d) represent respectively the effective material loss and effective refractive index of an ideal and a real spider-web and rectangular COC porous fibres. The diameter of the COC fibres are 550 μm diameter. Similar to PMMA porous fibres the porosity of real porous fibres are 8-10% less than those of ideal porous fibres. Moreover, the cross-section of resultant fibres are elliptical, which introduces birefringence in spider-web porous fibres and decreases the birefringence in rectangular porous fibres. However, this is less noticeable for COC fibres since the dielectric property (material loss and refractive index) values of COC is smaller than those of PMMA.

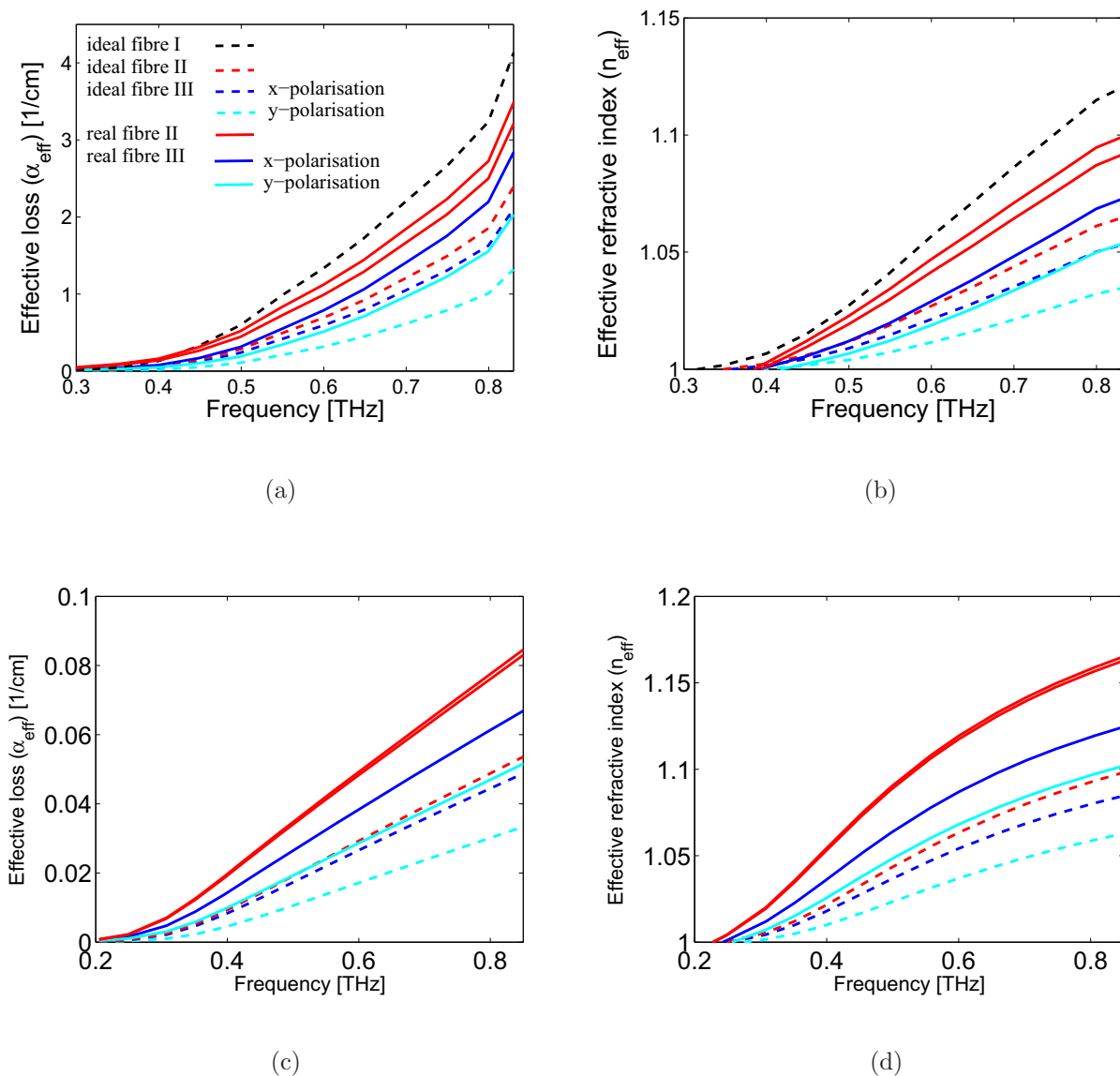


Figure 5.15. THz modelling of the ideal and real polymer porous fibres. (a) Effective material loss and (b) effective refractive index of ideal and real 300 μm diameter hexagonal array circular (black), 350 μm diameter spider-web (red) and 350 μm diameter rectangular (blue and cyan) PMMA porous fibres. (c) Effective material loss and (d) effective refractive index of ideal and real 550 μm diameter spider-web (red) and 550 μm diameter rectangular (blue and cyan) COC porous fibres. The hexagonal array circular air-hole, spider-web, and rectangular porous fibres are respectively presented as fibre I, fibre II, and fibre III in the legend. The dashed lines represent the simulation results of ideal polymer porous fibres, while the solid lines represent the simulation results of real polymer porous fibres. The blue and cyan stand for the x - and y -polarisations of the fundamental mode of the rectangular porous fibre.

5.5 Chapter Summary

Spider-web (symmetrical) and rectangular (asymmetrical) air-hole shaped porous fibres have been successfully fabricated for the first time, achieving high porosity values of $\approx 57\%$ and 65% , respectively. The fibre preforms were fabricated via extrusion technique and then drawn down to fibres, where, PMMA and COC are the polymer materials used for fibre fabrication. The important step in this method of fabrication is the die design, which determines the fibre preform cross-section. The preform cross-section is well preserved during the drawing process. The final achieved porosities in the fibres are 8-15% lower than the porosity values for the die design.

The thin-walled porous polymer fibres are mechanically soft and therefore require non-trivial cleaving to achieve high quality end facets. Apart from conventional cleaving approach we have exploited three different methods to cleave THz porous fibres made up of PMMA and COC. The cleaves obtained using the SD dicing saw and the UV laser, are more than 500 times faster and free of ion deposition compared to those achieved by FIB milling. For PMMA porous fibres, both using UV laser and FIB milling result in a good quality end-face. Although the end-face of these fibres cleaved with the SD saw is chipped, the structure is well maintained. For COC porous fibres, where the material has a lower glass transition temperature, only the UV laser technique is applicable. Using the dicing saw and FIB milling results in smearing the end-face and unreasonable cleaving time for COC fibres, respectively. Moreover the high reproducibility of UV laser cleaves, place this technique as the best for cleaving of extremely porous polymer fibres. Overall, we observe that although the porosity of rectangular porous fibre is higher, the mechanical stability of this fibre is better compared to that of the spider-web porous fibre and we attribute that to the orthogonality of the struts.

The slight blackening of the UV laser cleaved fibre end-face, noticeable in Fig. 5.13(b), may be due to oxidation during the cleaving process. A possible solution to this could be to carry out the UV 193 nm laser cleaving process in an argon or nitrogen purged environment. This also will reduce the cleaving time further. It is also worth mentioning that the traces left from the UV laser cleaves on the cleaved end-face, due to ablation, can possibly be reduced by pressurizing one end of the fibre with an oxygen-free gas. The gas flow to the site of the cleave will blow away ablated material and reduce oxidation and blackening of the cleaved end-face of the fibre, even if it is not carried out in an oxygen-free environment. Further studies of the porous fibres stresses during the drawing process

might reveal more information regarding the higher mechanical stability of rectangular porous fibres.

We have theoretically characterised and compared the designed and fabricated porous fibres. For this purpose we have used the die exit design and SEM image of fibre cross-section. The slight deformation of the fibre cross-section from a circle to an ellipse has reduced the attainable birefringence in rectangular porous fibre and meanwhile has introduced a small birefringence in spider-web porous fibres.

Building upon our successful demonstration of porous fibre fabrication, the following Chapter revolves around the characterisation of these fibres in terms of their performance (i.e. measurement of effective loss and effective refractive index of guided mode) in guiding THz radiation.

THz characterization of porous fibres

THIS Chapter proposes two techniques for characterizing porous fibres. In the first approach the waveguide is situated directly between the emitter, a photoconductive array of antennas, and detector, a centre-excited photoconductive dipole, for characterisation. Good agreement is achieved between theoretical and experimental values of effective refractive indices indicating a lower dispersion for THz porous fibres compared to THz microwires. A birefringence of 0.012 at 0.65 THz is also measured for a rectangular PMMA porous fibre. In the second approach a probe-tip is employed as detector for sampling of the THz signal along the fibre. Two different setup configurations—with and without parabolic mirrors for coupling into the waveguide—are utilized for characterisation of a COC porous fibre. The measured effective loss and effective refractive index of the propagating mode are close to the expected theoretical values. Moreover, for the first time the evanescent field of a THz waveguide is probed directly.

6.1 Introduction

Terahertz spectroscopy systems in transmission mode are employed for characterization of THz waveguides, i.e. the loss and dispersion properties as a function of frequency. Generally, different arrangements of emitters, detectors, and THz optics (mirrors, and lenses) can be utilised for characterisation of a THz waveguide, which is summarised in Fig. 6.1. Usually, photoconductive antennas and nonlinear crystals are employed in the generation of THz pulses. The generated THz pulses are normally manipulated and focused employing parabolic mirrors and silicon/dielectric lenses, as seen in examples A and B in Fig. 6.1. Among the waveguides discussed in Chapter 2, McGowan *et al.* (1999), Gallot *et al.* (2000), and Mendis and Grischkowsky (2001b) employed option A, while Chen *et al.* (2006), Ponseca *et al.* (2008), and Lai *et al.* (2009) employed option B for coupling THz pulses into the waveguides. When the waveguide dimensions are less than the operating wavelength (less than 500 μm) silicon/dielectric lenses are utilised to achieve a smaller spot size and consequently to increase the coupling into the waveguide. An alternative approach is positioning the waveguide on the emitter, shown by option C in Fig. 6.1, for coupling into the waveguide. This approach was, for example, used by Jeon *et al.* (2005) and Wächter *et al.* (2005).

Similar arrangements as the ones used for coupling into the waveguides are employed for coupling out the THz pulses from the waveguide, as shown in the right hand side (options D to F) of Fig. 6.1. Employing electrooptical detectors for measuring THz pulses is known as coherent detection. In this approach both the amplitude and the phase of electric field and consequently the absorption coefficient (effective material loss) and effective refractive index of the propagating mode can be determined. The relevant equations are discussed later in Section 6.2. Among the waveguides discussed in Chapter 2, McGowan *et al.* (1999), Gallot *et al.* (2000), Mendis and Grischkowsky (2001b) employed the option D, Ponseca *et al.* (2008) employed the option E, and Jeon *et al.* (2005), Wang and Mittleman (2004) utilised the option F.

Thermal detectors (e.g. bolometer and pyroelectric devices) are also employed to measure the intensity of the THz radiation, from which only the absorption coefficient of the propagating mode can be determined. Among the waveguides discussed in Chapter 2, Chen *et al.* (2006), Bowden *et al.* (2007), and Lai *et al.* (2009) used the thermal detection method, option G in Fig. 6.1.

Any combination of options A to C and options D to G in Fig. 6.1 can be used for the characterisation of THz waveguides. The waveguides are mostly characterised in transmission mode, i.e. the THz pulse is launched into the waveguide from one end and coupled out and measured from the other end. To date only one reflection mode characterisation technique has been reported (Nielsen *et al.* 2009), where the THz pulses are coupled into and out of fibre from one end, and a metal plate is positioned at the end of the fibre to reflect the beam.

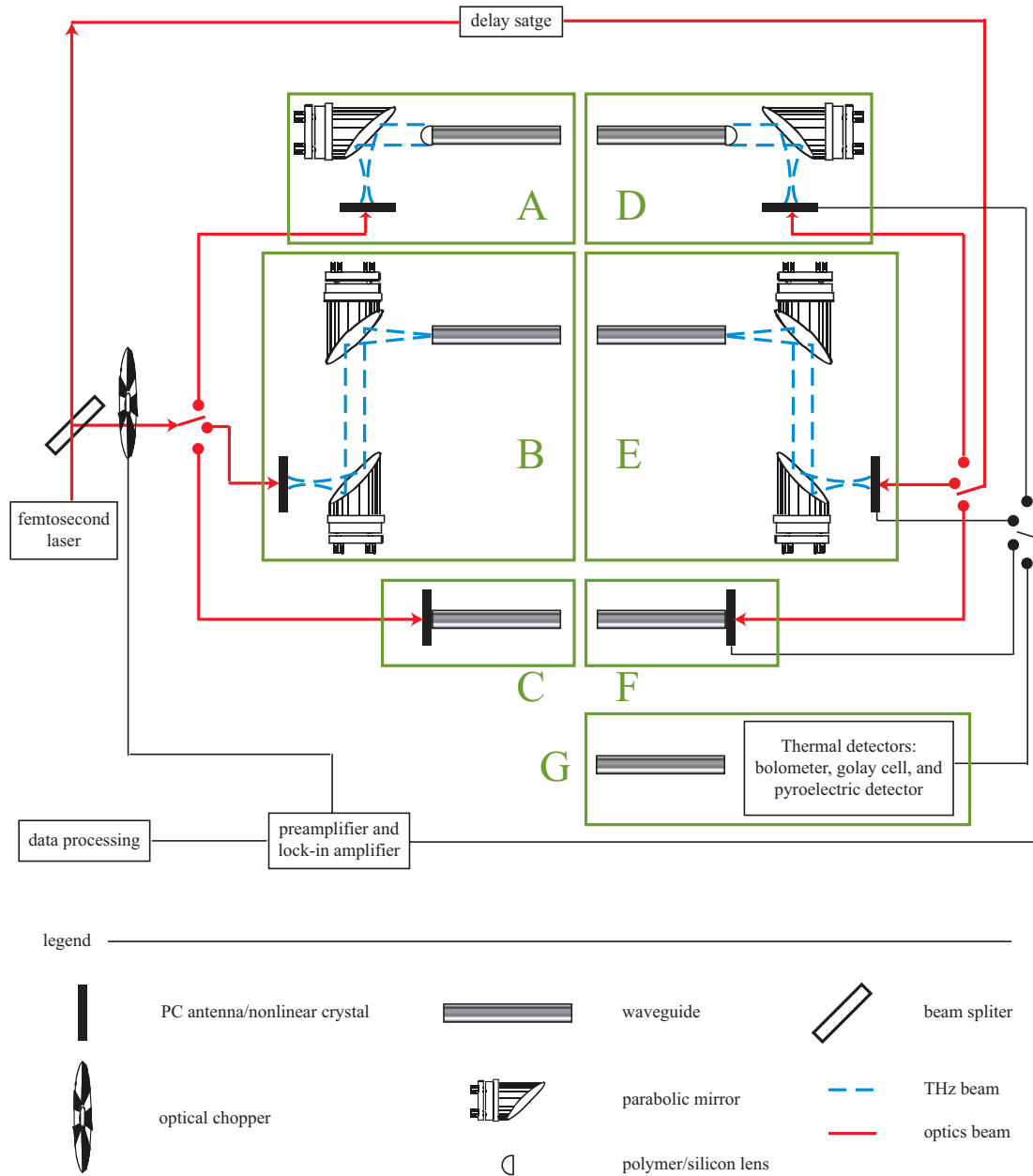


Figure 6.1. Standard THz measurement systems employed for characterisation of THz waveguides. Schematic of the devices required for characterization of THz waveguides are demonstrated. The standard generation and coupling in techniques are shown in the left hand side of the figure (options A to C), while the detection and coupling out techniques are shown in the right hand side of the figure (options D to G). Different combinations of these techniques can be employed for characterisation of waveguides, which are discussed in the text.

6.1.1 Objective and framework

In this chapter, in Section 6.2 we explain the technique and necessary equations employed for characterisation of THz waveguides. Then in Section 6.3 we investigate two different measurement methods for characterisation of porous waveguide. The first approach discussed in Subsection 6.3.1, is based on standard measurement techniques (options C and F, shown in Fig. 6.1), where the waveguide ends are directly positioned on the emitter and detector. The second approach discussed in Subsection 6.3.2, exploits the expansion of propagating modes into the air-cladding for characterisation of the porous waveguide.

6.2 Characterization of waveguides

In this thesis, the term *waveguide characterisation* is used to imply the study of loss and dispersion properties of the waveguide as a function of frequency/wavelength. Two different methods have been used for characterization of THz waveguides. In the first approach, two pulses are measured: a reference pulse when all the steering and coupling devices are in the system except the waveguide and one with the waveguide in place. The loss and dispersion parameters are calculated from these two measurements. For example, references McGowan *et al.* (1999), Gallot *et al.* (2000), Mendis and Grischkowsky (2001b), and Mendis (2001) all used this approach for characterisation of THz waveguides. In the second approach, THz pulses propagating through two different lengths of a waveguide are measured and compared, where the loss and dispersion parameters are calculated (Grischkowsky 2000, Chen *et al.* 2006, Nagel *et al.* 2006b). In this work, different lengths of a waveguide, via the second approach explained above, is used for characterisation of porous waveguides. This approach, also known in optics as the *cut-back* method, is explained further here.

In order to attain the absorption coefficient (α_{eff}) and/or effective refractive index (β_{eff}) values of a waveguide, THz pulses propagating through different lengths of a waveguide are measured. Assuming single mode propagation, the equation governing the input and output electric fields of the waveguide can be written in the frequency domain as (Grischkowsky 2000):

$$E_{\text{out}}(\omega) = E_{\text{ref}}(\omega) C^2 \exp(-\alpha_{\text{eff}}L/2) \exp(-j\beta_{\text{eff}}L), \quad (6.1)$$

where, $E_{\text{out}}(\omega)$ and $E_{\text{ref}}(\omega)$ are the complex electric fields at angular frequency ω on the entrance and exit of the waveguide, respectively; C is the coupling coefficient, the same

for the entrance and exit faces and takes into account the reflections at the entrance and exit faces; β_{eff} is the propagation constant of the fundamental mode; α_{eff} is the effective material loss that the propagating mode experiences; and L is the waveguide length.

At least two different lengths of a waveguide are required for calculating the THz properties (α_{eff} and n_{eff}) of the waveguide. Applying Eq. (6.1) to two different lengths (L_1 and L_2), the transfer function determined from the ratio of $E_{\text{out1}}(\omega)$ and $E_{\text{out2}}(\omega)$ reads as:

$$\frac{E_{\text{out1}}(\omega)}{E_{\text{out2}}(\omega)} = \frac{C_1^2}{C_2^2} \exp(-\alpha_{\text{eff}}(L_1 - L_2)/2) \exp(-j\beta_{\text{eff}}(L_1 - L_2)). \quad (6.2)$$

If the facet of the in/output of the waveguides are prepared identically and the waveguides are aligned so that the coupling in/out conditions are similar for each case, Eq. 6.2 will be simplified further to:

$$\frac{E_{\text{out1}}(\omega)}{E_{\text{out2}}(\omega)} = \exp(-\alpha_{\text{eff}}(L_1 - L_2)/2) \exp(-j\beta_{\text{eff}}(L_1 - L_2)). \quad (6.3)$$

The coupling and transmission coefficients are cancelled. In order to achieve this, first the experiment is conducted for the longest length. Then without changing the input coupling arrangements, i.e. keeping fixed the input end arrangements, the output end of the waveguide is cut to achieve the shorter length. The THz pulse transferred through both lengths is measured, from which the transfer function (Eq. 6.3) is constructed. Consequently, the α_{eff} and β_{eff} of the waveguide are obtained from the amplitude and the phase of the transfer function (Eq. 6.3). Since the waveguide is cut from the output end, this method is called the *cut-back* method. The procedure can be repeated for different lengths.

6.3 Porous fibre characterisation

In this section we characterise our fabricated porous fibres. We employ two different measurement techniques for characterisation of porous fibres. In the first approach, Subsection 6.3.1, we position the fibre directly between the emitter and detector, as shown in Fig. 6.2. This experiment has been carried out at RWTH Aachen University²³. In the

²³I visited the Institute of Semiconductor Electronics (ISE), at RWTH Aachen University, Germany, and conducted the experiments over there commencing October 2008. I gratefully acknowledge Markus Wächter and Mohammad Awad for assistance with THz hardware, and Dr Michael Nagel for his assistance with analysing and interpreting the waveguide experimental results.

second approach, Subsection 6.3.2, we situate the emitter, and fibre on a sliding table, while the detector is fixed in place. The THz pulse is measured at different positions along the fibre, which is equivalent to different lengths via cut-back measurements, for characterisation of the fibre. This method of measurement is applicable to waveguides with the propagating mode expanded outside the waveguide.

6.3.1 First characterisation technique

The THz properties of the fabricated porous fibres are investigated by using terahertz time domain spectroscopy (THz-TDS). A mode-locked Ti:sapphire laser with a pulse width of less than 170 fs, central wavelength of 800 nm and a repetition rate of 76 MHz is used to drive the photoconductive switches used as emitter and detector. As shown in Fig. 6.2, the laser beam is split into two beams, the excitation and detection beams. The excitation beam is modulated by a chopper and focused onto the emitter. The chopper is employed to reduce the fluctuations in the THz pulses affected by the $1/f$ noise characteristic of the mode-locked laser (Son *et al.* 1992, Poppe *et al.* 1998). The emitter is a photoconductive array of antennas, consisting of two sets of 10 inter-digitated electrodes with an active area of $290 \times 318 \mu\text{m}^2$ on a $500 \mu\text{m}$ thick optically and terahertz transparent sapphire substrate (Awad *et al.* 2007, Wächter *et al.* 2007). Each set of electrodes forms an LT-GaAs based photoconductive switch. The 100 mW excitation laser pulse fully illuminates the emitter, which is biased with 100 V DC voltage. The detector is a centre-excited dipole between coplanar strip lines photoconductive switch with a $5 \mu\text{m}$ gap, which is fabricated on an ion-implanted silicon-on-sapphire substrate. The detection beam is passed through a delay stage and focused on the detector. The laser power on the detector is 10 mW. As explained in Subsection 2.2.3 the delay stage maps out the THz pulse in the time domain. The emitter is excited with a laser beam polarised in the x direction, consequently the generated THz pulses are polarised in the x direction. Thus the detector is placed as that the gap between electrodes are orientated in the x direction and is illuminated with the x polarised detection laser beam.

The waveguide tips are directly launched on the emitter and detector. A holder consisting of a 2.5 cm diameter circular hole in an 0.5 cm thick aluminum slab, shown in Fig. 6.3(a), is used for holding the spider-web porous fibres and microwires. A rotational mount is used instead of an aluminum slab, shown in Fig. 6.3(b), for rectangular porous fibre. The rotational mount enables the rotation of the rectangular porous fibre with respect to the emitter and consequently facilitates the excitation of different polarisations of the

NOTE:
This figure is included on page 174 of the print copy of
the thesis held in the University of Adelaide Library.

Figure 6.2. Schematic of the THz-TDS setup I for waveguide characterisation. Schematic of the terahertz time-domain spectroscopy setup employed for characterisation of porous fibres and microwire. The emitter and detector are shown in the inset (Atakaramians *et al.* 2009c).

propagating modes. Two terahertz transparent polyester films with $100\ \mu\text{m}$ thickness are attached to the sides of the holders with $500\ \mu\text{m}$ holes in the centre for holding the waveguide.

Three different waveguides are characterised in this section: PMMA spider-web and rectangular porous fibres, and a microwire. We have fabricated the porous fibres as explained in Chapter 5. We have used an extruded polymer optical fibre with $250\ \mu\text{m}$ outer diameter (Ebendorff-Heidepriem *et al.* 2007) as a THz microwire. The THz properties of the billet used for the microwire are the same as that of the porous fibre.

As discussed in Section 5.3, *in situ* cleaving of porous fibres, where the fibre cross-section is preserved is very challenging. Therefore, different fibre lengths are prepared in advance for characterisation. Here, we use three lengths for characterisation of the waveguide. The input end of the waveguide is aligned to the centre of the antenna array, the emitter. Then the detector is aligned to the output end of the waveguide. These two steps are repeated for each length of the waveguide. In order to have consistent measurements, we make sure that the photocurrent of the emitter and detector is the same for the three samples of each waveguide. This introduces uncertainties in the loss measurement of the

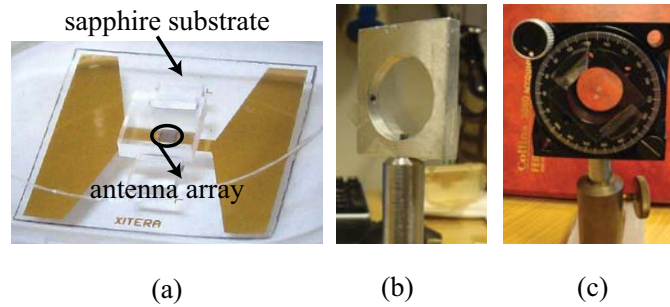


Figure 6.3. Images of the waveguide holders. Images of waveguide holders used for characterisation of (a) spider-web porous fibre and microwire (b) rectangular porous fibre. The holder (a) consists of a two optically and terahertz transparent plastic sheets glued on an aluminum holder with a 2.5 cm circular hole. The holder (b) consists of a two optically and terahertz transparent plastic sheets glued on a rotational mount.

waveguides, since the amplitude of the field guided by the waveguide depends on the alignment of the waveguide tip with the antenna (i.e. the coupling efficiency) and cleaved end-face of the fibres. However, the effective refractive index of the fibres, which depends on the phase of the transfer function and is independent from the coupling coefficient, C , can be determined accurately.

The photocurrent generated on the detector is first amplified with a low noise amplifier, and then is fed to a lock-in amplifier (LIA). The LIA is employed to demodulate the THz signal with a reference signal from chopper. The process involves two steps. First, the multiplication of the both input signals (THz and chopper signals), which creates sum ($2f_{\text{chopper}}$) and difference (DC) components. Second, the DC component is filtered out utilising a narrowband low pass filter. The bandwidth of the filter is inversely proportional to time constant (τ) of the LIA. For this measurement in order to have higher SNR the time constant of LIA is set to 1 s.

Figures 6.4(a), 6.4(d) and 6.4(g) show the electric fields of the terahertz pulse measured for three different lengths of a 200 μm and 350 μm diameter spider-web porous fibres and a 250 μm diameter microwire, respectively. The pulses are separated vertically for clear display. The red (top), green (middle) and blue (bottom) lines represent the pulses through the three different lengths, from the longest to shortest. The fibre lengths used for characterisation of the 200 μm and 350 μm diameters spider-web porous fibre are 24.4, 21.0 and 15.4 mm, and 24.9, 20.4 and 16.0 mm, respectively. 25.0, 20.2 and 17.7 mm are the lengths of microwires. Each pulse represent a single scan with a time constant 1 s.

The emitter is mounted such that the LT-GaAs antenna directly faces the excitation laser beam, while the terahertz radiation is coupled out through the sapphire substrate facing the waveguide. The substrate results in reflections that are well separated in free space from the main pulse, e.g. the first reflection appears 10 ps after the main THz pulse. Based on known parameters, i.e. substrate thickness, l , time difference between the main pulse and the reflection, Δt , the refractive index of the substrate can be calculated as follows:

$$n_{\text{sapphire}} = \frac{\Delta c}{2\Delta l} = \frac{10 \times 10^{-12} \cdot 3 \times 10^8}{2 \times 500 \times 10^{-6}} = 3. \quad (6.4)$$

The calculations confirm that this reflection is from the substrate, since the calculated refractive index is consistent with the refractive index of sapphire ($n_0 = 3.07$) reported by McGowan and Grischkowsky (1999).

When THz pulses propagate through a long dispersive medium, e.g. dielectric fibres, the first reflection from substrate is not clearly separated from the main pulse. However, it is still noticeable, i.e. it introduces a phase change in the time domain after which the signal becomes stronger as well. In order to avoid artifacts caused by these reflections, the signals are cut-off at the zero crossing just before the reflection (shown with arrow points in Figs. 6.4(b), 6.4(e) and 6.4(h)) and padded with zeroes. The same number of peaks is considered for the three lengths of each waveguide structure. The spectral amplitude of the signals after zero padding are shown in Figs. 6.4(c), 6.4(f) and 6.4(i) for the 200 μm and 350 μm diameter spider-web porous fibres and the 250 μm diameter microwire, respectively. Padding the reflection with zeroes reduces the oscillations in the spectral amplitude and the resulted artifacts in loss and refractive index values.

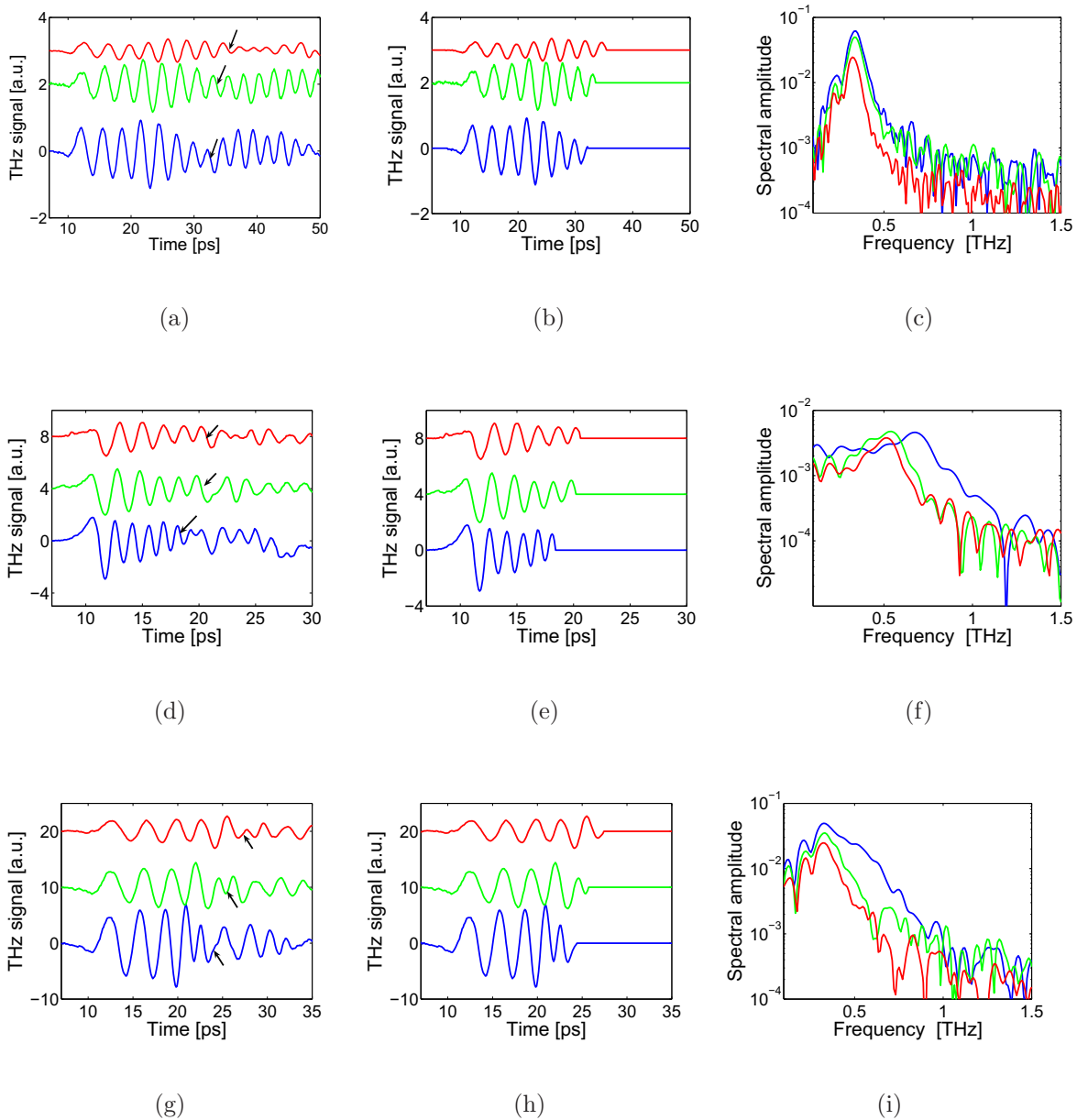


Figure 6.4. Measured THz signals and spectral amplitudes of PMMA porous fibres and a microwire. The first column, i.e. Figs. (a), (d) and (g), represents the measured electric fields, the second column, i.e. Figs. (b), (e) and (h), represents the measured electric fields where the reflection is padded with zeroes, and the third column, i.e. Figs. (c), (f) and (i), represents the spectral amplitudes of the measured fields for a $250\ \mu\text{m}$ diameter of microwire (first row), $200\ \mu\text{m}$ diameters of spider-web porous fibre (second row), and $350\ \mu\text{m}$ diameters of spider-web porous fibre (third row). The red, green and blue signals represent the measured terahertz pulse and spectral amplitude of long, medium and short length of fibres, respectively. The vertical offset in the time domain has been introduced intentionally for clear display. The arrows in Figs. (a), (d) and (g) indicate the cut-off point for each waveguide length.

Applying Eq. 6.3 to any two combination of the three scans for each waveguide results in absorption coefficient (effective material loss) and effective refractive index of that pair. Since there are three scans for each waveguide, three different combinations of pairs and consequently three values of effective material loss (α_{eff}) and effective refractive index (n_{eff}) are achieved for each frequency. The final α_{eff} and n_{eff} curves are the average of those three values. Figures 6.5(a) and 6.5(b) illustrate respectively the measured effective material loss and effective refractive index for the 200 μm and 350 μm diameter spider-web porous fibres and the 200 μm diameter microwire. The theoretically calculated values of the real waveguides, which are obtained from SEM images, are also shown in Figs. 6.5(a) and 6.5(b) with solid lines.

There are two major sources of errors that are considered: waveguide length and data processing uncertainties as explained below. A ± 0.1 mm variation is considered for the length uncertainty. As mentioned earlier in this Section, the THz signal is modulated by employing a chopper to reduce the fluctuations in the THz pulses affected by the $1/f$ noise characteristic of the mode-locked laser. However, the scans still have very slow oscillations. In order to remove these oscillations two techniques are used, which are base line removal and high pass filtering. The difference between these methods and the effect of variation of the cut-off frequency of the high pass filter are considered as the source of data processing uncertainty. The error bars shown in Figs. 6.5(a) and 6.5(b) represents the quadrature sum of standard deviations obtained from the two sources of uncertainty described above.

The measured absorption coefficients are higher than the expected theoretical values, as shown in Fig. 6.5(a). The measurement method employed here could be one of the reasons. As stated earlier, three different lengths have been prepared for each waveguide. For each experiment the waveguide input end is adjusted to the centre of the emitter antenna. Then the detector is aligned to the centre of the output end of the waveguide. The waveguides ends are aligned with great care to make sure that alignments are identical for each set of measurements. However, still this could introduce uncertainty in the loss values since the coupling coefficients are not identical and thus cannot be canceled. Moreover, the waveguides under experiment are also slightly bent, which may be another reason for higher effective material loss values than the expected theoretical values.

There is a good agreement between the theoretical and experimental calculated values of the effective refractive indices. Figure 6.5(b) indicates that the effective refractive index of the propagating mode of porous fibres are relatively flat functions of frequency relative

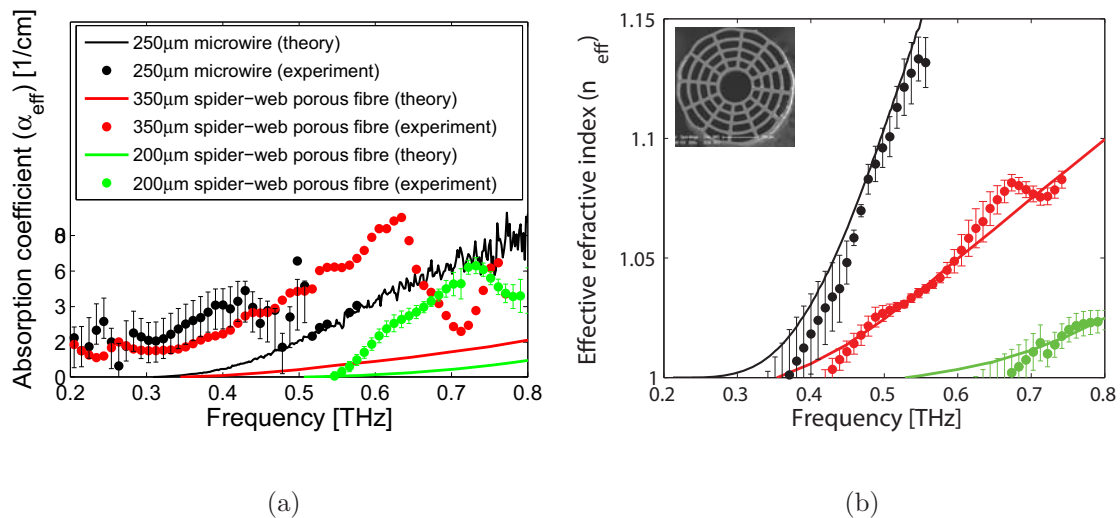


Figure 6.5. Effective material loss and effective refractive index of PMMA porous fibres and a microwire. (a) Effective material loss (absorption coefficient) and (b) effective refractive index of a 200 μm (green) and a 350 μm (red) diameter spider-web porous fibre, and a 250 μm diameter microwire (black). The solid lines represent the theoretical results based on the real waveguide (SEM images) while the circles represent the measured experimental results.

to that of the microwire. This corresponds to a slight drop in the group velocity of porous fibre compared to that of the microwire resulting in lower dispersion for THz porous fibre, as discussed in Section 4.4. It is worth mentioning that the difference between the experimental and theoretical values at lower effective refractive index values is most likely due to the slight bending of the fibres. The confinement of the propagating mode at lower frequencies is weak, thus any gentle bend or perturbation couples the propagating mode into the radiation waves.

The experiment is repeated to define the THz properties of the x - and y -polarisation of the fundamental mode of a 350 μm diameter rectangular porous fibre. The waveguide is mounted on a rotational mount and the alignment of the tip of the fibre with the photoconductive antenna is monitored with a magnifier. The x - and y -polarisation modes are acquired when the generated THz pulse on the antenna is parallel to the long and short sides of the rectangles, respectively. The waveguide lengths considered for the experiment are 30.0, 34.1 and 38.2 mm.

The measured electric fields for the three lengths of x - and y -polarisations are shown in Figs. 6.6(a) and 6.6(d). The signals are cut-off at the zero crossing just before the

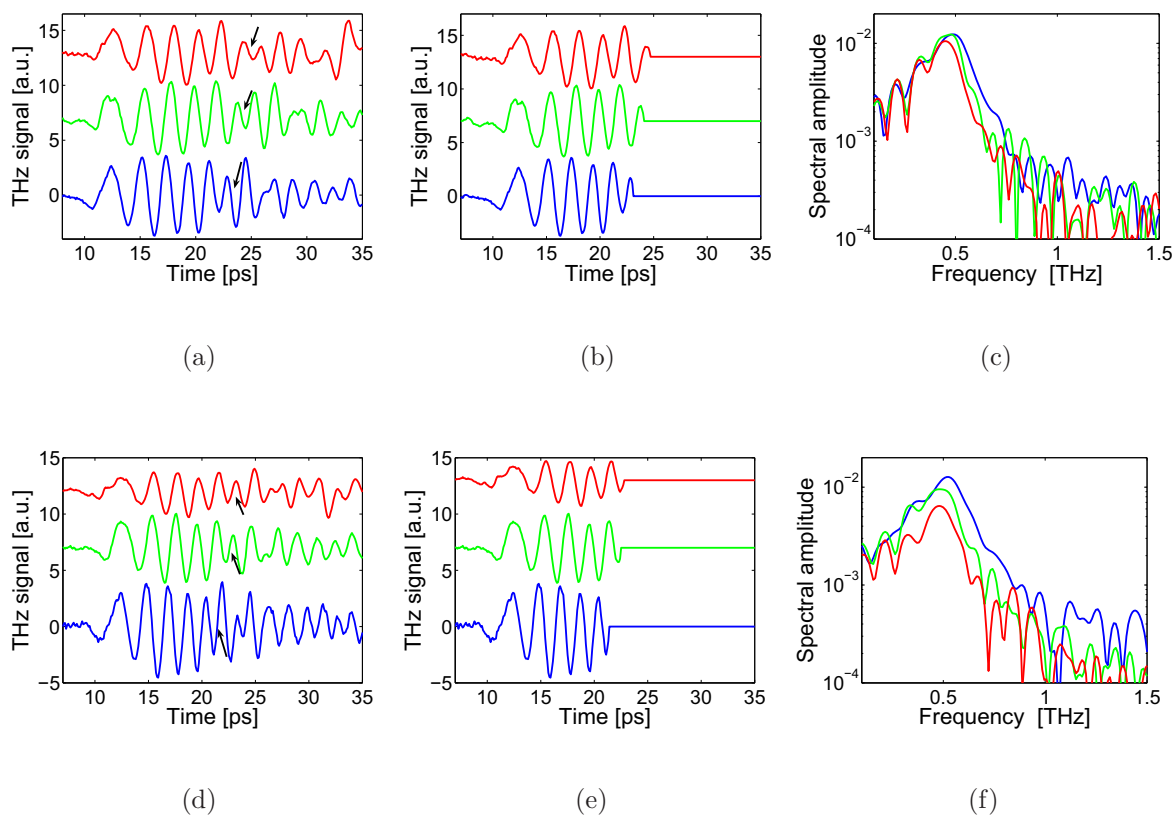


Figure 6.6. Measured THz signals and spectral amplitudes of PMMA rectangular porous fibres. The electric fields of the terahertz pulse measured for (a) x - and (d) y -polarisations of a $250\ \mu\text{m}$ diameters of rectangular porous fibre. Figures (b) and (e) represent the measured electric signal where the reflection is padded with zeroes. Figures (d) and (f) represent the spectral amplitudes of the measured electric fields. The red, green and blue signals represent the measured terahertz pulse of long, medium and short length of waveguides, respectively. The vertical offset has been introduced intentionally for clear display. The arrows indicate the cut-off point for each scan.

reflection (indicated with arrows) and padded with zeroes as shown in Figs. 6.6(b) and 6.6(e). Then the spectral amplitude of the signals is taken, as shown in Figs. 6.6(c) and 6.6(f), to evaluate absorption coefficients and effective refractive indices.

Figures 6.7(a) and 6.7(b) show the experimentally measured absorption coefficient and refractive indices of the x - and y -polarisation modes for the $250\ \mu\text{m}$ diameter rectangular porous fibre together with the theoretically calculated values of the real waveguide structure (based on SEM images). For the same reasons discussed earlier for spider-web porous fibre measurements in this section, the measured absorption coefficient curves are higher than the expected theoretical values. Experimentally, a 0.012 birefringence ($n_{\text{eff}}^x - n_{\text{eff}}^y$)

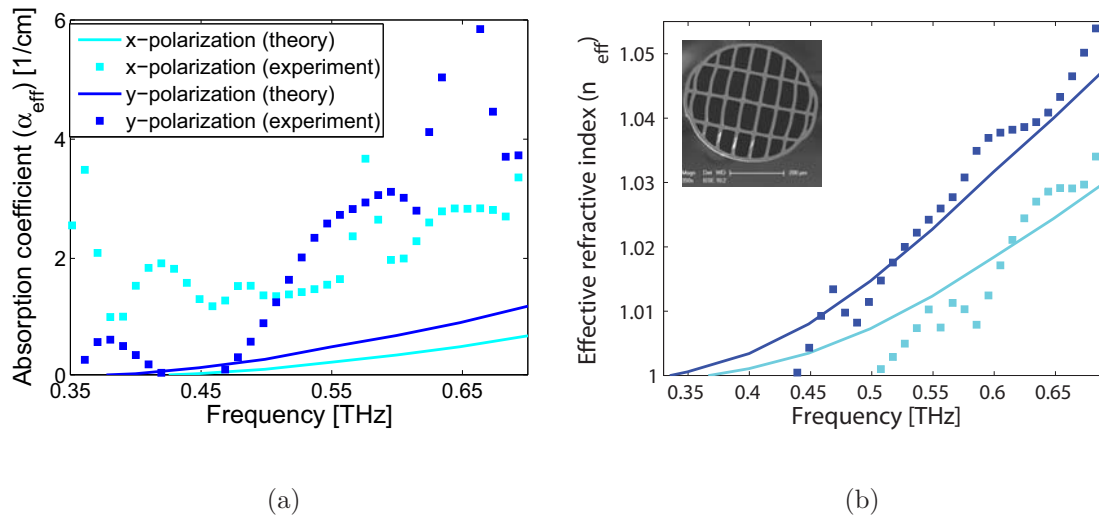


Figure 6.7. Absorption coefficients and effective refractive indices of a PMMA rectangular porous fibre. (a) Effective material loss (absorption coefficient) and (b) effective refractive index of the x -polarisation (blue) and y -polarisation (cyan) of a $250 \mu\text{m}$ diameter of rectangular porous fibre as a function of frequency. The solid lines represent the theoretical results based on the real waveguide (SEM images) while the squares represent the measured experimental results.

is achieved for 0.65 THz which is comparable to the expected theoretical results. The measured value is lower than the designed values, due to the slight deformation of the fibre core from circular to elliptical shape along the short side of rectangles. As mentioned before for the lower effective refractive indices, the experimental data does not match well with the theory and this can be attributed to unwanted waveguide bending. The slight oscillation in the measured n_{eff} values may be due to the different signal noise levels of the three lengths. Note that the theoretical calculations based on the SEM image of the fabricated porous fibres confirm that these fibres are in their single mode operating regime.

6.3.2 Second characterisation technique: probing the evanescent field

Any combination of the options A to C and D to G shown in Fig. 6.1 can be employed for characterisation of waveguides. The THz pulses are launched from the input end of the waveguide and measured from the output end of the waveguide. Note that the THz waveguides act either as pipes where the mode propagated inside the waveguide, e.g.

NOTE:
This figure is included on page 182 of the print copy of
the thesis held in the University of Adelaide Library.

Figure 6.8. Output coupler for sampling THz pulses. A second waveguide, called an output coupler, is located in parallel with the waveguide under investigation, and is employed to direct THz pulses to the bolometer for the loss measurement. After Dupuis *et al.* (2009).

parallel-plate waveguides and hollow-core microstructured band-gap fibres, or as rails where the propagating mode is guided on the waveguide surface or is expanded outside the waveguide, e.g. bare metal wires, slit waveguides, microwires, and porous fibres. In these particular cases where the propagating mode is fully or partially expanded outside of the waveguide other methods can also be employed for characterisation of THz waveguide.

The THz pulses do not need to be launched from the input end and measured from the output end of the waveguide. The mode can be excited from the side, i.e. positioning the waveguide in the electromagnetic field of another waveguide. Such a method was employed by Wang and Mittleman (2004), i.e. a test/coupler waveguide was used for excitation of bare metal wire as shown in Fig. 2.11. Moreover, in these waveguides the THz pulses can be sampled (detected) from the side of the waveguide instead of the output end of the waveguide. Such an approach has been employed by Wächter *et al.* (2005), Wächter *et al.* (2007), and Dupuis *et al.* (2009) for characterisation of a bare metal wire, slit waveguide, and porous fibres, respectively. A sliding photoconductive switch was employed for sampling THz pulses along the bare metal wire and slit waveguide as shown in Figs. 2.13 and 2.14(b), respectively. Dupuis *et al.* (2009) have employed a second waveguide called output coupler, located in parallel with the waveguide under investigation, to direct THz pulses to a bolometer for measurement as shown in Fig. 6.8. Employing a second waveguide makes the loss value calculation more reliable and consistent since the main waveguide under investigation can be kept constant, while the test waveguide can move along the main waveguide to sample the beam at different locations. However, maintaining a constant separation between the two waveguides is challenging.

In this subsection, we employ a probe-tip for characterisation of porous fibres. The probe-tip allows sampling of THz pulses along the waveguide. This is possible because the propagating mode along the waveguide (porous fibre) expands into the air-clad of

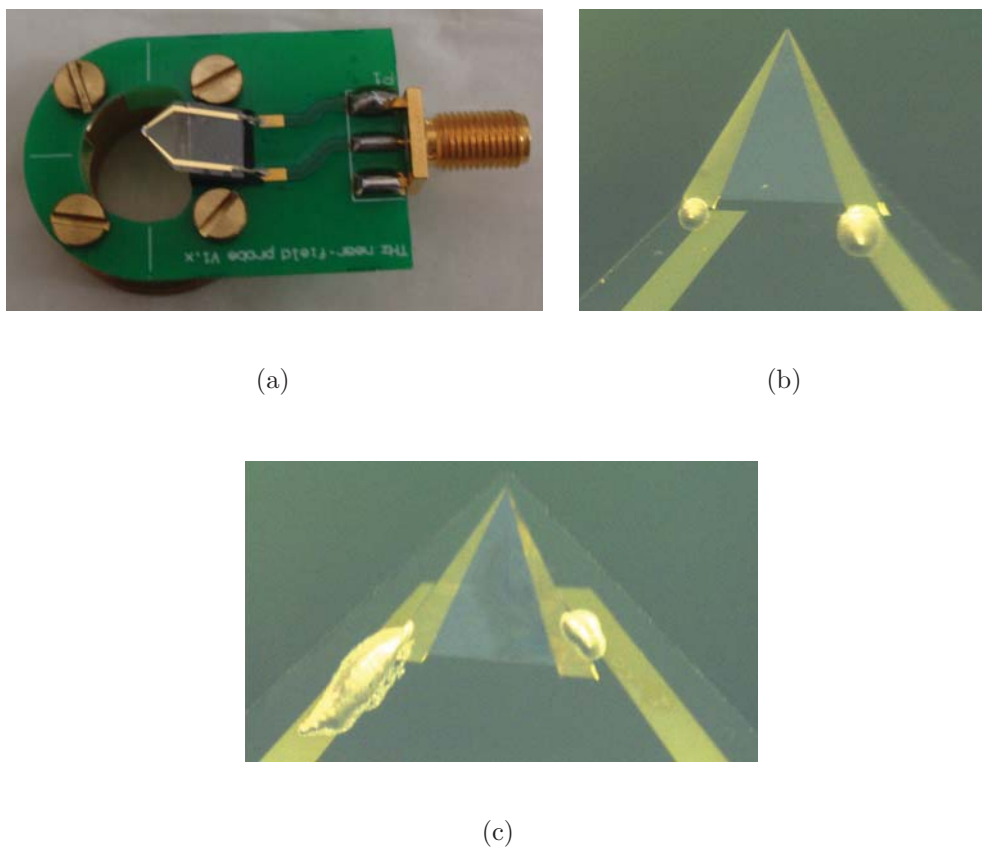
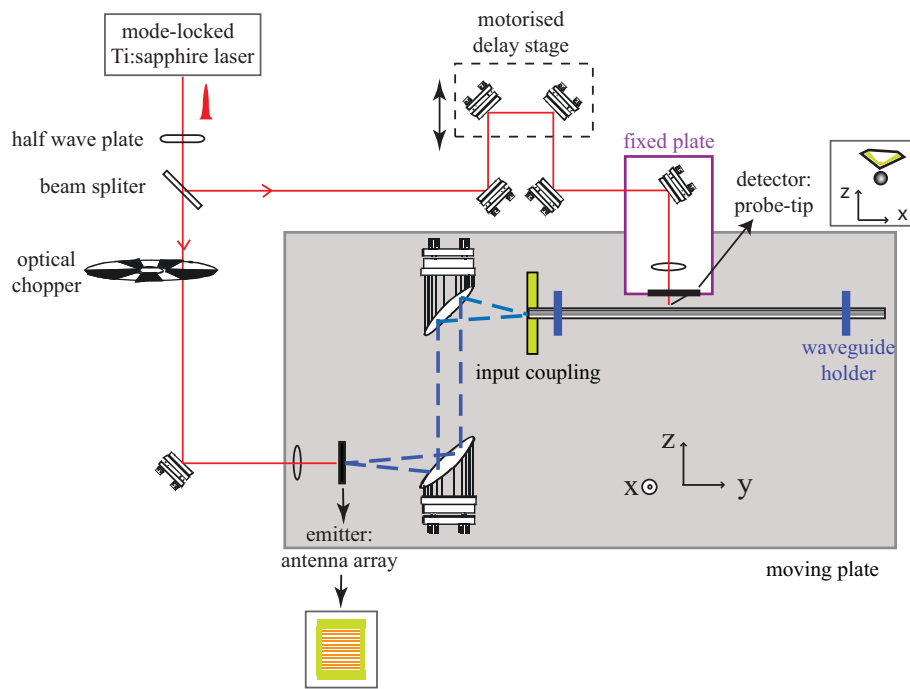


Figure 6.9. The image of the probe-tip detector. The images of (a) the mounted THz probe-tip, and the close-up image of the photoconductive triangular-shaped LT-GaAs switch, (b) without (free standing) and (c) with a sapphire substrate. The probe tip was fabricated by AMO GmbH, Aachen.

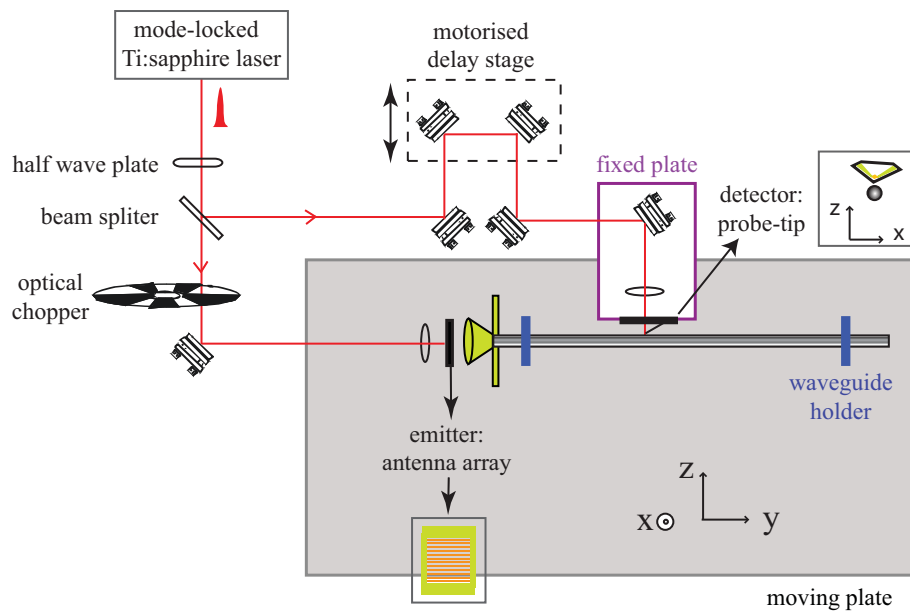
the waveguide. Therefore, instead of measuring three different waveguides, as outlined in Subsection 6.3.1, the propagating mode is sampled on three different positions along the waveguide. The probe-tip employed here is a photoconductive switch with a tapered electrodes on a triangular-shaped LT-GaAs substrate (Wächter *et al.* 2009), as shown in Fig. 6.9(a). This miniaturized photoconductive antenna, probe-tip, has $3\ \mu\text{m}$ gap between the electrodes at the apex. The PC film on LT-GaAs can be either free-standing, Fig. 6.9(b), or backed with a sapphire substrate, Fig. 6.9(c). The freestanding probe-tip is very brittle and can easily be damaged if the probe-tip comes in contact with fibre. Thus here, we use a probe-tip mounted on the sapphire substrate, shown in Fig. 6.9(c) for characterisation of porous fibres. The probe-tip is illuminated by a 1.6-1.7 mW laser beam.

An antenna array (Saeedkia *et al.* 2005) consisting of 10 antenna elements on a 1.7 mm thick silica substrate is used for generation of THz pulses. The effective area of the antenna is $1.1 \times 1.1 \text{ mm}^2$. The emitter is biased with a 29 V DC voltage and is excited with a 50 mW excitation laser pulse. A mode-locked Ti:sapphire laser with a pulse width of less than 100 fs, central frequency of 800 nm and a repetition rate of 80 MHz is used to drive the emitter and detector.

Here, we utilise two different setup arrangements for characterisation of COC spider-web porous fibres. In the first approach two parabolic mirrors and a metallic cone are used for coupling THz pulses into the waveguide. While, in the second approach no parabolic mirrors are used, and the metallic cone and the waveguide are located after the emitter. In both configurations the emitter (antenna array), focusing optical lens, parabolic mirrors and/or metallic cone, and the waveguide are situated on a sliding table while the detector (probe-tip) is fixed on the optical table, as shown in Figs. 6.10(a) and 6.10(b). The moving table is an in-house fabricated optical table which moves on two parallel rails. The moving table is slid back and forth to sample THz pulse at different locations along the waveguide. The position of the table for each point is manually recorded using a ruler.



(a)



(b)

Figure 6.10. Schematic of the THz-TDS setup for waveguide characterisation. Schematic of the terahertz time-domain spectroscopy setup employed for characterisation of porous fibres: (a) two parabolic mirrors and a metallic cone, and (b) only a metallic cone is employed to couple the THz pulses into the waveguide. The emitter and detector are shown in the inset.

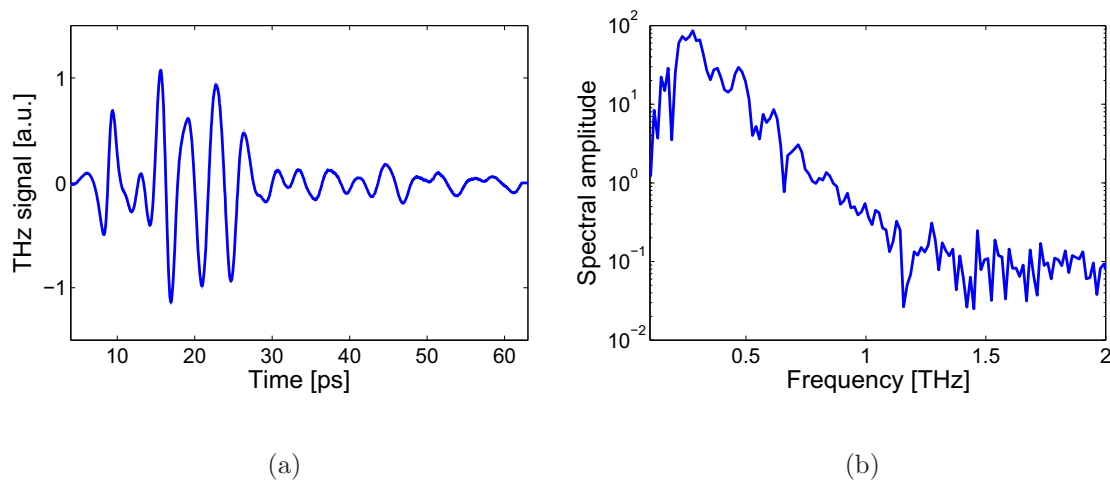


Figure 6.11. Measured THz signal and spectrum. The THz signal and spectrum are measured when the probe-tip is located at the focal point of second parabolic mirror shown in Fig. 6.10(a).

We aim to measure the transverse electric field of the propagating mode. Therefore, the probe-tip must be situated so that the gap of electrodes at the apex is parallel to the fibre length. Considering that the waveguide is aligned along the y axis, in Figs. 6.10(a) and 6.10(b), the probe-tip should be located so that the tip is parallel to the xz -plane. Moreover, the detection laser beam is required to be parallel to the gap of electrodes at the apex, i.e. polarised in the x direction. Therefore, a half wave plate is used to rotate the polarisation of the linearly polarised laser beam (z direction) for 90° into x direction. Consequently the emitter is rotated 90° so that the generated THz pulses are linearly polarised in the x direction. The excitation beam is modulated by a chopper at $f_c = 668$ Hz and focused onto the emitter, while the detection beam is passed through a motorised delay stage and focused onto the detector.

First approach (with parabolic mirrors)

The schematic diagram of the first approach employed for characterisation of porous fibres is shown in Fig. 6.10(a). Before replacing the metallic input coupling and the waveguide in the setup, the system is aligned and the system parameter variations are investigated. For this purpose the table is slid to the left up to the point where the probe-tip falls into the focal point of the second parabolic mirror. The system is aligned so that the maximum bandwidth is achieved. The THz time domain signal and spectral amplitude after the alignment are shown respectively in Figs. 6.11(a) and 6.11(b).

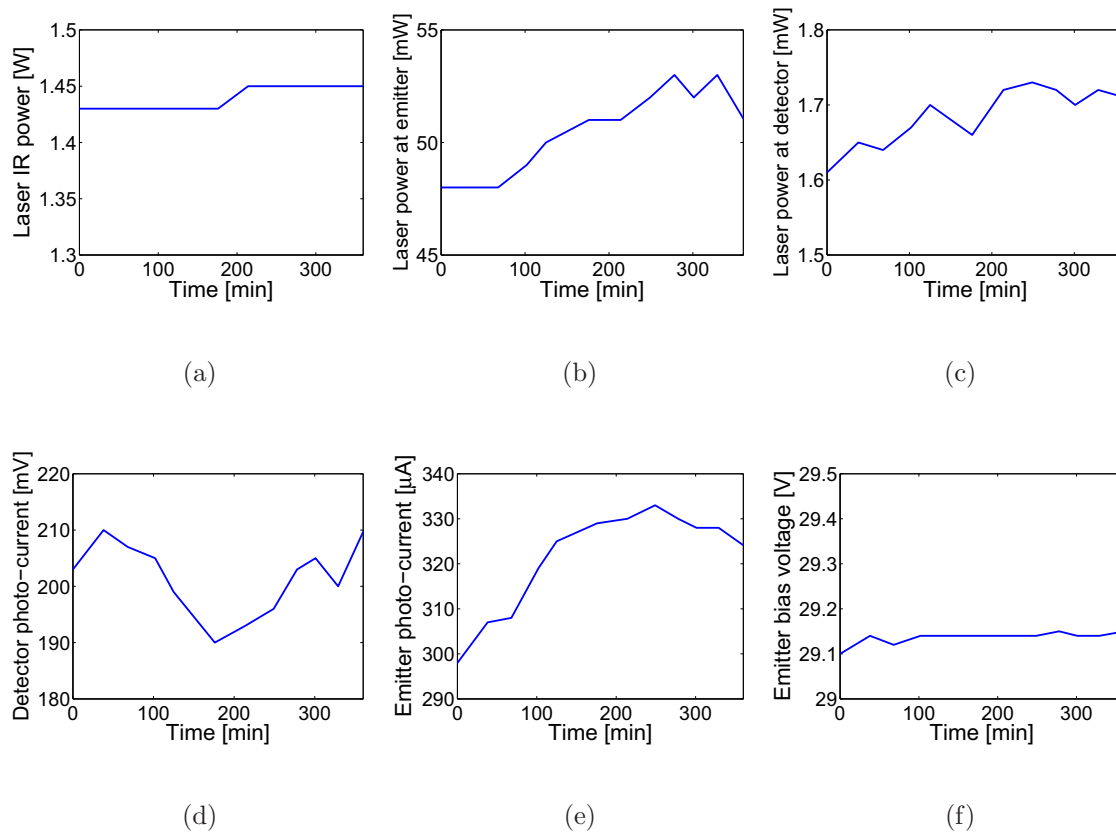


Figure 6.12. System parameters variation in time. (a) Laser IR power, laser power at the (b) emitter and (c) detector, (d) emitter and (e) detector photo-currents, and (f) emitter biased voltage variation in time.

Moreover, before commencing the experiments, i.e. inserting the waveguide in the set-up, we observe system parameters variation with time, thus establishing a base line for these measurements. For this purpose, we monitor the laser IR power, laser power at the emitter and detector, emitter and detector photo-currents, and emitter biased voltage for six hours. It generally takes six hours to conduct a set of measurements for a waveguide considering all the alignments. The variation of these system parameters with time are shown in Fig. 6.12.

The laser IR power has drifted 0.02 W, from 1.43 to 1.45 W during the six hours. While, the recorded powers at the emitter and detector varies from 48 to 53 mW and 1.61 to 1.73 mW, respectively. The emitter bias voltage stays almost steady, i.e. only changes by 0.04 V. The antennas may also heat up during these six hours. All these parameters result in a 30 μA drift in emitter photo-current and 20 mV drift in the voltage measured after the preamplifier.

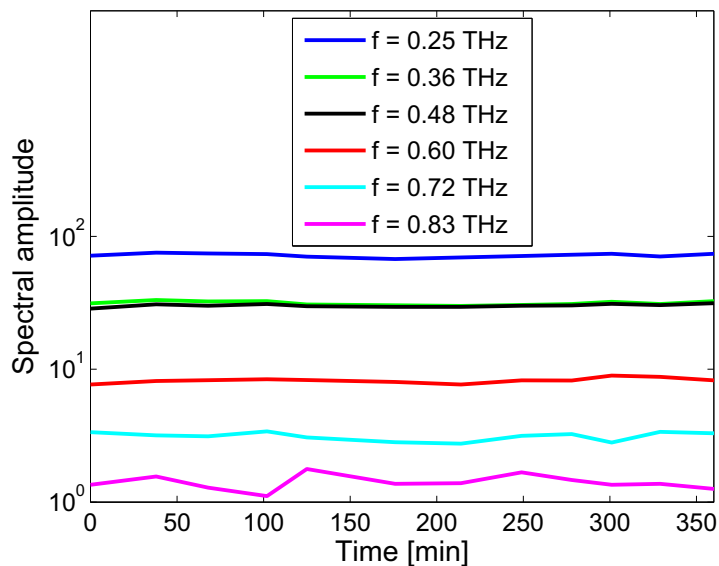


Figure 6.13. Spectral amplitude variation in time. The effect of system parameters variation on the spectral amplitude of the THz pulse in time is shown for six different frequencies.

We also analyse the system parameters effect on the spectral amplitude of the THz pulse. From the THz pulses recorded during this period the standard deviation of the spectral amplitude as a function of time can be calculated. The effect of system parameter variations, as a function of time, on the spectral amplitude are shown for six frequencies in Fig. 6.13. Standard deviations of the spectral amplitude for 0.25, 0.36, and 0.48 THz are 4.68, 2.12 and 1.6, respectively. The standard deviation calculated here is adjusted (according to the ratio of spectral amplitude for each frequency) and is used later as a benchmark for characterisation of the porous fibres.

To facilitate the alignment of the porous fibre, a suitable holder is designed to allow the fibre to be adjusted in three dimensions, minimal interference to the propagating mode. Two 3D manual moving stages, shown in Fig. 6.14, are used for adjusting the waveguide in the system. The fibre is mounted in a plastic ring holder as shown in the inset of Fig. 6.14. The porous fibre is glued to the centre of the plastic holder, which itself is connected to the outer ring via three slim struts outer ring of the plastic holder. Then the plastic holder is placed inside a fibre mount and is mounted on the 3D stages.

For waveguide characterisation, the waveguide and holders are first positioned in the system. For this purpose, the moving table/plate is slid to the left and the waveguide input end is positioned at the focal point of second parabolic mirror. In order to prevent stray beams (not coupled into the waveguide) reaching the detector and also increasing

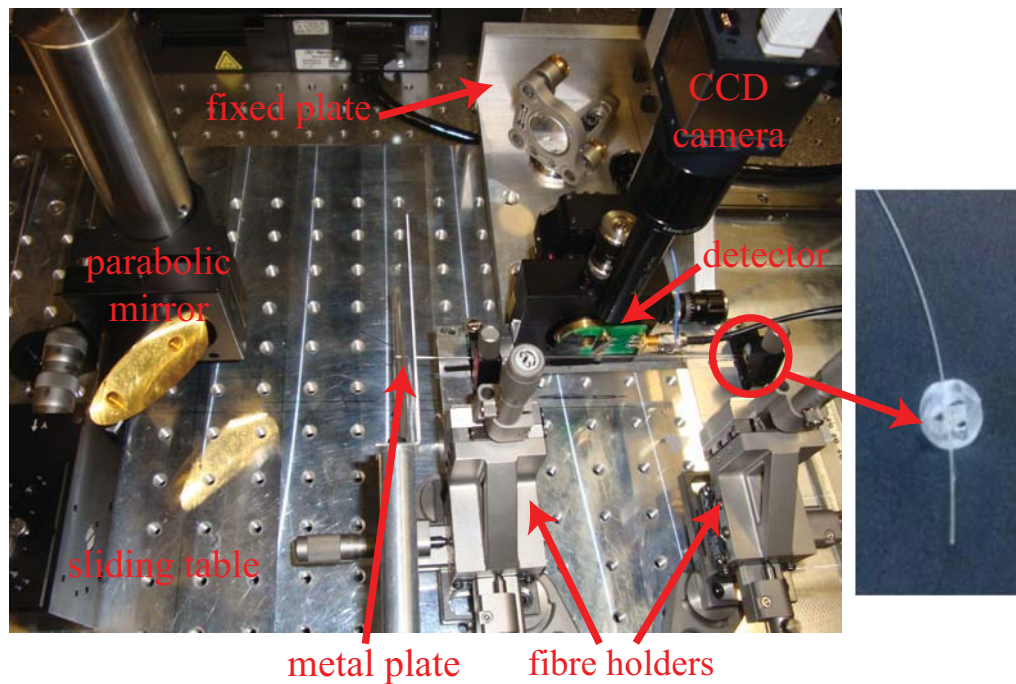


Figure 6.14. Image of a section of the experimental setup. The image illustrates a section of experimental setup that includes the waveguide holders, detector, metal plated employed for blocking of stray beams, and second parabolic. The special plastic holder, which has minimal interference with the propagating mode outside the waveguide, is shown in the inset.

the coupling of THz pulses into the waveguide, three different techniques are employed, as shown in Fig. 6.15. A silicon lens located in a metal plate, Fig. 6.15(a), a 600 μm pin-hole in a metal plate, Fig. 6.15(d), and a metallic cone with a 60° opening angle and 800 μm pin-hole at the vertex of the cone, Fig. 6.15(g), are examined. The THz pulse and spectral amplitude of the propagated pulse along the waveguide after 87-89 mm are recorded and shown in red in the right hand side figures of each coupling methods. The black lines shown in the figures are recorded pulses and spectral amplitudes when only the waveguide is removed from the system. In order to quantify the results, for each case we compare the peak to peak ratio of the signals, i.e. signal samples when the waveguide is in the system (red curves) and signal sampled when the waveguide is removed (black curves). These ratios are 1.5, 1.8, and 3.1 for the silicon lens located in a metal plate, pin-hole in a metal plate, and metallic cone, respectively. This indicates that using the cone for coupling the THz pulses into the waveguide is a better option for both input coupling and blocking stray beams. Thus for the experiments in this chapter the metal cone is used.

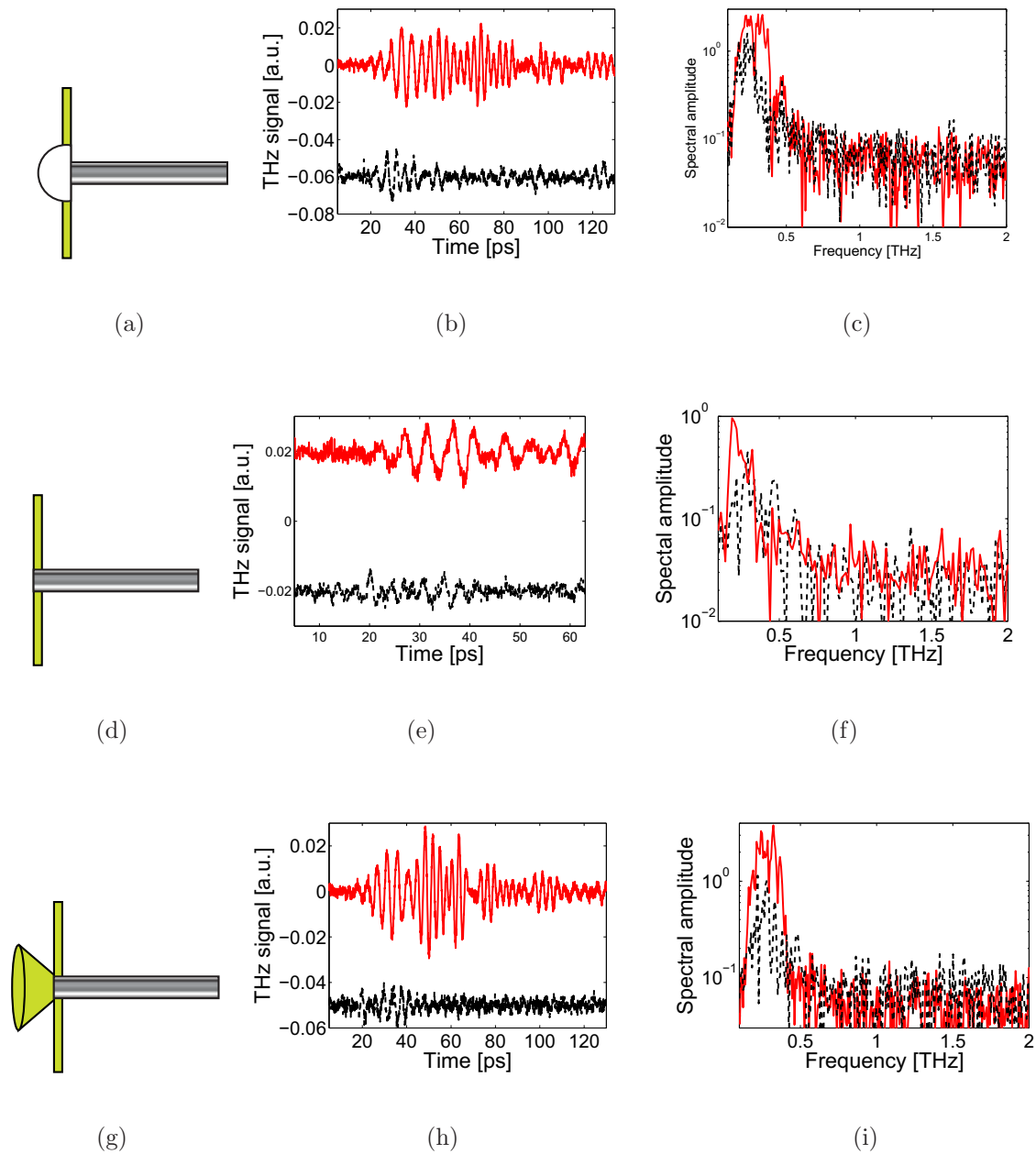


Figure 6.15. Three methods employed for input coupling into the waveguides. The first column represents the arrangement of different methods—(a) a silicon lens located in the metal plate, (b) a 600 μm pin-hole in a metal plate, and (c) a cone with a 60° opening angle—employed for coupling THz pulses into the waveguide. The second and third columns represent, respectively, measured THz signal in the time and frequency domains with (red lines) and without (black lines) waveguide in the system.

For characterisation of a COC spider-web porous fibre, the THz pulse at three different locations along the waveguide is sampled. First, the pulse is sampled at 75 mm from the waveguide input end, position A. Then the moving table/plate is slid 10 mm (position B) and 20 mm (position C) respectively to the left for the second and third sampling positions. The sampled THz signal and spectral amplitude for three positions are shown in Figs. 6.16(a) and 6.16(b), respectively. Also, the spectral amplitude of the signal sampled at position A when the waveguide is removed from the system is shown with a blue dotted line in Fig. 6.16(b). This spectral amplitude is used to define the noise floor of our measurement, i.e. the frequency window that the waveguide parameters (n_{eff} and α_{eff}) are valid. For this purpose a horizontal line is drawn that passes from the maximum of this curve. This line intercepts with the spectral amplitude curves at two points. These two points define the frequency limits of acceptable measurement data.

As discussed in the previous subsection (6.3.1), we set the time constant of the LIA to 1 s to increase the SNR. Another approach is to decrease the time constant (10 ms) and average the output signal with respect to time. The averaging in time reduces the white noise in the signal. Here, we select the second approach, i.e. each pulse in Fig. 6.16(a) represents the average of 10 scans each conducted with 10 ms time constant. The variation of the recorded signals during the scans are included in the error calculation, as discussed later.

Keeping the distance between the probe-tip and waveguide constant is the major challenge of this approach. Thus we use two cameras to monitor the alignment of the probe-tip and waveguide. The probe-tip distance from the waveguide is monitored by a CCD camera from a bird's eye view, as shown in Fig. 6.17(a). For each position the probe-tip is aligned so that it gently touches the waveguide. The horizontal alignment of the waveguide with the probe-tip is also monitored by another camera located in the same plane with the waveguide and probe-tip, as shown in Fig. 6.17(b). This second camera is used to make sure that the waveguide is aligned at the centre of the probe-tip.

Figures 6.16(c) and 6.16(d) illustrate the measured absorption coefficient (α_{eff}) and effective refractive index (n_{eff}) for a 600 μm diameter COC porous fibre. The α_{eff} and n_{eff} of the propagating mode is the average of the α_{eff} and n_{eff} values obtained by the comparison of the pulses sampled at positions A, B, and C, i.e. (A,B), (A,C), and (B,C). Theoretical values of α_{eff} and n_{eff} of real porous fibre (calculated based on SEM image) is also shown in red dotted lines. The theoretically calculated absorption coefficients, and effective refractive indices of both polarisations are shown in Figs. 6.16(c) and 6.16(d).

As mentioned in Chapter 5, this birefringence in spider-web fibres are by virtue of the ellipticity of the fabricated fibres. The measured values are in a good agreement with the expected theoretical values within the frequency range defined with the noise floor.

The error bars in Figs. 6.16(c) and 6.16(d) represent the standard deviation of the α_{eff} and n_{eff} values due to two major sources: length and signal variation during the 15 scans. For the length uncertainty, we consider ± 1 mm error in the values recorded from the ruler. These sources of error are independent, thus the total standard deviation for the measurements is equal to the quadrature sum of standard deviations obtained from the two sources described above. Absorption coefficients less than 0.08 cm^{-1} are measured at the frequency range of 0.2 to 0.35 THz, with the minimum of 0.003 at 0.24 THz. The measured effective refractive index curve follows closely the expected theoretical values, i.e. $n_{\text{eff}} < 1.05$ for $0.2 < f < 0.35$ THz. This leads to a normalized group velocity (ν_{g}/c) greater than 0.8, which is equivalent of dispersion values in between -1.3 and -0.5 ps/m/ μm for $0.2 < f < 0.35$ THz, with a zero-dispersion at 0.5 THz.

In this approach, no cleaving of the waveguide under investigation and consequently no realignment of the waveguide tips with the emitter and detector are required. Thus the uncertainty introduced due to this reason is reduced and the measured loss values are at the vicinity of expected theoretical values, shown in Fig. 6.16(c). The measured refractive index of the propagating mode closely follows the expected theoretical values as shown in Fig. 6.16(d).

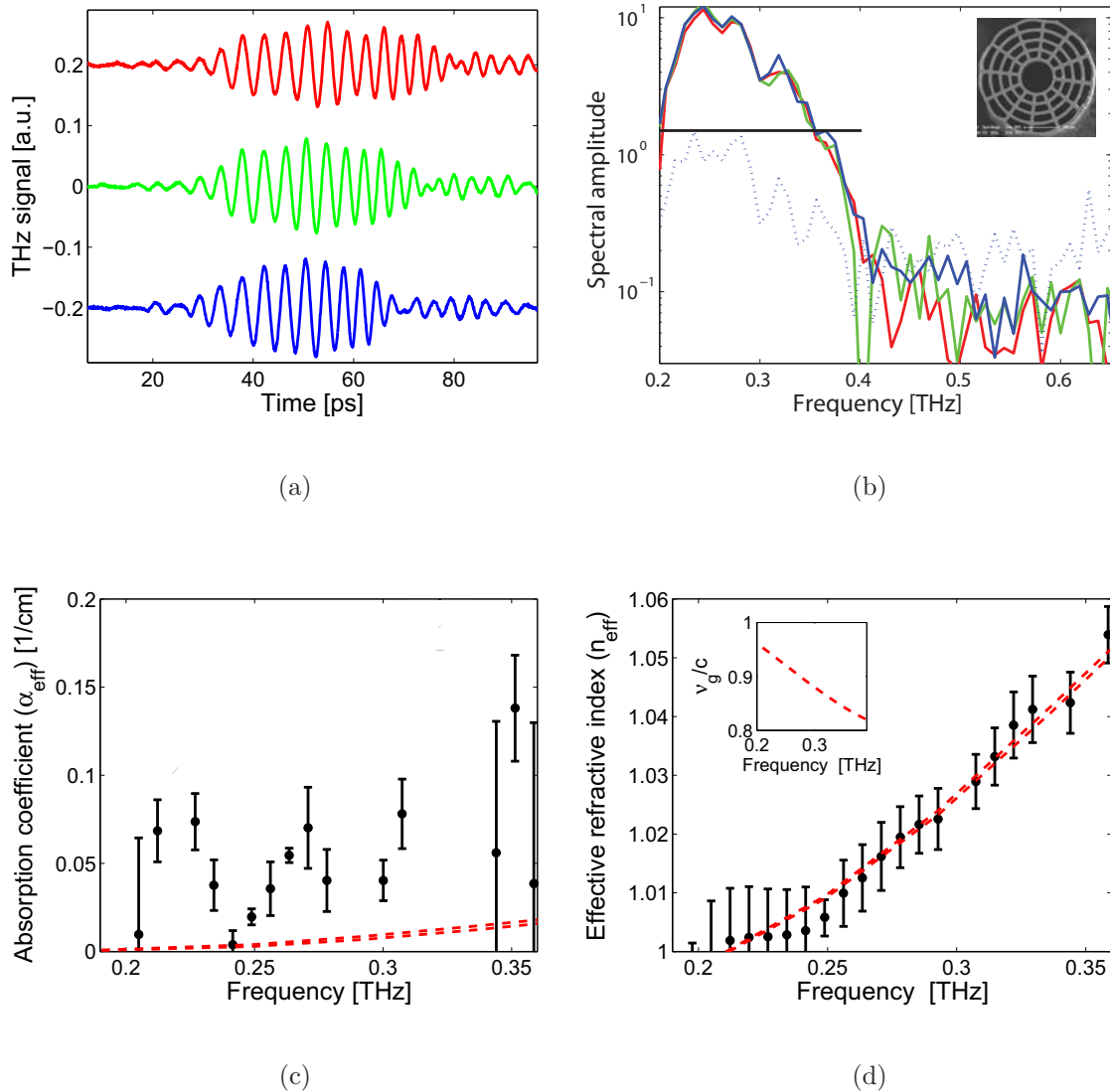


Figure 6.16. Measured THz signal, spectrum amplitude, and THz properties of a 600 μm COC spider-web porous fibre. (a) THz signal sampled at three different positions along the waveguide 10 mm apart. The pulses are separated vertically for clear display. The pulse samples at position A (closest to the tapered end of the waveguide), B, and C (furthest to the tapered end of the waveguide) are shown in respectively red (top), green (middle) and blue (bottom) lines. (b) Spectral amplitude of the three sampled pulses (solid line), and THz signal measured at position A when waveguide is removed. The horizontal black lines define the noise floor of the system. (c) Absorption coefficient (loss) and (d) effective refractive index of the propagating mode in the waveguide.

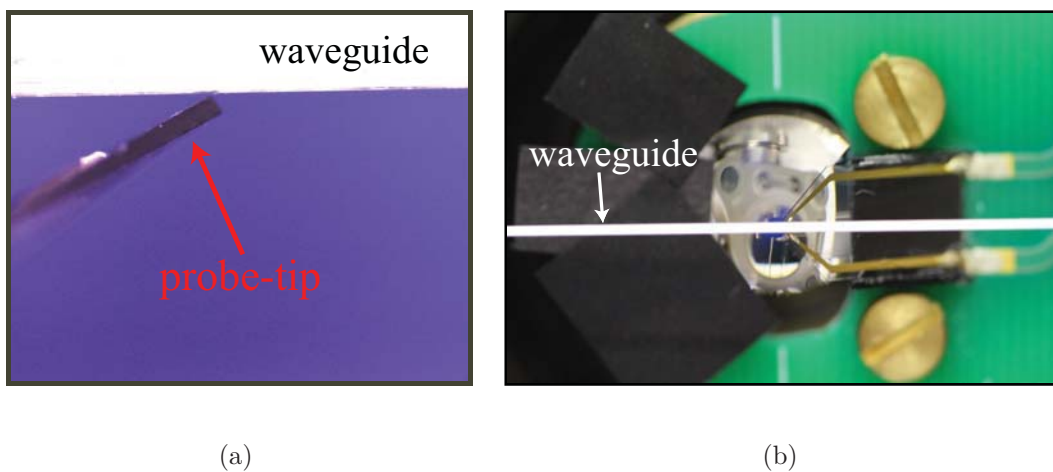


Figure 6.17. Monitoring the alignment of the probe-tip. The probe-tip and waveguide distance and alignment are monitored employing two cameras: (a) a CCD camera located at the bird's eye view and (b) a photographic camera with high zooming properties located in the same plane with the waveguide and probe-tip.

Second approach (without parabolic mirrors)

The schematic of the second arrangement of the experimental set-up employed for characterisation of porous fibres is shown in Fig. 6.10(b). As mentioned earlier, in this set-up no parabolic mirror is used for manipulating THz pulses. The waveguide and the coupling in cone are directly situated after the emitter (antenna array). In this arrangement also the emitter, focusing optical lens, and waveguide are situated on a sliding table and the detector (probe-tip) is fixed on the optical table, Fig. 6.10(b). The moving table is slid back and forth to sample the THz pulse at different locations along the waveguide. The position of the table for each point is recorded by a ruler with millimetre precision.

Figures 6.18(a) and 6.18(b) show respectively THz signals and spectral amplitudes recorded on four different positions along a $540\ \mu\text{m}$ diameter porous fibre. The first point, position A (shown in blue), is located at 100 mm from the waveguide input end. The next three positions, i.e. B (green), C (red), and D (black), are each located 50 mm apart. As in the first approach, each signal represents the average of 10 scans with 10 ms time constant.

Due to the low loss characteristics of the COC porous fibres, the calculated spectra for the chosen points (50 mm apart) are very close. Even for some points the spectrum amplitude of the longer lengths (e.g. scan at position D) is higher than the points before hand due to the environmental noise and system parameter variations. Thus for the absorption coefficient and refractive index calculation, we only consider (A,B) and (B,C) scan pairs.

In order to achieve a reliable data set, where the amplitude reduction in the time domain is mainly due to the loss and not dispersion, longer lengths (300 mm) in between the two sampling points are required. As an example for a 540 μm diameter COC porous fibre a $\Delta L = 50$ mm results in $\Delta P = 0.98$ and 0.95 respectively at $f = 0.29$ and 0.34 THz, while a $\Delta L = 300$ mm results in $\Delta P = 0.87$ and 0.75 respectively at $f = 0.29$ and 0.34 THz. However, due to system design and arrangements (sliding table dimension, waveguide holders, and emitter and probe-tip holder) the maximum movement (maximum distance between the first and last point) is limited to 150 mm in the current setup.

Figures 6.18(c) and 6.18(d) show the measured absorption coefficient and effective refractive index. The number of points on Fig. 6.18(c) is less than the number of points on Fig. 6.18(d). This is because the ratio of amplitudes at some frequencies is negative, i.e. the amplitude of the spectrum for the longer length is stronger than that of the shorter lengths. Thus, these points, where “pseudo” amplification of the spectral amplitude occurs, are omitted from the graph. The vertical dotted lines on Figs. 6.18(c) and 6.18(d) represent the region over which the calculation is valid, i.e. the spectrum amplitude propagated through waveguide is higher than the noise level. For these measurements the spectrum amplitude of the system when the waveguide is removed, Fig. 6.19(b), is considered as the noise level of the system.

In order to verify that the measured signals are associated with the mode traveling through the waveguide and to find out the noise level, we also measure the signals after removing the waveguide for each position. Figure 6.19 shows the signals recorded at positions A and D, with (solid lines) and without (dotted lines) the waveguide in the system. The opening pin-hole at the vertex of the cone is 800 μm . This leads to small stray beams going through the cone, shown with dotted lines. The spectrum of the signal at position A with and without the waveguide, and position D without the waveguide are shown in Fig. 6.19(b). The black vertical line represents the noise floor in the system, which intercepts with the signal spectrum propagating through the waveguide at 2.2 and 3.2 THz. These frequencies are identical to the positions of vertical lines illustrated in Figs. 6.18(c) and 6.18(d). The noise floor in this approach is higher than that of the previous approach, Fig. 6.16(b). We mainly contribute this to waveguide dimension, i.e. the waveguide diameters are 600 μm and 540 μm respectively for the first and second approaches, while the pin-hole size at the vertex for both approaches are 800 μm . This leads to more stray beams for the second approach, resulting in a higher noise floor.

We have also measured the frequency-dependent radial field distribution of the waveguide. For this purpose, the probe-tip has been moved away from the waveguide and the THz pulse is measured at different positions. Figure 6.20 shows the measured radial electric field distribution at three different frequencies, 0.18, 0.23, and 0.28 THz. The fields are normalised to the respective maximum amplitude at the waveguide surface. The curves indicate that increasing the frequency increases the confinement of the field to the waveguide. For comparison, the theoretical values of the normalised radial distribution of the electric fields of a real spider-web porous fibre are calculated and shown in solid lines. According to the measurements, the diameter of the waveguide under investigation varies from 570 μm to 640 μm . Thus, a 600 μm diameter porous fibre is considered for the theoretical calculation.

The vertical error bars in Fig. 6.20 represent the standard variations of the signal alteration during the measurement. For each position 8 scans with a 10 ms time constant are recorded. The horizontal error bars represent the total standard deviation due to the elliptical shape of the waveguide, and polarisation state at the measurement point. The real waveguide has a slightly elliptical cross-section as shown in Fig. 5.12(c). The measurement carried out can be starting from any location of this elliptical surface. The results are depicted from 300 μm (average waveguide radius) and the diameter variation is considered as a horizontal source of error. Moreover, the elliptical surface results in birefringence, i.e. the effective refractive index of the mode continuously varies with the electric field orientation angle between maximum and minimum values that are spaced 90°. The polarisation state of the linearly polarised THz pulse changes from linear to elliptical and circular as the pulse propagates along the waveguide. Thus, the detector at any location along the waveguide samples the projection of the electric field along the probe-tip. This projection could be x - or y -components or the total electric field of the propagating mode, depending of the polarisation at the probe-tip location. There is a subtle difference in the decay rate of these three electric fields. The x -component of the electric field is depicted and the difference is included as a horizontal error source in the measured curves.

With all the error sources considered, the experimental results are in a good agreement with the simulated results based on fabricated waveguide, i.e. the experimental curves follow closely the trend of the simulated curves. This indicates the low invasiveness of the applied probe-tip. In order to observe the effect of the presence of the probe-tip, a thorough investigation is required. Exploiting the probe-tip of characterisation of

the waveguide, especially measuring the evanescent electric field open up new doors for sensing applications, especially where the interaction of electric with dipole molecules are required.

6.4 Chapter Summary

In this chapter, we used two different techniques to characterise porous fibres. In the first method for characterisation of a waveguide, the waveguide is positioned in between the emitter and detector, and three waveguides with different lengths are measured for each experiment. The measurement is carried out for PMMA spider-web and rectangular porous fibres, and a microwire. The measured refractive indices show a good agreement with the expected theoretical values. A birefringence of 0.012 at 0.65 THz is achieved for the rectangular porous fibre. However, the measured loss values are higher than expected theoretical values. We attribute this mainly to the method of the measurement, i.e. employing three different lengths for each waveguide and slight curvature of the waveguides.

One practical consideration is the annealing of polymer porous fibres before the experiment. This reduces the stress generated during fibre drawing resulting in a straighter fibre for the experiment. Subsequently the radiation losses due to the fibre curvature will be suppressed especially for the first method where the waveguide is held with only one holder in the centre.

In the second method we have employed a probe-tip for the sampling of THz pulses. The existence of the field in the air-cladding of the waveguide allows the sampling of the propagating mode from the waveguide side. Thus instead of using three different lengths, we sampled THz pulses at three different locations along a waveguide. The measurements are carried out for COC spider-web porous fibres. A metal cone terminating with a pin-hole of 800 μm is used for coupling the THz pulses into the waveguide. The pin-hole almost blocks the stray THz beams and the cone increases the coupling into the waveguide. Two different arrangements are proposed, one employing parabolic mirrors for manipulating THz pulses and the other situating the waveguide straight after the emitter. The resulting absorption coefficient and refractive index are in agreement with the expected theoretical values. Moreover, the radial distribution of electric field as a function of frequency has been investigated. As expected the electric field becomes more confined to the structure as the frequency increases. The waveguides in the second method of measurement are

almost straight, since the waveguide is held from both ends, which reduces the bending losses.

A practical consideration is the theoretical study of the affect of the metal cone on the signal. This coupling device introduces a low frequency cut-off in the main signal that results in complication in the analysis of the extreme low frequency region of the waveguide.

The results presented in this chapter suggest that these porous fibres have low loss and low dispersion characteristics and can be practically designed to maintain polarization of the field. Therefore these waveguides are a promising polymer waveguide solution and a good substitute for free-space THz propagation. This also opens up new opportunities in THz biosensing, where the porous fibres can be used to sense ultra small sample sizes.

An outline of the practical issues faced during the experiment is that the length of moving plate and arrangement of the setup on the optical table was not appropriate to accommodate waveguides longer than 300-350 mm. Therefore, the system needs to be modified to accommodate longer waveguides so the measured loss values closely follow the expected theoretical values.

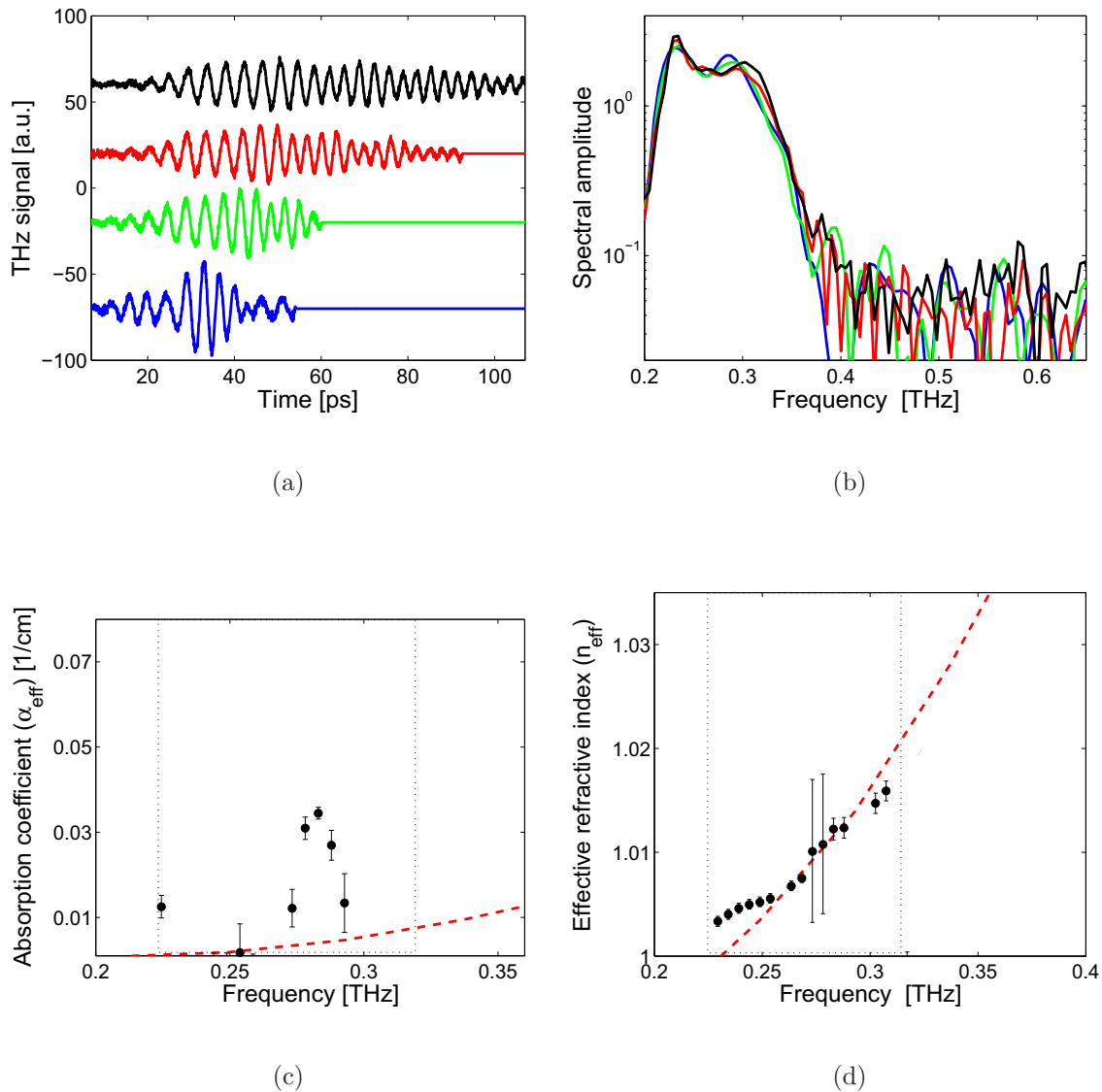


Figure 6.18. Measured THz signal, spectrum amplitude, and THz properties of a 540 μm diameter COC spider-web porous fibre. (a) THz signal sampled at four different positions along the waveguide 50 mm apart. The pulses are separated vertically for clear display. The pulse samples at position A (closest to the input end of the waveguide), B, C, and D (furthest to the input end of the waveguide) are shown in respectively blue, green, red, and black colours. (b) Spectral amplitude of the four sampled pulses. (c) Absorption coefficient (loss) and (d) effective refractive index of the propagating mode in the waveguide. The vertical dotted lines represent the region where the spectrum amplitude of the signal is higher than the noise level, shown with vertical solid line in Fig. 6.19(b).

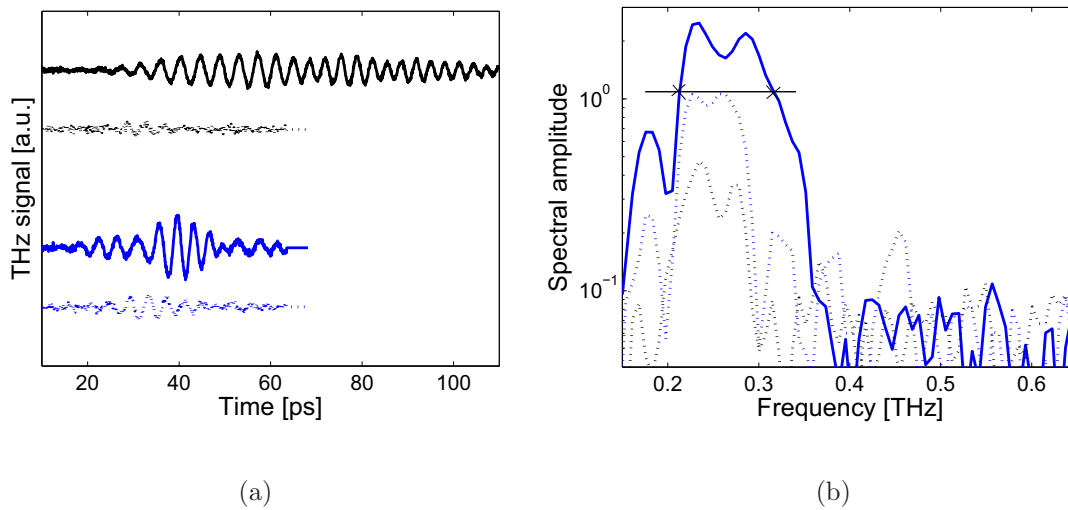


Figure 6.19. Measured THz signal with and without waveguide in the system. (a) THz signal is measured at two different locations along a $540 \mu\text{m}$ diameter COC spider-web porous fibre: blue solid line (closer to the input end of the waveguide: position A) and black solid line (closer to the output end of the waveguide: position B). The dotted lines represent the stray THz beams and are measured when only the waveguide is removed from the system. The vertical separation is for clear display. (b) The spectrum of measured signal at position A (solid blue line) and the stray beams at positions A and D (dotted blue and black lines, respectively). The black horizontal line represents the noise floor, i.e. above this line the spectrum amplitude propagated through waveguide is higher than that of the stray beams in the system. Note that the calculated n_{eff} and α_{eff} values are valid for the frequencies in between the crosses.

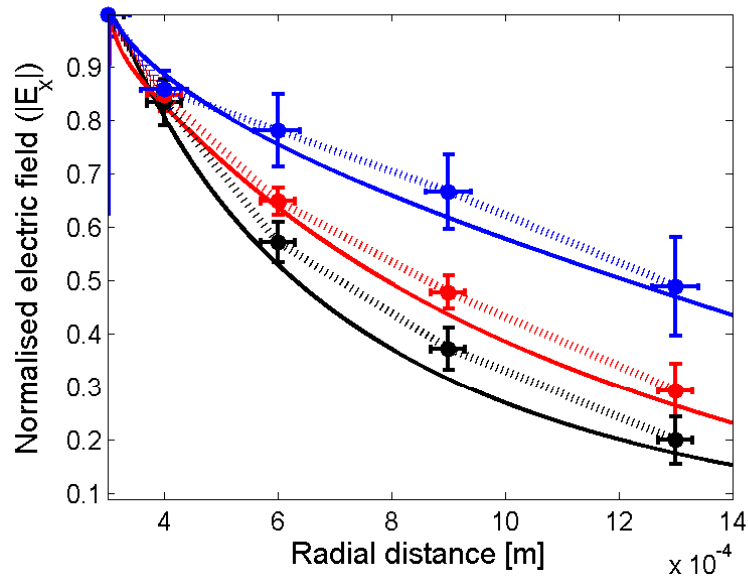


Figure 6.20. Frequency-dependent radial field distribution of a 600 μm diameter COC spider-web porous fibre. Measured radial field distribution from the waveguide interface for three different frequencies: 0.18 THz (blue dotted line), 0.23 THz (red dotted line), and 0.28 THz (black dotted line). The solid lines represent the theoretical values (simulated for a 600 μm diameter porous fibre based on SEM image) of normalised radial distribution of x -component of the electric fields for the same three frequencies.

Chapter 7

Conclusion and future work

THIS chapter summarises the key conclusions of this thesis and suggests further directions for future work. Chapters 1 and 2 contain introduction and review material that embraces THz generation, detection and waveguides. Chapters 3 to 6 contain the original contributions of this work on porous fibres design, fabrication and characterisation.

7.1 Introduction

The efficient transmission of THz signals using waveguides has been a major challenge since early days of THz science. Loss and dispersion are the primary parameters in THz waveguides that one aims to minimize in order to obtain undistorted propagation of THz pulses. Metallic waveguides suffer from Ohmic losses while dielectric waveguides suffer from material absorption losses. Dry air is the best transparent medium for THz pulses. Therefore, intelligent design of waveguides are required to overcome Ohmic and material loss limitations. Porous fibres proposed in this thesis are an example of this approach. This chapter focuses on summarising the thesis, and author's contributions, and discusses possible future directions for continued development in this domain.

7.2 Thesis summary and author's contribution

A thorough review of THz waveguides, especially focused on dielectric waveguides has been conducted in Chapter 2.

Employing air-clad sub-wavelength dielectric waveguide, i.e. microwire, is an approach to improve the loss and dispersion. We have analysed the microwire concept with different glass and polymer host materials (Withayachumnankul *et al.* 2007). First, THz properties of four glasses and two polymers have been investigated in Chapter 3. Although the glasses are suitable material for far infrared and optics, they have higher absorption losses (more than 10 times) compared to polymers. The concept of guiding through air-clad sub-wavelength waveguides (microwires) has been examined in detail. For this purpose we have evaluated propagating mode properties, i.e. effective refractive index, field distribution, power fraction, effective area, effective material and bend losses, and dispersion for both glass and polymer materials. The vectorial form of Maxwell's equation has been employed to evaluate the propagation constants of the modes. Moreover, the Poynting vector is employed for representation of the energy flux of the propagating mode and evaluation of waveguide parameters. We illustrate that regardless of host material employed, an effective material loss less than 0.01 cm^{-1} is achievable for microwires (Withayachumnankul *et al.* 2007). This is due to the fact that almost most of the mode power is in the air-cladding, which makes microwires susceptible to any gentle bend and environmental perturbation. We have also demonstrated that the diameter at which low material loss is achieved, the higher limit of the microwire loss when most of the mode is in the core, and the frequency dependent of the loss and dispersion depend on

the host material properties. As expected, polymer microwires have lower material loss and dispersion compared to that of glass microwires. We have also shown that dominant loss mechanism in microwires is effective material loss provided that the waveguide is kept straight. The work in this Chapter has resulted in four conference papers—(Atakaramians *et al.* 2006a), (Atakaramians *et al.* 2006b), (Afshar Vahid *et al.* 2007), and (Atakaramians *et al.* 2007)—and a journal paper—(Withayachumnankul *et al.* 2007) ²⁴.

Low losses are achieved in air-clad sub-wavelength waveguides, microwires, because almost all the mode propagates in the medium surrounding the structure, air. This, however, results in weak confinement of the guided mode within the structure that makes the guided mode susceptible to any small perturbation on the surface or vicinity of the structure, since a large portion of the guided power can be readily coupled into radiation modes. Furthermore, the guided modes within these structures suffer strong bend loss. In Chapter 4, we propose a novel class of dielectric waveguides, porous fibres, to improve the confinement of the mode while still maintaining the low loss characteristics (Atakaramians *et al.* 2008e). These waveguides have porous transverse cross-section, i.e. sub-wavelength features in the core, which leads to enhancement and confinement of the field within the holes. For similar loss values, porous fibers enable reduced distortion (frequency dependent loss and dispersion) of a broadband THz pulse compared to microwires. We also demonstrate for the first time that introducing asymmetrical sub-wavelength air-holes in the core of porous fibres leads to a birefringence $|n_x - n_y| \approx 0.026$. This value is comparable to recently achieved high birefringence in THz and optical microstructured fibres (Chen *et al.* 2004, Cho *et al.* 2008, Ren *et al.* 2008). This opens up the potential for realisation of novel polarisation preserving fibres in the terahertz regime (Atakaramians *et al.* 2008a). The work in this Chapter has resulted to three conference papers—(Atakaramians *et al.* 2008c), (Atakaramians *et al.* 2008d), and (Atakaramians *et al.* 2008b)—and two journal papers—(Atakaramians *et al.* 2008e) and (Atakaramians *et al.* 2008a) ²⁵.

Fabrication of highly porous fibres is not trivial. There have been attempts that were not very successful as described in Chapter 5. We demonstrate the first successful design

²⁴All the theoretical work, analytical and numerical code, and experiments conducted in Chapter 3 are the PhD candidate's work. The THz spectroscopy of the bulk material and initial material loss studies of microwires were conducted before commencing date of author's candidature, i.e. during a visiting period at The University of Adelaide.

²⁵All the theoretical and numerical code is developed by the PhD candidate. The numerical code is expanded and further developed for porous fibre purposes from the general fibre code written by Dr Kris Roland for which I am thankful.

and fabrication of highly porous polymer THz waveguides exploiting the extrusion technique. Two different porous fibres, with symmetrical and asymmetrical sub-wavelength features, with porosities higher than 50% have been fabricated successfully (Atakaramians *et al.* 2009c). The numerical analysis of waveguide cross-sections based on SEM images of fabricated waveguides reveals that the fabricated waveguides are almost similar to the designed cross-sections. Furthermore as discussed in Chapter 5, the cleaving process of polymer porous fibres with high air-filling factor is challenging. Conventional cleaving techniques (e.g. utilising cleaving blades) used for cleaving of optical fibres, squashes and deforms the soft fibre structure. In collaboration with researchers at MicroEngineering group at DSTO Edinburgh Adelaide, Australian Microscopy and Microanalysis Research Facility (AMMRF), and Interdisciplinary Photonics Laboratories (iPL) at University of Sydney, several techniques have been investigated for cleaving of THz porous fibres. The investigations reveal that employing the 193 nm ultraviolet laser leads to fast and reproducible cleaves (Atakaramians *et al.* 2009d). The combination of work in this Chapter and next Chapter has been published in two conference papers—(Atakaramians *et al.* 2009b) and (Atakaramians *et al.* 2009a)—and two journal papers—(Atakaramians *et al.* 2009c) and (Atakaramians *et al.* 2009d) ²⁶.

In Chapter 6, we have demonstrated the first experimental characterization of effective refractive indices (n_{eff}) of symmetrical and asymmetrical porous fibres in collaboration with researchers at Institut für Halbleitertechnik at RWTH Aachen University (Atakaramians *et al.* 2008e). There is a great uncertainty in the measured loss values in this approach, which we attribute to waveguide realignment, cleaving, and bend losses. The PhD candidate has developed a measurement technique exploiting a sampling probe-tip for the first time for characterisation of THz fibres. The probe-tip allows sampling the propagating mode along the waveguide eliminating the need for cleaving of porous fibres, which is required for waveguide characterisation. The measured loss values in this approach are

²⁶The PhD candidate designed the rectangular porous fibre die exit, and conducted all the preform fabrication processes (preparation and execution) discussed in this work, with significant guidance and education from Dr Heike Ebendorff-Heidepriem. The fibre drawing process was conducted by Roger Moore with the PhD candidate's assistance for by-the-minute microscope fibre structure diagnosis. The PhD candidate visited all the mentioned institutions for collaboration and directly worked with the researchers for conducting the experiments. All the preparation of the samples, analysis of the results, and SEM images were carried out by the PhD candidate, save for the operation of the equipment that was conducted by Dean Stone, Leonard Green, and Dr Kevin Cook for which the author is thankful. Many thanks from Dr Heike Ebendorff-Heidepriem and Prof John Canning for their assistance in analysing and interpreting the cleaving results.

in the vicinity of expected theoretical values. For the first time, we have measured the evanescent field distribution of the propagating mode of THz porous fibres²⁷.

7.3 Potential future directions

In summary, this thesis has laid the groundwork for a powerful new form of THz guiding fibre, the porous fibre. There are now strong opportunities for using it for practical applications, most particularly for biosensing. These fibres, if used as biosensors, will increase the field interaction with biosample and will reduce the amount of sample required. This section surveys the scope of the future work in the area of THz porous fibres and microwires and application as THz biosensors.

7.3.1 Mode profile of THz microwire and porous fibre

The probe-tip employed for the sampling of THz pulses along the waveguide enables the measurement of the frequency-dependent radial field distribution of the waveguide. Furthermore, the system can be modified to measure the frequency dependent waveguide cross-section mode profile. This near-field THz detection will potentially confirm the single mode propagation and field enhancement at the core-clad surface of microwire and in the sub-wavelength air-holes of porous fibres.

7.3.2 THz beam coupling into THz microwire and porous fibre

Different techniques can be employed to couple the THz beam into the THz microwire and porous fibre, as illustrated in Chapter 6. A straight forward way of coupling the field into the waveguide is by simply abutting the structure on the planar THz emitter. As improving the coupling efficiency is desirable, other methods of coupling, off-axis parabolic mirrors in conjunction with hyper hemispherical lenses, and a metallic cone starting from a diameter equal to the beam width down to the waveguide diameter can

²⁷The PhD candidate visited and conducted the first set of waveguide measurements at the Institute of Semiconductors at RWTH Aachen University. The design and implementation of the second approach was carried out by the PhD candidate, which resulted in construction of the first THz waveguide characterization system in Australia. Many thanks from Markus Wächter and Dr Michael Nagal from Institut für Halbleitertechnik at RWTH Aachen University for assistance with THz hardware during the visit, and assistance with analysing and interpreting the results, respectively.

be investigated experimentally. A thorough theoretical evaluation of the coupling beam into the waveguide accompanied by experimental verification can be conducted to discover the best approach in terms of maximum beam coupling into the waveguide, and minimal stray beams in the vicinity of the waveguide.

7.3.3 Bending loss of the THz microwire and porous fibre

Another practical investigation is the bending loss of THz microwires and porous fibres. Employing the probe-tip will allow sampling along the bend curvature of the waveguide. This will result in detailed evaluation of the radiation losses at every point along the curvature.

7.3.4 THz microwire as a biosensor

Due to the field enhancement at the air-clad interface and large power fraction in the evanescent field of the THz microwire, if a biosample is placed at the vicinity of the core-clad interface, the waveguide can be used as THz biosensor. Even when a short length of THz microwire is dipped into the sample material, the propagation properties will change depending on the dielectric function of the sample in the THz frequency range. The microwires can be designed in a similar fashion to suspended nanowires (Ebendorff-Heidepriem *et al.* 2009) to limit the sample volume in between the core and a thin tube layer. By comparing the field propagation in air to the propagation in the sample, we can extract the dielectric function of the sample as a function of frequency in order to obtain a spectral “fingerprint”. As the field decays quite quickly from the microwire surface, only a small volume of the sample surrounding the waveguide is required. Artificial RNA strands, and lysozyme (fibrous and non-fibrous) are the example of samples that can be considered for this purpose (Nagel *et al.* 2003, Fischer *et al.* 2005). Furthermore, the possibility of surface modification of a polymer microwire in order to enhance protein or DNA binding directly on the surface of the waveguide can be investigated. These macro-molecules are the best to study since they have vibrational modes located in THz spectrum.

7.3.5 THz porous fibre as a biosensor

Although the small volume of the sample used for the biosensor proposed based on microwire will be minute, this volume would still be rather large for applications involving biomolecules such as proteins and DNA. Thus THz porous fibres can be employed as biosensors that exploit field enhancement in the sub-wavelength air-holes. Basic capillary effects can be utilised to load a liquid sample into the waveguide. An important point that should be considered for this investigation is the optimum number of the holes that is required to be filled with sample to obtain the optimal SNR and compare the results to that of the microwire. The initial experiment can be carried out using water and a solution of sugar, such as lactose, in a small straight length of THz porous fibre (to avoid bend loss). Later, polymer surface modification can be considered in order to extend this technique to complex biomolecules such as proteins and DNA. The amount of biosample required will be limited to the volume of sub-wavelength air-hole filled with the sample (very small compared to the sample required for free-space spectroscopy), and due to the strong field confinement, in the sub-wavelength air-hole, there will be a strong interaction between the sample and THz field.

7.4 Chapter summary

This Chapter has summarised an overview of the major conclusions of this Thesis accompanied by a number of recommendations for future work on THz waveguides. The work herein is unique, original, and is the foundation (concept, design, fabrication and experiment) of a powerful new form of THz guiding fibre, the porous fibre.

Derivation microwire equations

THIS appendix summarises the derivation of electromagnetic fields and the eigenvalue equation of the hybrid mode of a microwire. These equations are used in Chapter 3, Section 3.4.

It is possible to analytically calculate the propagation constant and electromagnetic fields of a microwire, air-clad solid core fibre. For this reason, we assume that the structure has a circular cross-section, an infinite air clad, and a step-index profile. It is also assumed that the wire is uniform in diameter and has a smooth sidewall. Moreover, we consider that the refractive index of air is equal to unity and the permeabilities of both media (core and clad) are equal to that of free-space.

The electromagnetic fields in an optical fibre are expressed in cylindrical coordinates as follows (Snyder and Love 2000, Okamoto 2000, Balanis 1989):

$$\vec{E} = \vec{E}(r, \phi) \exp j(\omega t - \beta_{\text{eff}} z), \quad (\text{A.1})$$

$$\vec{H} = \vec{H}(r, \phi) \exp j(\omega t - \beta_{\text{eff}} z), \quad (\text{A.2})$$

where β_{eff} is the propagation constant of the hybrid mode. Substituting Eqn. A.1 into Maxwell's equations, results into two sets of wave equations:

$$\frac{\partial^2 E_z}{\partial r^2} + \frac{1}{r} \frac{\partial E_z}{\partial r} + \frac{1}{r^2} \frac{\partial^2 E_z}{\partial \phi^2} + [\beta_0^2 n(r)^2] - \beta_{\text{eff}}^2 E_z = 0 \quad (\text{A.3})$$

$$\frac{\partial^2 H_z}{\partial r^2} + \frac{1}{r} \frac{\partial H_z}{\partial r} + \frac{1}{r^2} \frac{\partial^2 H_z}{\partial \phi^2} + [\beta_0^2 n(r)^2] - \beta_{\text{eff}}^2 H_z = 0 \quad (\text{A.4})$$

where β_0 is free-space propagation constant, $n(r)$ is the refractive index of the medium, i.e. for microwire $n(r) = n_{\text{core}}$ for $r \leq a$ and $n(r) = 1$ for $r > a$. The transverse electromagnetic fields are related to E_z and H_z as follows:

$$E_r = -\frac{j}{[\beta_0^2 n(r)^2] - \beta_{\text{eff}}^2} \left(\beta \frac{\partial E_z}{\partial r} + \frac{\omega \mu_0}{r} \frac{\partial H_z}{\partial \phi} \right) \quad (\text{A.5})$$

$$H_\phi = -\frac{j}{[\beta_0^2 n(r)^2] - \beta_{\text{eff}}^2} \left(\frac{\beta}{r} \frac{\partial E_z}{\partial \phi} - \omega \mu_0 \frac{\partial H_z}{\partial r} \right) \quad (\text{A.6})$$

$$E_r = -\frac{j}{[\beta_0^2 n(r)^2] - \beta_{\text{eff}}^2} \left(\beta \frac{\partial H_z}{\partial r} - \frac{\omega \epsilon_0 n(r)^2}{r} \frac{\partial E_z}{\partial \phi} \right) \quad (\text{A.7})$$

$$H_\phi = -\frac{j}{[\beta_0^2 n(r)^2] - \beta_{\text{eff}}^2} \left(\frac{\beta}{r} \frac{\partial H_z}{\partial \phi} + \omega \epsilon_0 n(r)^2 \frac{\partial E_z}{\partial r} \right). \quad (\text{A.8})$$

The solution of Eqn. A.3 in the cylindrical coordinates for microwire are given by the product of n th-order Bessel functions and $\cos(n\phi + \psi)$ and $\sin(n\phi + \psi)$ angular variations (Okamoto 2000, Balanis 1989). The boundary conditions on the core and air-clad

interface state that E_z and H_z should be continuous. Also, Eqns. A.5 to A.8 indicate that $\partial E_z/\partial r$ and $\partial H_z/\partial \phi$ (or $\partial E_z/\partial \phi$ and $\partial H_z/\partial r$) have the same ϕ dependencies. Therefore, the z -component of the electromagnetic field of a microwire are expressed by

$$E_z = \begin{cases} AJ_n(\frac{u}{a}r) \cos(n\phi + \psi) & (0 \leq r \leq a) \\ A\frac{J_n(u)}{K_n(w)}K_n(\frac{w}{a}r) \cos(n\phi + \psi) & (r > a) \end{cases} \quad (\text{A.9})$$

$$H_z = \begin{cases} CJ_n(\frac{u}{a}r) \sin(n\phi + \psi) & (0 \leq r \leq a) \\ C\frac{J_n(u)}{K_n(w)}K_n(\frac{w}{a}r) \sin(n\phi + \psi) & (r > a) \end{cases} \quad (\text{A.10})$$

where, A and C are constants, ψ is the phase of the fields, J_n is the Bessel function of the first kind, and K_n is the modified Bessel function of the second kind. Here, u and w are normalised transverse wave numbers in the dielectric (Eqn. 3.9) and air (Eqn. 3.10) region, respectively. The equations are repeated here for convenience:

$$u = a\sqrt{\beta_0^2 n_1^2 - \beta_{\text{eff}}^2} \quad (\text{A.11})$$

$$w = a\sqrt{\beta_{\text{eff}}^2 - \beta_0^2}. \quad (\text{A.12})$$

Substituting Eqns. A.9 and A.10 in Eqns. A.5 to A.8 leads to transverse component of the electromagnetic field for microwires:

$$E_r = \begin{cases} -\frac{ja^2}{u^2} [A\beta_{\text{eff}}\frac{u}{a}J_n'(\frac{u}{a}r) + C\omega\mu_0\frac{n}{r}J_n(\frac{u}{a}r)] \cos(n\phi + \psi) & (0 \leq r \leq a) \\ \frac{ja^2}{w^2} [A\beta_{\text{eff}}\frac{w}{a}K_n'(\frac{w}{a}r) + C\omega\mu_0\frac{n}{r}K_n(\frac{w}{a}r)] \frac{J_n(u)}{K_n(w)} \cos(n\phi + \psi) & (r > a) \end{cases} \quad (\text{A.13})$$

$$E_\phi = \begin{cases} -\frac{ja^2}{u^2} [-A\beta_{\text{eff}}\frac{n}{r}J_n(\frac{u}{a}r) - C\omega\mu_0\frac{u}{a}J_n'(\frac{u}{a}r)] \sin(n\phi + \psi) & (0 \leq r \leq a) \\ \frac{ja^2}{w^2} [-A\beta_{\text{eff}}\frac{n}{r}K_n(\frac{w}{a}r) - C\omega\mu_0\frac{w}{a}K_n'(\frac{w}{a}r)] \frac{J_n(u)}{K_n(w)} \sin(n\phi + \psi) & (r > a) \end{cases} \quad (\text{A.14})$$

$$H_r = \begin{cases} -\frac{ja^2}{u^2} [A\omega\epsilon_0 n_{\text{core}}^2 \frac{n}{r}J_n(\frac{u}{a}r) + C\beta_{\text{eff}}\frac{u}{a}J_n'(\frac{u}{a}r)] \sin(n\phi + \psi) & (0 \leq r \leq a) \\ \frac{ja^2}{w^2} [A\omega\epsilon_0 \frac{n}{r}K_n(\frac{w}{a}r) + C\beta_{\text{eff}}\frac{w}{a}K_n'(\frac{w}{a}r)] \frac{J_n(u)}{K_n(w)} \sin(n\phi + \psi) & (r > a) \end{cases} \quad (\text{A.15})$$

$$H_\phi = \begin{cases} -\frac{ja^2}{u^2} [A\omega\epsilon_0 n_{\text{core}}^2 \frac{n}{r}J_n'(\frac{u}{a}r) + C\beta_{\text{eff}}\frac{n}{r}J_n(\frac{u}{a}r)] \cos(n\phi + \psi) & (0 \leq r \leq a) \\ \frac{ja^2}{w^2} [A\omega\epsilon_0 \frac{w}{a}K_n'(\frac{w}{a}r) + C\beta_{\text{eff}}\frac{n}{r}K_n(\frac{w}{a}r)] \frac{J_n(u)}{K_n(w)} \cos(n\phi + \psi) & (r > a) \end{cases} \quad (\text{A.16})$$

The continuity of E_ϕ at $r = a$ in Eqn. A.14 leads to:

$$A\beta \left(\frac{1}{u^2} + \frac{1}{w^2} \right) n = -C\omega\mu_0 \left[\frac{J'_n(u)}{uJ_n(u)} + \frac{K'_n(w)}{wK_n(w)} \right] \quad (\text{A.17})$$

and the continuity of H_ϕ at $r = a$ brings in Eqn. A.30 leads to:

$$A\omega\epsilon_0 \left[n_{\text{core}}^2 \frac{J'_n(u)}{uJ_n(u)} + \frac{K'_n(w)}{wK_n(w)} \right] = -C\beta \left(\frac{1}{u^2} + \frac{1}{w^2} \right) n. \quad (\text{A.18})$$

Combining the Eqns. A.17 and A.18 and eliminating constants A and C, results into the eigenvalue equation, Eqn. 3.8. This equation is also known as dispersion equation and is repeated here for convenience.

$$\left[\frac{J'_n(u)}{uJ_n(u)} + \frac{K'_n(w)}{wK_n(w)} \right] \left[\frac{J'_n(u)}{uJ_n(u)} + \left(\frac{1}{n_{\text{core}}} \right)^2 \frac{K'_n(w)}{wK_n(w)} \right] = n_{\text{core}}^2 \left(\frac{1}{u^2} + \frac{1}{w^2} \right) \left[\frac{1}{u^2} + \left(\frac{1}{n_1} \right)^2 \frac{1}{w^2} \right]. \quad (\text{A.19})$$

The propagation constant of the hybrid mode is calculated by solving Eqn. A.19. The constant C can be written from Eqn. A.17 as

$$C = -A \frac{\beta_{\text{eff}}}{\omega\mu_0} s \quad (\text{A.20})$$

where s is given by

$$s = \frac{n \left(\frac{1}{u^2} + \frac{1}{w^2} \right)}{\left[\frac{J'_n(u)}{uJ_n(u)} + \frac{K'_n(w)}{wK_n(w)} \right]}. \quad (\text{A.21})$$

Applying the following recurrence relations for the Bessel functions

$$J'_n(z) = \frac{1}{2} [J_{n-1}(z) - J_{n+1}(z)], \quad (\text{A.22})$$

$$\frac{n}{z} J_n(z) = \frac{1}{2} [J_{n-1}(z) + J_{n+1}(z)], \quad (\text{A.23})$$

$$K'_n(z) = -\frac{1}{2} [K_{n-1}(z) - K_{n+1}(z)], \quad (\text{A.24})$$

$$\frac{n}{z} K_n(z) = -\frac{1}{2} [K_{n-1}(z) + K_{n+1}(z)], \quad (\text{A.25})$$

the electromagnetic fields of hybrid mode of microwire are found as follows:

$$E_r = \begin{cases} -jA\beta_{\text{eff}} \frac{a}{u} \left[\frac{(1-s)}{2} J_{n-1}\left(\frac{u}{a}r\right) - \frac{(1+s)}{2} J_{n+1}\left(\frac{u}{a}r\right) \right] \cos(n\phi + \psi) & (0 \leq r \leq a) \\ -jA\beta_{\text{eff}} \frac{aJ_n(u)}{wK_n(w)} \left[\frac{(1-s)}{2} K_{n-1}\left(\frac{w}{a}r\right) + \frac{(1+s)}{2} K_{n+1}\left(\frac{w}{a}r\right) \right] \cos(n\phi + \psi) & (r > a) \end{cases} \quad (\text{A.26})$$

$$E_\phi = \begin{cases} jA\beta_{\text{eff}} \frac{a}{u} \left[\frac{(1-s)}{2} J_{n-1}\left(\frac{u}{a}r\right) + \frac{(1+s)}{2} J_{n+1}\left(\frac{u}{a}r\right) \right] \sin(n\phi + \psi) & (0 \leq r \leq a) \\ jA\beta_{\text{eff}} \frac{aJ_n(u)}{wK_n(w)} \left[\frac{(1-s)}{2} K_{n-1}\left(\frac{w}{a}r\right) - \frac{(1+s)}{2} K_{n+1}\left(\frac{w}{a}r\right) \right] \sin(n\phi + \psi) & (r > a) \end{cases} \quad (\text{A.27})$$

$$E_z = \begin{cases} AJ_n\left(\frac{u}{a}r\right) \cos(n\phi + \psi) & (0 \leq r \leq a) \\ A \frac{J_n(u)}{K_n(w)} K_n\left(\frac{w}{a}r\right) \cos(n\phi + \psi) & (r > a) \end{cases} \quad (\text{A.28})$$

$$H_r = \begin{cases} -jA\omega\epsilon_0 n_{\text{core}}^2 \frac{a}{u} \left[\frac{(1-s_1)}{2} J_{n-1}\left(\frac{u}{a}r\right) + \frac{(1+s_1)}{2} J_{n+1}\left(\frac{u}{a}r\right) \right] \sin(n\phi + \psi) & (0 \leq r \leq a) \\ -jA\omega\epsilon_0 \frac{aJ_n(u)}{wK_n(w)} \left[\frac{(1-s_0)}{2} K_{n-1}\left(\frac{w}{a}r\right) - \frac{(1+s_0)}{2} K_{n+1}\left(\frac{w}{a}r\right) \right] \sin(n\phi + \psi) & (r > a) \end{cases} \quad (\text{A.29})$$

$$H_\phi = \begin{cases} -jA\omega\epsilon_0 n_{\text{core}}^2 \frac{a}{u} \left[\frac{(1-s_1)}{2} J_{n-1}\left(\frac{u}{a}r\right) - \frac{(1+s_1)}{2} J_{n+1}\left(\frac{u}{a}r\right) \right] \cos(n\phi + \psi) & (0 \leq r \leq a) \\ -jA\omega\epsilon_0 \frac{aJ_n(u)}{wK_n(w)} \left[\frac{(1-s_0)}{2} K_{n-1}\left(\frac{w}{a}r\right) + \frac{(1+s_0)}{2} K_{n+1}\left(\frac{w}{a}r\right) \right] \cos(n\phi + \psi) & (r > a) \end{cases} \quad (\text{A.30})$$

$$H_z = \begin{cases} -A \frac{\beta_{\text{eff}}}{\omega\mu_0} s J_n\left(\frac{u}{a}r\right) \sin(n\phi + \psi) & (0 \leq r \leq a) \\ -A \frac{\beta_{\text{eff}}}{\omega\mu_0} s \frac{J_n(u)}{K_n(w)} K_n\left(\frac{w}{a}r\right) \sin(n\phi + \psi) & (r > a) \end{cases} \quad (\text{A.31})$$

where

$$s_1 = \frac{\beta_{\text{eff}}^2}{\beta_0^2 n_{\text{core}}^2} s \quad (\text{A.32})$$

$$s_0 = \frac{\beta_{\text{eff}}^2}{\beta_0^2} s. \quad (\text{A.33})$$

Data processing algorithms

THIS appendix outlines some of the algorithms used for characterisation of bulk materials and waveguides from raw THz waveforms. These algorithms are implemented in MATLAB. Moreover, it also provides the analytical MATLAB files employed for analysing microwires, and numerical FEM algorithms implemented in MATLAB for analysing porous fibres. These algorithms are used in Chapters [3](#), [4](#), and [6](#).

B.1 Conventional THz-TDS analysis program

This Section is consist of MATLAB mfiles used for extraction absorption coefficient and refractive index from raw THz waveforms. Part B.1.1 contains the main file and Part B.1.2 contains the functions used in the main file.

B.1.1 Main mfile

```
% This is the main mfile that needs to be run to evaluate absorption
% coefficient and refractive index from raw THz waveforms
% by: Shaghik Atakaramians
% The University of Adelaide
% May 2006

clc;clear all;
mu=pi*4e-7;e0=8.854e-12;
c=1/sqrt(mu*e0);
Sampthic=5.4e-3; % in meter
[Ert,Erf,timestep,freqstep]=drawRef(); % averaging and plotting reference pulses
[Est,Esf]=drawSam(); % averaging and plotting sample pulses
m=size(Esf);
omega=2e12*pi*freqstep;
beta0=omega/c;
phi=(angle(Esf)-angle(Erf));
AA=abs(Esf./Erf);
% Amplitude and unwrapped phase
figure(100);hold on;
plot(freqstep(1:m/2),phi(1:m/2),'r')
plot(freqstep(1:m/2),unwrap(phi(1:m/2)),'k')
lowerF=input('Enter the lower frequency in THz');
upperF=input('Enter the upper frequency in THz');
deltaF=mean(diff(freqstep));
% Two different unwrapping techniques are employed for comparison
[Phi,lowerIndex,upperIndex]=myUnwrap(phi,deltaF,lowerF,upperF);
[PhiT,lowerIndexT,upperIndexT]=myUnwrapLS(phi,freqstep,deltaF,lowerF,upperF);
```

```

figure(100);hold on;
plot(freqstep(1:upperIndex),Phi(1:upperIndex),'r') %n_omega
plot(freqstep(1:upperIndex),PhiT(1:upperIndex),'g') %n_omega
% Calculation of absorption and refractive index
n_omega=(-1*PhiT./(Sampthic*beta0))+ones(size(PhiT));
CC=((n_omega+ones(size(n_omega))).^2)./(4*n_omega);
alpha=-2*(log(CC.*AA))/Sampthic;
Alpha=0.01*alpha; % 1/cm
figure(1); hold all;
subplot(2,2,3);
plot(freqstep(lowerIndex:upperIndex),n_omega(lowerIndex:upperIndex),'r')
xlabel('Frequency [THz]');
ylabel('Index of Refraction n');
subplot(2,2,4);
plot(freqstep(lowerIndex:upperIndex),Alpha(lowerIndex:upperIndex),'m')
xlabel('Frequency [THz]');
ylabel('Absorption Coefficient  $\alpha$  [1/cm]');
% Averaging the results for better look and save
M=length(Alpha(lowerIndex:upperIndex));
for nn=1:M
Blpha(nn)=mean(Alpha(lowerIndex-1+nn_lowerIndex+3+nn));
end
plot(freqstep(lowerIndex:upperIndex),Blpha(1:M),'k');
save bulkTOPASsample.txt ForExport -ascii
save file_name freqstep n_omega Alpha

```

B.1.2 Functions

The Part contains three functions employed in Part [B.1.1](#).

Read and average the reference signals

```
% This file, which is called by the main mfile reads and averages the reference
signals.
```

```
% by: Shaghik Atakaramians
```

```
% The University of Adelaide
```

```
% May 2006
```

```
function [St,Sf,timestep,freq]=drawRef(n_ref,Fix_path,fix_fn,Ifile_type)
f_type=Ifile_type;
file_name=strcat(Fix_path,fix_fn,f_type);
fid=fopen(file_name,'r');
Ref=textscan(fid,'%f %f','headerlines',2);
if ii==1
Ref_sig=Ref:,2;
time_sig=Ref:,1;
else
Ref_sig=Ref_sig+Ref:,2;
time_sig=time_sig+Ref:,1;
end
fclose(fid);
St=(1/n_ref)*[time_sig,Ref_sig];
[m,n]=size(St);
X=St(1:32,2);
shift=mean(X);
Y=St(1:m,2)-shift;
timestep=mean(diff(St(1:m,1)));
for jj=1:(length(Y)-1)
test(jj)=Y(jj)/Y(jj+1);
if test(jj)<0
zero_pos(jj)=jj;
end
end
zero_index=find(zero_pos);
for kk=length(Y)-100:length(Y)
Y(kk)=0;
end
subplot(2,2,1);
plot(St(1:m,1),Y,'b');
ylabel('THz Signal [a.u.]');
```



```

xlabel('Time [ps]');
subplot(2,2,2);
Y=St(1:m,2);
Sf=fft(Y-shift,m);
freq =(0:m-1)'/timestep/m;
semilogy(freq(1:m/2),abs(Sf(1:m/2)),'b');
xlabel('Frequency [THz]');
ylabel('Spectral Amplitude');
return

```

Read and average the sample signals

```

% This file, which is called by the main mfile reads and averages the sample
signals.
% by: Shaghik Atakaramians
% The University of Adelaide
% May 2006

function [St,Sf]=drawSam(n_sam,Fix_path,fix_fn,Ifile_type)
for ii=1:1:n_sam
extension=int2str(ii);
f_type=Ifile_type;
file_name=strcat(Fix_path,fix_fn,extension,f_type);
fid=fopen(file_name,'r');
Ref=textscan(fid,'%f %f','headerlines',2);
if ii==1
Ref_sig=Ref:,2;
time_sig=Ref:,1;
else
Ref_sig=Ref_sig+Ref:,2;
time_sig=time_sig+Ref:,1;
end
fclose(fid);
end
St=(1/n_sam)*[time_sig,Ref_sig];

```

```
[m,n]=size(St);
X=St(1:32,2);
shift=mean(X);
Y=St(1:m,2)-shift;
timestep=mean(diff(St(1:m,1)));
for jj=1:(length(Y)-1)
test(jj)=Y(jj)/Y(jj+1);
if test(jj)<0
zero_pos(jj)=jj;
end
end
zero_index=find(zero_pos);
for kk=length(Y)-100:length(Y)
Y(kk)=0;
end
subplot(2,2,1);
plot(St(1:m,1),Y,'r');
hold on;
ylabel('THz Signal [a.u.]');
xlabel('Time [ps]');
subplot(2,2,2);
Sf=fft(Y,m);
freq =(0:m-1)'/timestep/m;
semilogy(freq(1:m/2),abs(Sf(1:m/2)),'r');
hold on;
xlabel('Frequency [THz]');
ylabel('Spectral Amplitude');
return
```

Unwrapping the phase of transfer function

Method1

```
% This file unwraps the phase data by employing linear line fitting and extrapolating
to low frequency.
```

```
% by: Shaghik Atakaramians
```

```

% The University of Adelaide
% May 2006

function [unwrappedphi,lowerBoundIndex,upperBoundIndex]=
myUnwrap(inputphi,deltaF,lowerBound,upperBound)
lowerBoundIndex=ceil(lowerBound/deltaF);
upperBoundIndex=floor(upperBound/deltaF);
x=unwrap(inputphi);
averageSlope=mean(diff(x(lowerBoundIndex:upperBoundIndex)));
X1=length(x(1:lowerBoundIndex));
x1(1:lowerBoundIndex)=averageSlope*linspace(0,lowerBoundIndex,X1);
shift=-x1(lowerBoundIndex)+x(lowerBoundIndex);
x(1:lowerBoundIndex-1)=x1(1:lowerBoundIndex-1);
x(lowerBoundIndex:upperBoundIndex)=x(lowerBoundIndex:upperBoundIndex)
-shift*ones(size(x(lowerBoundIndex:upperBoundIndex)));
unwrappedphi=x ;
return

```

Method2

```

% This file unwraps the phase data by employing Least-Square line fitting and
extrapolating to low frequency.
% by: Withawat Withayachumnankul
% modified by: Shaghik Atakaramians
% The University of Adelaide
% June 2006

function [unwrappedphi,lowerBoundIndex,upperBoundIndex]
=myUnwrapLS(inputphi,freqstep,deltaF,lowerBound,upperBound)
upperBoundIndex=floor(upperBound/deltaF);
x=unwrap(inputphi);
NN=upperBoundIndex-lowerBoundIndex+1;
X1=sum(freqstep(lowerBoundIndex:upperBoundIndex));
X2=sum(freqstep(lowerBoundIndex:upperBoundIndex).^2);
XY=sum(freqstep(lowerBoundIndex:upperBoundIndex).*...

```

```
x(lowerBoundIndex:upperBoundIndex));
Y1=sum(x(lowerBoundIndex:upperBoundIndex));
AA=inv([NN X1; X1 X2])*[Y1;XY];
x(1:lowerBoundIndex-1)=AA(2)*freqstep(1:lowerBoundIndex-1);
x(lowerBoundIndex:end)=(x(lowerBoundIndex:end)-AA(1)*...
ones(size(x(lowerBoundIndex:end)))));
unwrappedphi=x;
return
```

B.2 THz waveguide analysis program

This Section consists of MATLAB mfiles used for extraction absorption coefficient and effective refractive index from raw THz waveguide waveforms. Part [B.2.1](#) contains the main file and Part [B.2.2](#) contains the functions used in the main file.

B.2.1 Main mfile

```
% This is the main mfile that needs to be run to evaluate absorption coefficient
% and effective refractive index from raw THz waveguide waveforms
% by: Shaghik Atakaramians
% The University of Adelaide
% December 2008

clear all;clc;
mu=pi*4e-7;e0=8.854e-12;
c=1/sqrt(mu*e0);
numstep=500;
mm=512;dx=2*15e-6;dt=dx/c;
t=1e12*(0:dt:(numstep-1)*dt); % ps
x=15e-6*(0:1:(numstep-1))*1e3; % mm
% Length of the fibres L1=16e-3;L2=20.4e-3; L3=24.9e-3;
delta_t1=(L3-L1)/c;
delta_t2=(L3-L2)/c;
```

```
% Load the data file A1=load('spiderweb500_S_scan001.dat');
A2=load('spiderweb500_M_scan004.dat');
A3=load('spiderweb500_L_scan002.dat');
% Processing options
Proc_opt='line';
switch lower(Proc_opt)
case 'non'
BFT1=A1;BFT2=A2;BFT3=A3;
case 'filter'
F_type = 'high';
F_order=100;
switch lower(F_type)
case 'high'
disp('Highpass filter')
Wn=0.03; case 'bandpass'
disp('Bandpass filter')
Wn=[0.01,0.8;0.02,0.8;0.05,0.8];
end
for ii=1:max(size(Wn))
wn=Wn(ii);
b = fir1(F_order,wn,F_type);
BF1=conv(A1,b);BFT1=BF1((0.5*F_order+2):(length(BF1)-0.5*F_order));
BF2=conv(A2,b);BFT2=BF2((0.5*F_order+2):(length(BF2)-0.5*F_order));
BF3=conv(A3,b);BFT3=BF3((0.5*F_order+2):(length(BF3)-0.5*F_order));
end
case 'line'
BFT1=detrend(A1(1:440));
BFT2=detrend(A2(1:430));
BFT3=detrend(A3(1:460));
end
% Zeropadding of the signals
[SL1]=Zeropadding(BFTS1,80,4,231,1,mm);
[SL2]=Zeropadding(BFTS2,80,3,255,1,mm);
[SL3]=Zeropadding(BFTS3,80,3,273,1,mm);
figure(4); hold all;
```

```
plot(SL1,'b');plot(SL2,'g');plot(SL3,'r');
ylabel('Zeropad THz Signal [a.u.]');
xlabel('distance [a.u.]');
% Signals plot in the time domain
figure(5);hold on;
time_v=1e12*(0:dt:(mm-1)*dt);
plot(time_v,SL1,'b',time_v,SL2,'g',time_v,SL3,'r');
ylabel('THz Signal [a.u.]');
xlabel('Time [ps]');
% Signals plot in the frequency domain
figure(6);hold all;
Sf1=fft(SL1,MM);Sf2=fft(SL2,MM);Sf3=fft(SL3,MM);
freq =(0:MM-1)'/dt/MM;
semilogy(freq(1:MM/4)*1e-12,abs(Sf1(1:MM/4)),'b');
semilogy(freq(1:MM/4)*1e-12,abs(Sf2(1:MM/4)),'g');
semilogy(freq(1:MM/4)*1e-12,abs(Sf3(1:MM/4)),'r');
xlabel('Frequency [THz]');
ylabel('Spectral Amplitude');
% Calculating fibre parameters
delta_t3=delta_t1-delta_t2;
[n_omega1,Alpha1,freqstep1]=Mainfile(Sf2,Sf1,freq,0.18,0.75,(L2-L1),...
delta_t3,c,MM,0);
[n_omega2,Alpha2,freqstep2]=Mainfile(Sf3,Sf1,freq,0.14,0.6,(L3-L1),...
delta_t1,c,MM,0);
[n_omega3,Alpha3,freqstep3]=Mainfile(Sf3,Sf2,freq,0.15,0.57,(L3-L2),...
delta_t2,c,MM,0);
% Averaaging and displaying the results
n_omegaM=(n_omega1+n_omega2+n_omega3)/3;
plot(freqstep1,n_omegaM,'oK');
figure(8);hold on;
Alpha_mean=(Alpha1+Alpha2+Alpha3)/3;
plot(freqstep1,(Alpha_mean),'oK')
```

B.2.2 Functions

The Part contains three functions employed in Part [B.2.1](#).

Zeropad the signal

```
% This function paddes the begining and end of the signal with zeroes.
```

```
% by: Shaghik Atakaramians
```

```
% The University of Adelaide
```

```
% December 2008
```

```
function [Y]=Zeropadding(Y,point1,kk,point2,ll,mm)
```

```
Y1=Y;
```

```
for jj=1:(length(Y)-1)
```

```
test(jj)=Y(jj)/Y(jj+1);
```

```
if test(jj)<0
```

```
zero_pos(jj)=jj;
```

```
else
```

```
zero_pos(jj)=0;
```

```
end
```

```
end
```

```
zero_index1=find(zero_pos<point1 & zero_pos>0);
```

```
[n1,m1]=size(zero_index1);
```

```
if (n1>0 & m1>0)
```

```
for kk=1:zero_index1(kk)
```

```
Y(kk)=0;
```

```
end
```

```
end
```

```
zero_index2=find(zero_pos>point2);
```

```
[n2,m2]=size(zero_index2);
```

```
if (n2>0 & m2>0)
```

```
Zero_2=zero_index2(ll);
```

```
else
```

```
a=min(abs(Y1(point2:length(Y1))));
```

```
Zero_2=find(Y1==a);
```

```
end
```

```
for kk=Zero_2:mm
Y(kk)=0;
end
```

Calculating absorption coefficient and effective refractive index

```
% This file evaluates and averages the absorption coefficient
% and effective refractive index of the waveguide.
% by: Shaghik Atakaramians
% The University of Adelaide
% December 2008

function [NN,ALAL,FfFf]=Mainfile(Esf,Erf,freq,lowerF,upperF,Sampthic,...
delta_t,c,mm,ii)
freqstep=freq*1e-12;omega=2*pi*freq;
beta0=omega/c;
phi=(angle(Esf)-(delta_t*omega)-angle(Erf));
AA=abs(Esf./Erf);
deltaF=mean(diff(freqstep));
lowerIndex=ceil(lowerF/deltaF);
upperIndex=floor(upperF/deltaF);
Phi = myWGUunwrap(phi,freqstep,lowerIndex,upperIndex,mm);
plot(freqstep(1:mm/4),Phi(1:mm/4),'b')
figure(7)
n_omega=(-1*(Phi)./(Sampthic*beta0));
plot(freqstep(lowerIndex:2*upperIndex),n_omega(lowerIndex:2*upperIndex),'m')
xlabel('Frequency [THz]');
ylabel('Index of Refraction n');
figure(8)
alpha=-2*(log(AA))/Sampthic;
Alpha=0.01*alpha;
plot(freqstep(2*lowerIndex:upperIndex),Alpha(2*lowerIndex:upperIndex),'*r')
xlabel('Frequency [THz]');
ylabel('Absorption Coefficient  $\alpha$  [1/cm]');
NN=n_omega;ALAL=Alpha;FfFf=freqstep;
```



```
return
```

B.3 Microwire

This Section consists of MATLAB mfiles used for calculating the propagation constant, electromagnetic fields, power fraction, and effective area of a microwire. Part [B.3.1](#) contains the main file that calculates the propagation constant of the microwire, and Part [B.3.2](#) contains the functions.

B.3.1 Main mfile

```
% This file evaluates the propagation constant of the
% fundamental mode of a microwire.
% by: Shaghik Atakaramians
% The University of Adelaide
% March 2007

clear all;clc;
n=1;mu=pi*4e-7;e0=8.854e-12;
freq=0.5;
bulkinfo=load('bulkTOPASSsample.txt');
deltaF=bulkinfo(2,1);
Index=ceil(freq/deltaF);
f=bulkinfo(Index,1)*1e12;
n1=bulkinfo(Index,2);
alpha1=bulkinfo(Index,3);
n0=1;ns=0.0005;
lambda=1/(f*sqrt(mu*e0));
omega=2*pi*f;
beta0=(2*pi)/lambda;
m1=0;
for D=140:10:600
d=D*1e-6;a=d/2;
```

```
nn=n1-ns;
C0=dispersionnl(n,nn,n0,n1,beta0,a);
U=0;mm=0;
while (U==0 & nn>4(n0+ns))
nn=nn-ns;
C1=dispersionnl(n,nn,n0,n1,beta0,a);
if sign(C1)==sign(C0)
C0=C1;
else
U=1;C0=C1;
end
if U==1
[neff,fval,exitflagn]=fsolve(@(nn) dispersionnl(n,nn,n0,n1,beta0,a),nn);
if exitflagn==1
U=1;mm=1;
else
U=0;
end
end
end
if mm==1
m1=m1+1;
[Pcore,Pair]=PWR(n,beta0,neff,n1,n0,a,omega,e0);
P_core(m1)=Pcore/(Pcore+Pair);
Ptot(m1)=Pair/(Pcore+Pair);
Diam(m1)=D;
end
end
% Save the results
save TOPAS_PowerFraction.mat Ptot P_core Diam
```

B.3.2 Functions

The Part contains three functions employed in Part [B.3.1](#)

Eigenvalue equation

```
%This file contains the eigenvalue equation from which
% the propagation constant of the fundamental mode is calculated.
% by: Shaghik Atakaramians
% The University of Adelaide
% March 2007
```

```
function [disp]=dispersionnl(n,nn,n0,n1,beta0,a)
u=a*beta0*sqrt(n1^2-nn^2);
w=a*beta0*sqrt(nn^2-n0^2);
CC1=0.5*(besselj(n-1,u)-besselj(n+1,u))/(u*besselj(n,u));
CC2=-0.5*(besselk(n-1,w)+besselk(n+1,w))/(w*besselk(n,w));
CC3=(1/u)^2;CC4=(1/w)^2;
disp=(CC1+CC2)*(CC1+(n0/n1)^2*CC2)-n^2*(CC3+CC4)*(CC3+(n0/n1)^2*CC4);
return
```

Electromagnetic fields

```
%This file evaluated and plots the electromagnetic fields
% of the fundamental mode of a microwire.
% by: Shaghik Atakaramians
% The University of Adelaide
% March 2007
```

```
function [er,et,ez,hr,ht,hz]=EHfield(n,r,teta,psi,K0,neff,n1,n0,...
a,omega,e0,mu)
A=1;
u=a*K0*sqrt(n1^2-neff^2);
w=a*K0*sqrt(neff^2-n0^2);
CC1=0.5*(besselj(n-1,u)-besselj(n+1,u))/(u*besselj(n,u));
CC2=-0.5*(besselk(n-1,w)+besselk(n+1,w))/(w*besselk(n,w));
CC3=(1/u)^2;CC4=(1/w)^2;
s=n*(CC3+CC4)/(CC1+CC2);
s1=(neff/n1)^2*s;s0=(neff/n0)^2*s;
```

```
EE1=j*A*K0*neff*a/u;
EE2=(j*A*K0*neff*a/w)*(besselj(n,u)/besselk(n,w));
HH1=j*A*omega*e0*n1^2*a/u;
HH2=(j*A*omega*e0*n0^2*a/w)*(besselj(n,u)/besselk(n,w));
kappa=u*r/a;sigma=w*r/a;
if (r<a)
er=-1*EE1*(0.5*(1-s)*besselj(n-1,kappa)-0.5*(1+s)*besselj(n+1,kappa))*...
cos(n*teta+psi);
et=EE1*(0.5*(1-s)*besselj(n-1,kappa)+0.5*(1+s)*besselj(n+1,kappa))*...
sin(n*teta+psi);
ez=A*besselj(n,kappa)*cos(n*teta+psi);
hr=-1*HH1*(0.5*(1-s1)*besselj(n-1,kappa)+0.5*(1+s1)*besselj(n+1,kappa))*...
sin(n*teta+psi);
ht=-1*HH1*(0.5*(1-s1)*besselj(n-1,kappa)-0.5*(1+s1)*besselj(n+1,kappa))*...
cos(n*teta+psi);
hz=-1*A*K0*neff*s*besselj(n,kappa)*sin(n*teta+psi)/(omega*mu);
else
er=-1*EE2*(0.5*(1-s)*besselk(n-1,sigma)+0.5*(1+s)*besselk(n+1,sigma))*...
cos(n*teta+psi);
et=EE2*(0.5*(1-s)*besselk(n-1,sigma)-0.5*(1+s)*besselk(n+1,sigma))*...
sin(n*teta+psi);
ez=A*(besselj(n,u)/besselk(n,w))*besselk(n,sigma)*cos(n*teta+psi);
hr=-1*HH2*(0.5*(1-s0)*besselk(n-1,sigma)-0.5*(1+s0)*besselk(n+1,sigma))*...
sin(n*teta+psi);
ht=-1*HH2*(0.5*(1-s0)*besselk(n-1,sigma)+0.5*(1+s0)*besselk(n+1,sigma))*...
cos(n*teta+psi);
hz=-1*A*K0*neff*s*(besselj(n,u)/besselk(n,w))*besselk(n,sigma)*...
sin(n*teta+psi)/(omega*mu);
end
return
```

Power fraction

```
%This file evaluated the power fraction in the core
% and clad of a microwire.
```

```

% by: Shaghik Atakaramians
% The University of Adelaide
% March 2007

function [pcore,pclad]=PWR(n,beta0,neff,n1,n0,a,omega,e0)
A=1;
u=a*beta0*sqrt(n12-neff2);
w=a*beta0*sqrt(neff2-n02);
CC1=(pi/4)*omega*e0*n12*beta0*neff*(a/u)2*(abs(A))2;
CC2=(pi/4)*omega*e0*n02*beta0*neff*(a/w)2*(abs(A))2*(besselj(n,u)/...
besselk(n,w))2;
SS1=0.5*(besselj(n-1,u)-besselj(n+1,u))/(u*besselj(n,u));
SS2=-0.5*(besselk(n-1,w)+besselk(n+1,w))/(w*besselk(n,w));
SS3=(1/u)2;SS4=(1/w)2;
s=n*(SS3+SS4)/(SS1+SS2);
s1=(neff/n1)2*s;s0=(neff/n0)2*s;
% These are the integral formula of the bessel functions
intbesj1=(a2/2)*((besselj(n-1,u))2-besselj(n-2,u)*besselj(n,u));
intbesj2=(a2/2)*((besselj(n+1,u))2-besselj(n,u)*besselj(n+2,u));
intbesk1=(a2/2)*(besselk(n-2,w)*besselk(n,w)-(besselk(n-1,w))2);
intbesk2=(a2/2)*(besselk(n,w)*besselk(n+2,w)-(besselk(n+1,w))2);
pcore=CC1*((1-s)*(1-s1)*intbesj1+(1+s)*(1+s1)*intbesj2);
pclad=CC2*((1-s)*(1-s0)*intbesk1+(1+s)*(1+s0)*intbesk2);
return

```

B.4 Porous fibre

This Section consists of numerical FEM code implemented in MATLAB mfiles used for calculating propagation constant, power fraction, effective area, and field distribution of porous fibres. Part [B.4.1](#) contains the main mfile where the FEMlab code is also included, while Part [B.4.1](#) contains the functions used in the main file.

B.4.1 Main mfile

```
% This file is the set-up file for analysing Porous fibres.
% Waveguide parameters such as the material propertise, frequency range,
% and dimension of the fibre are set in this file.
% by: Kris Rowland
% modified by: Shaghik Atakaramians
% The Univeristy of Adleiaide
% January 2008

clear all; flclear fem; format long e;
mu=pi*4e-7;e0=8.854e-12;
eta_0=sqrt(mu/e0);
% Loading the measured bulk material information from a txt file
bulkinfo=load('bulkPMMAsample.txt');
deltaF=bulkinfo(2,1);
Index=ceil(freq/deltaF);
f=bulkinfo(Index,1)*1e12;
n_CORE=bulkinfo(Index,2);
n_CLAD=1;
alpha_core=bulkinfo(Index,3);
measurement_lambda=1/(f*sqrt(mu*e0));
% Define the Geometry parameters for the structure
porosity=0.5;
rcore_vect=[200]*1e-6;
rhole_vect=0.1*rcore_vect;
pml_r_vect=2000e-6;
% Define mesh parameters
haut0=1;hmax_core_vect=10e-7;hmax_holes_vect=5e-6;
% Number of eigen-solutions guess value for solutions
neigs=2;
neff_guess=1.2;
for ll=1:length(measurement_lambda)
lambda=measurement_lambda(ll);
iii=iii+1;
```

```
% Define Geometry
Geometry
% Define subdomains and boundary indices
Substdomains=[2];
Claddomains=[5 6];
Holedomains=[1 3 4 8:11 14:31];
edges:pm=[1 3:10];
edges:pe=[2 13:23 25 12 28 29 30];
% FEMlab codes
clear fem appl
shift=-(2*pi*neff:guess/lambda)^2;
fem.geom=G;
nsub=get(G,'nmr');
nedge=get(G,'nbs');
clear G
fem.const='nSubst',nSubst,'nHole',nHole,'r0',pml_r,'d',pml_w,...
'A',pml_A,'epsilon_r',nSubst^2;
Mesh
clear appl
appl.mode.class = 'PerpendicularWaves';
appl.module='EM';
clear prop
prop.analysis='mode';
prop.inputvar='lambda';
prop.eigtype='propconst';
appl.prop=prop;
clear bnd
bnd.type='E0','cont','H0';
bnd.ind=2*ones(1,nedge);
E0edge=edges_pe;
H0edge=edges_pm;
bnd.ind(E0edge)=1;
bnd.ind(H0edge)=3;
appl.bnd=bnd;
clear equ
```

```
equ.init=0;
equ.usage=1;
equ.mutype='iso','iso','aniso';
equ.epstype='iso','iso','aniso';
equ.epsilonr=1; equ.mur=1;
equ.matparams='n','n','epsr';
equ.n='nSubst','nHole',1;
equ.ntensor=1;
equ.ntytype='iso';
equ.murtensor=1,1,'Lxx';'Lyy';'Lzz';
equ.epsrtensor=1,1,'epsilon_r*Lxx';'epsilon_r*Lyy';'epsilon_r*Lzz';
equ.sigma=0;
equ.sigmatensor=0;
equ.sigtype='iso';
equ.ind=2*ones(1,nsub);
equ.ind(Substdomains)=1;
equ.ind(PMLdomains)=3;
appl.equ=equ;
appl.var = 'lambda0',lambda;
fem.appl1 = appl;
fem.border=1;
fem.units='SI';
clear equ
equ.ind=4*ones(1,nsub);
equ.ind(PMLdomains)=[1,2,3];
equ.dim = 'hx','hy','hz';
equ.expr = 'Lxx','sy*sz/sx','sy*sz/sx','sy*sz/sx','','Lyy',...
'sx*sz/sy','sx*sz/sy','sx*sz/sy','','Lzz','sx*sy/sz','sx*sy/sz','sx*sy/sz','','
'sx',1,'1-j*A*((x-r0)/d)^2','1-j*A*((x-r0)/d)^2','','...
'sy','1-j*A*((y-r0)/d)^2','1-j*A*((y-r0)/d)^2',1','','sz',1,1,1,'';
fem.equ = equ;
fem.expr=;
fem.functions=;
fem=multiphysics(fem);
fem.xmesh=meshextend(fem);
```



```
fem.sol=femeig(fem,'solcomp','thxhy','hz','outcomp','hz','thxhy',...
'neigs',neigs,'shift',shift);
% Post processing
for ii=1:neigs
neff(iii,ii)=sqrt(-fem.sol.lambda(ii))*lambda/2/pi;
end
PostProcess
end
```

Functions

Geometry: hexagonal lattice

```
% The waveguide, porous fibre, geometry is defined in here.
% by: Shaghik Atakaramians
% The Univeristy of Adleiade
% January 2008

rcore=rcore_vect(1);
rhole=rhole_vect(1);
% Create a vertual ring for increasing the mesh density
carr=curve2([0,rcore+10e-6,rcore+10e-6],[rcore+10e-6,rcore+10e-6,0], ...
[1,sqrt(0.5),1]),curve2([rcore+10e-6,0],[0,rcore+10e-6],[1,sqrt(0.5)]);
g1=geomcoerce('solid',carr);
carr=curve2([0,0],[rcore+10e-6,0],[1,1]), ...
curve2([0,rcore+10e-6],[0,0],[1,1]), ...
curve2([rcore+10e-6,0],[0,rcore+10e-6],[1,1]);
g2=geomcoerce('solid',carr);
g3=geomcomp(g1,g2,'ns','g1','g2','sf','g1+g2','edge','none');
g4=geomdel(g3);
G=g4;
% Create a quarter of the core
carr=curve2([0,rcore,rcore],[rcore,rcore,0],[1,sqrt(0.5),1]), ...
curve2([rcore,0],[0,rcore],[1,sqrt(0.5)]);
g1=geomcoerce('solid',carr);
carr=curve2([0,0],[rcore,0],[1,1]), ...
curve2([0,rcore],[0,0],[1,1]), ...
curve2([rcore,0],[0,rcore],[1,1]);
g2=geomcoerce('solid',carr);
g3=geomcomp(g1,g2,'ns','g1','g2','sf','g1+g2','edge','none');
g4=geomdel(g3);
G=G+g4;
% Adding circular holes
tetap=linspace(0,2*pi,100);
X1_core=rcore*cos(tetap);
```

```

Y1_core=rcore*sin(tetap);
abs_core=abs(X1_core+j*Y1_core);
x1_hole=rhole*cos(tetap);
y1_hole=rhole*sin(tetap);
abs_hole=abs(x1_hole+j*y1_hole);
domain_count=3;
if (rcore-max(abs(x1_hole+j*y1_hole)))>0
G=G-ellip2(rhole,rhole,'base','center','pos',[0,0]);
domain_count=domain_count+1;
% Hexagonal lattice displacements
HH=sqrt(pi/(2*sqrt(3)*porosity))*rhole;
rv=sqrt(3)*HH;rh=2*HH;
Vdis=0;Hdis=(rh:rh:rcore);
for ii=1:1:length(Hdis)
x2_hole=x1_hole+ Hdis(ii)*ones(size(x1_hole));
y2_hole=y1_hole+ Vdis*ones(size(y1_hole));
abs_hole=abs(x2_hole+j*y2_hole);
if min(abs_core-abs_hole)>0
domain_count=domain_count+1;
G=G-ellip2(rhole,rhole,'base','center','pos',[Hdis(ii), Vdis]);
end
end
Vdis=(2*rv:2*rv:rcore);Hdis=0;
for ii=1:1:length(Vdis)
x2_hole=x1_hole+ Hdis*ones(size(x1_hole));
y2_hole=y1_hole+ Vdis(ii)*ones(size(y1_hole));
abs_hole=abs(x2_hole+j*y2_hole);
if min(abs_core-abs_hole)>0
domain_count=domain_count+1;
G=G-ellip2(rhole,rhole,'base','center','pos',[Hdis, Vdis(ii)]);
end
end
for jj=1:1:ceil(rcore/rv)
Vdis=jj*rv;
chord=sqrt(rcore2-Vdis2);

```

```
if rem(jj,2)==1
Hdis=(rh/2:rh:chord);
else
Hdis=(rh:rh:chord);
end
for ii=1:1:length(Hdis)
x2_hole=x1_hole+ Hdis(ii)*ones(size(x1_hole));
y2_hole=y1_hole+ Vdis*ones(size(y1_hole));
abs_hole=abs(x2_hole+j*y2_hole);
if min(abs_core-abs_hole)>0
domain_count=domain_count+1;
G=G-ellip2(rhole,rhole,'base','center','pos',[Hdis(ii), Vdis]);
end
end
end
G=rect2(pml_r+pml_w,pml_r+pml_w,'base','corner','pos',0,0)+G;
else
disp(['dimension of the holes are greater than that of the core']);
end
```

Post processing functions

```
% The waveguide parameters such as power fraction, field distribution,
% effective area, and effective material loss are evaluated here.
% Shaghik Atakaramians
% The Univeristy of Adleide
% January 2008

format long e
disp(['Calculating waveguide parameters...'])
Neff1(iii)=neff(iii,1);
Neff2(iii)=neff(iii,2);
% Parameters evaluation
power_hole_1(iii)=postint(fem,'Pozav','Dl',Holedomains,'solnum',1);
power_core_1(iii)=postint(fem,'Pozav','Dl',Substdomains,'solnum',1);
```

```
power_ground_1(iii)=postint(fem,'Pozav','Dl',Claddomains,'solnum',1);
Area_eff_1(iii)=...
4*(postint(fem,'Pozav','Dl',[Holedomains,Substdomains,Claddomains],'solnum',1))^2/...
postint(fem,'Pozav2','Dl',[Holedomains,Substdomains,Claddomains],'solnum',1);
Alpha_eff_1(iii)=sqrt(8.854187817e-12/(4*pi*1e-7))*(nSubst*alpha_core)*...
postint(fem,'(normE)2','Dl',Substdomains,'solnum',1)/...
(2*postint(fem,'Pozav','Dl',[Holedomains,Substdomains,Claddomains],'solnum',1));
power_hole_2(iii)=postint(fem,'Pozav','Dl',Holedomains,'solnum',2);
power_core_2(iii)=postint(fem,'Pozav','Dl',Substdomains,'solnum',2);
power_ground_2(iii)=postint(fem,'Pozav','Dl',Claddomains,'solnum',2);
Area_eff_2(iii)=...
4*(postint(fem,'Pozav','Dl',[Holedomains,Substdomains,Claddomains],'solnum',2))^2/...
(2*postint(fem,'Pozav2','Dl',[Holedomains,Substdomains,Claddomains],'solnum',2);
Alpha_eff_2(iii)=sqrt(8.854187817e-12/(4*pi*1e-7))*(ncore*alpha_core)*...
postint(fem,'(normE)2','Dl',Substdomains,'solnum',2)/...
(2*postint(fem,'Pozav','Dl',[Holedomains,Substdomains,Claddomains],'solnum',2));
```


Equipment for THz measurements

THE equipment used to conduct THz experiments is listed in this appendix. Table C.1 outlines the equipment used at The University of Adelaide to study the THz properties of bulk materials, and Table C.2 outlines the equipment used at The University of Adelaide to characterise THz waveguides.

Table C.1. List of equipment used at University of Adelaide A. The Table includes the major equipment used at The University of Adelaide to study the THz properties of bulk materials. These equipments are used for experiments carried out in Section 3.3.

Purpose	Equipment type	Manufacturer	Model
Femtosecond laser pulse generation	Ultrafast laser	Spectra Physics	Mai Tai
THz generation	Fibre-coupled	Picometrix	T-ray 2000
THz detection	Fibre-coupled	Picometrix	T-ray 2000

Table C.2. List of equipment used at University of Adelaide B. The Table includes the major equipment used at The University of Adelaide for fibre characterisation. This equipment is used for experiments carried out in Section 6.3.2.

Purpose	Equipment type	Manufacturer	Model
Femtosecond laser pulse generation	Ultrafast laser	Spectra Physics	Mai Tai
THz generation	Aperture array	T-Ray Science Inc.	T-LUX TM type AA
THz detection	THz-Tip (tapered PCA)	AMO GmbH	PC-FP-001-3-850
Motion controller	Motion controller	Newport	ESP300-1111N2
Delay stage	Motorised translation stage	Newport	ILS50PP
Pre-amplifier	Current amplifier	FEMTO	DLPCA-200
Phase sensitive detection	Lock-in amplifier	Coherent Scientific	SR810
Optical modulation	Chopper	THORLABS Inc.	MC1000A
Power supply	DC bias to aperture array	Topward Electric Instruments	TPS-400
Monitoring fibre and detector distance	USB CCD Camera	THORLABS Inc.	DCU224C
Measuring power	Power meter	Newport	1918-C & 818p

Bibliography

- ABBOTT-D AND ZHANG-X.-C (2007). Scanning the issue: T-ray imaging, sensing, and refection, *Proceedings of the IEEE*, **95**(8), pp. 1509–1513. [1.1](#), [1.1](#)
- ADEMGIL-H AND HAXHA-S (2008). Highly birefringent photonic crystal fibers with ultralow chromatic dispersion and low confinement losses, *Journal of Lightwave Technology*, **26**(1-4), pp. 441–448. [4.3](#)
- AFSHAR VAHID-S, ATAKARAMIANS-S, FISCHER-B. M, EBENDORFF-HEIDPRIEM-H, MONRO-T. M AND ABBOTT-D (2007). Low loss, low dispersion T-ray transmission in microwires, *Proc. CLEO/QELS*, Baltimore, Maryland, p. JWA105. [7.2](#)
- AFSHAR V.-S AND MONRO-T. M (2009). A full vectorial model for pulse propagation in emerging waveguides with subwavelength structures part i: Kerr nonlinearity, *Optics Express*, **17**(4), pp. 2298–2318. [3.4.2](#)
- AGC (Accessed: February 2010). *Asahi Glass*, <<http://www.agc.co.jp/>>. [3.3](#)
- AGRAWAL-G. P (2001). *Nonlinear Fiber Optics*, Academic Press. [3.4.2](#)
- AKALIN-T, TREIZEBRE-A AND BOCQUET-B (2006). Single-wire transmission lines at terahertz frequencies, *IEEE Transactions on Microwave Theory and Techniques*, **54**(6), pp. 2762–2767. [2.1](#)
- ALMEIDA-V. R, XU-Q, BARRIOS-C. A AND LIPSON-M (2004). Guiding and confining light in void nanostructure, *Optics Letters*, **29**(11), pp. 1209–1211. [2.3.2](#), [4.1](#)
- ARGYROS-A AND PLA-J (2007). Hollow-core polymer fibres with a kagome lattice: potential for transmission in the infrared, *Optics Express*, **15**(12), pp. 7713–7719. [2.3.2](#), [2.3.2](#)
- ARGYROS-A, LEON-SAVAL-S. G, PLA-J AND DOCHERTY-A (2008). Antiresonant reflection and inhibited coupling in hollow-core square lattice optical fibres, *Optics Express*, **16**(8), pp. 5642–5648. [2.3.2](#)
- ATAKARAMIANS-S, AFSHAR-S, FISCHER-B. M, ABBOTT-D AND MONRO-T. M (2008a). Low loss, low dispersion and highly birefringent terahertz porous fibers, *Optics Communications*, **282**(1), pp. 36–38. [4.5](#), [7.2](#)
- ATAKARAMIANS-S, AFSHAR VAHID-S, EBENDORFF-HEIDPRIEM-H, FISCHER-B. M, MONRO-T. M AND ABBOTT-D (2006a). Terahertz waveguides and materials, *Proc. Joint 31st International IEEE Conference on Infrared Millimeter Waves and 14th International Conference on Terahertz Electronics*, Shanghai, China, p. 281. [7.2](#)
- ATAKARAMIANS-S, AFSHAR VAHID-S, FISCHER-B. M, ABBOTT-D AND MONRO-T. M (2007). Loss mechanisms for T-ray microwires, *Proc. Joint 32nd International IEEE Conference on Infrared and Millimeter Waves and 15th International Conference on Terahertz Electronics*, Cardiff, UK, pp. 811–812. [7.2](#)
- ATAKARAMIANS-S, AFSHAR VAHID-S, FISCHER-B. M, ABBOTT-D AND MONRO-T. M (2008b). Highly birefringent, low loss and low dispersion THz waveguides with sub-wavelength porous structure, *Proc. EOS Annual Meeting 2008*, Paris, France. [7.2](#)

- ATAKARAMIANS-S, AFSHAR VAHID-S, FISCHER-B. M, ABBOTT-D AND MONRO-T. M (2008c). Porous fiber: a novel THz waveguide, *Proc. OECC/ACOFT*, art. no. ThE-3, Sydney, Australia. [7.2](#)
- ATAKARAMIANS-S, AFSHAR VAHID-S, FISCHER-B. M, ABBOTT-D AND MONRO-T. M (2008d). Porous fiber: reduced THz distortion compared to microwire, *Proc. The 33rd International IEEE Conference on Infrared, Millimeter, and Terahertz Waves*, Pasadena, California, USA. [7.2](#)
- ATAKARAMIANS-S, AFSHAR VAHID-S, FISCHER-B. M, ABBOTT-D AND MONRO-T. M (2008e). Porous fibers: a novel approach to low loss THz waveguides, *Optics Express*, **16**(12), pp. 8845–8854. [1.3](#), [4.4.3](#), [7.2](#)
- ATAKARAMIANS-S, AFSHAR VAHID-S, FISCHER-B. M, EBENDORFF-HEIDPRIEM-H, MONRO-T. M AND ABBOTT-D (2006b). Low loss terahertz transmission, *Proc. Proceedings SPIE Micro- and Nanotechnology: Smart Materials, Nano- and Micro-Smart Systems*, art. no. 64140I, Adelaide, Australia, 10-13 Dec. [3.1](#), [7.2](#)
- ATAKARAMIANS-S, AFSHAR VAHID-S, NAGEL-M, EBENDORFF-HEIDPRIEM-H, FISCHER-B. M, ABBOTT-D AND MONRO-T. M (2009a). Experimental investigation of dispersion properties of THz porous fibers, *Proc. The 33rd International IEEE Conference on Infrared, Millimeter, and Terahertz Waves*, Busan, Korea. [7.2](#)
- ATAKARAMIANS-S, AFSHAR VAHID-S, NAGEL-M, EBENDORFF-HEIDPRIEM-H, FISCHER-B. M, ABBOTT-D AND MONRO-T. M (2009b). Experimental validation of low dispersion and high birefringence properties of THz polymer porous fibers, *Proc. The 18th International Conference on Plastic Optical Fibers*, Sydney, Australia. [7.2](#)
- ATAKARAMIANS-S, AFSHAR VAHID-S, NAGEL-M, EBENDORFF-HEIDPRIEM-H, FISCHER-B. M, ABBOTT-D AND MONRO-T. M (2009c). THz porous fibers: design, fabrication and experimental characterization, *Optics Express*, **17**(19), pp. 14053–14062. [5.2](#), [5.10](#), [6.2](#), [7.2](#)
- ATAKARAMIANS-S, COOK-K, EBENDORFF-HEIDPRIEM-H, AFSHAR V.-S, CANNING-J, ABBOTT-D AND MONRO-T. M (2009d). Cleaving of extremely porous polymer fibers, *IEEE Photonics Journal*, **1**(6), pp. 288–292. [1.3](#), [5.6](#), [5.8](#), [5.10](#), [5.3.3](#), [5.12](#), [5.13](#), [7.2](#)
- AUSTON-D. H, CHEUNG-K. P AND SMITH-P. R (1984). Picosecond photoconducting hertzian dipoles, *Applied Physics Letters*, **45**(3), pp. 284–286. [1.1](#)
- AUSTON-D. H, JOHNSON-A. M, SMITH-P. R AND BEAN-J. C (1980). Picosecond optoelectronic detection, sampling, and correlation-measurements in amorphous-semiconductors, *Applied Physics Letters*, **37**(4), pp. 371–373. [1.1](#), [2.1](#), [2.1](#)
- AWAD-M, NAGEL-M, KURZ-H, HERFORT-J AND PLOOG-K (2007). Characterization of low temperature gas antenna array terahertz emitters, *Applied Physics Letters*, **91**(18). [6.3.1](#)
- BAGGETT-J. C, MONRO-T. M, FURUSAWA-K, FINAZZI-V AND RICHARDSON-D. J (2003). Understanding bending losses in holey optical fibers, *Optics Communications*, **227**, pp. 317–335. [3.5.1](#), [4.4.2](#)
- BALANIS-C. A (1989). *Advanced Engineering Electromagnetics*, John Wiley & Sons, Inc. [3.4](#), [3.4.1](#), [3.5.1](#), [3.5.1](#), [4.3](#), [A](#), [A](#)

- BARTON-G, VAN EIJKELNBORG-M. A, HENRY-G, LARGE-M. C. J AND ZAGARI-J (2004). Fabrication of microstructured polymer optical fibres, *Optical Fiber Technology*, **10**(4), pp. 325–335. [5.1](#)
- BENABID-F, ROBERTS-P. J, COUNY-F AND LIGHT-P. S (2009). Light and gas confinement in hollow-core photonic crystal fibre based photonic microcells, *Journal of the European Optical Society-Rapid Publications*, **4**, art. no. 09004. [2.3.2](#), [2.3.2](#)
- BINGHAM-A AND GRISCHKOWSKY-D (2007). High Q, one-dimensional terahertz photonic waveguides, *Applied Physics Letters*, **90**, art. no. 091105. [2.3.1](#)
- BINGHAM-A AND GRISCHKOWSKY-D (2008). Terahertz 2-D photonic crystal waveguides, *Microwave and Wireless Components Letters*, **18**(7), pp. 428–430. [1.1](#), [2.3.1](#)
- BIRCH-J. R, DROMEY-J. D AND LESURF-J (1981). The optical-constants of some common low-loss polymers between 4 and 40 cm^{-1} , *Infrared Physics*, **21**(4), pp. 225–228. [2.3.2](#)
- BOWDEN-B, HARRINGTON-J. A AND MITROFANOV-O (2007). Silver/polystyrene-coated hollow glass waveguides for the transmission of terahertz radiation, *Optics Letters*, **32**(20), pp. 2945–2947. [2.3.2](#), [6.1](#)
- BOWDEN-B, HARRINGTON-J. A AND MITROFANOV-O (2008a). Fabrication of terahertz hollow-glass metallic waveguides with inner dielectric coatings, *Journal of Applied Physics*, **104**(9), art. no. 093110. [2.3.2](#)
- BOWDEN-B, HARRINGTON-J. A AND MITROFANOV-O (2008b). Low-loss modes in hollow metallic terahertz waveguides with dielectric coatings, *Applied Physics Letters*, **93**(18), art. no. 181104. [2.3.2](#), [2.4](#)
- BUCK-J. A (2004). *Fundamentals of Optical Fibers*, second edn, John Wiley & Sons, Inc., New Jersey. [3.5.2](#)
- CANNING-J, BUCKLEY-E, GROOTHOFF-N, LUTHER-DAVIES-B AND ZAGARI-J (2002). UV laser cleaving of airpolymer structured fibre, *Optics Communications*, **202**, pp. 139–143. [5.1](#), [5.3.3](#), [5.3.3](#)
- CHEN-D. R AND CHEN-H. B (2010). A novel low-loss terahertz waveguide: Polymer tube, *Optics Express*, **18**(4), pp. 3762–3767. [2.3.2](#)
- CHEN-H. W, CHIU-C. M, LAI-C. H, KUO-J. L, CHIANG-P. J, HWANG-Y. J, CHANG-H. C AND SUN-C. K (2009). Subwavelength dielectric-fiber-based THz coupler, *Journal of Lightwave Technology*, **27**(11), pp. 1489–1495. [2.3.2](#), [3.5.1](#)
- CHEN-L.-J, CHEN-H.-W, KAO-T.-F, LU-J.-Y AND SUN-C.-K (2006). Low-loss subwavelength plastic fiber for terahertz waveguiding, *Optics Letters*, **31**(3), pp. 308–310. [1.1](#), [2.3.2](#), [2.20](#), [2.4](#), [3.1](#), [3.5.1](#), [3.5.1](#), [3.20](#), [6.1](#), [6.2](#)
- CHEN-X, LI-M.-J, VENKATARAMAN-N, GALLAGHER-M. T, WOOD-W. A, CROWLEY-A. M, CARBERRY-J. P, ZENTENO-L. A AND KOCH-K. W (2004). Highly birefringent hollow-core photonic bandgap fiber, *Optics Express*, **12**(16), pp. 3888–3893. [1.3](#), [4.4.3](#), [7.2](#)
- CHIN-C. M, CHEN-H. W, HUANG-Y. R, HWANG-Y. J, LEE-W. J, HUANG-H. Y AND SUN-C. K (2009). All-terahertz fiber-scanning near-field microscopy, *Optics Letters*, **34**(7), pp. 1084–1086. [1.1](#)

- CHO-M, KIM-J, PARK-H, HAN-Y, MOON-K, JUNG-E AND HAN-H (2008). Highly birefringent terahertz polarization maintaining plastic photonic crystal fibers, *Optics Express*, **16**(1), pp. 7–12. [1.3](#), [4.4.3](#), [5.1](#), [7.2](#)
- COLEMAN-S AND GRISCHKOWSKY-D (2003). A THz transverse electromagnetic mode two-dimensional interconnect layer incorporating quasi-optics, *Applied Physics Letters*, **83**(18), pp. 3556–3558. [2.10](#), [2.3.1](#)
- COMSOL (Accessed: February 2010). *COMSOL Multiphysics*, <<http://comsol.com/>>. [4.3](#)
- COOPER-D. E (1985). Picosecond optoelectronic measurement of microstrip dispersion, *Applied Physics Letters*, **47**(1), pp. 33–35. [1.1](#), [2.1](#), [2.1](#)
- CORREA-R. A AND KNIGHT-J (2008). Novel process eases production of hollow-core fiber, *Laser Focus World*, **44**(5), pp. 67–71. [2.3.2](#), [2.16](#)
- COUNY-F, BENABID-F AND LIGHT-P. S (2006). Large-pitch kagome-structured hollow-core photonic crystal fiber, *Optics Letters*, **31**(24), pp. 3574–3576. [2.3.2](#), [2.19](#), [2.3.2](#)
- COUNY-F, ROBERTS-P. J, BIRKS-T. A AND BENABID-F (2008). Square-lattice large-pitch hollow-core photonic crystal fiber, *Optics Express*, **16**(25), pp. 20626–20636. [2.3.2](#)
- DAZHANG-L, CUNNINGHAM-J, BYRNE-M. B, KHANNA-S, WOOD-C. D, BURNETT-A. D, ERSHAD-S. M, LINFIELD-E. H AND DAVIES-A. G (2009). On-chip terahertz goubau-line waveguides with integrated photoconductive emitters and mode-discriminating detectors, *Applied Physics Letters*, **95**(9), art. no. 092903. [2.1](#)
- DELBRIDGE-A (2001). *The Macquarie Dictionary*, 3rd edn edn, The Macquarie Library, North Ryde, NSW, Australia.
- DEXHEIMER-S. L (2008). *Terahertz Spectroscopy Principles and Applications*, CRC Press. [2.1](#), [2.2.2](#)
- DODDS-R. H, ANDERSON-T. L AND KIRK-M. T (1991). A framework to correlate a/w ratio effects on elastic-plastic fracture-toughness (J_c), *International Journal of Fracture*, **48**(1), pp. 1–22. [5.3](#)
- DUPUIS-A, C. O. ALLARD-J.-F, MORRIS-D, STOEFFLER-K, DUBOIS-C AND SKOROBOGATIY-M (2009). Fabrication and THz loss measurements of porous subwavelength fibers using a directional coupler method, *Optics Express*, **17**(10), pp. 8012–8028. [5.1](#), [5.1](#), [6.8](#), [6.3.2](#)
- DUPUIS-A, MAZHOROVA-A, DÉSEVÉDAVY-F, ROZÉ-M AND SKOROBOGATIY-M (2010). Spectral characterization of porous dielectric subwavelength THz fibers fabricated using a microstructured molding technique, *Optics Express*, **18**(13), pp. 13813–13828. [5.1](#), [5.1](#)
- EBENDORFF-HEIDPRIEM-H AND MONRO-T. M (2007). Extrusion of complex preforms for microstructured optical fibers, *Optics Express*, **15**(23), pp. 15086–15096. [4.5](#), [5.1](#), [5.2](#), [5.2](#)
- EBENDORFF-HEIDPRIEM-H, MONRO-T. M, VAN EIJKELNBORG-M. A AND LARGE-M. C. J (2007). Extruded high-na microstructured polymer optical fibre, *Optics Communications*, **273**(1), pp. 133–137. [5.2](#), [5.2](#), [5.2](#), [6.3.1](#)
- EBENDORFF-HEIDPRIEM-H, MOORE-R. C AND MONRO-T. M (2008). Progress in the fabrication of the next-generation soft glass microstructured optical fibers, *Proc. 1st Workshop on Specialty Optical Fibers and Their Applications*, Sao Pedro, Brazil, pp. 95–98. [4.5](#), [5.1](#)

- EBENDORFF-HEIDEPRIEM-H, PETROPOULOS-P, ASIMAKIS-S, FINAZZI-V, MOORE-R. C, FRAMPTON-K, KOIZUMI-F, RICHARDSON-D. J AND MONRO-T. M (2004). Bismuth glass holey fibers with high nonlinearity, *Optics Express*, **12**(21), pp. 5082–5087. [3.2](#)
- EBENDORFF-HEIDEPRIEM-H, WARREN-SMITH-S. C AND MONRO-T. M (2009). Suspended nanowires: Fabrication, design and characterization of fibers with nanoscale cores, *Optics Express*, **17**(4), pp. 2646–2657. [3.2](#), [3.5.1](#), [7.3.4](#)
- ELSASSER-W. M (1949). Attenuation in a dielectric circular rod, *Journal of Applied Physics*, **20**, pp. 1193–1196. [3.5.1](#), [3.5.1](#)
- ESHRAGHIAN-K (2006). SoC emerging technologies, *Proceedings of the IEEE*, **94**(6), pp. 1197–1213. [1.1](#)
- FATTINGER-C AND GRISCHKOWSKY-D (1988). Point-source terahertz optics, *Applied Physics Letters*, **53**(16), pp. 1480–1482. [1.1](#)
- FEDERICI-J. F, SCHULKIN-B, HUANG-F, GARY-D, BARAT-R, OLIVEIRA-F AND ZIMDARS-D (2005). THz imaging and sensing for security applications - explosives, weapons and drugs, *Semiconductor Science and Technology*, **20**(7), pp. S266–S280. [1.1](#)
- FISCHER-B. M (2005). *Broadband THz Time-Domain Spectroscopy of Biomolecules*, PhD thesis, University of Freiburg. [2.3.2](#), [3.3](#)
- FISCHER-B. M, HELM-H AND JEPSEN-P. U (2007). Chemical recognition with broadband THz spectroscopy, *Proceedings of the IEEE*, **95**(8), pp. 1592–1604. [1.1](#)
- FISCHER-B. M, HOFFMANN-M, HELM-H, WILK-R, RUTZ-F, KLEINE-OSTMANN-T, KOCH-M AND JEPSEN-P. U (2005). Terahertz time-domain spectroscopy and imaging of artificial RNA, *Optics Express*, **13**(14), pp. 5205–5215. [7.3.4](#)
- FITZGERALD-A. J, BERRY-E, ZINOVEV-N. N, WALKER-G. C, SMITH-M. A AND CHAMBERLAIN-J. M (2002). An introduction to medical imaging with coherent terahertz frequency radiation, *Physics in Medicine and Biology*, **47**(7), pp. R67–R84. [1.1](#)
- GALLOT-G, JAMISON-S. P, MCGOWAN-R. W AND GRISCHKOWSKY-D (2000). Terahertz waveguides, *Journal of Optical Society of America B*, **17**(5), pp. 851–863. [1.1](#), [2.3.1](#), [2.3.1](#), [2.4](#), [6.1](#), [6.2](#)
- GENG-Y. F, TAN-X. L, WANG-P AND YAO-J. Q (2008a). Transmission loss and dispersion in plastic terahertz photonic band-gap fibers, *Applied Physics B-Lasers and Optics*, **91**(2), pp. 333–336. [2.3.2](#), [2.16](#), [2.3.2](#)
- GENG-Y. F, TAN-X. L, ZHONG-K, WANG-P AND YAO-J. Q (2008b). Low loss plastic terahertz photonic band-gap fibres, *Chinese Physics Letters*, **25**(11), pp. 3961–3963. [2.3.2](#), [2.3.2](#)
- GÉRÔME-F, JAMIER-R, AUGUSTE-J. L, HUMBERT-G AND BLONDY-J. M (2010). Simplified hollow-core photonic crystal fiber, *Optics Letters*, **35**(8), pp. 1157–1159. [2.3.2](#)
- GOLESTANIRAD-L, MATTES-M AND MOSIG-J. R (2009). Introducing symmetry conditions in the integral equation technique applied to quasi-waveguide structures, *Proc. 2009 13th International Symposium on Antenna Technology and Applied Electromagnetics and the Canadian Radio Sciences Meeting, Antem/Ursi*, pp. 121–123. [4.3](#)

- GOTO-M, QUEMA-A, TAKAHASHI-H, ONO-S AND SARUKURA-N (2004). Teflon photonic crystal fiber as terahertz waveguide, *Japanese Journal of Applied Physics Part 2-Letters*, **43**(2B), pp. L317–L319. [2.3.2](#), [2.21](#), [2.4](#)
- GRIFFITH-A. A (1921). The phenomena of rupture and flow in solids, *Transactions of the Royal Society of London, Series A*, **221**, pp. 163–198. [5.3](#)
- GRISCHKOWSKY-D (2000). Optoelectronic characterization of transmission lines and waveguides by terahertz time-domain spectroscopy, *IEEE Journal on Selected Topics in Quantum Electronics*, **6**(6), pp. 1122–1135. [2.1](#), [2.1](#), [6.2](#)
- GRISCHKOWSKY-D, III-N. I. D, CHEN-J. C AND CHI-C.-C (1987). Electromagnetic shock waves from transmission lines, *Physical Review Letters*, **59**(15), pp. 1663–1666. [2.1](#), [3](#), [2.1](#)
- GUPTA-K. C, GRAG-R, BAHL-I AND BHARTIA-P (1996). *Microstrip Lines and Slotlines*, Artech House, Inc. [1](#)
- HAN-H, PARK-H, CHO-M AND KIM-J (2002). Terahertz pulse propagation in a plastic photonic crystal fiber, *Applied Physics Letters*, **80**(15), pp. 2634–2636. [1.1](#), [2.3.2](#), [2.21](#), [2.4](#), [5.1](#)
- HARRINGTON-J. A (2000). A review of IR transmitting, hollow waveguides, *Fiber and Integrated Optics*, **19**(3), pp. 211–227. [2.3.2](#)
- HARRINGTON-J. A, GEORGE-R, PEDERSEN-P AND MUELLER-E (2004). Hollow polycarbonate waveguides with inner Cu coatings for delivery of terahertz radiation, *Optics Express*, **12**(21), pp. 5263–5268. [2.3.2](#)
- HASSANI-A, DUPUIS-A AND SKOROBOGATIY-M (2008a). Low loss porous terahertz fibers containing multiple subwavelength holes, *Applied Physics Letters*, **92**, art. no. 071101. [4.4.3](#), [4.5](#)
- HASSANI-A, DUPUIS-A AND SKOROBOGATIY-M (2008b). Porous polymer fibers for low-loss terahertz guiding, *Optics Express*, **16**(9), pp. 6340–6351. [4.4.3](#), [4.5](#)
- HIDAKA-T, MINAMIDE-H, ITO-H, I. NISHIZAWA-J, TAMURA-K AND ICHIKAWA-S (2005). Ferroelectric pvdf cladding terahertz waveguide, *Journal of Lightwave Technology*, **23**(8), pp. 2469–2473. [2.3.2](#), [2.4](#)
- HIDAKA-T, MINAMIDE-H, ITO-H, MAETA-S.-I AND AKIYAMA-T (2003). Ferroelectric PVDF cladding THz waveguide, *Proc. Proceedings of SPIE, Optical Information, Data Processing and Storage, and Laser Communication Technologies*, pp. 70–77. [2.3.2](#)
- HIDAKA-T, MOROHASHI-I, KOMORI-K, NAKAGAWA-H AND ITO-H (2000). THz wave hollow waveguide with ferroelectric PVDF polymer as the cladding material, *Proc. IEEE Lasers and Electro-Optics Europe*. [2.3.2](#)
- ITOH-T (1989). *Numerical Techniques for Microwave and Millimeter-Wave Passive Structures*, John Wiley & Sons, Inc. [4.3](#), [15](#)
- ITO-T, MATSUURA-Y, MIYAGI-M, MINARNIDE-H AND ITO-H (2007). Flexible terahertz fiber optics with low bend-induced losses, *Journal of the Optical Society of America B-Optical Physics*, **24**(5), pp. 1230–1235. [2.3.2](#)

- JÄCKLE-J AND KAWASAKI-K (1995). Intrinsic roughness of glass surfaces, *Journal of Physics-Condensed Matter*, **7**(23), pp. 4351–4358. [3.5.1](#)
- JAMISON-S. P, MCGOWAN-R. W AND GRISCHKOWSKY-D (2000). Single-mode waveguide propagation and reshaping of sub-ps terahertz pulses in sapphire fibers, *Applied Physics Letters*, **76**(15), pp. 1987–1989. [1.1](#), [2.3.2](#), [2.4](#)
- JEON-T.-I AND GRISCHKOWSKY-D (2004). Direct optoelectronic generation and detection of sub-ps-electrical pulses on sub-mm-coaxial transmission lines, *Applied Physics Letters*, **85**(25), pp. 6092–6094. [1.1](#), [2.3.1](#)
- JEON-T.-I AND GRISCHKOWSKY-D (2006). THz Zenneck surface wave (THz surface plasmon) propagation on a metal sheet, *Applied Physics Letters*, **88**, art. no. 061113. [1.1](#)
- JEON-T.-I, ZHANG-J AND GOOSSEN-K. W (2005). THz Sommerfeld wave propagation on a single metal wire, *Applied Physics Letters*, **86**, p. 161904. [1.1](#), [2.3.1](#), [2.3.1](#), [2.12](#), [2.4](#), [6.1](#)
- JEPSEN-P. U AND FISCHER-B. M (2005). Dynamic range in terahertz time-domain transmission and reflection spectroscopy, *Optics Letters*, **30**(1), pp. 29–31. [3.3](#)
- KARPOWICZ-N, DAI-J, LU-X, CHEN-Y, YAMAGUCHI-M, ZHAO-H, ZHANG-X.-C, ZHANG-L, ZHANG-C, PRICE-GALLAGHER-M, FLECTCHER-C, MAMER-O, LESIMPLE-A AND KEITH-J (2008). Coherent heterodyne time-domain spectrometry covering the entire terahertz gap, *Applied Physics Letters*, **92**, p. 011131. [4.4.3](#)
- KATAGIRI-T, MATSUURA-Y AND MIYAGI-M (2004). Photonic bandgap fiber with a silica core and multilayer dielectric cladding, *Optics Letters*, **29**(6), pp. 557–559. [2.3.2](#), [2.3.2](#)
- KEISER-G (1991). *Optical Fiber Communications*, second edn, McGraw-Hill. [3.5.1](#), [3.5.2](#)
- KETCHEN-M. B, GRISCHKOWSKY-D, CHEN-T. C, CHI-C. C, DULING-N. I, HALAS-N. J, HALBOUT-J.-M, KASH-J. A AND LI-G. P (1986). Generation of subpicosecond electrical pulses on coplanar transmission lines, *Applied Physics Letters*, **48**(12), pp. 751–753. [1.1](#), [2.1](#)
- KING-M. J AND WILTSE-J. C (1962). Surface-wave propagation on coated or uncoated metal wires at millimeter wavelengths, *Institute of Radio Engineers Transactions on Antennas and Propagation*, **10**(3), pp. 246–254. [2.3.1](#)
- KNIGHT-J. C, BIRKS-T. A, RUSSELL-P. S AND ATKIN-D. M (1996). All-silica single-mode optical fiber with photonic crystal cladding, *Optics Letters*, **21**(19), pp. 1547–1549. [2.3.2](#), [2.3.2](#)
- KNIGHT-J. C, BROENG-J, BIRKS-T. A AND RUSSEL-P. S. J (1998). Photonic band cap guidance in optical fibers, *Science*, **282**(5393), pp. 1476–1478. [2.3.2](#), [2.3.2](#)
- LAI-C.-H, HSUEH-Y.-C, CHEN-H.-W, HUANG-Y.-J, CHANG-H.-C AND SUN-C.-K (2009). Low-index terahertz pipe waveguides, *Optics Letters*, **34**(21), pp. 3457–3459. [2.3.2](#), [2.15](#), [2.4](#), [3.5](#), [6.1](#)
- LAMBERT-D. K AND RICHARDS-P. L (1978). Martin-Puplett interferometer: an analysis, *Applied Optics*, **17**(10), pp. 1595–1602. [2.3.2](#)
- LAW-S. H, HARVEY-J. D, KRHLAK-R. J, SONG-M, WU-E, BARTON-G. W, v. EIJKELENBORG-M. A AND LARGE-M. C. J (2006a). Cleaving of microstructured polymer optical fibres, *Optics Communications*, **258**, pp. 193–202–. [5.3](#)

- LAW-S. H, VAN EIJKELBORG-M. A, BARTON-G. W, YAN-C, LWIN-R AND GAN-J (2006b). Cleaved end-face quality of microstructured polymer optical fibres, *Optics Communications*, **265**, pp. 513–520. [5.1](#), [5.3](#)
- LEE-Y.-S (2009). *Principles of Terahertz Science and Technology*, Springer Science+Business Media, NY, USA. [2.2](#), [2.2](#), [2.2.1](#), [2.3](#), [2.4](#), [2.5](#)
- LIPPERT-T AND DICKINSON-J. T (2003). Chemical and spectroscopic aspects of polymer ablation: Special features and novel directions, *Chemical Reviews*, **103**(2), pp. 453–485. [5.3.3](#)
- LLOMBART-N, MAZZINGHI-A, SIEGEL-P. H AND FRENI-A (2009). Design of a low loss metallo-dielectric ebg waveguide at submillimeter wavelengths, *IEEE Microwave and Wireless Components Letters*, **19**(7), pp. 437–439. [2.3.2](#)
- LONG-X.-C AND BRUECK-S. R. J (1999). Composition dependence of the photoinduced refractive-index change in lead silicate glasses, *Optics Letters*, **24**(16), pp. 1136–1138. [3.1](#)
- LU-J. Y, CHIU-C. M, KUO-C. C, LAI-C, CHANG-H. C, HWANG-Y. J, PAN-C. L AND SUN-C. K (2008a). Terahertz scanning imaging with a subwavelength plastic fiber, *Applied Physics Letters*, **92**(8), art. no. 084102. [2.3.2](#), [3.5.1](#)
- LU-J.-Y, KUO-C.-C, CHIU-C.-M, CHEN-H.-W, HWANG-Y.-J, PAN-C.-L AND SUN-C.-K (2008b). THz interferometric imaging using subwavelength plastic fiber based THz endoscopes, *Optics Express*, **16**(4), pp. 2494–2501. [2.3.2](#), [3.5.1](#)
- LU-J.-Y, YU-C.-P, CHANG-H.-C, CHEN-H.-W, LI-Y.-T, PAN-C.-L AND SUN-C.-K (2008c). Terahertz air-core microstructure fiber, *Applied Physics Letters*, **92**, art. no. 064105. [2.3.2](#), [2.19](#), [2.3.2](#), [2.4](#), [5.1](#)
- MATSUURA-Y AND TAKEDA-E (2008). Hollow optical fibers loaded with an inner dielectric film for terahertz broadband spectroscopy, *Journal of the Optical Society of America B-Optical Physics*, **25**(12), pp. 1949–1954. [2.3.2](#), [2.4](#)
- MBONYE-M, MENDIS-R AND MITTLEMAN-D. M (2009). A terahertz two-wire waveguide with low bending loss, *Applied Physics Letters*, **95**(23), art. no. 051105. [2.3.1](#)
- MCGOWAN-R. W AND GRISCHKOWSKY-D (1999). Experimental time-domain study of THz signals from impulse excitation of a horizontal surface dipole, *Applied Physics Letters*, **74**(12), pp. 1764–1766. [6.3.1](#)
- MCGOWAN-R. W, GALLOT-G AND GRISCHKOWSKY-D (1999). Propagation of ultrawideband short pulses of terahertz radiation through submillimeter-diameter circular waveguides, *Optics Express*, **24**(20), pp. 1431–1433. [1.1](#), [2.1](#), [2.3.1](#), [2.3.1](#), [2.4](#), [6.1](#), [6.2](#)
- MENDIS-R (2001). *First Broadband Experimental Study of Planar THz Waveguides*, PhD thesis, Oklahoma State University. [2.9](#), [2.3.1](#), [2.10](#), [6.2](#)
- MENDIS-R (2006). Nature of subpicosecond terahertz pulse propagation in practical dielectric-filled parallel-plate waveguides, *Optics Letters*, **31**(17), pp. 2643–2645. [1.1](#)
- MENDIS-R AND GRISCHKOWSKY-D (2000). Plastic ribbon THz waveguides, *Journal of Applied Physics*, **88**(7), pp. 4449–4451. [1.1](#), [2.3.2](#), [2.4](#)

- MENDIS-R AND GRISCHKOWSKY-D (2001a). THz interconnect with low-loss and low-group velocity dispersion, *Microwave and Wireless Components Letters*, **11**(11), pp. 444–446. [1.1](#), [2.3.1](#), [2.4](#)
- MENDIS-R AND GRISCHKOWSKY-D (2001b). Undistorted guided-wave propagation of subpicosecond terahertz pulses, *Optics Letters*, **26**(11), pp. 846–848. [1.1](#), [2.3.1](#), [2.4](#), [6.1](#), [6.2](#)
- MENDIS-R AND MITTLEMAN-D. M (2009a). Comparison of the lowest-order transverse-electric (TE₁) and transverse-magnetic (TEM) modes of the parallel-plate waveguide for terahertz pulse applications, *Optics Express*, **17**(17), pp. 14839–14850. [2.3.1](#), [2.3.1](#), [2.4](#), [3.5](#)
- MENDIS-R AND MITTLEMAN-D. M (2009b). An investigation of the lowest-order transverse-electric (TE₁) mode of the parallel-plate waveguide for THz pulse propagation, *Journal of the Optical Society of America B-Optical Physics*, **26**(9), pp. A6–A13. [2.3.1](#), [2.4](#)
- MENDIS-R, ASTLEY-V, LIU-J. B AND MITTLEMAN-D. M (2009). Terahertz microfluidic sensor based on a parallel-plate waveguide resonant cavity, *Applied Physics Letters*, **95**(17). [1.1](#)
- MILLIGAN-T. A (2005). *Modern Antenna Design*, second edn, John Wiley & Sons, Inc. [4.3](#)
- MITTLEMAN-D (2003). *Sensing with Terahertz Radiation*, Springer-Verlag. [1.1](#), [3.3](#)
- MOHR-P. J AND TAYLOR-B. N (2005). CODATA recommended values of the fundamental physical constants: 2002, *Reviews of Modern Physics*, **77**(7), pp. 1–107.
- MONRO-T. M (2007). Beyond the diffraction limit, *Nature Photonics*, **1**, pp. 89–90. [4.1](#), [4.2](#)
- MONRO-T. M AND EBENDORFF-HEIDEPRIEM-H (2006). Progress in microstructured optical fibers, *Annual Review of Materials Research*, **36**, pp. 467–495. [5.1](#)
- MOUROU-G, STANCAMPIANO-C. V AND BLUMENTHAL-D (1981a). Picosecond microwave pulse generation, *Applied Physics Letters*, **38**(6), pp. 470–472. [1.1](#)
- MOUROU-G, STANCAMPIANO-C. V, ANTONETTI-A AND ORSZAG-A (1981b). Picosecond microwave pulses generated with a subpicosecond laser-driven semiconductor switch, *Applied Physics Letters*, **39**(4), pp. 295–296. [1.1](#)
- NAFTALY-M AND MILES-R. E (2007). Terahertz time-domain spectroscopy for material characterization, *Proceedings of the IEEE*, **95**(8), pp. 1658–1665. [1.1](#)
- NAGEL-M, FORST-M AND KURZ-H (2006a). THz biosensing devices: fundamentals and technology, *Journal of Physics-Condensed Matter*, **18**(18), pp. S601–S618. [1.1](#), [2.3.2](#)
- NAGEL-M, MARCHEWKA-A AND KURZ-H (2006b). Low-index discontinuity terahertz waveguides, *Optics Express*, **14**(21), pp. 9944–9954. [1.1](#), [2.3.2](#), [2.23](#), [2.3.2](#), [2.4](#), [4.1](#), [4.2](#), [6.2](#)
- NAGEL-M, RICHTER-F, HARING-BOLVIAR-P AND KURZ-H (2003). A functionalized THz sensor for marker-free DNA analysis, *Physics in Medicine and Biology*, **48**, pp. 3625–3636. [7.3.4](#)
- NGUYEN-C (2000). *Analysis Methods for RF, Microwave, and Millimeter-Wave Planar Transmission Line Structures*, John Wiley & Sons, Inc. [2](#)
- NIELSEN-K, RASMUSSEN-H. K, ADAM-A. J. L, PLANKEN-P. C. M, BANG-O AND JEPSEN-P. U (2009). Bendable, low-loss topas fibers for the terahertz frequency range, *Optics Express*, **17**(11), pp. 8592–8601. [2.3.2](#), [2.22](#), [2.4](#), [5.1](#), [6.1](#)

- NODA-J, OKAMOTO-K AND SASAKI-Y (1986). Polarization-maintaining fibers and their applications, *Journal of Lightwave Technology*, **4**(8), pp. 1071–1089. [3.5.2](#)
- OKAMOTO-K (2000). *Fundamentals of Optical Waveguides*, Academic Press, San Diego. [3.4](#), [3.4](#), [A](#), [A](#)
- PEDROTTI-F. L AND PEDROTTI-L. S (1993). *Intorduction to Optics*, Prentice-Hall, Inc. [3.3](#)
- PICOMETRIX (Accessed: July 2010). *PICOMETRIX*, <<http://www.picometrix.com/>>. [3.3](#)
- PNG-G. M (2010). *Terahertz spectroscopy and modelling of biotissue*, PhD thesis, The University of Adelaide. [1.1](#)
- PONSECA-C. S, POBRE-R, ESTACIO-E, SARUKURA-N, ARGYROS-A, LARGE-M. C. J AND VAN EIJKELNBORG-M. A (2008). Transmission of terahertz radiation using a microstructured polymer optical fiber, *Optics Letters*, **33**(9), pp. 902–904. [2.3.2](#), [2.17](#), [2.3.2](#), [2.18](#), [2.4](#), [5.1](#), [6.1](#)
- POPPE-A, XU-L, KRAUSZ-F AND SPIELMANN-C (1998). Noise characterization of sub-10-fs Ti:sapphire oscillators, *IEEE Journal of Selected Topics in Quantum Electronics*, **4**(2), pp. 179–184. [6.3.1](#)
- REN-G, GONG-Y, SHUM-P, YU-X, HU-J, WANG-G, CHUEN-M. O. L AND PAULOSE-V (2008). Low-loss air-core polarization maintaining terahertz fiber, *Optics Express*, **16**(18), pp. 13593–13598. [1.3](#), [2.3.2](#), [2.3.2](#), [4.4.3](#), [7.2](#)
- ROBERTS-P. J, COUNY-F, SABERT-H, MANGAN-B. J, BIRKS-T. A, KNIGHT-J. C AND RUSSELL-P. S. J (2005). Loss in solid-core photonic crystal fibers due to interface roughness scattering, *Optics Express*, **13**(20), pp. 7779–7793. [2.3.2](#), [3.5.1](#), [3.5.1](#)
- RØNNE-C, ÅSTRAND-P.-O AND KEIDING-S. R (1999). THz spectroscopy of liquid H₂O and D₂O, *Physical Review Letters*, **82**(14), pp. 2888–2891. [3.3](#)
- ROWLAND-K. J (2010). *Guiding Light in Low-Index Media via Multilayer Waveguides*, PhD thesis, The University of Adelaide. [2.3.2](#), [2.3.2](#), [2.17](#)
- SAEEDKIA-D, MANSOUR-R. R AND SAFAVI-NAEINI-S (2005). Analysis and design of a continuous-wave terahertz photoconductive photomixer array source, *IEEE Transactions on Antennas and Propagation*, **53**(12), pp. 4044–4050. [6.3.2](#)
- SAITOH-K AND KOSHIBA-M (2005). Numerical modeling of photonic crystal fibers, *Journal of Lightwave Technology*, **23**(11), pp. 3580–3590. [4.3](#)
- SAKAI-K (2005). *Terahertz Optoelectronics*, Springer, Berlin, Heidelberg. [1.1](#), [1.1](#), [2.2](#), [2.6](#), [2.1](#), [2.8](#), [8](#)
- SCHELLER-M, JORDENS-C AND KOCH-M (2010). Terahertz form birefringence, *Optics Express*, **18**(10), pp. 10137–10142. [4.4.3](#)
- SCHOTT (Accessed: February 2010). *SCHOTT glass made of ideas*, <<http://www.schott.com/>>. [3.3](#)
- SHI-J. W, CHU-S. W, TIEN-M. C, SUN-C. K, CHIU-Y. J AND BOWERS-J. E (2002). Edge-coupled membrane terahertz photonic transmitters based on metal-semiconductor-metal traveling-wave photodetectors, *Applied Physics Letters*, **81**(27), pp. 5108–5110. [11](#)
- SKOROBOGATIY-M AND DUPUIS-A (2007). Ferroelectric all-polymer hollow bragg fibers for terahertz guidance, *Applied Physics Letters*, **90**, art. no. 113514. [2.3.2](#), [2.3.2](#), [2.4](#)

- SMITH-P. R, AUSTON-D. H AND AUGUSTYNYIAK-W. M (1981). Measurement of gas field-effect transistor electronic impulse-response by picosecond optical electronics, *Applied Physics Letters*, **39**(9), pp. 739–741. [1.1](#), [2.1](#)
- SNYDER-A. W AND LOVE-J. D (2000). *Optical Waveguide Theory*, Kluwer, London. [3.4](#), [3.4](#), [3.4.1](#), [3.4.1](#), [3.4.2](#), [3.5.1](#), [3.5.1](#), [14](#), [3.5.1](#), [3.5.1](#), [3.5.1](#), [3.5.1](#), [3.5.1](#), [4.3](#), [A](#)
- SOMMERFELD-A (1952). *Electrodynamics*, Academic, New York. [3.2](#)
- SON-J, RUDD-J. V AND WHITAKER-J. F (1992). Noise characterization of a self-mode-locked Ti:Sapphire laser, *Optics Letters*, **17**(10), pp. 733–735. [6.3.1](#)
- SPRIK-R, DULING-I. N, CHI-C. C AND GRISCHKOWSKY-D (1987). Far infrared-spectroscopy with subpicosecond electrical pulses on transmission-lines, *Applied Physics Letters*, **51**(7), pp. 548–550. [2.1](#)
- STRATTON-J (1941). *Electromagnetic Theory*, McGraw-Hill, New York. [3.2](#)
- SUGIMOTO-N, KANBARA-H, FUJIWARA-S, TANAKA-K, SHIMIZUGAWA-Y AND HIRAO-K (1999). Third-order optical nonlinearities and their ultrafast response in $\text{Bi}_2\text{O}_3\text{B}_2\text{O}_3\text{SiO}_2$ glasses, *Journal of Optical Society of America B*, **16**(11), pp. 1904–1908. [3.3](#), [3.1](#)
- SUMETSKY-M, DULASHKO-Y AND A.-H (2004). Fabrication and study of bent and coiled free silica nanowires: Self-coupling microloop optical interferometer, *Optics Express*, **12**(15), pp. 3521–3531. [3.5.1](#), [3.5.1](#)
- SUZUKI-K, KUBOTA-H, KAWANISHI-S, TANAKA-M AND FUJITA-M (2001). Optical properties of a low-loss polarization-maintaining photonic crystal fiber, *Optics Express*, **19**(13), pp. 676–680. [3.5.2](#), [4.4.3](#)
- TANG-X. L, SHI-Y. W, MATSUURA-Y, IWAI-K AND MIYAGI-M (2009). Transmission characteristics of terahertz hollow fiber with an absorptive dielectric inner-coating film, *Optics Letters*, **34**(14), pp. 2231–2233. [2.3.2](#)
- TEMELKURAN-B, HART-S. D, BENOIT-G, JOANNOPOULOS-J. D AND FINK-Y (2002). Wavelength-scalable hollow optical fibres with large photonic bandgaps for CO_2 laser transmission, *Nature*, **420**(6916), pp. 650–653. [2.3.2](#), [2.3.2](#)
- TIEN-M. C, CHANG-H. H, LU-J. Y, CHEN-L. J, CHEN-S. Y, WU-R. B, LIU-W. S, CHYI-J. I AND SUN-C. K (2004). Device saturation behavior of submillimeter-wave membrane photonic transmitters, *IEEE Photonics Technology Letters*, **16**(3), pp. 873–875. [11](#)
- TONG-L, GATTASS-R. R, ASHCOM-J. B, HE-S, LOU-J, SHEN-M, MAXWELL-I AND MAZUR-E (2003). Subwavelength-diameter silica wires for low-loss optical wave guiding, *Nature*, **426**(18), pp. 816–819. [2.3.2](#), [3.1](#), [3.1](#), [3.2](#), [3.2](#)
- TONOUCHI-M (2007). Cutting-edge terahertz technology, *Nature Photonics*, **1**(2), pp. 97–105. [1.1](#)
- TREIZEBRE-A, AKALIN-T AND BOCQUET-B (2005). Planar excitation of Goubau transmission lines for THz BioMEMS, *IEEE Microwave and Wireless Components Letters*, **15**(12), pp. 886–888. [2.1](#)

- VAN EXTER-M, FATTINGER-C AND GRISCHKOWSKY-D (1989a). High-brightness terahertz beams characterized with an ultrafast detector, *Applied Physics Letters*, **55**(4), pp. 337–339. [1.1](#), [2.1](#), [2.2.2](#)
- VAN EXTER-M, FATTINGER-C AND GRISCHKOWSKY-D (1989b). Terahertz time-domain spectroscopy of water vapor, *Optics Letters*, **14**(20), pp. 1128–1130. [1.1](#), [2.1](#), [3.3](#)
- VINCETTI-L (2009a). Hollow core photonic band gap fiber for THz applications, *Microwave and Optical Technology Letters*, **51**(7), pp. 1711–1714. [2.16](#), [2.3.2](#), [2.3.2](#), [2.4](#)
- VINCETTI-L (2009b). Numerical analysis of plastic hollow core microstructured fiber for terahertz applications, *Optical Fiber Technology*, **15**(4), pp. 398–401. [2.3.2](#), [2.3.2](#), [2.4](#)
- VINCETTI-L (2010). Single-mode propagation in triangular tube lattice hollow-core terahertz fibers, *Optics Communications*, **283**(6), pp. 979–984. [2.3.2](#), [2.4](#)
- VINCETTI-L AND POLEMI-A (2009). Hollow core fibre for THz applications, *Proc. IEEE, Antennas and Propagation Society International Symposium*, 10.1109/APS.2009.5171653, pp. 1–4. [2.3.2](#)
- WÄCHTER-M, NAGEL-M AND KURZ-H (2005). Frequency-dependent characterization of THz Sommerfeld wave propagation on single-wires, *Optics Express*, **13**(26), pp. 10815–10822. [1.1](#), [2.3.1](#), [2.3.1](#), [2.13](#), [2.4](#), [6.1](#), [6.3.2](#)
- WÄCHTER-M, NAGEL-M AND KURZ-H (2007). Metallic slit waveguide for dispersion-free low-loss terahertz signal transmission, *Applied Physics Letters*, **90**, art. no. 061111. [1.1](#), [2.3.1](#), [2.3.1](#), [2.3.1](#), [2.14](#), [2.4](#), [6.3.1](#), [6.3.2](#)
- WÄCHTER-M, NAGEL-M AND KURZ-H (2009). Tapered photoconductive terahertz field probe tip with subwavelength spatial resolution, *Applied Physics Letters*, **95**(4), art. no. 041112. [6.3.2](#)
- WANG-K AND MITTLEMAN-D. M (2004). Metal wires for terahertz wave guiding, *Nature*, **432**, pp. 376–379. [1.1](#), [2.3.1](#), [2.3.1](#), [2.11](#), [2.4](#), [6.1](#), [6.3.2](#)
- WANG-S.-Y (2002). *Microstructured Optical Fiber with Improved Transmission Efficiency and Durability*, United States Patent. [4.3](#)
- WEN-C. P (1969). Coplanar waveguide . a surface strip transmission line suitable for nonreciprocal gyro-magnetic device applications, *IEEE Transactions on Microwave Theory and Techniques*, **MT17**(12), pp. 1087–1090. [2](#)
- WIEDERHECHER-G. S, CORDEIRO-C. M. B, COUNY-F, BENABID-F, MAIER-S. A, KNIGHT-J. C, CRUS-C. H. B AND L. FRAGNITO-H (2007). Field enhancement within an optical fibre with a subwavelength air core, *Nature Photonics*, **1**, pp. 115–118. [4.1](#), [4.2](#)
- WILLIAMS-B. S (2007). Terahertz quantum-cascade lasers, *Nature Photonics*, **1**(9), pp. 517–525. [2.2.1](#)
- WITHAYACHUMNANKUL-W (2009). *Engineering Aspects of Terahertz Time-Domain Spectroscopy*, PhD thesis, The University of Adelaide. [1.1](#), [3](#)
- WITHAYACHUMNANKUL-W, FISCHER-B. M, FERGUSON-B, DAVIS-B. R AND ABBOTT-D (2010). A systemized view of superluminal wave propagation, *Proceedings of the IEEE*, **98**(10), pp. 1775–1786. [3.5.2](#)

- WITHAYACHUMNANKUL-W, PNG-G. M, YIN-X, ATAKARAMIANS-S, JONES-I, LIN-H, UNG-B, BALAKRISHNAN-J, NG-B. W.-H, FERGUSON-B, MICKAN-S. P, FISCHER-B. M AND ABBOTT-D (2007). T-ray sensing and imaging, *Proceedings of the IEEE*, **95**(8), pp. 1528–1558. [1.3](#), [7.2](#)
- XU-Y AND BOSISIO-R. G (2007). A comprehensive study on the planar type of Goubau line for millimetre and submillimetre wave integrated circuits, *IET Microwaves Antennas and Propagation*, **1**(3), pp. 681–687. [2.1](#)
- XU-Y. S, SINGH-J, JASON-T. H. S, RAMAKRISHNA-K, PREMCHANDRAN-C. S, KELVIN-C. W. S, KUAN-C. T, CHEN-N. G, OLIVO-M. C AND SHEPPARD-C. J. R (2007). MEMS based non-rotatory circumferential scanning optical probe for endoscopic optical coherence tomography, *Proc. Optical Coherence Tomography and Coherence Techniques III*, Bellingham, p. 62715. [2.3](#)
- YAN-M AND MORTENSEN-N. A (2009). Hollow-core infrared fiber incorporating metal-wire metamaterial, *Optics Express*, **17**(17), pp. 14851–14864. [2.3.2](#)
- YOU-B, LIU-T. A, PENG-J. L, PAN-C. L AND LU-J. Y (2009). A terahertz plastic wire based evanescent field sensor for high sensitivity liquid detection, *Optics Express*, **17**(23), pp. 20675–20683. [2.3.2](#), [3.5.1](#)
- YOU-B. W, LU-J. Y, LIU-T. A, PENG-J. L AND PAN-C. L (2010). Subwavelength plastic wire terahertz time-domain spectroscopy, *Applied Physics Letters*, **96**(5), art. no. 051105. [2.3.2](#), [3.5.1](#)
- YU-R. J, ZHANG-B, ZHANG-Y. Q, WU-C. Q, TIAN-Z. G AND BAI-X. Z (2007). Proposal for ultralow loss hollow-core plastic Bragg fiber with cobweb-structured cladding for terahertz waveguiding, *IEEE Photonics Technology Letters*, **19**(9-12), pp. 910–912. [2.3.2](#), [2.17](#), [2.3.2](#), [2.4](#)
- ZHANG-X. C, JIN-Y, HEWITT-T. D, SANGSIRI-T, KINGSLEY-L. E AND WEINER-M (1993). Magnetic switching of THz beams, *Applied Physics Letters*, **62**(17), pp. 2003–2005. [8](#)
- ZHAO-C, WU-M, FAN-D AND WEN-S (2008). Field enhancement and power distribution characteristics of subwavelength-diameter terahertz hollow optical fiber, *Optics Communications*, **281**, pp. 1129–1133. [4.2](#)
- ZHELTIKOV-A (2005). Gaussian-mode analysis of waveguide-enhanced Kerr-type nonlinearity of optical fibers and photonic wires, *Journal of Optical Society of America B*, **22**(5), pp. 1100–1104. [4.3](#)
- ZHU-Z. M AND BROWN-T. G (2002). Full-vectorial finite-difference analysis of microstructured optical fibers, *Optics Express*, **10**(17), pp. 853–864. [4.3](#)

Glossary

The physical constants used in this thesis are in accordance with a recommendation of the Committee on Data for Science and Technology (Mohr and Taylor 2005).

Quantity	Symbol	Value
Boltzmann constant	k_b	$1.3806505 \times 10^{-23} \text{ J/K}$
		$8.617343 \times 10^{-5} \text{ eV/K}$
electron volt	eV	$1.60217653 \times 10^{-19} \text{ J}$
Planck constant	h	$6.6260693 \times 10^{-34} \text{ J.s}$
		$4.135\ 66743 \times 10^{-15} \text{ eV.s}$
speed of light in vacuum	c, c_0	$2.99792458 \times 10^8 \text{ m/s}$
vacuum permeability (magnetic constant)	μ_0	$4\pi \times 10^{-7} \text{ N/A}^2$
vacuum permittivity (electric constant)	ϵ_0	$8.854187817 \times 10^{-12} \text{ F/m}$

Acronyms

BOL	bolometer
BWO	backward wave oscillator
CCD camera	charge-coupled device camera
COC	cyclic-olefin copolymer
CP	cylindrically periodic
CW	continuous wave
DNA	deoxyribonucleic acid
EDX	energy dispersive X-ray
FDM	finite difference method
FEM	finite element method
FEL	free electron laser
FIB milling	focused ion beam milling
FTIR	Fourier transform infrared
GaAs	gallium arsenide
GDC	grating dispersion compensator
GVD	group velocity dispersion
HCF	hollow-core fibre
HDPE	high density polyethylene
HEM	hybrid mode (combination of TE(H) and TM(E) modes)
InP	Indium phosphide
LIA	lock-in amplifier
IR	infrared
LT-GaAs	low temperature grown GaAs
MOF	microstructured optical fibre
PC	polycarbonate
PC antenna	photoconductive antenna

PCF	photonic crystal fibre
PE	polyethylene
PEC	perfect electric conductor
PM	polarisation maintaining
PMC	perfect magnetic conductor
PML	perfectly matched layer
PMMA	polymethyl methacrylate
PS	polystyrene
PVC	polyvinyl chloride
PVDF	ferroelectric poly vinylidene flouride
QCL	quantum cascade laser
RD-SOS	radiation damaged SOS
SD saw	semiconductor dicing saw
SEM	scanning electron microscope
SOS	silicon-on-sapphire
SNR	signal-to-noise ratio
TDS	time-domain spectroscopy
TE	transverse electric
TEM	transverse electric and magnetic
THz	terahertz
THz-TDS	terahertz time-domain spectroscopy
TM	transverse magnetic
UV	ultraviolet

Biography

Shaghik Atakaramians received her bachelors degree from Iran University of Science and Technology (IUST) in 2000 and the masters degree from University of Tehran in 2002. Her Masters thesis was entitled “An equivalent network model for full-wave analysis of two-dimensional photonic crystals.” She was awarded the first prize for the best telecommunication graduate of the Department of Electrical Engineering, IUST, in 2000, and first prize for the best telecommunication undergraduate in 1999 and the best job trainee of the electrical engineering faculty of IUST in the summer of 1999.

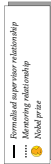


In 2006, Shaghik Atakaramians joined T-ray group of The University of Adelaide as a visiting scholar under Derek Abbott. In 2007, she was granted an Australian Endeavour International Postgraduate Research Scholarship (EIPRS) and University of Adelaide Scholarship for Postgraduate Research to study towards her PhD under the supervision of Prof Derek Abbott, Dr Shahraam Afshar V., Dr Bernd M. Fischer, and Prof Tanya M. Monro, within the Adelaide T-ray group, the School of Electrical & Electronic Engineering, The University of Adelaide.

During her candidature, she has received a poster presentation award at the Research Expo, organised by student chapter of the IEEE at University of Adelaide, 2009; ARC Nanotechnology Network (ARCNN) Overseas Travel Fellowship, 2008; IEEE South Australia Travel Assistance Award, 2008; Research Abroad Scholarship, University of Adelaide, 2008; and the Incubic/Milton Chang Travel Award for CLEO/QELS conference (USA), 2007. She has authored and co-authored 18 publications, and has given 8 presentations at conferences.

Shaghik Atakaramians is a member of the IEEE (Institute of Electrical and Electronics Engineers), OSA (Optical Society of America), and AOS (The Australian Optical Society). She has been serving as secretary of IEEE-SA Women In Engineering Affinity for two consecutive years.

Scientific Genealogy of Shaghik Atakaramians



This page can be read by zooming into the pdf version.

